Interactions between molecules and nanostructures using quartz crystal microbalance

Juan Antonio Rubio-Lara

Supervisor: Prof. Mark Welland

Advisor: Prof. Ashwin Seshia

Department of Engineering
University of Cambridge

This dissertation is submitted for the degree of:

Doctor of Philosophy

Fitzwilliam College September 2018

Declaration

This dissertation is the result of my own work and includes nothing which is the outcome of work done in collaboration except as declared in the Preface and specified in the text. It is not substantially the same as any that I have submitted, or, is being concurrently submitted for a degree or diploma or other qualification at the University of Cambridge or any other University or similar institution except as declared in the Preface and specified in the text. I further state that no substantial part of my dissertation has already been submitted, or, is being concurrently submitted for any such degree, diploma or other qualification at the University of Cambridge or any other University or similar institution except as declared in the Preface and specified in the text. This dissertation contains fewer than 65,000 words including appendices, bibliography, footnotes, tables and equations. There are no more than 150 figures in this document.

Juan Antonio Rubio-Lara

September 2018

Interactions between molecules and nanostructures using quartz crystal microbalance

Juan Antonio Rubio-Lara

Abstract

The understanding of protein behaviour at the nanoscale is critical for the development of new therapies and biosensing. The assembly of peptides for new therapies are performed on the surface of a biosensor and because of the rough nature of this sample, the characterisation is usually performed on a separate substrate that will provide a higher contrast with a different technique. The ideal scenario is for the same surface to be used in both sensing and characterisation stages. For biosensing, the rough nature of the surface could increase the range of mass measurement for biosensors with micro and nanoscale surfaces. Additionally, the interaction of proteins with nanostructures open the possibility of altering the dynamics of protein adsorption. These changes could be translated to different mechanical properties of the sensed protein. Furthermore, the induced conformational change might allow for a permanent attachment of the protein, increasing the limit of detection of a biosensor. However, the behaviour of proteins with nanoscale features is not well understood. Therefore, the fabrication of nanostructured surfaces along with eliminating such features on QCM biosensors for sensing and characterisation of proteins is pursued in this dissertation.

Multiple novel methods of nanofabrication on top of QCM gold electrodes were created using ZnO nanowires (Chapter 1), gold nanoparticles (Chapter 2), and e-beam lithography (Chapter 5). These techniques were further optimised to obtain simple protocols to be followed by any user. Subsequently, optimal surfaces were used for protein adsorption and their results show less protein adsorption than the expected by the area increase of the features (50-70%), suggesting protein conformational changes (spreading) upon binding.

The observation of protein conformational changes on nanostructures suggested that the roughness of standard gold QCM electrodes might also play a role in protein adsorption. A novel fabrication process is developed for the transfer of an atomically flat surface of gold onto a QCM Au electrode, the pressure-forming template stripped (PTS) technique. In Chapter 3, the PTS method is presented with the crucial parameters for obtaining an atomically flat gold surface on QCM resonators and their optimisation to obtain a roughness of 0.35 nm ± 0.05 root mean square and a required thickness of 100 nm of Au QCM electrodes. Furthermore, the QCM with PTS electrodes (PTS QCM) is used to adsorb model protein bovine serum albumin (BSA). This is compared against resonators with a standard electrode roughness from different companies, and against resonators build in-house with higher roughness than commercial samples. It is showed by both QCM mass monitoring and AFM of the same PTS QCM sample that

BSA adsorption of BSA occurs in a self-assemble like manner, a tightly packed monolayer. More BSA areal mass is adsorbed on PTS QCM (15%) and high roughness QCM (17%) resonators than QCM samples with standard roughness. In contrast with standard QCM, high roughness QCM resonators induce aggregates on the surface increasing the mass adsorbed and obtaining similar areal mass to the tightly packed adsorption on PTS QCM devices.

I dedicate this to my beloved wife, Dulce Aguilar-Garza, and my family, who have been a very great support through these years…

Acknowledgements

I would like to state that there are not enough words to express my gratitude to the persons that have been helpful along the process of completing this thesis. Their support, patience, assistance and advice has been part of my growth as a scientist.

First, I would like to express all the gratitude to my wife Dulce Aguilar-Garza, who has supported me in all my endeavours since I decided to make a career in research. Her constant listening and questioning of the projects I have developed here had made me think in different ways that I would normally thought in a more complicated way. She has been part of helping me get through my PhD by distracting me with extra academic activities like travelling. She has been there with me on my first talk in a conference, where she also presented her work.

All my gratitude goes to my supervisor Prof. Sir Mark Welland. He has been guiding me through the whole project. With him, I have learned how to manage my time and step by step I learned how to efficiently work in the lab. He has been given me freedom and advice to pursue my research ideas, which in other cases might have been a waste of resources and time. I have obtained under his guidance a strong foundation to become an independent researcher in the future.

I would like to extend my gratitude to Fitzwilliam College and the tutors I had through my PhD (Dr. David Coomes and Dr. Roger Kievit). My tutors had been part of the support I received when applying to funding during an extension of my PhD due to delay of materials. This has been crucial for the completion of my doctoral dissertation. The college has been part of the amazing experience I had in Cambridge. The rowing team and the table tennis squad were excellent recreational activities that helped me keep physically active.

My work could also not be possible without the support of the researchers at the Nanoscience Centre. Dr. Yury Alaverdyan, Dr. Simon Attwood, Dr. Iris Batalha and Dr. David Hasko have provided me with their expertise in equipment handling, fabrication and discussion that have enriched my PhD. Additionally, all the technicians that have helped me by fixing equipment, making fixtures and required parts for my research and have kept running some of the old systems that I have used: Roger Bourne, Duncan Bulman and Ian Ganney. I thank all of them for their time, for making easy to assimilate all the fabrication techniques and characterisation tools.

I would like to thank my fellow researchers from the Nanoscience Centre and the Electrical Engineering division, whose constant discussion and challenging of ideas had made my PhD more fruitful. Dr. Jerome Charmet, Dr. Nikhil Tiwale, Dr. Iris Batalha, Edward Tan, Zhuocong Xiao, Sonja Kinna, and Alexandra Vaideanu have been there when I lacked the expertise in certain areas and their profound knowledge has let me quickly understand topics that otherwise it would have taken longer. All these

colleagues have shared with me time as lab-buddies and have speed up the learning of some techniques I used by sharing their experience.

Finally, I would like to thank the support of my family: both my parents and parents in law. My family has been there to support us through everything and have welcomed us back every time we travel back to Mexico. My parents have supported me since I decided to study abroad. Their constant encouragement has been part of my strength to complete this PhD. Their moral support has always been there and their constant communication with us has never let us miss our culture and country. I will also extend my gratitude to all my friends that have been part of this journey as well as my brothers and sister, cousins, brother in law and all the relatives that have been there for us.

Preface

You are about to read the dissertation “Interactions between molecules and nanostructures using quartz crystal microbalance” which is an exploration of fabrication techniques along with biosensing measurements using the quartz crystal microbalance (QCM). It has been written to fulfil the graduation requirements for PhD in Engineering at the University of Cambridge.

The research project was taken at the Nanoscience Centre, University of Cambridge, under the supervision of Prof. Sir Mark Welland, Division of Electrical Engineering. Two publications were product of this work, and the relevant material can be found in Chapter 3 (Langmuir) and Chapter 5 (Scientific Reports).

This dissertation is intended for those that seek to get involved in using gold for biosensing, characterisation of surfaces, and device fabrication using techniques from the semiconductor industry like physical vapor deposition methods, template stripped techniques, and e-beam lithography. The contents are enough for the reader to understand the experimental work and its results. The reader is also referred to multiple sources through the text to get detailed information in the topics not covered by this document.

Part of this work has been presented in the following publications:

Rubio-Lara, J.A.; Bergler, F.; Attwood S.J.; Edwardson, M.; Welland, M. (2019) Ultraflat Gold QCM Electrodes Fabricated with Pressure-Forming Template Stripping for Protein Studies at the Nanoscale. Langmuir. https://doi.org/10.1021/acs.langmuir.8b03782

Tan, E. K. W.; Rughoobur, G.; Rubio-Lara, J.; Tiwale, N.; Xiao, Z.; Davidson, C. A. B.. Lowe, C. R.; Occhipinti, L. G. (2018). Nanofabrication of Conductive Metallic Structures on Elastomeric Materials. Scientific Reports, 1–9. https://doi.org/10.1038/s41598-018-24901-2

Contents

List of Figures

List of Tables

List of Abbreviations

ALD	Atomic layer deposition
BSA	Bovine serum albumin
CMP	Chemical-mechanically polished
CVTC	Chemical vapour transport and condensation
CWTS	Cold-welded template-stripping
DRS	Dot resist sensitivity
EBL	E-beam lithography
ELISA	Enzyme-linked immunosorbent assay
FS	Field size
GB	Grain boundaries
HCl	hydrochloric acid
HFFQCM	High fundamental frequency quartz crystal microbalance
HPLC	High performance liquid chromatography
HSQ	hydrogen silsesquioxane
IPA	Isopropyl alcohol
LE	Laboratory equipment
MIBK	Methyl isobutyl ketone
MSM-RCA	Modified standard multistep RCA cleaning method
MPTMS	3-mercaptopropyl trimethoxysilane
NCP	Nano-contact printing
NPs	Nanoparticles
NWs	Nanowires
PBS	Phosphate-buffered saline
PDDA	Polydiallyldimethylammonium chloride
PDMS	Polydimethylsiloxane

PL	Photolithography
PMMA	Poly(methyl methacrylate)
POC	Point-of-care
PS	Polystyrene
PTFE	Polytetrafluoroethylene
PTS	Pressure-forming template stripping
PVD	Physical vapour deposition
QCM	Quartz crystal microbalance
QCM-D	Quartz crystal microbalance with dissipation
QCM-NP	Quartz crystal microbalance with nanoparticles
RCA-1	RCA laboratories cleaning procedure number one
RMS	Root mean square
SEM	Scanning electron microscopy
SFA	Surface force apparatus
SPM	Sulfuric peroxide mix
SPR	Surface plasmon resonance
STD	Standard deviation
STEM	Scanning transmission electron microscopy
STM	Scanning tunnelling microscope
SZM	Structure zone model
TSA	Template-stripped aluminium
T_m	Melting point temperature
T_s	Substrate temperature
TSG	Template stripped gold
ω_e	Cut-off frequency of the electrode
ω_s	Cut-off frequency of the surrounding area to the electrode

XPS	X-ray photoelectron spectroscopy
ZnO	Zinc Oxide

Chapter 1
Introduction

1 Introduction

1.1 Background

Biosensors are analytical equipment that requires a biological recognition element to perform an analysis of a biomolecule. The most famous example is the glucose sensor used for the monitoring of diabetes mellitus[1]. Still, they have different applications besides medical diagnostics, like pharmacology, food and process control, environmental monitoring, and defence and security. Furthermore, the biosensors market is growing tremendously, especially in the medical sector with a net worth of 13 billion US dollars[2] and an annual growth rate of 10.16% is expected for period of 2013-2018[3]. Additionally, it is believed that the major driver for this growth is the personalised medicine and the increase in technological innovations which makes biosensors cost-effective for their use in diagnosis and treatment.

Biosensors for medical applications can be classified into two major groups: laboratory equipment (LE) and portable devices for point-of-care (POC) diagnostics. In LE, an accurate measurement of complex biological interactions is necessary. In POC, the major focus is on convenience and portability for use of untrained individuals. Most common applications of POC are measuring the concentration or detection of certain molecules mainly in blood and urine. LE study the analysis of interaction of molecules and biomolecules, concentration, bioaffinity, detection at low levels, and characteristics of the biological element.

Current improvements of nanofabrication and synthetic receptors is leading the way to more robust, sensitive and versatile biosensors. For example, the advances of nanotechnology and semi-synthetic nucleotides led to create the real-time DNA sequencer[4]. Furthermore, a semiconductor sequencer has also been created using CMOS technology[5]. These next generation sequencers are fast, mass producible and economic. They are capable of mapping a whole genome sequence[6], [7] in days for under $1000 USD, opening up the doors to a more personalised treatment. With personalised profiles, biosensors could achieve a new height. Instead of making a sensor for a broad range of diseases, custom biosensors could be tailored for the needs of the patient, e.g. sensing the proteins required for the prognosis of a disease.

To realise a personalised biosensor, different advancements must be achieved. One of the main targets of biosensor research is the improvement of the lowest concentration detectable of a compound, also called limit of detection (LOD). It is believed that lowering the LOD will allow the detection of diseases at an early stage. It is recommended that this level should be better than current enzyme-linked immunosorbent assay (ELISA), which is ~1pM. In comparison, current LOD of several biosensor technologies are summarised by Arlett *et al* in Figure 1-1[8].

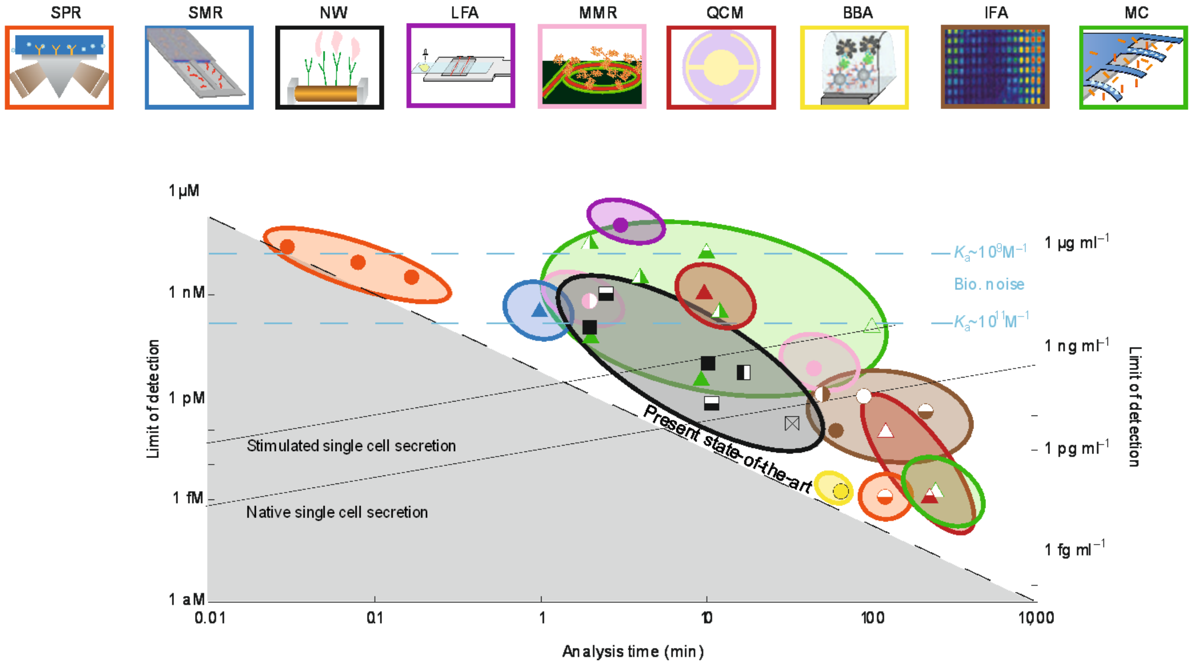

Figure 1-1. Limits of detection for protein measurements of different biosensors. The graph shoes range of values measured by similar technologies under different conditions. The black dashed line represents the state-of-the-art measurements at different analysis time. The measured value under ideal conditions is very good for some devices, however, the blue dashed line represents the limit of detection created by non-specific binding for target-receptor affinities of $1nM^{-1}$ *and* $100nM^{-1}$ *and a non-specific binding association of* 10^4 M^{-1}*. In comparison to physiological values, black solid lines represent the secretion of tumour necrosis factor alpha (TNF-α) from a single monomyelocytic cell for both native single cell secretion and stimulated single cell secretion. SPR: surface-plasmon resonance; SMR: suspended microchannel resonator; NW: nanowire; LFA: lateral flow assay129; MRR: microring resonator; QCM: quartz crystal microbalance; BBA: biobarcode amplification assay; IFA: immunofluorescent assay; MC: microcantilever. Reprinted from Arlett et al,*[8].

Another task is to find new ways to sense the characteristics of the biomolecule and its interaction with other proteins or structures. These biosensors could map the molecular structure of the molecule and sense their dynamic information, like the surface enhanced Raman spectroscopy using gold nanoparticles[9]. Also, in adsorbed biomolecules on a flat surface, the quartz crystal microbalance (QCM) could detect the characteristics of the layer: viscosity, elasticity, thickness, kinetics and mass[10]. QCM is one of the more versatile biosensors, it can detect shape properties of the adsorbed biomolecule and its change of conformation in real time[11]. Another application of biosensors could be the representation of biological events, like diffusion in organs and cell membrane transport.

A biosensor must be able to represent what it is sensing. For this, the use of mathematical modelling or simulations must be corroborated with the experiment. If a new biosensor technique is created, its results should be evaluated according to another biosensor, also known as calibrated measurement. Finally, the mixing of biosensing techniques could potentially lead to the ultimate biosensor which will determine different parameters of the biomolecule interaction using the strengths of each method.

1.2 Motivation: To Make Nanostructures for Protein Sensing and Characterisation.

The QCM is a biosensor capable of sensing the characteristics of proteins. It has been used for understanding protein aggregation of amyloid-β in Alzheimer's disease[12], [13]. Also, it can detect parameters like solvent content, viscoelastic properties and thickness of the mass adsorbed[14]. It is a versatile analytical biosensor that could help to understand complex biological interactions. It can be applied in observational studies, disease detection and diagnosis. The QCM can detect protein concentrations in the range of the ELISA assay (~1pM) as seen in Figure 1-1. However, not everything can be modelled by this system and not everything is understood so far. The full understanding of what is happening at the interface of this sensor is a big opportunity for research. For this, the building of nanostructures on top of the sensing layer could increase the range of analyte concentration, sensitivity and a better understanding of biomolecule interaction. Widening the area of application of the QCM could lead to a better understanding of the role of proteins in diseases and of biomaterials fabrication.

Other authors have already observed how proteins interact with certain nanostructures[15]–[17], i.e. roughness increase on the sensing surface. It has also been observed how Bovine Serum Albumin (BSA) denatures in prolonged exposure to muscovite mica[18]. It has also been explored the interaction of BSA with NPs in solution using spectroscopy. Here we expand the field by looking at the interaction of BSA with gold on QCM resonators, using featureless (atomically flat gold) and nanostructured surfaces using Au nanoparticles and Au nanostructures fabricated using e-beam lithography and physical vapour deposition methods.

1.3 Project Objectives

The aim of this thesis is to fabricate and analyse nanostructures on top of the QCM electrode to study the behaviour of protein adsorption. The material of choice for the electrodes and the nanostructures is gold. Zinc Oxide (ZnO) was another interesting material but was discarded as shown in Chapter 2 because of the complexity of growing nanowires (NWs) of this material. Numerous experiments were performed to create nanostructures where their practical fabrication was assessed. The factors that play a role were nanostructure dimensions and their density per area. Additionally, fabrication using e-beam lithography was pursued to compare the results of the initial experiments in a more controlled manner.

Besides structuring the surface, it is important to analyse if the electrode surface is being perceived as a nanostructure by proteins. The idea is to flatten out the surface of the electrode and compare it against a standard surface, for this a new technique was developed named Pressure-forming Template Stripping (PTS).

The main aim of this dissertation is to understand the difference in adsorption behaviour of BSA on physical nanostructures. The comparison is made on gold among atomically flat, standard, rough and nanostructured surfaces. So far, only fabricated rough surfaces have been compared against standard (small roughness) gold surfaces in the literature, attributing more mass adsorbed on rougher surfaces due to the conformational shape change of the protein upon binding[19]. It is sought to obtain similar results where a flatter surface should have less mass adsorbed as well as conclude the cause of mass adsorption change due to physical changes on the surface.

The following objectives were accomplished in the timeframe of this thesis:

1. In Chapter 2, a study of BSA adsorption to QCM resonators is shown. The optimal steps for the experiment are achieved in order to have reproducible results which was be the baseline for future experiments. Additionally, the optimisation of the fabrication of ZnO nanowires on top of Sapphire (Al_2O_3) is achieved. The vertical growth of nanowires on QCM was one of the first attempts to nanostructure the QCM electrode. The vertical growth of these nanowires is essential for the characterisation of the behaviour of proteins around nanostructures in a controlled manner. The process was previously developed at the Nanoscience Centre, but one specific problem of contamination made the nanowires grow in random directions. The strategy of growing vertical nanowires relied on the flatness and crystal structure of the target substrate along with its cleanliness. In this chapter, it is shown how to fully control the growth of ZnO NWs and how difficult it would be to achieve this on a quartz QCM resonator, including the thermal incompatibilities of both the ZnO NW process and the maximum temperature exposure of QCM resonators. To solve this issue, it is proposed to substitute the QCM resonator (quartz) with gallium orthophosphate and grow the ZnO NW forest using a spin coated zinc naphthenate precursor on top of the electrode of the resonator.

2. In Chapter 2 onwards, gold was decided to be used as the material for protein interactions. The first experiment relied on the deposition of Nanoparticles (NPs) on the electrodes of QCM. By adding ions to the colloidal solution, the distance between nanoparticles was tuned. This relative control of the distance of the NPs will help to understand how proteins binding to their surface behave, and if it is the distance between the NPs or only the NPs having an influence on protein adsorption. The NPs were deposited on top of the QCM electrode, previously coated with a polyelectrolyte, having an array of NPs evenly spaced. The absorption of BSA on top of QCM was analysed at different concentrations of NPs. The increase of NP density was assessed as an equivalent to a surface area increase. In this experiment, it is observed how the increase of mass is a fraction of the expected by the NPs' area increase.

3. In Chapter 3, a novel method named Pressure-forming Template Stripping (PTS) to achieve atomically flat gold on QCM electrodes is described. A literature review is presented of previous methods to achieve a surface with this characteristic and their incompatibility with QCM samples are outlined. An adsorption experiment of BSA on QCM with PTS gold electrodes is performed and their results discussed in comparison with standard QCM resonators and QCM electrodes with a rough finishing. It is shown by liquid AFM how BSA protein mass binds onto an atomically flat gold compared against a rough surface.

4. In Chapter 4, it is presented the fabrication of nanopillars on top of a QCM of high fundamental frequency using e-beam lithography (EBL). A small literature review is presented to obtain

high resolution patterns using EBL and the protocol for the fabrication of patterns on top of a High Fundamental Frequency QCM (HFFQCM). This patterned HFFQCM device was used to adsorb BSA. The experiment showed a similar result to NPs deposited on the electrode surface, less mass than the expected area increase is adsorbed on the surface. The advantages of EBL were the precise location of the structures and their size variability was minimum, corroborating the results obtained by a nanoparticulated surface.

5. In Chapter 5 the conclusions are summarised and a model of BSA mass adsorption onto flat, standard, rough and nanoparticulated surfaces is presented. An additional experiment for the interaction of proteins with a chemically patterned surface is presented as a future project. It works on the principle of changing the charges on the surface of the QCM using nanocontact printing. The fabrication of the stamp was achieved with high resolution patterning (20 nm feature size). The idea is to chemically attach a molecule to the stamp and transfer the pattern to a substrate. This has been previously done using other methods but not at this resolution. The stamp was fabricated but the chemical soaking was not performed and it is left for future work. In the conclusions section,

1.4 Advancements Over Previous Work

The present work contributes to previous findings by multiple deliveries. First, a new protocol for direct gold nanoparticle deposition on top of gold surfaces will be useful for researchers looking for enhancing protein mass attachment (by area increase), specially for small peptides that lead to very small or imperceptible changes in mass using QCM monitoring. This protocol is used in this work as a way of explaining how BSA adsorbs onto features with curvatures (NPs), and the results are compared against standard gold surfaces. The results of BSA binding to NPs agrees with previous findings by other authors on rough titanium oxide, where BSA spreads and adsorbs less mass per area[19]. Second, a novel fabrication method for atomically flat gold, Pressure-forming Template Stripping (PTS), that is applicable on substrates of different topographies (relieves)[20]. This method is used here for QCM resonators but can be applicable to any semiconductor-fabricated device. PTS QCM resonators were used to observe the behaviour of protein adsorption on atomically flat gold, which is an experiment that has not been previously studied, particularly on QCM. It is observed, for the first time, by liquid AFM and QCM monitoring that the BSA tightly packs as a monolayer on atomically flat gold surfaces. This is compared to standard gold surfaces of QCM resonators where there is less BSA areal mass adsorbed. It is also compared against rough gold QCM electrodes that show an enhancement of mass adsorption, but this enhancement is attributed to BSA aggregates, which is corroborated by a liquid AFM image. These findings let to the building of a model of how BSA adsorbs at the nanoscale on gold surfaces where the differences rely only on physical (geometrical) interactions. Third, a protocol is devised for the fabrication of gold nanostructures on top of High Fundamental Frequency QCM (HFFQCM) resonators using e-beam lithography. It is shown that the results of BSA mass adsorption on top of these structures are similar to those found by nanoparticulated QCM resonators, but these fabricated devices can be controlled at the nanoscale level with less variation in the arrangement of the features on the surface. Finally, a new method which combines the fabrication protocol of e-beam lithography and the expertise of atomically flat template stripped surfaces is presented to create chemical stamps with nanometre arrangement for a future project on printing chemicals on the surface of the QCM electrodes[21].

1.5 Thesis Outline

This dissertation is organised in individual chapters for each set of experiments performed for this project. Chapter 2 contains the theoretical background and initial experiments performed to minimise the variability of mass measurements using QCM. In this chapter, multiple techniques were used to characterise the possible errors or contamination found in sensing protein mass. The core of Chapter 2 is an experiment depositing Nanoparticles (NPs) on the QCM electrode. The control of the distance (density) among the particles is detailed and a simple protocol outlined. These nanoparticulated QCM resonators are used for measuring the mass of Bovine Serum Albumin (BSA) and compared against standard resonators. Additionally, the fabrication of ZnO nanowires on QCM resonators is explored and the difficulties outlined. Chapter 3 is dedicated to a novel method to transfer atomically flat gold to QCM electrodes of gold. It starts with a literature review of flat surfaces used for characterisation of biomolecules and different ways of making flat gold. The literature review focuses on the microstructural growth of thin films. The techniques explained to make flat gold are further developed in a new method which is the core of this chapter: Pressure-Forming Template Stripping (PTS). Then, the method of PTS is used on QCM resonators and this atomically flat surface is compared against a standard QCM resonator for mass sensing of a monolayer of BSA. In Chapter 4, the use of E-beam Lithography (EBL) to fabricate nanostructures reminiscent of the NPs in a more precise controlled manner is detailed. The steps required to achieve high resolution are detailed in a small literature review of the technique, with special focus on the fabrication step known as development. A BSA mass measurement of a nanostructured QCM was performed and compared against a standard resonator. Finally, in Chapter 5 it is detailed where these experiments might lead with the inclusion of a new experiment, at its initial stage, about making chemical nanocontact printing stamps for chemical interaction of proteins with patterned charges.

Chapter 2
QCM and Initial Experiments

2 QCM and Initial Experiments

2.1 Summary

This chapter introduces the QCM as a biosensing technique to study protein interaction with nanostructures. The first section starts by giving a brief introduction to the technique and the experimental difficulties found during the setup. The protocol for cleaning the samples is detailed as it would be used throughout this dissertation and it is crucial for the discussion in Section 2.6: QCM Experiment with Nanoparticles on Electrodes. The cleaning method is followed by studying the stability of QCM measurement of proteins and all the required steps to minimise their variability. This will set the foundation for reliable measurements for the experiments in the remaining chapters.

This chapter focuses on the development of a methodology for the deposition of nanoparticles (NPs) on QCM electrodes. Methods of characterisation for analysing the surface and the NP distribution are explained. NP density and interparticle distance was controlled by the addition of salts during the deposition. X-ray photoelectron spectroscopy showed that gold NPs diffuse inside the bulk of gold electrodes during the cleaning process. The observed diffusion of gold NPs inside the gold electrode lead to the experiment of ageing of QCM gold electrodes in Section 2.7. Leading to the investigation of whether the electrode surface itself might undergo structural changes over time (ageing) given that the electrode contains a nanostructure: the grains of gold created by a Physical Vapour Deposition (PVD) method. Therefore, changes were analysed such as roughness and grain size using Atomic Force Microscopy (AFM) of the QCM electrodes of different brands across multiple uses. Finally, the differential adsorption of bovine serum albumin (BSA) onto QCM resonators coated with different density of NPs was investigated.

In the last part of this chapter, an experimental method of growing Zinc Oxide Nanowires (ZnO NWs) is presented. The aim is to grow the ZnO NWs on top of the QCM electrode to increase the surface area using the high aspect ratio of ZnO NWs. The method was previously developed at the Nanoscience Centre and its viability on QCM resonators is assessed. Due to the complicated requirements of growing standard ZnO NWs vertically to the surface, another alternative method is presented, but this might require further optimisation and could be used for a future project. The ZnO NWs experiment closes the chapter of initial experiments to create nanostructures on top of QCM electrodes.

2.2 Quartz Crystal Microbalance

Since the piezoelectric effect was discovered by Jacques and Pierre Curie in 1880[22], the study of piezoelectric materials has been intensive. Their use in biosensing applications has seen enormous progress in the last decades due to advancements in radiofrequency telecommunication technologies[23]. The piezoelectric effect consists of the generation of electric charge/voltage in a material as a result of inducing a mechanical stress on that material. When applying an oscillating voltage, the material mechanically oscillates at the same frequency. Quartz crystal microbalance (QCM) employs an AT-cut quartz crystal resonator, which resonates at a specific frequency depending on its thickness. Therefore, a deposition of a thin film at the surface of the QCM sensor causes a change on its resonating frequency, see Figure 2-1. QCM as a method of mass sensing was first described by Sauerbrey in 1959[24] and it is known as the gravimetric technique. The QCM can directly detect the deposition of biomolecules on an appropriate interface in real time. By using a mechanical principle, QCM is able to measure the deposition of any type of material on the electrode, whereas techniques such as Surface Plasmon Resonance (SPR) only allow the use of materials with certain optical properties[25][26]. Additionally, the solution in which the target molecule is dissolved does not affect the measurement like in Field Effect Transistors for biological applications (bioFETs)[27]. Instead, the different behaviour of the proteins under different ionic conditions can give additional information of the adsorbed layer on the QCM.

One other advantage of QCM is that it can measure certain characteristics of the adsorbed layer, such as the shear modulus and density. These properties can be qualitatively translated into the shape and charge of the adsorbed molecule. For example, when comparing the adsorption of a protein like BSA to two different surfaces, it will attach preferentially to the most hydrophobic surface, which can be measured as more mass on the resonator. There are different models used to study protein adsorption on quartz resonators[28]–[30], but the most widely used, and the first, was developed by Sauerbrey[31]. The model is based on a small phase shift of the acoustic wave while propagating on the mass deposited on the electrode. The limitation of the Sauerbrey model is that it only gives an accurate mass measurement for a thin film of a rigid material. The model is applicable to the study of protein adsorption as proteins behave as hard plastic films with densities of around 1.37 [g/cm^3][32]. Additionally, it has been shown that most models work under uniformly distributed coatings on the surface of the electrode. The resonator sensitivity is higher at the centre and decreases to zero just outside of the edge of the electrode. Higher mass density at specific points on the electrode will give different sensitivities and it can only be normalised if position is known[33]–[35]. It is crucial that protein studies must be undertaken using proteins that form a monolayer on top of the electrode. Nevertheless, non-saturated protein coatings can also be measured in terms of mass if they are uniformly distributed on the surface. For the development of the Sauerbrey equation the reader is referred to the original paper[31] or to the book “Piezoelectric Transducers and Applications”[24]. The Sauerbrey model is presented in the following equation:

$$\Delta f_s = \frac{-2f_0^2 \rho_c h_c}{Z_{cq}} = \frac{-2f_0^2 m_c}{Z_{cq}} \therefore m_c = \frac{\Delta f_s \times Z_{cq}}{-2f_0^2} \qquad (\ 2.1\ )$$

Where $m_c = m/A_c = \rho_c h_c$ is the surface density of the coating (areal mass); ρ_c and h_c is the density and height of the coating respectively; $Z_{cq} = 8.839 \times 10^6$ [N*s/m^3] is the quartz characteristic impedance; f_0 is the resonant fundamental frequency and Δf_s is the change of frequency after mass adsorption. This equation is applicable to the study of proteins that behave as a hard coating when adsorbed at the surface and it does not require any further information about the protein. However, the model is not suitable for viscous materials. In that case, other models and further information, such as height of the deposited material, might be required. This is referred as the non-gravimetric regime of the QCM, see Vives [24].

There are three main types of QCM sensors which can be used to study protein adsorption: (i) QCM using oscillators;(ii) QCM by impedance analysis; and (iii) QCM with dissipation (QCM-D). QCM sensors using oscillators work at a fixed frequency. QCM sensors by impedance analysis use a frequency spectrum to analyse the deposition. QCM-D uses an ON-OFF system and measures the dissipation of the oscillation at a monitored frequency. When the mass is adsorbed to the surface, a change of frequency or signal intensity (e.g. phase for standard QCM) on the resonance occurs, see b) and c) in Figure 2-1. If the layer is not a solid, there is a change of dissipation (quality factor) directly related to the viscosity of the material, see d) in Figure 2-1. Dissipation is an important parameter but no substantial change was detected on this work and will be analysed qualitatively as small changes in dissipation might reflect on the rigidity and integrity of the protein coating.

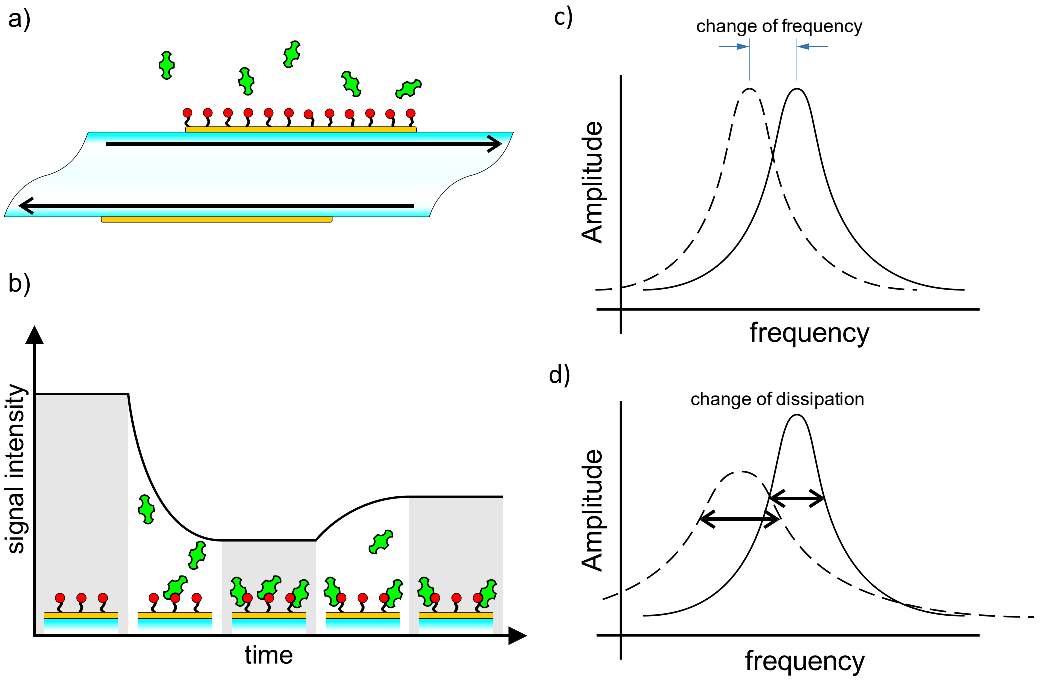

Figure 2-1. a) Diagram of QCM in biosensing applications. The resonator moves tangentially to the surface in an onscillating manner. When mass is adsorbed energy is lost and the resonance frequency changes. b) The changes of the signal intensity caused by the mass adsorption on the electrode. The protein binds dynamically, therefore the signal changes until protein binding reaches an equilibrium. c)When a layer is adsorbed on the surface, a change of frequency is detected, and d)any energy lost is caused by a viscous material (not solid) and it is recorded as a change of dissipation.

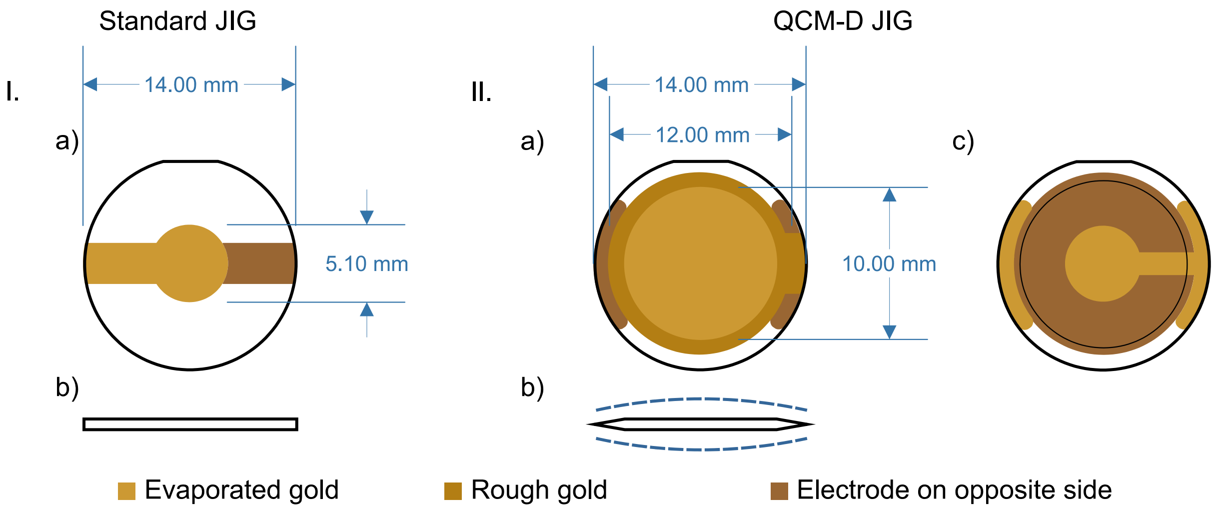

Figure 2-2. The standard QCM design (jig) is shown in I.a); both sides of the quartz wafer have the same electrode design. The lateral view of the standard QCM without electrodes is shown in figure I.b) not to scale. Figure II.a) shows the sensing side view of the QCM-D jig; the sensing area of the QCM-D is the 10 mm inner diameter of the electrode. II.b) shows the lateral view, not to scale, of the QCM-D which has an optical lapping on both sides (dotted line represents the spherical curvature). Both sides of the QCM-D are lapped into a spherical shape from the edge and up to the 10 mm sensing area of the electrode. Figure II.c) shows the backside of the QCM-D resonator which has a different design to the sensing electrode. Additionally, the backside might have a thinned 10 mm area to achieve the required resonance frequency.

The three different QCM techniques can give the same information: frequency change, and dissipation. In some systems, they are given as different parameters but can be converted. All methods require the same AT-cut quartz crystals. It is only a matter of the electrode design and resonance frequency required by the user. Some designs are custom made by the suppliers to be compatible only with their system. The two most common designs are the standard QCM jig and the QCM-D jig, see Figure 2-2.

Although there is versatility in using the QCM technique, there are still some opportunities for improvement. Some of the challenges for QCM biosensors are increasing the sensitivity, the limit of detection, its multiplexing capabilities, and reliability. Here, it was investigated the coverage of QCM electrodes with nanostructures to increase the surface area available for biomolecule adsorption. This is due to the limitations of QCM when higher sensitivity is required, i.e. the electrode size is small (~1mm) for higher frequencies that are required for higher sensitivity. It can also increase the range of mass measurement and the permanent binding of molecules due to the induction of conformational shape change of the molecule caused by nanostructures. Before the start of this study, the right setup for measurements of proteins on QCM, including the cleaning protocol, was assessed. The goal was to answer the following questions:

- Does the cleaning step affect the subsequent use of the QCM?
- Are QCM resonators measurements consistent across different batches of crystals and what is the protocol required to measure mass precisely?

2.3 Materials and Equipment

The following materials are used in this chapter for multiple experiments. High Performance Liquid Chromatography (HPLC) grade water was obtained from Fisher Scientific. A Fisherbrand ultrasonic cleaning bath, hydrogen peroxide (30%) and ammonia (35%) solution were purchased from Fisher Scientific. QCM resonators (QCM-D jig) were purchased from QuartzPro and Biolin Scientific. Bovine Serum Albumin (BSA) was purchased from Sigma Aldrich: purified by heat shock fraction, protease free, fatty acid free, essentially globulin free, pH 7, ≥98%. Gold nanoparticles of 40 nm diameter with InnovaCoat carboxyl modified were purchased from Innova Biosciences. Carbon powder of <20µm and Zinc Oxide powder <100 nm were purchased from Sigma Aldrich.

The equipment used for thermal evaporation is an Edwards evaporator A306 with Auto FL 400 chamber. The e-beam evaporator is a PVD 75 e-beam evaporation system from Kurt J. Lesker. Both thermal and e-beam evaporation systems monitor the thickness of the deposited materials with a calibrated QCM monitor. A Carbolite tube furnace was used with Haldenwanger alumina combustion boats with dimensions of 115 mm x 16mm x 9mm from Fisher Scientific. The QCM monitoring system used for protein adsorption was the Q-Sense E4 from Biolin Scientific. A built in-house excimer photon cleaner and the ProCleaner from BioForce Nanosciences was used for UV ozone cleaning.

2.4 Cleaning Protocol: Modified RCA-1

The cleaning protocol used for QCM and QCM-D sensors was the method employed by Kern and Poutine[36] in their work at RCA laboratories. It is known as RCA standard clean 1 (RCA-1). It was designed to remove organic contaminations by oxidative breakdown and dissolution[37]. This method creates ammonium hydroxide, which dissolves at a low rate the gold on the electrode. For this reason, the sensor is immersed in the solution for only a short period of time.

A UV lamp treatment is added prior and after the RCA-1. The UV lamp treatment helps to remove all carbonaceous depositions on most surfaces[38]. Before the RCA-1 clean, the UV ozone cleaning helps for the breakdown of organic molecules like big proteins. After the cleaning, it is well known that the Au surface changes its contact angle from its natural hydrophilic state to hydrophobic in a matter of a couple of minutes due to deposition of carbonaceous airborne contaminants, and the contact angle plateaus at its maximum hydrophobic state at around 100 minutes[39]. Using the UV lamp treatment after the cleaning, any airborne contaminant can be removed. Additionally, the Au gets oxidised protecting the surface of the electrode as well as making the surface hydrophilic for a longer time. This oxidation to Au_2O_3 can be reversed to Au by flowing water through the electrode for at least an hour[40]. This rinsing is usually performed during the stabilisation step of the QCM resonator prior to the protein adsorption experiment guaranteeing a pure gold surface.

The two steps of UV lamp treatment plus the RCA-1 are coined herein “modified RCA-1”. The steps of the protocol are the following:

1- UV lamp treatment

    UV Lamp treatment for 15 minutes at optimal distance from the source (1 cm maximum using the ProCleaner).

2- Second step: RCA-1
    a. Heat to 75°C a mixture of DI water, ammonia (30%) and hydrogen peroxide (30%) at a ratio of 5:1:1. Avoid Pyrex beakers if contamination might be an issue.
    b. Immerse sensors in the solution using a Polytetrafluoroethylene (PTFE) cleaning holder for 5 minutes.
    c. Clean tweezers in the same beaker.
    d. Rinse with DI water and dry with N_2 Gun.

3- UV lamp treatment
    a. UV Lamp treatment for 15 minutes at optimal distance from the source (1 cm maximum using the ProCleaner).

4- Rinsing
    a. Rinsing of the surface with degassed distilled water for 1.5 hours. Recommended to be performed inside QCM monitor systems (during stabilisation).

This cleaning procedure is used on all experiments performed in this dissertation.

2.5 Study of Variations in QCM Measurements: Do QCM Resonators Age?

One of the initial experiments in this thesis project was the study of BSA adsorption on QCM resonators with Au electrodes. The aim was to assess mass measurement variations on the system as it has not been previously done in our group. This experiment will evolve in the following chapters towards the study of nanostructures and roughness on the surface of the QCM electrode. At this stage, the aim was not to characterise the surface, but only to measure the resonator response and possible causes of variability and failure.

The objectives of this experiment are:

1. Understand the setup required for the QCM system that will minimise the variation between measurements.
2. Understand if the BSA can form monolayers when dissolved in water.
3. Study the ageing of QCM sensors by determining if multiple uses of the resonators have an impact on the amount of mass adsorbed on the surface.

For the first aim, multiple tests of different conditions for the right setup were tried such as the order of the cleaning steps, degassing of the solvent, and the use of a PTFE holder and tweezers with soft tips to avoid scratches during the handling of the resonators. As discussed previously, QCM resonators with gold electrodes tend to become hydrophobic after RCA-1 cleaning, a drawback that can be overcome by optimising the time and distance from the source during the UV lamp treatment. In UV lamp systems such as the built-in house at the Nanoscience Centre, 10-15 minutes treatment was enough. If UV treatment fails due to a poor optimisation, the hydrophobicity can be detected when bubbles adsorb to the surface on the signal response as steps during the stabilisation.

One important step is to degas the background solution required for the experiment, in this case the HPLC grade water, using a vacuum pump assisted by sonication. If a bubble sits on top of the electrode, the QCM system monitors a change of frequency in the opposite direction to mass adsorption. When this occurs, the resonator might become hydrophobic at the position of the bubble as observed during the experiments. This step is crucial to have consistent measurements of protein adsorption. The system relies on reaching a plateau and stable signal after protein adsorption, but bubbles make the signal drift. Furthermore, BSA adsorbs electrostatically to the surface and the higher the hydrophobicity of the surface, the higher the mass adsorbed. The degassed solution needs to be run through the resonator soon after the electrode surface has been treated with the second step of UV lamp cleaning.

The QCM resonator is not stable when installed in the monitoring system and will require time to get to a near zero background frequency change. Reaching the stability of the signal takes time due to the boundary conditions and the presence of o-rings in the equipment, additional details are explained in Chapter 3. If stability is not reached, the QCM will show a drifting in the monitored frequency. Overnight stabilisation of at least 16 hours is recommended for QCM-D resonators with Au electrodes. This will also assist the removal of the oxide layer present on the surface of gold from the UV lamp cleaning, as previously discussed. If the steps are followed carefully, the variations of the QCM signal will be minimal across measurements.

2.5.1 Experiment: Ageing of QCM Resonators

To investigate the ageing of QCM resonators and the variation of measurements across samples, a simple experiment was performed. It relies on multiple measurements of BSA using the same resonator. First, the sample is going to be cleaned using the protocol modified RCA-1. Secondly, a BSA solution will run through the QCM electrode at a concentration that will create a monolayer. The mass would be measured after rinsing of the BSA solution and reaching stabilisation. It will be followed by cleaning again the sample using modified RCA-1 and the steps would be repeated. This is referred as ageing the sample due to harsh conditions of the cleaning protocol. All resonators had a resonance of 5 MHz and were purchased from the same company, Biolin Scientific with QCM-D jig, see Figure 2-2 II.a). The system used was the Q-Sense E4. Samples were installed after being cleaned using modified RCA-1 and left for stabilisation overnight. For this experiment, 1 mL of 100 μM BSA in HPLC water was run through the resonator with the objective of depositing one monolayer of protein. The flow rate was set at 100 μL/min. Multiple injections of the BSA solution did not alter the final frequency change (mass) on the resonator and proved the presence of a monolayer. This protein batch was compared to an old one. The old one showed multilayer deposition. This could be because of the protein purification method or due to a bad batch. The experimental plots for the multilayer and monolayer deposition can be found in the Appendix for this section.

To assess variability for the monolayer depositions of BSA, four sensors were cleaned followed by the BSA mass measurements, then cleaned again and then the deposition was repeated, for a total of five repetitions for each sensor. The variation across sensors, and across reuses for each sensor is shown in Figure 2-3. All measurements were taken after waiting the same time for stabilisation after rinsing the remnants of the protein solution.

The results demonstrate low variability between measurements. The overall standard deviation (STD) of the measurements for all resonators is ±6.52% which is below the published variability of other authors [14], [41] see Table 2-1. These results were analysed only in terms of change of frequency (Δf), but they are consistent even if the mass model (Δf/f) was used to calculate the deviation, where f is the resonance frequency. The change of frequency is proportional to the mass measured by a constant, see Equation 2.1.

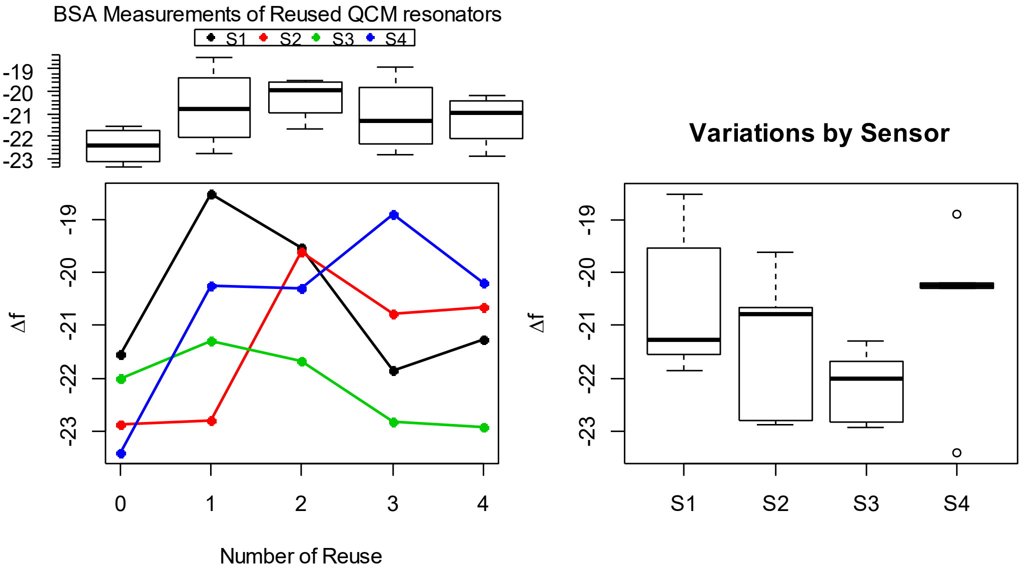

Figure 2-3. Plot of mass measured by each sensor after every use. The box plot on the left is the variation of mass measured by each sensor and by the number of reuses. The box plot on the right displays the variations of measurements for each sensor. Sensors are labelled as S1, S2, S3 and S4.

Table 2-1. Variations of BSA mass measured by QCM-D resonators 5 consecutive times. The results are compared against the works of Ouberai et al[14]*s and Reimhult et al*[41].

No. of Reuse	Sensor Label			
	S1	S2	S3	S4
0	-21.54	-22.86	-22.00	-23.40
1	-18.52	-22.80	-21.30	-20.25
2	-19.53	-19.61	-21.68	-20.30
3	-21.85	-20.78	-22.81	-18.91
4	-21.27	-20.65	-22.92	-20.19
STD	1.29	1.28	0.63	1.49
STD%	6.29%	6.01%	2.85%	7.22%

	Overall STD	±1.38
	% Overall STD	±6.52%
Ouberai *et al**	% Overall STD	±9.79%
Reimhult *et al**	% Overall STD	±17.19%

The results show that using modified RCA-1, degassed background solution, and overnight stabilisation of the resonators for 16 hours, the measurements have minimal variation. The measurements are compared against the variability of the results of other authors[14], [41] using the same QCM-D system, but different background solution (phosphate-buffered saline). Given the low variability, this protocol was used throughout the thesis.

2.6 QCM Experiment with Nanoparticles on Electrodes

2.6.1 Introduction

The idea to have nanostructures on QCM electrodes emerged from colloidal lithography, where nanoparticles (NPs) of polystyrene are drop casted on a surface. It is well known that colloidal lithography can be used to deposit patterns of nanostructures on large areas (cm^2)[42]. The principle is to place a droplet of colloidal solution of charged particles on top of a surface with an opposite charge. The NPs electrostatically attach to the surface, and their density can be controlled by changing the electrostatic particle-particle interaction. This is done by adding salt to the colloidal solution. Once the NPs are on top of the surface, they will serve as a mask for a subsequent evaporation step. The NPs

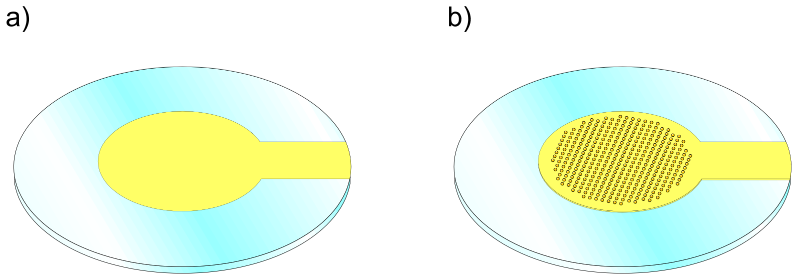

Figure 2-4. The aim of this experiment is to deposit nanoparticles on top of sensing surfaces. a) QCM resonator with Standard QCM JIG, and b) the deposition of gold nanoparticles on top of the electrode of a standard QCM. Figures not drawn to scale.

protect a projected circle on the surface from an evaporated material. A further strip of the NPs by tape stripping or etching will allow the surface to have a patterned area with circular holes, which can be further processed to deposit nanopillars inside if the surface is a resist.

Instead of using the NPs as a mask, they can be used directly as a nanostructure, see Figure 2-4. It will also use Au NPs instead of the original polystyrene NPs. The deposition can be done in very simple steps without needing further semiconductor fabrication techniques such as etching and Physical Vapor Deposition (PVD) methods as other authors have done[43].

The NPs need to be coated with a molecule to avoid aggregation, usual coatings make the surface negatively charged and repulsion among nanoparticles will be due to the electrostatic charge. It was opted to acquire commercially available NPs from Innova Biosciences, Innovacoat NPs. These NPs have a proprietary coating with a carboxyl end group (negatively charged), are highly monodisperse, and work well with the protocol used in colloidal lithography.

The surface of the QCM electrode was positively charged by coating it with a polymer previously used in colloidal lithography, polydiallyldimethylammonium chloride (PDDA) solution with average molecular weight of 200,000-350,000[42], [44]. NaCl was added to the colloidal solution to reduce the electrostatic repulsion between NPs. The higher the concentration of salt the closer the NPs can be in solution, and hence the closer the NPs will be to each other once they are deposited on the electrode surface.

2.6.2 Protocol: Au Nanoparticle Deposition on QCM

The protocol used for this experiment is based on the work by Fredriksson *et al* with minor modifications[44].

Au NPs were deposited on top of the QCM electrode using the following steps:

1- Drop cast 2% of polydiallyldimethylammonium chloride (PDDA) in water on top of the target surface, in this case the QCM electrode.
2- After 5 minutes, rinse with plenty of DI water and dry with N_2 gun.
3- Deposit the colloidal solution of Au NPs (InnovaCoat Au NPs 40 nm at an initial concentration of 10 optical density) on top of the electrode for 2 hours to reach full saturation. This is based on the highest concentration of salt at 500 mM NaCl to decrease the distance between NPs. The solution is kept on top of the electrode without spilling out of the chip by using a hydrophobic tape, e.g. blue tape used in wafer dicing, around the target area. It is important for this tape not to leave any residues on the resonator. A hole puncher of 9.5 mm diameter was used to cut the tape. Water is added to humidify the working area and avoid the drying of the colloidal droplet.
4- Rinse with water thoroughly such that the surface is kept wet all the time. This is usually performed by holding the resonator perpendicular to the flow of the water.

5- Keeping the sample on a flat surface, dry it with N_2 gun by quickly shooting the stream perpendicular to the electrode to avoid any capillary forces affecting the deposition. Weak pressure might affect the NP distribution and lead to aggregation.

6- Treat with O_2 plasma for at least 7 seconds, using Diener O_2 plasma at 100% power and pressure of 0.8 mBar.

7- Use modified RCA1 solution to clean the sample for 10-15 seconds in solution instead of 5 minutes.

The resulting device can be used for QCM sensing but only once. If the device gets cleaned before reusing it, the NP tend to diffuse inside the gold electrode to minimise surface energy. With each additional cleaning, the NPs diffuse further inside the bulk, losing their structure and the electrode becomes rough instead. Cleaning an Au surface of a QCM with Au NPs would be very useful for making very rough gold surfaces without needing a cleanroom. It is believed that the gold diffusion occurs because of the temperature of the reaction of the modified RCA-1 cleaning method along with the contact of the NPs with the surface, see Figure 2-5. Due to the electrostatic interaction of the positive charge of PDDA, and the negative charge of the carboxyl end group on the Au NPs (measured by dynamic light scattering and not shown in this work) the NPs stay in place. Once the step of O2 plasma is performed, both PDDA and the organic coating of the AuNP will be destroyed, placing the NP in direct contact with the surface. At this stage it appears that the NP are attached via Van der Waals forces. This has been noticed while taking AFM images, where if the O_2 plasma step is not performed the NPs can still be detached from the surface. It is theorised that the direct contact of the NPs, along with the increase of temperature during the modified RCA-1, makes the NPs diffuse inside the bulk of the electrode. This phenomenon is believed to occur at temperatures >75˚C (temperature used in the cleaning protocol) and in highly pure Au.

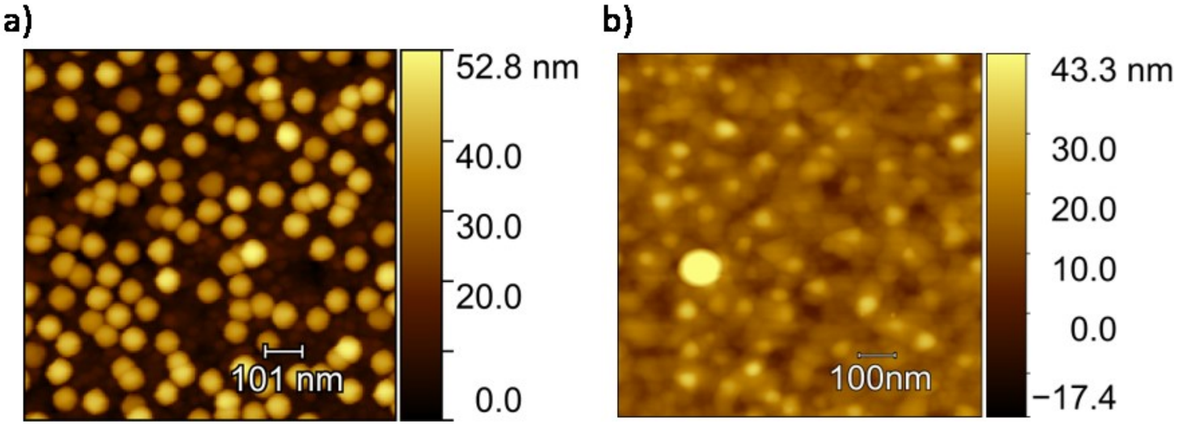

Figure 2-5. AFM images of Au NPs deposited on QCM electrodes with the developed protocol in this work. Figure a) The NPs are round spheres on the surface as expected, but after cleaning the resonator with modified RCA-1, figure b), the NPs diffuse inside the electrode roughening the surface.

The nanoparticulated QCM resonator (QCM-NP) using O_2 plasma is presented in the AFM image in Figure 2-5 a). The rough surfaces after a modified RCA1 cleaning can be seen in Figure 2-5 b) with roughness of 4.9 nm RMS. The big particle in the rough sample might be from an external contamination such as dust and it is not considered in the roughness measurement. This methodology could inspire the development of electrodes with very high roughness without the need of cleanroom equipment. Roughness could be increased by having multiple steps of NP deposition, or by using NPs with higher diameter than the ones used in this experiment. However, it was not an aim of this thesis project and it is only briefly discussed in the Chapter of Future Work.

2.6.3 Characterisation of Au NP Size

The characterisation of Nanoparticles (NPs) is crucial to understand their dispersity and their behaviour on surfaces. It can be performed in solution as colloids using Dynamic Light Scattering (DLS). DLS can measure the NP diameter but it overestimates the size of the NPs by measuring the hydrated shell. For example, an initial result of InnovaCoat NPs of 40 nm diameter showed NP size of 54 nm compared to the results of image analysis of 43 nm size on average. Other techniques, like Atomic Force Microscopy (AFM) and Scanning Electron Microscopy (SEM), are more useful for NPs that are deposited on a surface. Still, there are issues with each technique. With AFM a cantilever scans the surface by moving up and down giving a topographic image. A tip is at the end of the cantilever. If this tip was a very small, close to zero nm in diameter, then the topographic image would have an error only based on the division of dots, or lines, per distance the system is scanning. However, because of the tip radius, it will overestimate the sphere volume of the NPs by adding the AFM tip radius to the featured being scanned. This would be in the x and y axis; standard tips have no bigger than 10 nm radius, for a 43nm NP it would be measured as a 63 nm NP. Nevertheless, the AFM can obtain the diameter of individual NPs, by extracting the maximum height of each nanoparticle, and assuming they are a perfect sphere and the surface is flat. Additionally, any contaminant that might be present between the surface and the NPs could be imaged, something that might not be possible on SEM.

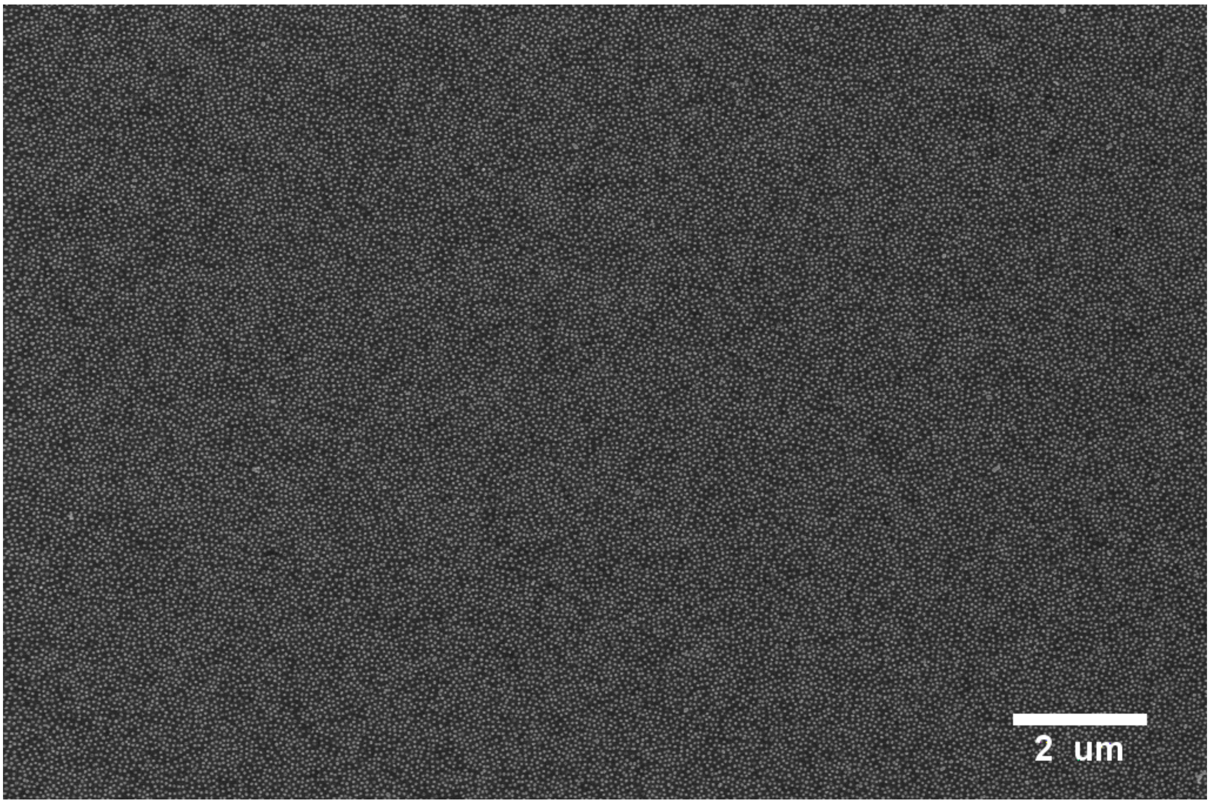

Figure 2-6. Characterising the deposition of nanoparticles on the QCM electrode is possible using SEM, as it faster to more precise than other methods. The image shows a nanostructured gold electrode using InnovaCoat gold nanoparticles (40 nm) using a colloidal lithography deposition process.

The SEM is the technique of choice when the sample is clean of contaminants and conductive as in the case of gold. It can quickly characterise different samples, and the contrast caused by the shape of the nanoparticle is high to perform image analysis of their diameter. It is also important to understand that the time scales to do the process are in the order of seconds. AFM images take multiple minutes. Compared to the AFM, the calibration of the SEM is standard and takes no more than a couple of minutes. In contrast, the AFM requires a calibration by the user and installing tips on the AFM system, adding time to the already slow image acquiring process. A disadvantage of SEM is that, even in vacuum, it is possible for the electron beam to attract contamination during the scanning and eventually deposit such contaminants on the area being imaged[45]. This is called the black box effect and can be minimised by exposing the area for a short time or not using any type of double-sided tape to fix the sample. Nevertheless, for its suitability, SEM was used to characterise the distance between NPs and their size. AFM was required only on those samples that showed unexpected contrast in SEM.

The NPs were purchased from Innova Biosciences as InnovaCoat gold NPs of 40nm diameter and a concentration of 10 optical density. These nanoparticles have a proprietary coating functionalised with carboxyl end groups. The result is negatively charged NPs. Other NPs were tested, using different coatings to stop aggregation on the surface, but the simplest protocol was obtained with the InnovaCoat NPs. To deposit the Au NPs on the electrode of the QCM, a similar protocol for depositing Polystyrene (PS) NPs was used [44] (see Section 2.6.2). The PS NPs are also negatively charged, for details see the original paper[42]. By using a polyelectrolyte positively charged on the surface, Au NPs can attach by electrostatic attraction. By adding ions to the solution in form of NaCl, the NPs will be closer reducing the Debbye length (Debye screening) [46]. This is caused by counterions (positively charged) being attracted to the surface of Au NPs (negatively charged), screening the AuNPs charge and reducing the repulsion between them.

Two batches of Au NPs of 40 nm size were purchased from Innova Biosciences. Initial batch used for depositing NPs on gold substrates were not monodisperse, which caused several problems. This difference between diameters made small Au NPs aggregate with bigger ones. The variance of the distance between NPs was also substantial and size dependant, which made the nanostructured pattern inconsistent, see Figure 2-7 a). When the same protocol was followed in highly monodispersed NPs, batch 2, the distance distribution became less varied, see b) in Figure 2-7. The pattern is evenly distributed in batch 2.

Batch 2 was used throughout the rest of the experiments. The image analysis using ImageJ showed that the NPs have a diameter of 43.3 nm on average, see histogram in Figure 2-7 b). Additionally, 13 nm

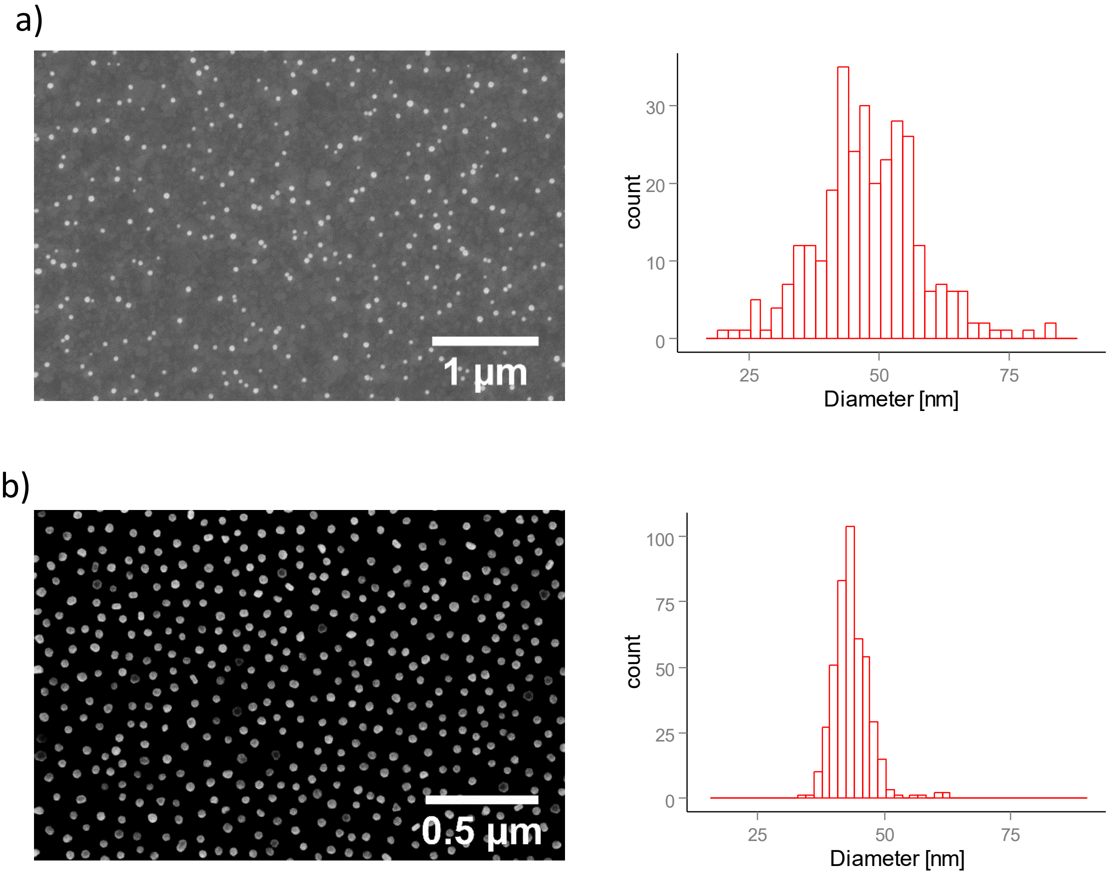

Figure 2-7. Au InnovaCoat nanoparticles with carboxyl end groups deposited using the protocol for polystyrene nanoparticles from Fredriksson et al[44]. *In a), SEM image and histogram of Au nanoparticles with high diameter variance, batch 1. Au nanoparticles can be evenly distributed on top of the QCM electrode by following the same protocol but with a highly monodisperse solution, see b).*

monodispersed InnovaCoat Au NPs with carboxyl end groups were purchased from Innova Biosciences.

2.6.4 Experiment: Au NPs Density Variation on QCM Electrodes

The Au NPs can be used as nanostructures on top of the QCM electrode. The difficulty relies in controlling their position. If different concentrations of NaCl are added to the colloidal solution, then the Au NPs will get closer by screening their surface charge with counterions from the NaCl. Compared to e-beam lithography or any semiconductor fabrication technique, colloids are less precise. But there is one important advantage over these processes: colloids can be used in large areas, like those of QCM electrodes (5-10 mm diameter).

The experiment consisted in adding different NaCl concentrations and keeping the concentration of the Au NPs constant. The NaCl solution and colloids were mixed at a ratio of 1:10. All samples were deposited using the same protocol (see Section 2.6.2). The experiments included 5 different salt concentrations for 43 nm, and 4 variations for 13 nm samples. Samples were imaged with SEM and analysed with ImageJ. The process to analyse the image requires the software ImageJ: first, it requires to make the image binary; and secondly, to use the built-in algorithm “analyze particles” in the software, see Figure 2-8. The output is a summary of the area for each NP. The area increase can be calculated by using the total area covered by nanoparticles in an image and building a simple model.

If the NP is larger than two times the size of the protein to analyse, the area increase caused by a nanoparticle in a specific area can be calculated with the following model. First, the area of the top half sphere is available for protein adsorption, see Figure 2-9. For simplicity, the area of the bottom hemisphere can be considered as a cylinder. The BSA adsorbed to the substrate surface next to the cylinder will not allow more proteins to bind to the wall of the cylinder, reducing its area available for adsorption.

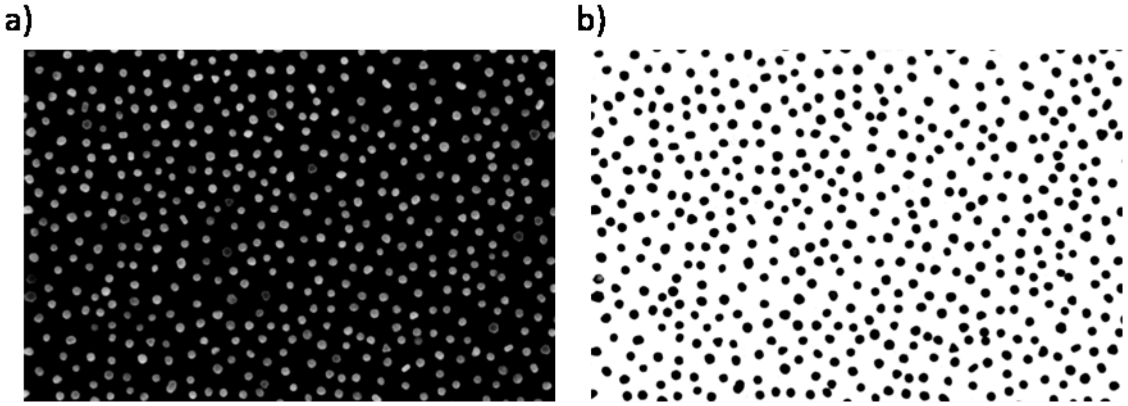

Figure 2-8. Figure a) the image of NPs deposited on gold electrodes using SEM. Figure b) the binarization of the SEM image to extract the NP diameter and the area coverage.

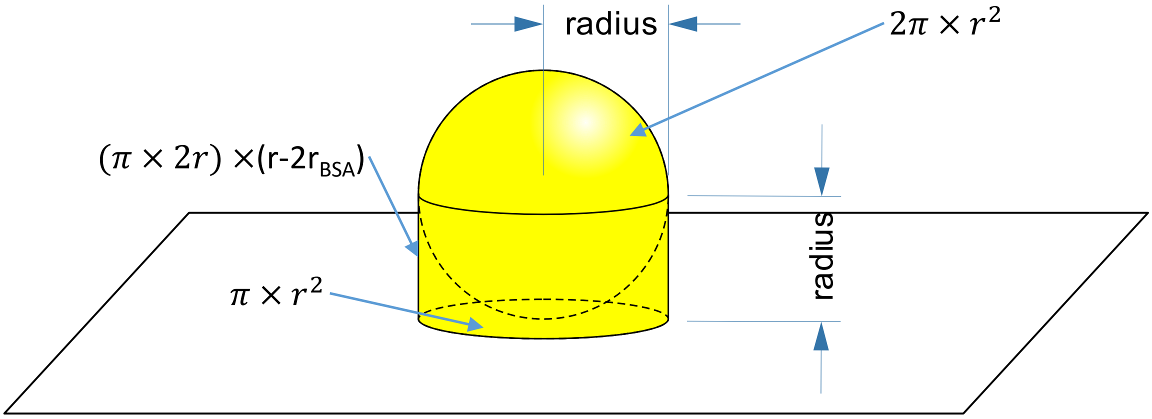

Figure 2-9. Model of the area available for adsorption of proteins on a nanoparticle attached to a surface. Three equations show the areas used for the model of area increase. Top equation shows the area of a hemisphere. The equation from the middle shows the cylinder area increase. The bottom equation shows the area of the (projected) circle at the bottom of the sphere.

Therefore, the total height of the cylinder available for area increase is the radius of the NP minus the maximum size of the protein (hydrodynamic diameter). Additionally, the NP is sitting on a projected circle, which must be subtracted from the area increase as it would be screened. The model is summarised as follows:

$$A_{increase} = A_{hemisphere} + A_{Cylinder} - A_{ProjectedCircle}$$

$$A_{increase} = 2\pi r^2 + 2\pi r(r - 2r_{BSA}) - \pi r^2$$

$$A_{increase} = \pi r^2 + 2\pi r(r - 2r_{BSA}) \qquad (2.2)$$

The first term of Equation 2.2 is the area occupied by a projected NP in the SEM image. The whole equation can be written in terms of the projected area:

$$A_{increase} = \pi r^2 \left(1 + 2 - \frac{4r_{BSA}}{r}\right) \qquad (2.3)$$

Where for 43 nm NPs and $r_{BSA} = 3.56$ nm the factor for area increase based on the projected area is:

$$\left(1 + 2 - \frac{4r_{BSA}}{r}\right) = 2.338 \qquad (2.4)$$

The total area increase can be obtained from the total projected area result from the image analysis using ImageJ and multiplying it by factor from Equation 2.4. The density of NPs plateaued after the NaCl concentration of the colloidal solution was above 150mM, see Table 2-2. The model for 13 nm NP is a simple model of a hemisphere. The reason is that the bottom hemisphere of the NP is screened from adsorption by proteins bound to the original surface surrounding it, because of its size, making

Table 2-2. Results of area increase after depositing nanoparticles with different salt concentrations on top of QCM electrodes.

NP size	Final Salt Concentration [mM]	Projected Increase (ImageJ)	Area Increase of Model
43nm	500	25.00%	58.45%
43nm	300	24.97%	58.38%
43nm	150	24.97%	58.38%
43nm	75	22.60%	52.84%
43nm	16.2	17.49%	40.89%
43nm	0	15.40%	36.01%
13nm	300	14.40%	--
13nm	150	15.00%	--
13nm	75	13.49%	--
13nm	16.2	8.20%	--
13nm	0	~5.0%	--

$(r - 2r_{BSA}) \cong 0$. Using image analysis, the coverage increase for 13 nm NPs is only the area of circles of projected NPs according to the model.

The 13 nm NPs could not get a higher than 15% area increase. This might be due to the concentration of carboxyl on the surface. This could be increased if the chemistry is optimised but it was not the aim of this project. The amount of carboxyl end groups was not disclosed by the company. The plots of the area increase by salt concentration increase, for both 43 nm and 13 nm Au NP covered surfaces, can be seen in Figure 2-10.

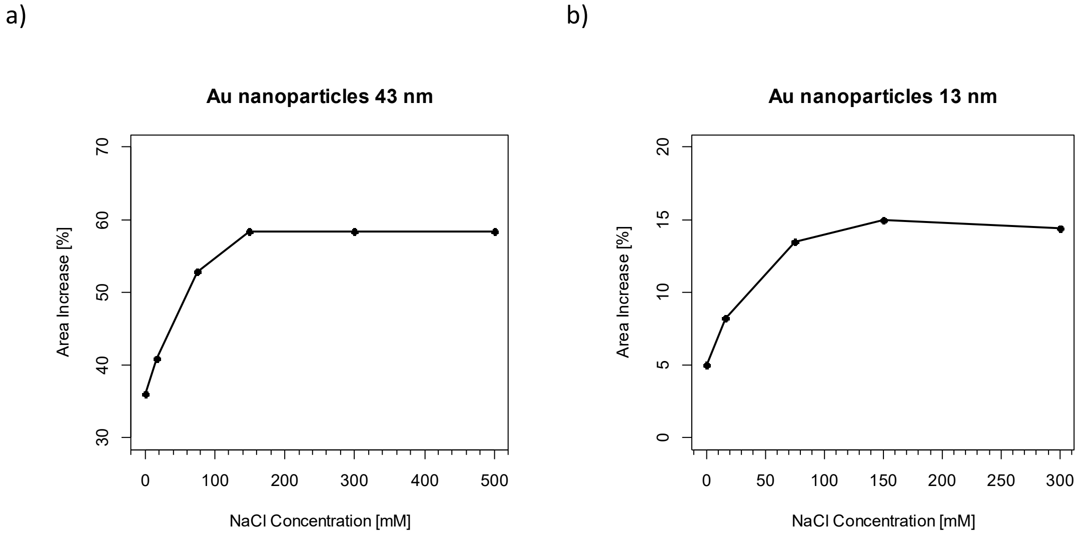

Figure 2-10. Curves of coverage based on modelling the area increase of 43 nm NP and 13 nm NP. The 43 nm NP uses the model of Equation 2.3, while the 13 nm NP uses the model of the area of a hemisphere.

Table 2-3. Values of the binding energy of an x-ray photoelectron spectrum attributed to the presence of bovine serum albumin on a surface[47], [48]. *The core levels of C 1s and N 1s are characteristic of this protein, with peak label C1 attributed to carbonaceous contamination. Additionally, the core levels of Au 4f for the electrode and Au NPs is presented, see King*[49] *for more details.*

Core Level spectra	C 1s			N 1s	Au 4f			
Peak Label	C1	C2	C3	N1	Au1	Au2	Au3	Au4
Binding Energy	285	286.4	288.5	400.3	84.05	87.42	85.6	89.05
Assigned group	C-C C=C C-H	C-N C-O	O=C-O O=C-N	BSA Characteristic	Au Characteristic	Au Characteristic	Au_xO_x	Au_xO_x

The NPs will start to get closer the longer the colloids are kept stored. This was noticed after a few months of not using them. It is believed that the coating degrades with time and the magnitude of the charge on the NP surface decreases. This was not a problem for this project as this will allow to make a surface with the highest NP density possible.

As mentioned in a previous section, the only problem with this technique is that gold NPs diffuse inside the bulk of the electrode. After using these resonators for biosensing, the surface will change with every cleaning, eventually ending up with a rough surface instead of a nanoparticulated one. Therefore, these surfaces can only be used once. It was first thought that the mass surrounding the peaks, of what appeared to be NPs, was protein contamination that could not be removed by the cleaning protocol. An analysis of this behaviour was needed, to verify that the cleaning process is effective, and that the deformation of the surface is due to the NPs diffusing inside the electrode. The study was performed using x-ray photoelectron spectroscopy and it is described in the following section.

2.6.5 Analysis of Nanoparticulated Surfaces using X-ray Photoelectron Spectroscopy

X-ray Photoelectron Spectroscopy (XPS) is a technique used to detect the presence of chemical bonds between elements up to 10 nm deep from the surface. Using this principle, the presence of BSA can be detected by finding the spectra characteristic of this protein.

The spectrum of BSA using XPS has been previously analysed by other authors [47], [48]. When analysing BSA, it is expected to find one peak in the core levels of N 1s and four for C 1s, see Table 2-3. The spectrum for each element is a fingerprint for BSA and it is useful to compare its presence against a blank substrate.

Six samples were analysed to understand if the roughening of QCM electrodes with NPs is due to poor cleaning or a consequence of it (diffusing Au NPs into the Au film). The aim is also to look at the efficiency of the RCA-1 protocol (Modified RCA-1 with no UV Lamp treatment) to remove the BSA protein. For this experiment, the following samples were used:

1. Silicon sample with Ti layer (60nm) and Au layer (120nm) and RCA-1 cleaned: blank sample. This type of sample is regularly used for all the tests of all the experiments on this thesis. Black curve in Figure 2-11.

2. Silicon sample with Ti layer (60nm) and Au layer (120nm) and a layer of BSA on top: standard sample with protein on top. Red curve in Figure 2-11.
3. QCM resonator, RCA-1 cleaned: this sample is to compare it against standard samples of Si wafers (Sample 1). Green curve in Figure 2-11
4. QCM resonator, RCA-1 cleaned, a layer of BSA on top, and cleaned with RCA-1. Dark blue curve in Figure 2-11
5. QCM resonator, modified RCA-1 protocol, and deposition of NPs using protocol from Section 2.6.2: QCM-NP. It is important to emphasise that there is O_2 plasma treatment of the surface according to the protocol. Light blue curve in Figure 2-11.
6. QCM resonator, modified RCA-1 protocol, deposition of NPs using protocol from Section 2.6.2, followed by deposition of BSA on top, and finally RCA-1 cleaning. Purple curve in Figure 2-11.

The XPS spectra results for each element are shown on Figure 2-11. The cleaning protocol indeed removed the contamination and the BSA. Only the sample with no cleaning involved after BSA deposition showed the characteristic peak of N 1s and the fingerprint of C 1s characteristic of this protein, see red curve on Figure 2-11 c) and b) respectively. This result leads to the conclusion that NPs are diffusing inside the electrode of the QCM. Initial hypothesis was that the protein was not being removed, leaving residues around the NPs (like a meniscus). This agreed with the AFM image, but a topographic measurement could not discard the idea that the Au NPs are diffusing, which the XPS proved. The only modification on the surface is due to the deposition of carbonaceous contamination from the environment, as can be seen in the peak of C1 in all samples[47]. Another modification of the surface comes from the protocol of depositing the NPs. One of the steps is to treat the surface with O_2 plasma. This is done to remove the coating of the InnovaCoat NPs and the PDDA from the Au electrode, followed by a quick deep in RCA-1 solution. The O_2 plasma treated surface and the final step of UV lamp cleaning oxidises the Au. This phenomena has been previously explore by King[49], where the oxidation, as gold oxide, can be seen in the XPS spectrum of Au 4f, see light blue curve in Figure 2-11 a) (85.6 and 89.05 eV).The author also attributes the peaks at 529.61 and 531.36 eV to oxide and gold hydroxyl respectively which is shown in the light blue curve shift on Figure 2-11 d). These peaks are not present on the other samples as they were not treated with O_2 plasma or UV lamp, or were rinsed with water before the protein deposition. Rinsing will remove gold oxide, as has been previously investigated by Krozer[40]. A water rinsing step is normally performed to stabilise the QCM resonator before protein adsorption.

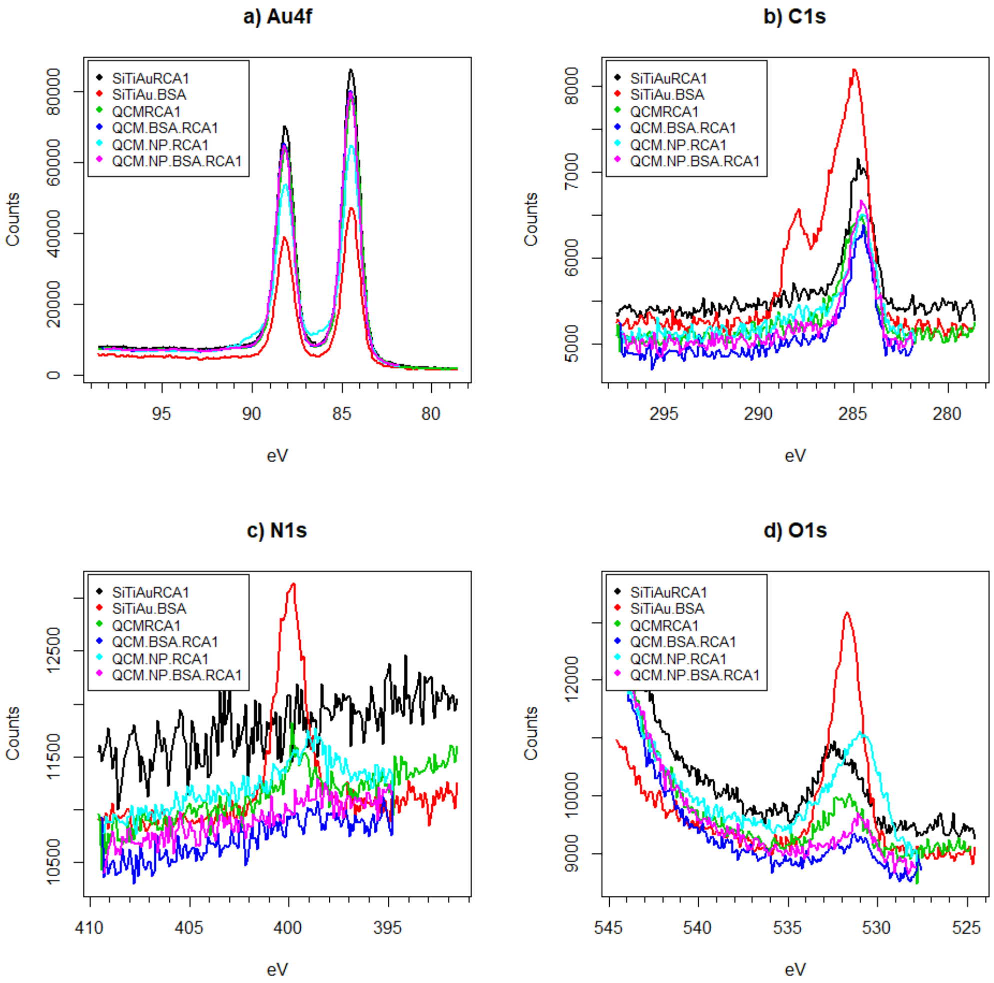

Figure 2-11. X-ray photoelectron spectroscopy (XPS) spectrum to detect the efficacy of cleaning bovine serum albumin using the modified RCA-1 protocol. The protein has a particular fingerprint for C 1s and a detectable peak for N 1s. All the elements of the substrates were analysed; Ti and Si did not give any signal and it is not shown in this image. Only the sample with BSA and no cleaning after protein deposition showed the fingerprint of the protein. QCM resonators with nanoparticulated patterns did not show these peaks, proving the efficacy of the cleaning method and that gold is diffusion inside the gold.

In this section, the efficiency of the cleaning method has been proved to remove BSA from the surface using XPS analysis. Therefore, it is proved that the NPs are diffusing inside the bulk of the Au electrode and that QCM-NP resonators, with NPs or any other structure of Au, can only be used once. This issue might arise from the gold diffusion when the resonator is being cleaned by solution and the rise of temperature needed for such protocol. This behaviour is further investigated and discussed in the following chapters. If gold diffuses under such conditions, it means that the surface which has a grainy surface due to PVD is changing with every cleaning. Although the cleaning protocol is efficient to remove a protein like BSA, it affects the surface of the electrode (roughness), especially with features like NPs of the same material as the bulk.

2.6.6 BSA measurements with QCM-NP resonators

QCM resonators with a nanoparticulated electrode (QCM-NP) can only be used once, as shown in the previous section. If the resonators are cleaned using the standard modified RCA-1 method, suggested by most companies and authors, then they will have a very rough finish instead of a patterned surface. Therefore, QCM-NP resonators were freshly fabricated and used once for each experiment to study the interaction of BSA with NPs. The NPs density was varied to analyse if the mass deposition changed linearly or if the higher density of NPs affected the protein adsorption.

The NPs were deposited on QCM electrodes by following the protocol from Section 2.6.2. The samples were freshly fabricated, followed by imaging of the surface using AFM and SEM. Before their installation in the chamber of the Q-Sense E4, the resonators were subjected to a UV lamp treatment to clean carbonaceous contamination from the exposure to air, and to make the surface hydrophilic. HPLC water was passed over the samples overnight to achieve stabilisation/drift of the signal of less than 1 Hz per hour. All resonators have the QCM-D jig (design) with fundamental frequency of 5 MHz which were bought from Q-Sense and cleaned with modified RCA-1 before the NP deposition protocol. The BSA was dissolved in HPLC water as has been shown previously to deposit monolayers on QCM resonators at a concentration of 100 uM. The required concentration for a monolayer on standard QCM-D resonators for a 1 ml of BSA solution is around 50-75 µM but given that the concentration required for a QCM-NP sample is not known, 100 µM was used to give room for the possible higher concentration required for the structured surfaces.

The results are summarised in Table 2-4. The column 'Δf' shows the raw response as a change of frequency for the mass adsorption for each resonator, all with different NP density. Column 'Δf' represents the mass on the resonator without using any mass model. If required, the areal mass on the resonator can be obtained by multiplying Δf by the constant 17.67 ng/Hz; which is obtained from the Sauerbrey mass model, Equation 2.1, using a QCM-D fundamental frequency of 5 MHz. The standard resonator with no NPs is the control sample, which all variations of QCM-NP resonators are compared against to calculate the mass increase. The mass increase is in the column 'increase by |Δf/f|'. There are three models represented on this table. The first model is a basic model and gives the number of NPs on the surface (density) as the column 'projected coverage'. This column is based on the analysis of the SEM images using ImageJ, as described previously. The second model is using Equation 2.3 from Section 2.6.4 and the projected coverage obtained from ImageJ, which is the main result of this table.

Table 2-4. Geometrical models of area increase for QCM with nanoparticles on the electrodes. The column 'Projected coverage' shows the image analysis of AFM (number of particles in a 1 um^2). The column 'Increase by Model' shows the linear change of projected area by the factor of Equation 2.4. The column 'Increase by AFM' is the topological area measure by the AFM. Finally, the result of mass increase measured by the QCM is shown as |Δf/f| where the standard measurement is the standard QCM resonator with no nanoparticles.

Measurement	Results			Models		
	Δf	|Δf/f| [E-6]	Increase by |Δf/f|	Projected coverage	Increase by Model	Increase by AFM
Standard	22.45	4.53	0	0	--	0
QCM-NP 1	26.33	5.31	17.2%	16.40%	38.34%	25.91%
QCM-NP 2	32.80	6.61	45.9%	22.80%	53.31%	34.89%
QCM-NP 3	34.20	6.90	52.3%	30.90%	72.24%	45.70%

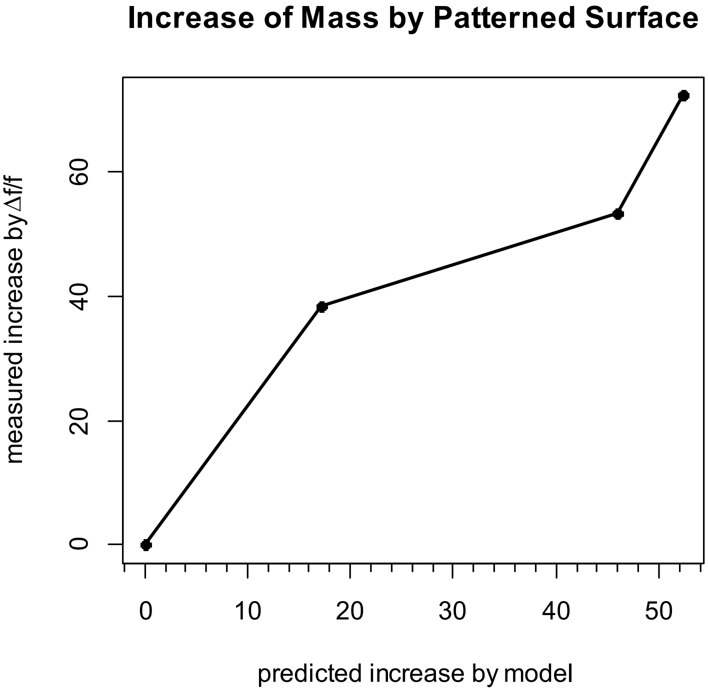

Figure 2-12. Plot of BSA mass adsorption on standard and nanoparticulated (NP) samples. The curve shows the linearity of the measured increase of mass by change of frequency against the predicted mass increase of the mathematical model. Because the mass is being linearly increased, it means that the protein is binding in the same way across different NP densities. The total coverage of the protein on the surface of the NP is only 68% compared against the same area on the surface of the electrode, leading to the believe that the protein BSA adsorbs different to the NP's curvature.

The third model is using the direct AFM topographic measurement, but this is expected to have the biggest error because of the tip radius added to the overall measurement.

The experiment was performed with two samples for each NP density, and four for standard measurement due to the limited number of resonators available. The plot of increase of mass by |Δf/f| against the predicted increase by the model can be seen in Figure 2-12. The curve has a linear tendency, which means that the protein is adsorbing in the extra surface in the same manner, and denser samples have no effect so far on the protein adsorption dynamics. If the ratio of the measured increase of mass over the increase expected by the model is taken, the protein adsorbed to the NP is only 68% (±17%) of the expected overall increase. This means that the BSA is not adsorbing in the same manner on the NP as it is on the surface. It can also be assumed that the protein takes a different kinetic behaviour after adsorption. Either by changing its conformational shape or landing angle, and eventually screening out other proteins to bind in a compact manner.

2.6.7 Conclusion

In terms of their use, QCM-NP resonators are very useful to increase the area available for protein adsorption. This will increase the signal for very small molecules that would otherwise be undetectable using the QCM resonator. These resonators can also be used for analysing the protein binding of molecules to NPs or the number of molecules in NPs for drug delivery, which can be useful for nanomedicine, where controlled quantities of drugs are required to understand their effect.

It is showed in this section how to make nanoparticulated surfaces with great control using NaCl, further optimisation can be accomplished using DLS to observe for the proximity of the NPs at higher NaCl concentrations. With time, it is expected that the coating of the NPs degrades and therefore their negative charge would be reduced, leading to a higher density of NPs on the surface of the polyelectrolyte (PDDA). The main finding is that the use of NPs lead to less mass adsorbed on their surface compared to the surface of the electrode. It is believed that this response is due to spreading of the BSA on the NP surface, but further confirmation is required and would be left for future work.

These samples can also be used for other applications. The use of NPs can be applied to resonators with limited area and very low limits of detection, where the event of a protein adsorption is less likely. On these sensors, the protein can bind and desorb quickly, if the quantities present in solution are low the event might not happen again. Instead, if the protein binds to a NP and change its conformational shape, there is a chance that the kinetic desorption changed, and the protein will either stay longer or bound forever to this surface due to denaturation. Further analysis of the behaviour of proteins on the surface of the NPs is required, as the results presented here are not enough to provide confirmation of the protein denaturation and a tailored study would be required for specific protein.

2.7 Experiment of Ageing of QCM Gold Electrodes: Surface Roughness Increase Due to Cleaning Protocol.

Due to the results shown for the nanoparticulated surface of QCM electrodes (Section 2.6.2 and 2.6.5), where the gold NPs showed diffusion inside the bulk of the gold electrode, another experiment was required to observe if these changes would also affect standard QCM gold electrode surfaces.

The QCM electrode is not flat if it is compared against the scale of proteins. The electrodes contain grains at the nanoscale because they are deposited using a physical vapor deposition (PVD) technique. These grains are considered nanostructures and can be characterised using AFM in terms of their number and diameter, as well as the overall roughness of the surface. Since different manufacturers use different techniques and conditions for electrode deposition, it is expected that the surface of electrodes would have different characteristics depending on the supplier. To investigate the changes of the electrodes through the consecutive use and cleaning (ageing) the roughness of the electrodes was measured using AFM before and after every cleaning.

The experiment consisted on analysing QCM sensors from different brands: QuartzPro, AWSensors, and Q-Sense. The samples were subjected to the modified RCA-1 cleaning protocol, Section 2.4. A second experiment comprised on subjecting one sample to an increase of temperature using an oven.

Measurements labelled as “New” were performed as soon as the resonators were received. The second measurement was after the modified RCA-1 cleaning protocol. The heated measurement was performed on a used sample that was previously cleaned an unknown number of times. Initially, the sample was in the “Pre-heating” state, then it was subjected to an increase of temperature, left to cool down and finally the measurement performed; this is the “Post-heating” measurement. All AFM measurements were analysed using the watershed algorithm from the Gwyddion software. This method finds the grain boundaries of an AFM topographic image and the area of each grain detected can be obtained, some results of this method in image form can be found in the Appendix.

To compare the results, a density plot was used instead of a histogram. The density plot better represents the percentage of grain sizes of a determined diameter. A histogram only plots the counts of grains, if the grains are small there would be more counts than larger grains making the comparison not normalised. A density plot normalises the results and can be used among different brands.

The QuartzPro resonators have the QCM-D design. They were purchased from QuartzPro Sweden and are packed and sealed in a class 10,000 room. These resonators are the roughest samples from across all brands. All the steps of the modified RCA-1 protocol were followed. The image and the analysis of the density plots can be found in Figure 2-13. The RMS roughness of the ‘New’ image from Figure 2-13 is 3.353 nm with average grain diameter of 54.43±13.72 nm (vertical red dashed line on the density plot). After the cleaning, the roughness changed to 2.153 nm RMS. Grains grew to 64.48±22.03 nm diameter (vertical green dashed line). In this case, the roughness decreased, flattening out the surface

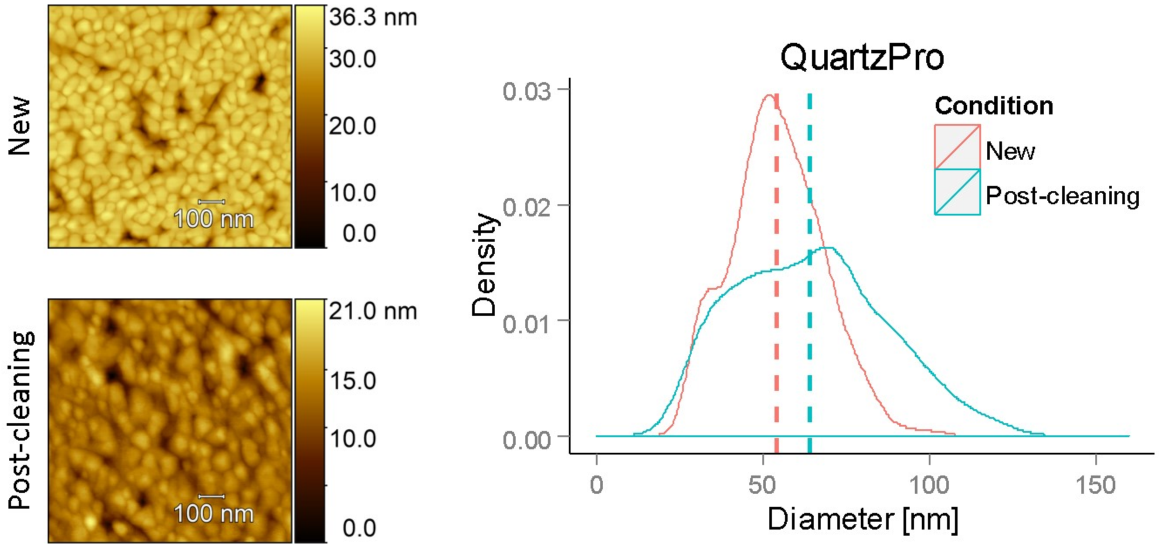

Figure 2-13. AFM grain analysis of grain coalescence of QCM-D resonators from QuartzPro. The Post-cleaning measurement increased the grain sizes close to 20% and moved the mean of the diameter of the grains from 54 nm to 64 nm. This shows that the cleaning protocol affects the surface of the gold deposited electrodes.

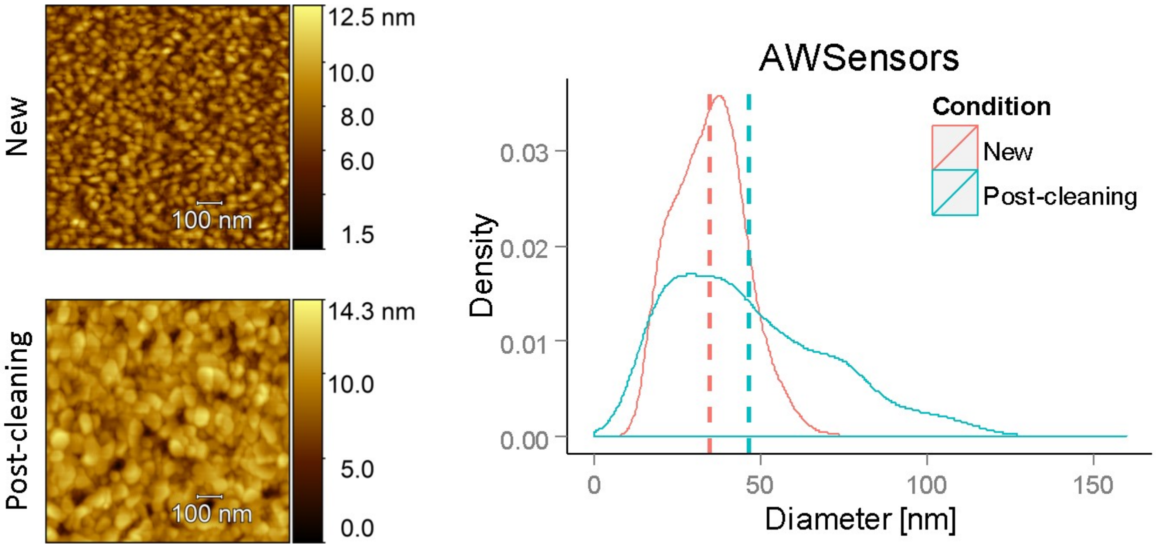

Figure 2-14. AFM grain analysis of the resonators from AWSensors. Grains coalesced after a cleaning step using the Modified RCA-1 protocol. Roughness of the sample increased along with the grain size. The increase of diameter was approximately 30%.

by increasing the grain sizes and reducing the depth of the channels of the grain boundaries. This is believed to be the cause of surface energy being minimised in the system.

The second brand, AWSensors, uses the QCM jig for standard QCM measurements. The roughness is 1.370 nm RMS with grains of 34.97±10.49 nm diameter, see Figure 2-14. Once the sample was cleaned using the modified RCA-1 method, the roughness increased to 1.679 nm RMS and the grains increased their size to 46.88±23.90 nm diameter. In contrast, the roughness did not decrease as in the QuartzPro resonators.

The third brand, from Q-Sense, also uses the QCM-D electrode design. This is the most common used brand at the Welland Group (Nanoscience Centre, University of Cambridge). For this brand, four samples were measured and labelled as P1, P2, P3 and P4. One of these samples (label unknown) was subjected to a second cleaning step. Another sample that was not initially measured, but has been used multiple times, was also characterised to observe the trend. All results are summarised in Figure 2-15 and Table 2-5. AFM images and density plots of all four samples can be found on the Appendix. For the "New" and "Post-cleaning" images, only the AFM image of P1 is shown in Figure 2-15. The density plot, however, is the average of all 4 samples for the "New" and "Post-cleaning" curves. For the "Second-cleaning" label, both image and density plot is from one of the initial four samples, which got scrambled and could not be identified.

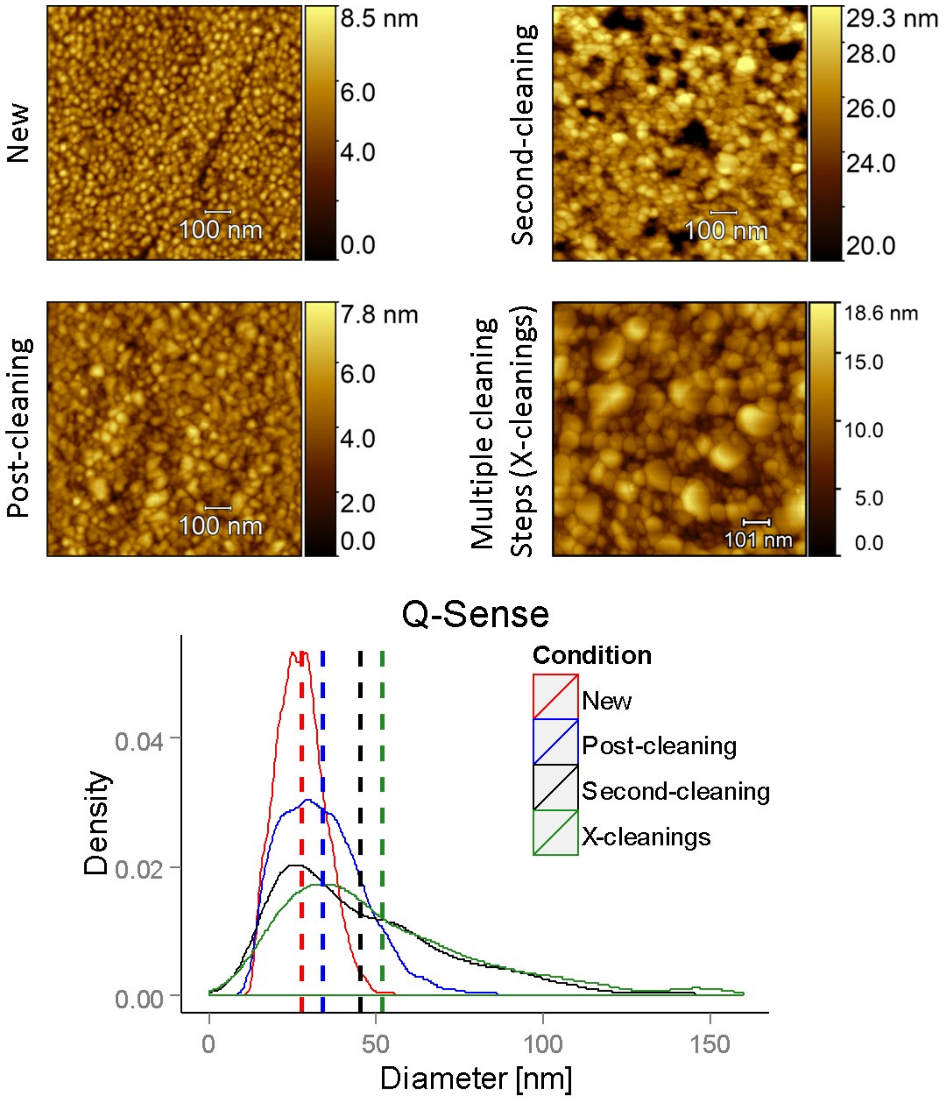

Figure 2-15. Measurements of Q-Sense resonators under different number of cleaning steps. The roughness of the surface kept increasing with multiple cleanings along with the grain size. The surface roughness and mean grain size stopped increasing with multiple cleaning steps as can be seen on the density curve of X-cleanings. The roughness changed from 1 nm RMS to 2.62 nm RMS and the grain size from 29.52 nm to 52.17 nm diameter on average.

The value of roughness for sample P1 in ‘New’ condition was 1.071 nm RMS and grain size of 29.52±7.10nm. After the ‘First-cleaning’ step, the values obtained were 0.920 nm RMS for roughness and grain size of 36.58±13.23 nm diameter. These results were not subjected to UV-lamp treatment during the modified RCA-1 cleaning protocol. For the ‘Second-cleaning’ experiment, the sample was subjected to UV lamp treatment. The roughness value was 2.116 nm RMS, with grain diameters of 45.68±25.10 nm. Both roughness and grain size increased. The UV-lamp showed that it plays an important role on the coarsening of the surface. This is probably due to the oxidation of Au grains after the UV ozone treatment, followed by etching of this oxidation during the RCA-1 leaving pure gold on the surface; Au grains usually contain the contamination of the PVD technique or from the environment, if any, on their surface. Once etching occurs of the upper layer of the surface, pure gold, and rise of temperature might facilitate the coalescence of adjacent grains; contamination limits the grain size, this is further discussed in Chapter 3. After a sample is used multiple times, the roughening stops, reaching a plateau for both roughness and grain size: this can be observed on the plot of the sample labelled 'X-cleaning'. The roughness obtained was 2.683 nm RMS with 52.17±30.22nm of grain diameter. The trend shows the surface reaching its maximum state of change, which is believed to be the minimum stable surface energy.

Table 2-5. Roughness and grain size diameter for QCM-D resonators from Q-Sense.

Label	Roughness RMS [nm]	Grain Size Diameter [nm]	
New	1.071	29.52	±7.10
1^{st} Cleaning	0.920	36.58	±13.23
2^{nd} Cleaning	2.116	45.68	±25.10
X^{th} Cleaning	2.683	52.17	±30.22

The last experiment was performed by only heat treating the sample. In this case, the temperature of the sample was raised to 200 °C for 10 mins in a vacuum oven and cooled down by taking the sample out of it. The pre-heated sample had a roughness of 1.715 nm RMS, with grain size of 41.91±20.12 nm. The heated sample had a value of 2.141 nm RMS with 39.96±24.16 nm of diameter for the grains. The difference was not substantial, but a subpopulation on the pre-heated sample can be seen at the density plot of Figure 2-16, which moved to higher grain size subpopulation after the temperature increase. It is believed that the reason the change was not substantial as previously observed with the cleaning experiment, is that, during cleaning, the sample heats up and at the same time is being cleaned and slightly etched by the solution. The cleanliness of grains favours coalescence. In the heated sample, which was previously cleaned but not immediately heated, the surface is contaminated by carbonaceous

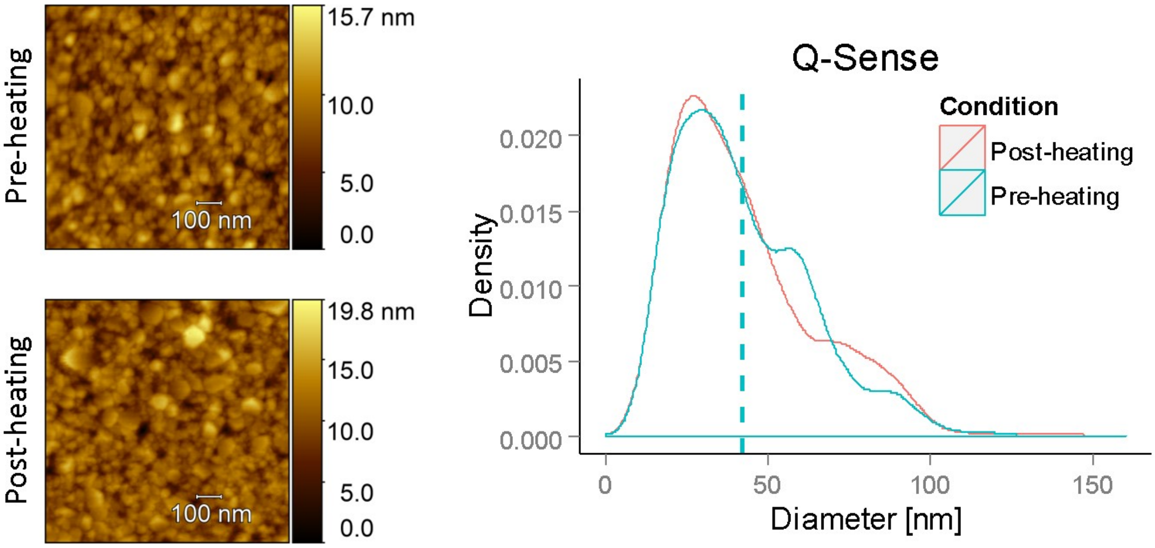

Figure 2-16. AFM image of the heat treatment experiment of QCM-D gold surfaces. The mean grain size did not change substantially. The vertical lines that represent the mean value are overlapping. Unexpectedly, the roughness changed, and can be seen by the change of size of the subpopulation from 60 nm (blue curve) to 85 nm (red curve). This experiment shows that both heating, solvent cleaning, and UV treatment affect the change of the gold grains by coalescence by different factors such as purity and mobility of adatoms among others.

deposition from the environment during storage, limiting the diffusion of the gold. It is believed that bigger grains favoured coalescence because the contact area under them is bigger (a higher purity area). So only this population of grains coalesced to other grains.

2.7.1.1 Conclusions of cleaning and heating QCM resonators

The modified RCA-1 cleaning method showed that it influences the coalescence of grains for the electrodes of QCM resonators. Standard QCM/QCM-D electrodes are evaporated with e-beam evaporation systems having a very low roughness and very small grains. When the sensor is cleaned multiple times, the roughness and the grain size increase until it reaches a plateau. In the opposite case, if the surface of gold is initially very rough, due to big grain sizes and steps between them, then the surface starts to decrease its roughness. Both surfaces, low roughness and high roughness electrodes, tend to reach a similar roughness value after multiple cleanings which is between 2-3nm RMS. The modified RCA-1 both etches away the gold and increases the temperature on the surface. The etching could cause an increase of grain size by grain coalescence of pure gold, which has been shown to occur using gold nanowires in proximity with no heat applied[50]. Additionally, cold welding of gold films can be accomplished at low pressure at room temperature on contaminated films, by using a compliant elastomer which will put both films in the closest proximity[51]. Considering these findings in the literature, and that the grain size of the films does not change over time when they are stored at room temperature, the hypothesis that grains coalesce by thermal energy, and possibly assisted by contact pressure due to surface strain, gained support.

Due to the lack of external pressure during cleaning, the mechanism of grain growth and coarsening is probably the result of annealing, which is caused by thermal exposure during the cleaning protocol. Annealing is a method generally used for increasing the grain size and crystallinity of gold films. The heating experiments showed an increase of grain size and roughness with 10 mins of exposure to 200°C, if this is repeated, as in the cleaning procedure, roughness will increase and will reach saturation after several exposures. However, the change is not as substantial as when they are cleaned using modified RCA-1 probably because of the lack of Au purity.

The changes of the surface roughness might affect some protein mass studies, especially those that are highly sensitive. The results obtained in this experiment show that electrodes with an average roughness of 2-3 nm RMS will not modify their surface as the roughness trends to these values. In addition, grain sizes between 50 and 60 nm diameter are required to minimise the changes. One last characteristic that was not taken into consideration, but might play a role on the surface change, is the steps between grains.

If a QCM resonator is manufactured as a flat electrode, the flatness will be lost after the first cleaning procedure. This would be, again, a result of increasing the temperature and the modified RCA-1 protocol. A requirement for these flat electrodes would be to keep them under vacuum sealed conditions to avoid any contaminants on the surface and use them just before the experiment; a UV lamp cleaning procedure would be enough to remove any carbonaceous contamination without involving any temperature increase.

2.8 Experiment: Nanowire Growth

2.8.1 Introduction to Nanowires

The great interest in nanowires (NWs) is due to their potential application in nanoscale electronics and optoelectronics. But their possibilities go further than these fields, they can also be used to increase the surface area of electrodes[52], and for energy harvesting[53], among others. Also, the mechanical rigidity they possess make them a good candidate as anchorage nanostructures for biomolecules in biosensors[54].

NWs are thin and long nanostructures with a length-to-width aspect ratio of at least 1000. The smaller dimension is that of the width, being between 1-200 nm. The length varies from one to tens of micrometres. They can be easily fabricated using different methods, one of the easiest to perform with a uniform outcome is the carbothermal growth.

Using the experience at the Nanoscience Centre, a carbothermal growth recipe for nanowires of ZnO was used. This recipe works for silicon wafers, but the growth is not directional, and has multiple angles of growth. In a-plane sapphire wafers, the lattice match of the surface with the ZnO nanowires allows them to grow in their c-plane direction and normal to the surface. It was the sapphire variation that needed to be optimised as it has stopped working. After solving the issues of the protocol, their application for nanostructuring QCM resonators was explored.

The aims of this experiment are:

1. To find out the reasons why the process of carbothermal growth of ZnO NW used at the Nanoscience Centre is not optimal on a-plane sapphire wafers.
2. Explore if the growth is possible on samples other than sapphire. Main aim of growing ZnO NWs is to do it on top of QCM electrodes.

2.8.2 Synthesis of ZnO NW using VLS mechanism

NWs are grown using a modification of the Chemical Vapour Transport and Condensation(CVTC) system that uses Vapour-Liquid-Solid (VLS) mechanism from Yang *et al*[55]. The VLS is widely used for its simplicity. The method of the Nanoscience Centre is from the works of Shin *et al*[56].The process starts by cutting a wafer into small squared pieces. A layer of Au is deposited on top of these samples using a Physical Vapor Deposition (PVD) method. Then, the samples are placed inside of an alumina boat which contains a bed of a mixture of ZnO and C powder. The boat is then placed inside a furnace. The VLS mechanism starts by melting the catalyst (Au in the case of ZnO NW) on top of a surface. The

Au layer granulates and works as seeds for the deposition of ZnO in the sample as nanowires. This step is called nucleation. Subsequently ZnO nanopowder is then evaporated by rising the temperature. Carbon powder is used to reduce the temperature of ZnO evaporation. When the ZnO vapour contacts the Au granules, an Au-ZnO droplet is formed, ZnO reaches certain saturation inside the droplet and the ZnO precipitates forming a crystal at the bottom. This second step is repeated forming the NW until the droplet is oversaturated and stops the growth.

2.8.3 NW Growth Method and its Re-optimisation

The NW growth method failed to grow NWs normal to the surface. The objective is to find out the reasons why this is happening. The method used is as follows. The ZnO NWs were grown on Sapphire (Al_2O_3). The sapphire wafer has the a-plane facing in the normal direction to the surface. The wafer was cut into squared samples of 5mm each side and a layer of Au of around 1 nm thick is deposited on top using the Lesker e-beam evaporator. A nanopowder bed with a 1:1 concentration of ZnO(<100nm):C(<20um) grinded mix was deposited in the middle of an alumina (Al_2O_3) boat. On top of the nanopowder, the squared samples were placed $\sim 2.5\text{mm}$ from each other. Subsequently, the alumina boat was placed in the middle of the tube of a furnace. The temperature in the furnace was increase up to 930°C at a rate of 10°C/min, and a dwelling time between 20-40min.

After changing the variables of the method, the growth of nanowires did not improve. The modified parameters were the following:

- Thickness of the Au catalyst layer.
- Dwelling temperature time.
- Rate of temperature increase.
- ZnO and C powder size.

After trying different combinations, a trend could not be obtained. The only possibility for the NWs not to grow vertically using this previously optimised protocol was that the template of the a-plane sapphire was mismatching with the crystal lattice of the c-plane ZnO NWs. The strongest hypothesis was that it was caused by contamination on the substrate. These wafers are sealed in a bag, but they had been purchased long before this project was taken, so the bag might leave a residue on the surface of the wafer. To find out if contamination was the issue, the sapphire wafers were cleaned using standard protocols, but the growth did not improve. Most standard cleaning procedures damage the flatness of wafers, hence their crystallinity, and subsequently the lattice mismatch with the c-plane of ZnO. Fortunately, it was found in the literature a cleaning protocol to keep the contact angle very low, i.e. to maintain the crystal flatness of the a-plane sapphire[57].

2.8.4 Cleaning Method of a-plane Sapphire Samples

2.8.4.1 Standard Cleaning of a-plane Sapphire

The standard cleaning method used at the Nanoscience Centre for sapphire samples is: sonication of the samples in acetone, followed by isopropanol, 15 minutes each, followed by rinse with DI water, and finally dry with N_2 gun. However, not very good results were obtained using this cleaning method. Beside this, other methods used in the cleanroom for fabrication were tried with no success: e.g. RCA-1, Piranha. For this reason, the modified standard multistep RCA cleaning method was used.

2.8.4.2 Modified Standard Multistep RCA Cleaning Method (MSM-RCA)

The following cleaning protocol is the work of Zhang *et al*[57]. It is a modification of three different protocols originally used in the RCA laboratories. These three methods are applied consecutively at optimised concentrations for a-plane sapphire. The following recipe has one step less than Zhang *et al* protocol, because of the unavailability of the solvent, but it still fixed the verticality of the NW growth:

1. Immersion in ethanol for 12 hours at room temperature.
2. Rinse with HPLC water, dry with N_2 gas.
3. Immersion in Sulfuric Peroxide Mix (SPM or Piranha) solution (H_2SO_4: H_2O_2 in a ratio of 3:1) for 20 mins at 80°C.
4. Rinse with HPLC water, dry with N_2 gas.
5. Immersion in RCA-1 solution ($NH_3(30\%)$: H_2O_2: H_2O in a ratio of 1:1:2) for 20 mins at 80°C.
6. Rinse with HPLC water, dry with N_2 gas.
7. Immersion in RCA-2 solution (HCl: H_2O_2: H_2O in a ratio of 1:1:2) for 20 mins at 80°C.
8. Rinse with HPLC water, dry with N_2 gas.

2.8.5 Experimental Results of ZnO Nanowire Growth and Their Use on QCM Surfaces

After subjecting the a-plane sapphire samples to the MSM-RCA cleaning method, it was found that the recipe of NW growth process was, indeed, optimise and the lack of vertical growth of the NW was a result of the contamination of the surface of the sapphire wafers caused possibly by the bags in which they were sealed. Figure 2-17 shows the growth of ZnO NWs on a-plane sapphire at normal angles from the surface. These NW have a 7 μm length and the width is around 150 nm. The wafers used for these experiments were not purchased new, they have been obtained a couple of years before. They come in sealed bags, but it seems that this might not be enough to keep them out of contaminants either coming from the sealed environment or the packaging itself. Such contaminants might be so small that are at the nanometre level. The only way to use these samples was to clean the surface without affecting the crystallinity.

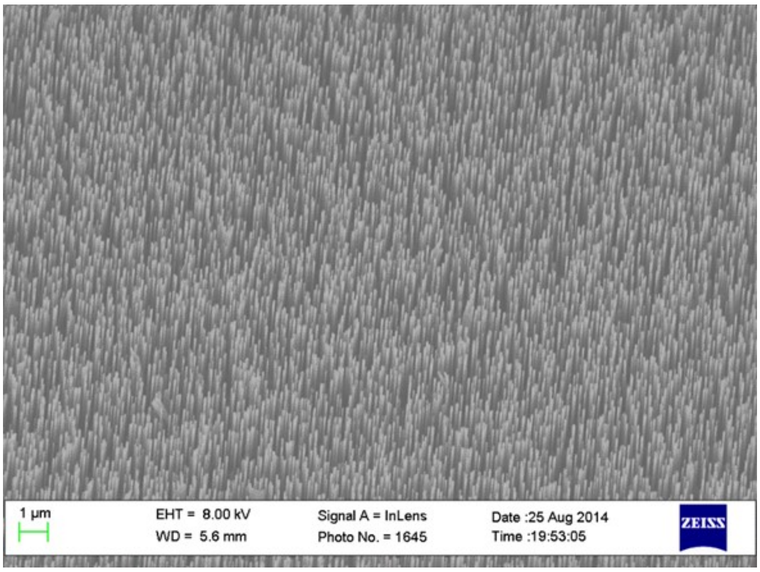

Figure 2-17. Highly aligned nanowire growth using the carbothermal method. Most NWs are at a 90° angle from the surface. This growth was achieved after several tries, observing that it was a problem of cleanliness of the surface.

After understanding the steps required to achieve this growth and its sensitivity to changes, it was concluded that it might not be possible to grow ZnO NWs vertically on top of QCM resonators using this protocol. QCM resonators have PVD materials as electrodes, and the crystallinity and the orientation are compromised. Instead, a solution is proposed. The use of thin films of ZnO as a seed layer to grow the nanowires. Tiwale worked on zinc naphthenate films that get decomposed into ZnO[58]. Using these films, it was possible to grow ZnO NWs using the NW growth method on any surface. The protocol was not optimised, but with a few tests, the proof of concept of growing vertical NWs was accomplished. Figure 2-18 shows the vertical growth of Nanowire on these films. The growth was done on a zinc naphthenate solution spin coated at 3000 RPM for 60 seconds. The film was not evenly flat, having a thicker edge bead and a thinner film at the centre. The vertical growth was on the edge bead. It is believed that the crystal orientation of the grains at the surface create this vertical growth. This orientation might be achieved at certain thickness of the film at specific decomposition parameters (e.g. 500 °C). Although no further details were investigated, this process could be useful for different substrates or nanopatterned samples of zinc naphthenate using e-beam lithography. The high temperature of the process is something that it is not compatible with standard QCM. Handling the quartz at temperatures higher than its Curie temperature (573°C)[59] would make it lose its properties. Instead a gallium orthophosphate ($GaPO_4$) crystal can be used. These resonators work with any QCM system if the required electrode design jig by the monitoring system is used. Crystals of $GaPO_4$ have a phase transition at 970°C, this temperature is when these resonators lose its properties, making them suitable with the temperature required for the NW Growth Method (930°C).

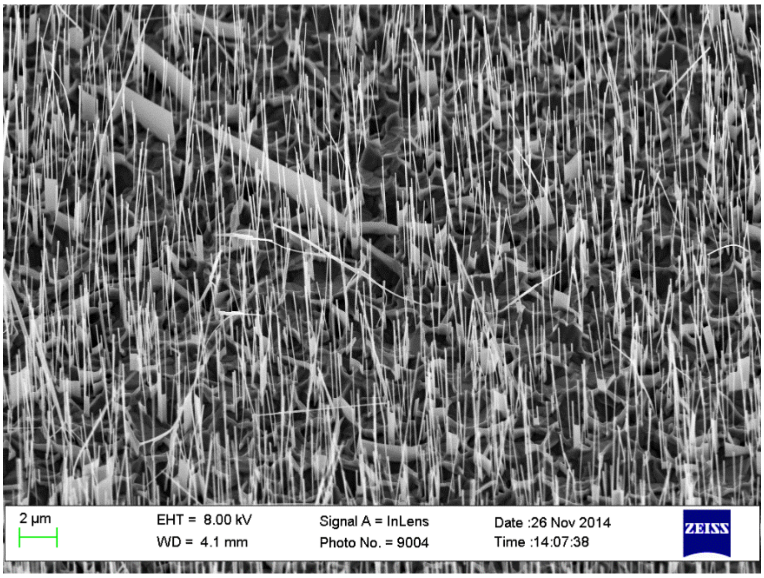

Figure 2-18. ZnO nanowire growth on top of a spin coated film of ZnO. The film is a decomposition of zinc naphthenate.

2.9 Results

The main aim of this chapter was to set the baseline experiments for the development of this manuscript. The experiment about variability in mass measurements showed that QCM-D resonators acquired from Q-Sense do not have significant changes over multiple uses. The experiment is reproducible as long as the protocol is strictly followed. This protocol will be used in the following chapters, where the surface characteristics of the resonator are changed, in order to get consistent results. The core result of this chapter is about the nanoparticulated QCM electrodes. BSA is believed to spread when it binds to 43 nm diameter nanoparticles. Increasing the range of mass measured compared against a standard surface, but less mass is adsorbed than the expected by the area increase of the NPs. It was obtained that only 68% of BSA was adsorbed on the area of the NP.

In the experiment of ageing of QCM electrodes, it was observed that gold electrodes change when they are used multiple times, and the quality of the maker is important to get consistent results. The obtained result is that electrodes with an initial 2-3 nm RMS roughness will have the same value across cleanings. This roughness, however, plays a role in BSA adsorption as shown in the following chapters.

The ZnO nanowire experiment showed that it is difficult to fabricate aligned nanowires on top of a surface that is not crystalline and matches the vertical crystal growth of the ZnO nanowire. It was shown that even the slightest contamination on top of a-plane sapphire changes the directionality of the ZnO nanowires. Instead, an alternative experiment that uses a ZnO precursor spin coated on top of the electrode is presented. Initial results showed that vertically aligned nanowires are possible in this manner on any surface despite not being crystalline. It is believed the thickness and the decomposition conditions of the precursor allows crystallinity on the surface of the coating, still this experiment is at its initial stage and requires further study and optimisation.

2.10 Conclusions

Different surface modifications were explored in this chapter. The feasibility was an important parameter for these techniques as the chosen ones are used in the following chapters. There were many differences between the patterning of surfaces. NWs were an attracting feature as their aspect ratio is higher compared to the other methods explored. However, the proposed protocol and the optimisation of it might be a whole project on its own, which would not give more time to explore other techniques. At the same time, the resonators required for this project are scarcer (the material gallium orthophosphate), more costly and would be difficult to dos tests on other materials. Gold, however, is a standard in biosensing, a cleanroom available material and can be used with multiple biological specimens due to its inertness. The drawback is that it has a smaller aspect ratio compared to nanowires (gold nanoparticles) but was not considered a major problem as NPs are still in the depth penetration (sensing length) of the QCM into the solution (<200nm), which in the case of NWs (~10µm height) might induce other effects on the QCM that are not currently modelled. Gold is very easy to evaporate, which can be used to make patterns using techniques of the semiconductor industry. Gold is a good candidate to look at protein interactions with physical structures, gold is a common electrode of QCM resonators, avoiding an extra step of depositing a specific material on the QCM electrode.

In terms of findings, it was presented different techniques of fabrication of nanostructures along with an experiment of BSA proteins binding to nanoparticles. It is shown how difficult these protocols can be as in the case of ZnO nanowire growth, and their use in QCM resonators might be a challenge. It is also shown how the topography of surfaces of physically deposited electrodes as in the case of gold changes with multiple uses. These changes are attributed to the cleaning conditions: rise in temperature and an oxidative chemical reaction. These factors induce grain coalescence and roughening of the surface. This could be crucial for obtaining consistent mass measurements of BSA adsorption and would be explored in the following chapters. However, we showed that Q-Sense resonators give reproducible results at least when used five times. Nanoparticles also coalesce with the gold electrode when they are attached to it and the resonators are cleaned. QCM resonators fabricated in this manner were only used once to avoid mass measurement variation and to keep the nanoparticle structure intact. The nanoparticles on top of the QCM electrode showed that BSA binds with a different conformational shape compared to the standard surface. It is believed that BSA spreads on top of the nanoparticles and retains a more globular shape on the surface of the electrode. This is concluded from the mass measurements of the QCM where on average 68% of the expected BSA on the nanoparticles was measured. Because of the complexity of other materials and to minimise the number of variables, gold was chosen to be the base material to make nanostructures for the rest of this dissertation. These experiments set the basis of the following chapters, where questions like "what happens when BSA binds on a featureless surface?" and "what are the difference of BSA adsorption among QCM electrodes of different roughness?” are answered. In the next chapter a new technique to make atomically flat gold on QCM electrodes is introduced and protein adsorption experiments are performed on these devices.

Chapter 3

Pressure-Forming Template Stripped Gold for QCM Electrodes

3 Pressure-forming Template Stripped Gold for QCM Electrodes

3.1 Summary

This chapter focuses on making measurements of bovine serum albumin adsorption on a flat featureless surface. It starts by introducing atomically flat surfaces with a literature review focused on gold substrates eventually leading to the feasibility of these techniques to create ultraflat gold electrodes on QCM resonators. The solution to this problem is presented as a new technique developed for this dissertation to fabricate atomically flat gold surfaces on QCM electrodes: the Pressure-Forming Template Stripping (PTS) technique. The PTS technique is the only technique to the best of our knowledge that can make ultraflat gold QCM electrodes without affecting the response of the piezoelectric resonator. The technique is characterised and optimised with a protocol outlined. It is showed how the thickness of the electrode play a role in the response of the QCM resonator affecting higher frequencies (harmonics). A bovine serum albumin adsorption is performed on PTS QCM gold electrodes and compared against standard and rough gold surfaces. Finally, the results are presented and compared among different electrode surface roughness leading to the conclusions.

3.2 Literature Review of Atomically Flat Gold Surfaces

3.2.1 Introduction

Atomically flat surfaces are useful in multiple bioengineering applications, e.g. they can be used for characterisation of molecules using Atomic Force Microscopy (AFM)[60] and optimisation of lipid bilayers[61], among others. However, some biomolecules are not compatible with readily available substrates like silicon wafers (that have a crystal flatness) or they require a specific material to attach to the surface like gold. This has led to the use of Physical Vapor Deposition (PVD) techniques on top of incompatible substrates. These methods create nanometre scale roughness on their surface. These rough samples, however, are considered flat in the scientific community and these materials are used in most biosensing applications. The problem arises when a sample needs to be characterised by multiple methods. For example, a QCM gold electrode is considered to have a flat surface and experiments are performed under this condition, when the sample is characterised by AFM (or another technique) the features on the surface start to affect or bias the observation of the results. A common solution to overcome this problem is to make an experiment on QCM resonators and a separate experiment on AFM using a different sample with a flat surface of the same material of the QCM electrode (e.g. Au or SiO_2). The flatness is required to increase the contrast in AFM measurements. However, conditions might differ from one sample to another, for example the flow of the solution might be different at the nanoscale. It is therefore crucial to be able to have a surface that is atomically flat and can be used for both sensing and post-characterisation.

First, it is required to define flatness. On a substrate, it is defined as having a levelled surface, with no curves in any direction, and no grooves or steps. In a PVD method, vapor of particles of material are transferred to the surface. Depending on the conditions, these particles form grains of different sizes and orientations on the substrate[62]. The surfaces of these films have grains in the range of 10-100 nm diameter with Grain Boundary (GB) steps ranging from 7-36 nm. This might be considered flat if a nanostructure like a nanoparticle of 100 nm diameter is seating on top of the surface. On the contrary, proteins are nanostructures that are well below 100 nm. Although several authors differ from each other, the most frequent agreement is that proteins are polypeptides made of more than 50 amino acids[63]. Most proteins fall in the range of 2-20 nm diameter with a few of them reaching higher or smaller dimensions. Because of similar scale to surfaces and GB with PVD materials, when proteins form a monolayer on a rough surface, the resulting topology of the protein monolayer film would be similar to the topology of the surface below. This presents a problem for the characterisation of proteins during and after adsorption on the surface, as the characterisation would be biased towards the substrate and not the protein. To increase the difference in scale, some techniques have been developed for the last three decades to improve the flatness of these surfaces. These methods required the understanding of several physical or chemical methods, and in some cases a combination of both. One of the methods is PVD of gold for biosensing and imaging. The PVD of gold is very well characterised under different parameters and the flatness of the final surface can be controlled. Another more recent development the Template Stripped Gold (TSG) and its variations, has also been useful for the creation of flat surfaces. In this chapter, these techniques applied to the fabrication of flat gold for biosensing applications are summarised with their advantages and disadvantages outlined. The main content is a new technique developed for this dissertation that allows the fabrication of atomically flat gold QCM electrodes.

3.2.2 Proteins at the nanoscale

The most important characteristics of a protein are its shape and size. The folding of proteins plays an important role for the determination of their geometrical form. This mechanism is driven by its chemical groups, specifically by the hydrophobic groups, which seek to minimise the surface energy of the protein and the contact with the solvent[32]. Therefore, proteins can be modelled as spherical particles of a certain volume. However, their molecular size plays a greater role on their final shape, the bigger the molecule the higher the probability that the molecule would have more than one domain and hence multiple globular regions that fold independently.

In order to analyse proteins and their physical behaviour, Erickson [32] uses the following useful principles:

1. The subunits and domains of a protein are closely packed atoms
2. There are no spaces and almost no water molecules in the protein interior

3. Proteins are rigid structures with a Young's modulus like hard dry plastic and all have approximately the same density (1.37 g/cm^3)

Furthermore, there are physical characteristics that make the proteins different from each other. A protein that is elongated is likely to be flexible. Another protein might have groups on the surface more hydrophilic, in some cases increasing its wettability, and the interaction would be different compared against a protein that has more hydrophobic groups: reorientation, reshaping etc. Both physical (shape) and chemical composition end up affecting the behaviour of proteins and how they interact with different environments.

It is only logical to think that the chemistry and the geometry of the environment might also affect the behaviour of a protein; either instantaneously or gradually. Taking a spherical protein as a reference, the protein is in a state that should not be changing as it is in its minimal energy state in solution. If the ions in the solution change, rearrangement of the protein might occur to minimise surface energy. In the environment with the geometrical case, the solution remains the same, but a flat surface is incorporated in the system which has a charge, or a specific chemical composition, this creates an electrostatic attraction or chemical bond with the target molecule respectively. When the molecule binds, it does so in an oriented manner, then the molecule proceeds to minimise surface energy in different scenarios. In the first case, the protein would create a blob-like structure on top of the surface. In the second case, the protein might unfold during the binding. Lastly, the protein might remain almost in the same shape on the surface as it is in solution. Following this same approach, if structures of the scale of proteins on the surface are introduced, these structures being of the same material as the substrate, it might change the behaviour of the protein; e.g. instead of remaining spherical and orientated normal to the surface as it would on an ideal flat surface, it might unfold on top of the nanostructure and orientate at different angles normal to the nanostructure. When proteins change their conformational shape, they also change their binding kinetics and their activity.

Most surfaces are considered flat, and most of these surfaces are used for protein studies or biosensing. It is, therefore, crucial to understand these surfaces at the nanoscale and explore if they play a role on protein adsorption.

3.2.3 Surfaces at the nanoscale

Surfaces of different substrates have different topologies. A silicon wafer has a crystal surface which is the smallest possible roughness for a substrate of this material, and it is characterised by the position of the atoms on the crystal lattice and its orientation. On crystal substrates, there are atomic steps in the range of tens of picometres. Other methods like PVD, rely on depositing a material on top of another substrate. For different materials, like gold, this is the only practical way of being able to use them for different applications. The PVD occurs by evaporation of the material or by mechanically ejecting the material from the source to the substrate (sputtering). The films created by these techniques have different structural characteristics as they grow, this is briefly analysed in Section 3.1.3.3. Roughness on these surfaces are in the scale of 1-4nm RMS, and it is important to highlight that the sizes of grains vary depending on the deposition technique used. The grain diameters have different lengths depending on the conditions of the deposition. For gold, the scale range is in the 10-80 nm diameter and have different step heights at the grain boundaries. To minimise this, samples can be chemical-mechanically polished (CMP) to flatten out the surface, further details can be found in the work of Franssila [64]. The method consists in using a slurry of particles and an etching solvent, which is fed between a polishing pad and the deposited material. Polishing will eliminate the irregularities (reduce the step height between GB) present on the surface. CMP surfaces of gold can have a roughness as low as 0.38 nm RMS[65], but usual values are around 1 nm RMS. Another technique is Atomic Layer Deposition (ALD), a conformational deposition method which could be deposited with atomic flatness if the target surface also has this low roughness, which is a limitation for several applications. Additionally, ALD has a limited number of materials that can be deposited, where gold is not an option. Therefore, if the methods that can deposit Au are compared against the size of proteins, both will have the same scales; e.g. a protein of ~7 nm in diameter, like Bovine Serum Albumin (BSA)[66], adsorbs on a deposited surface with very low roughness but highly grainy, it would be difficult to differentiate between a grain of the material or a BSA molecule. This problem usually arises in a topological AFM image. BSA is measured in air as approximately 2 nm height from minimum value to maximum value on a flat surface like muscovite (mica), considering the protein to be the cap of a sphere, the radius of the base would be approximately 14.1 nm plus tip radius, both height and diameter would be at the scale of the grain sizes of deposited materials.

The lack of compatibility of biomolecules with many crystal materials (like silicon wafers) and the roughness created by PVD methods have given way for many scientists to use other materials that are atomically flat and biocompatible like muscovite mica, atomically flat grown gold, or TSG. These materials are regularly used surfaces for biomolecular characterisation and are described below.

3.2.3.1 Muscovite Mica

Clay mineral muscovite mica, or just mica, is one of the flattest surfaces available for characterisation of biomolecules. It is a phyllosilicate formed by a stack of three sheets, see Figure 3-1. The two outer sheets are made by an infinite repetition of a building block: tetrahedrons of oxygen and Si^{4+} ions in their centres. The inner sheet is made by the repetition of octahedrons of oxygen with Al^{3+} in their centres, for highest quality mica (v1), or Mg^{2+} in their centres for lower quality[67]. The stack is held together with the next stack by electrostatic attraction created by an interlayer of potassium cations (K^{+}). This energy is weak and allows the mica to be cleaved along the (001) plane to get an atomically flat surface. In some cases, the mica has an interlayer of divalent cation Ca^{2+} or Mg^{2+}, which have a stronger binding of the stacked layers; these micas are known as brittle micas which are different from the true micas of interlayers made of K$^+$ or Na$^+$[68]. The potassium cations on the freshly cleaved mica can be easily dissolved in water[68].

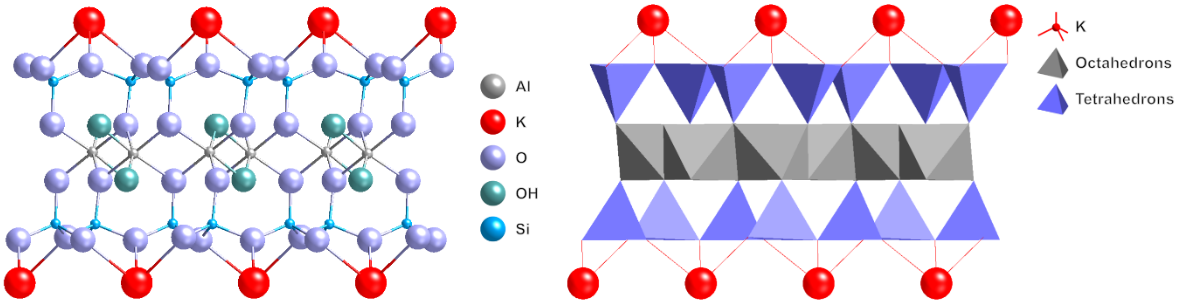

Figure 3-1. Crystal structure of muscovite mica showing the tetrahedron and octahedron sheets. Left side shows the position of the atoms and figure on the right shows the polyhedral representation. Crystal structure data obtained from Wyckoff[69] *and imaged in Crystal Maker.*

Mica is very useful for biological applications due to its properties: high flexibility, chemically inert to most liquids, and high tensile and shear stress. Because of these characteristics, muscovite mica is one of the most important minerals in research. It can be traced back to published work from the year 1836 and has been referred as “the most important single war material” during the World War II[68]. Its atomically flat surface made it a popular choice for surface interaction measurements as it was proven by its use in the first Surface Force Apparatus (SFA) experiments at the Cavendish Laboratory by Tabor and Winterton[70], and Israelachvili[71]. It is currently used as a standard substrate for AFM measurements of biomolecules. However, a recent review by Christenson and Thomson[68] argue that air cleaved mica is not as flat as previously thought; the possible presence of potassium carbonate crystals and defects detriment its atomic flatness in air if it is not freshly cleaved. Despite this recent discussion, published values of the roughness of mica measured by AFM are around 0.07nm RMS[72]. Still, researchers prefer this material over others in biosensing. But it lacks the ability to be grown or transferred to another surface, the biocompatibility of noble metals, or the ability to be incorporated in the semiconductor fabrication process used for biosensors.

To compensate its weaknesses, several researchers have adapted and use mica in combination with other techniques. The most common use is as a template surface to deposit flat materials on top using different techniques. One of the methods is controlling the growth of gold on mica by changing the deposition parameters, obtaining an atomically flat surface of gold.

3.2.3.2 Flat Gold Grown Epitaxially on Mica

Grown metal films on the (001) plane of muscovite mica is one of the most commonly used methods for making surfaces for biomolecular sensing and characterisation. The simplicity of the method and the commercial availability of the samples make it very attractive. Metals on mica have low roughness, especially if the metal is gold. The surface of the gold on mica can be flame-annealed before use to get an atomically flat surface free of contaminants. This combination has been researched for several years, and it was the development of new techniques for characterisation at the nanoscale over the years that allowed the full understanding of the way gold grows on this substrate.

Flat gold deposited on muscovite mica, was first researched by Reichelt and Lutz in 1970 using x-ray diffraction[73]. However, it was not until developments of the Scanning Tunnelling Microscope (STM) and AFM that this method got an increased attention. In 1988, Chidsey *et al* used STM measurements to characterise the growth mechanism[74]. In their publication, they briefly explain how during the evaporation of gold, the increase of temperature on mica improves the flattening of the gold topography, which starts irregular and with no grain coalescence, eventually reaching flat thin films but with grooves and holes. Higher temperatures were then associated to better epitaxy, but the temperature was not controlled precisely, and the variability was between 150 to 300°C, making the results inconclusive. In this paper, atomic steps of gold are already visible, and was the first step towards understanding this process. A year later, Putnam *et al*[75] published a paper solely focused on the flatness of gold at different mica temperatures at fixed rates of evaporation, improving the understanding of gold growth. The lack of structural analysis of the grains of the film led to a poor understanding of the method but again it was singled out that the mica temperature was key in the process. Further optimisation of the parameters of temperature during and before evaporation in a more controlled environment was accomplished by DeRose *et al*[76]. Higher temperature of the substrate increased the flatness of the gold surface which was characterised using AFM in terms of the root mean square roughness (RMS) at different set temperatures. They also tried different baking times of the mica before the evaporation. Results also show that rate of evaporation, chamber pressure, and film thickness did not affect considerably the flatness of the surface. Temperatures above 450°C of the mica allowed the gold atoms to reach enough surface mobility to rearrange into a minimum surface energy system. The grains then formed islands, and eventually a thin film was formed and started to grow. It is also discussed that these higher temperatures might lead to a cleaner mica surface, and consequently to a better epitaxy. The optimal conditions for this process accomplished a hexagonal faceting of gold with (111) plane. Up to this point, the studies have found out issues regarding the growth and evenness of the surface. It was regularly reported that holes and grooves were present at some rates of evaporation.

After the optimisation of crystal growth of Au on mica, another researcher explored the effect of post-annealing. Dishner *et al* [77] introduced the flame annealing method. It uses similar parameters of previous authors (DeRose *et al*) to reach good epitaxy and very low roughness: times of baking (before and after evaporation); the temperatures of the substrate; and fixed rates of evaporation. By introducing flame annealing, the sample increased its grain area 25 times larger than non-flame annealed samples. The advantage is that during the flame annealing, the contaminants on the surface are removed. However, the drawback is that it etches the gold (by evaporation). Despite this disadvantage, the only roughness seen on the surface is the atomic steps in the grains and small steps of grain boundaries. Because grains are bigger, the small number of boundaries is the variable that decreases the roughness on atomically flat samples. The values of RMS on flamed annealed samples are smaller than those of the standard method.

Before moving to the next method, TSG, it is important to understand the PVD of Au. The full mechanism of grain growth and thin film evolution of any metal is a complex phenomenon. There are several models that describe the physics and behaviour of this process. Several findings are discussed below which describes one specific model, that could help explain the way gold grows during the evaporation on mica and will help to better understand TSG.

3.2.3.3 Microstructural Thin Film Growth Evolution

The growth of gold on mica experiments were characterised using AFM, STM and TEM, leading to a basic description of how gold was growing onto a thin film in terms of coalescence of grains and the free energy of atoms to diffuse or migrate. An easy to understand model of how thin films grow on surfaces during evaporation was published in a review by Petrov *et al* in 2003[78] and it is presented in this section. There are more than one model and the reader is referred to the review of Kaiser [62] for a basic introduction.

Petrov *et al* explained that standard film depositions occur with the surface at temperatures of 20-30% of the melting point of the material (T_m) which are far from the thermodynamic equilibrium. The process is competitive and kinetic limitations introduces imperfections. The most crucial atomic processes involved in structure evolution on evaporated films are surface and bulk diffusion, which are affected by temperature of the substrate (T_s) at deposition; and energetic bombardment. These processes are not affected if the material is pure, which will make them reproducible, therefore it is crucial not to deposit multiple materials to avoid cross contamination. The ratio of T_s / T_m plays an important role to describe the final thin film characteristics and will be detailed later in the Section 3.2.3.3.1.

To understand polycrystalline film growth, a step by step movement of the evaporated ions when reaching the surface needs to be described.

In Figure 3-2, 1) ions reach the substrate and nucleation sites appear. After multiple ions reach the same nucleation site, they form isolated grains (islands), see 2). When the uneven film starts to thicken, grains can become larger and recrystallization through grain boundary migration can occur during or after island coalescence, see 3). The surface atom diffusion and GB motion play an important role at this stage. Islands with lower energy per atom consume other islands, by trying to minimise the interfacial energy, the result is a single crystal island. On this process, coarsening during coalescence is the principal factor for crystal orientation. Temperature and island size affect the rate of coarsening. The grains become wider in a liquid like coalescence, by rapid diffusion or by melting, after contact with the surface followed by crystallisation. Edge and surface energy are released during island coalescence, and rapid coalescence results in an open area of the substrate, which can be used for a secondary nucleation if the newly formed grain does not shadow the opened area.

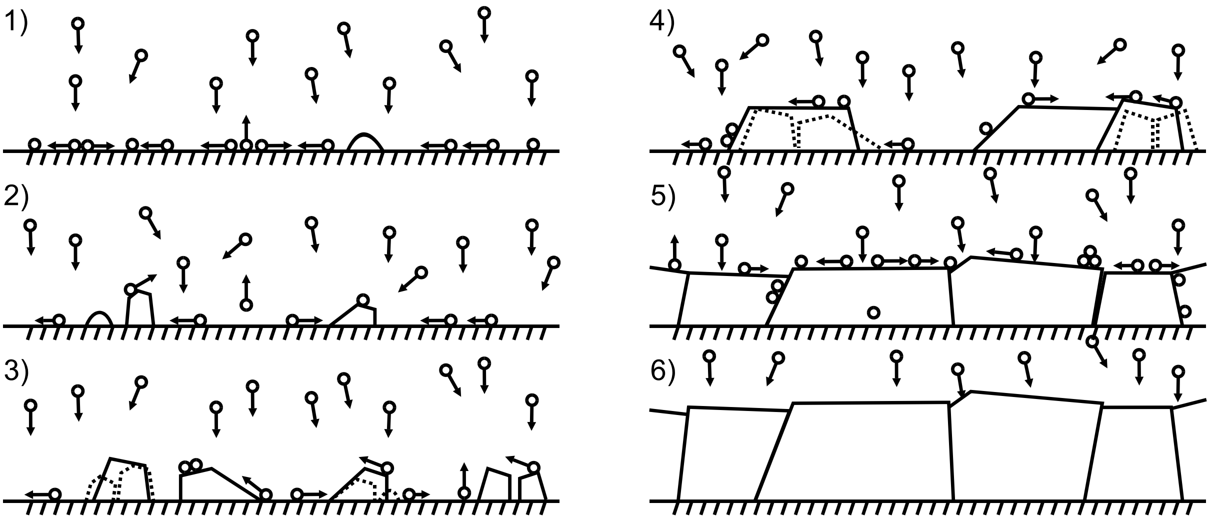

Figure 3-2. Thin film evolution growth:1) nucleation sites appear on the surface; 2) islands start to appear after multiple ions reach the same nucleation site; 3) the islands start to impinge, or coalesce with each other; 4) neighbouring islands reach a maximum size due to achieving minimal surface energy and do not coalesce anymore, instead they form polycrystalline islands; 5) empty space is filled with polycrystalline islands, and cannot grow laterally anymore, a thin film is formed; 6) the film grows vertically. Modified from [78].

If the substrate has a low temperature or large islands, then coarsening is driven by GB migration at a very slow rate until the island is sufficiently large that GB are immobile, see 4). Eventually, the polycrystalline islands cannot grow any more laterally forming a thing film, step 5). Subsequent deposition of particles will make the film thicken, step 6). The final characteristics of the film (column formation, grain size and orientation) can be explained using the structure zone model.

3.2.3.3.1 Structure Zone Model

Structure Zone Models (SZMs) were developed since 1969[79]. The SZM replicates the growth of thin films and it is represented in the SZM diagram as a schematic plot of film thickness against the rate of T_s / T_m. There are different models from different authors[62] but Barna and Adamik[80] developed a simple basic diagram that can be used for gold, see Figure 3-3. The model is categorised in three zones, which represent the final characteristics of the thin film after formation, where the transitions of zones gradually occur and are diffused:

- Zone I
    - At this zone there is no adatom diffusion or it is negligible, temperature is very low.
- Zone T
    - There is surface diffusion.
- Zone II
    - Surface and bulk diffusion are in operation at these temperatures and there is film growth.

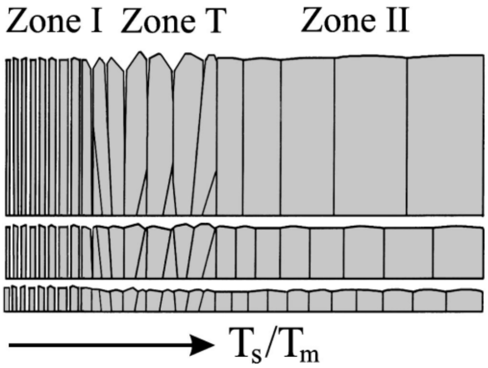

Figure 3-3. Different representations of the thin film at different thicknesses from thinnest (bottom) to thickest (top) using the Structure Zone Model. Increasing the ratio T_s / T_m will increase the grain size and the flatness of the surface at thicker films. Reprinted from Barna and Adamik [80].

Each zone is represented by a range of rates of T_s / T_m, where at small thickness (vertical axis), the steps between grains (columns) are very small and consequently low roughness in all zones. When the film starts to thicken, the differences of grain steps are more apparent. The roughness in zone I is similar through all thicknesses. In zone T, the thicker the film the rougher it becomes, grains start to compete for growing, and in different directions, leading to higher steps between grains. In zone II, grain columns widen when increasing the thickness, this leads to flatter terraces because the columns are directionally growing. The thinner the film in Zone II the rougher it would be due to the number of grain boundaries but still flatter than the other two zones.

3.2.3.3.2 Gold on Mica and the Structure Zone Model

Flat gold growth on mica was thoroughly studied by Higo *et al* using the SZM[81]. They obtained atomically flat gold with a roughness of 0.78±0.17 nm RMS, using a mica temperature of 473 ˚C and an evaporation rate of 2 nm/s.

The flat and contaminant free surface of mica is a good candidate to study this process. It can be performed using adhesive layers like Ti, however the temperature might need to be increased due to the impurity of the process (by incorporating Ti under the Au) and it is not a good candidate for Quartz because it can lose its piezoelectric properties at a temperature higher than the Curie temperature (573˚C). Furthermore, the chamber of the evaporator required for such conditions needs to be specially built for this kind of nonstandard process; a water-cooling system on the chamber wall would be necessary along with a substrate heater. Additionally, a flame annealing step might be necessary to increase the grain size. Because of these drawbacks, some researchers have preferred the use of TSG for flat gold on substrates other than mica.

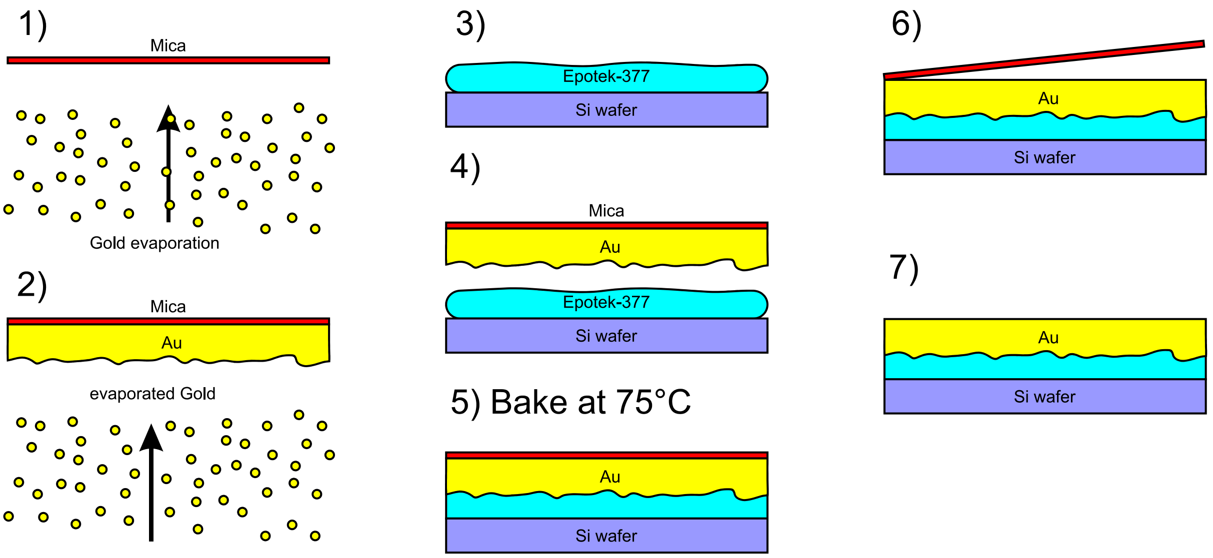

Figure 3-4. Template Stripped Gold (TSG) method. In 1), gold is evaporated on top of freshly cleaved mica. A thin film of gold is created on top of the mica in 2). On a substrate, an epoxy glue is deposited, step 3). Both epoxy and gold are placed in contact together, by carefully lying the mica on top of the substrate, step 4). in 5) the stack is baked at 75°C for 24 hours, or at 150°C for 2 hours. The mica is mechanically stripped in 6), leaving the templated gold exposed in step 7). Due to the nature of the spread of the glue, TSG can only be made on top of full substrates.

3.2.3.4 Template Stripped Gold (TSG)

The Template Stripped Gold (TSG) technique was developed by Hegner *et al*[82]. It is an ingenious method to make flat surfaces of physically deposited gold or other materials. The technique is described in Figure 3-4. First, a piece of mica with orientation plane (001) is freshly cleaved by tape or a razor blade (step 1) and it is exposed to a PVD of gold (step 2). Once a thin film is deposited on the mica, the gold exposed to air is glued to the target substrate, like a silicon wafer, using an epoxy resin like Epotek-377 (step 3 and 4). The sample is baked (step 5) for multiple hours depending on the temperature (2 hours for 150 °C, 24 hours for 75 °C). It is followed by a mechanical removal (by hand or tweezers) or chemical stripping with a solvent of the mica, leaving the gold that was interfaced with the mica (the template) as the flat surface (step 6 and 7). This method, theoretically, could give roughness values of gold similar to those of mica, but because of the nature of the microstructural growth of evaporated materials (grain boundaries) the roughness values can be one order of magnitude higher than those obtained on freshly cleaved mica.

Hegner *et al*[82] also decided to subject the TSG to different temperatures like the experiments of DeRose *et al*(Section 3.2.3.2). The roughness of the template stripped surface kept increasing from room temperature to 600 °C, with an initial value of 0.28±0.01 nm Ra in a 2.25um^2 at 25°C. In contrast but expected, the flatness of the exposed Au to air (DeRose's method) improved by increasing the temperature and reached its optimum at 300 °C, using an unchanged deposition rate of 1 Å/s. Higher roughness was obtained on lower and higher temperatures as can be seen on Table 3-1.

Table 3-1. Results from Hegner et al from both the outer and the template-stripped gold surface. Values of roughness Ra are in [nm]. Reprinted from [82].

Sample temperature (°C)	Outer surfaces		Template-stripped surfaces							
	AFM		AFM				STM			
	25.0 μm^2		25.0 μm^2		2.25 μm^2		25.0 μm^2		2.25 μm^2	
600	15.93	± 1.65	3.29	± 0.05	3.02	± 0.70	2.67	± 0.30	2.80	± 0.76
500	4.03	± 1.25	2.11	± 0.17	1.14	± 0.21	1.23	± 0.17	1.09	± 0.27
400	2.10	± 0.21	1.04	± 0.31	1.33	± 0.18	0.63	± 0.19	0.39	± 0.02
300	1.00	± 0.14	1.14	± 0.01	1.01	± 0.06	0.33	± 0.02	0.27	± 0.01
200	7.33	± 0.09	1.09	± 0.25	0.84	± 0.05	0.36	± 0.03	0.29	± 0.02
100	4.71	± 0.09	0.59	± 0.11	0.49	± 0.03	0.40	± 0.01	0.37	± 0.01
20-25	3.36	± 0.04	0.32	± 0.01	0.28	± 0.01	0.25	± 0.01	0.20	± 0.01

An analysis that Hegner *et al* might have missed, and that might be crucial for the understanding of the differences between the outer surface and the TSG surface, is the size of the grains. It is possible that TSG has a flatter surface at low temperatures because grains are smaller, they probably are polycrystalline (multiple grains in one column). An STM image on their paper can show the graininess of the sample. If the film has multilayers of grains, then when the TSG method goes into the baking step, grain coalescence might happen locally at the interface with the mica. By doing this, the energy release by these grains could be smaller and further rearrangement at the interface might be possible. However, if the same coalescence occurs when grains are bigger, and this happens by increasing the mica temperature during the evaporation, the released energy during the baking step for these bigger grains might be higher such that at the boundary of the newly formed grain grooves will be created. The area of the grains will be atomically flat, because they are templated by the mica, but the creation of these grooves (channels on the grain boundaries) will increase the overall roughness considerably in the imaged area, which is possible for roughness higher than 2 nm RMS obtained by Hegner *et al*, see Table 3-1.

One of the main drawbacks is that the application of the TSG to the direct semiconductor process is difficult. TSG could be applied only on a whole sample because of the spread of the epoxy on its surface, and further steps of fabrication cannot be involved: the use of solvents might detriment the epoxy; degassing of the epoxy might occur in high vacuum; and heating of the sample might change the flatness of the gold.

TSG might be the best option for use in QCM electrodes, but several of the drawbacks will complicate the fabrication process and reproducibility. Of the most importance will be the amount of glue on top of the electrode, which limits or screens completely the number of resonance frequencies detectable by the system. This is because the wave of resonance for mass measurement has a penetration depth that is less than 200 nm in liquid (i.e. thicker layers on top of the QCM sensing area might not be detected). The epoxy glue would be in the order of micrometres and it will affect the response, this is further discussed in the next section. Additionally, the use of solvents during the measurement will be limited. Therefore, the search for another method to make atomically flat QCM electrodes was required.

3.2.4 Are Atomically Flat Au QCM Electrodes Possible?

Flat surfaces of Au in combination with QCM could be used in biosensing and nanoscience studies. Atomically flat surfaces using TSG have been used in several applications before, for their high contrast in imaging proteins using AFM, and improving other experiments like the electric barrier in lipid bilayers[83]. TSG has also being used recently in optical applications like plasmonic triggered redox reactions at the nanoscale[84]. The versatility of TSG is favoured by many scientists for being easy to fabricate and its reproducibility of very low surface roughness. However, the applications of TSG are limited. The presence of the epoxy in the TSG reduces the chemicals that can be used in a QCM application. It also limits the area where flat Au can be used. The epoxy spreads on the substrate making it useful for large areas covering the whole substrate but futile for microscale or localised macroscale like the electrodes of the QCM resonator. Additionally, the limitations of the thickness of the epoxy are present. The glue is at least one micron thick if it is optimised as shown by Richter and Brisson[85], which is a serious drawback for QCM applications (this will be discussed in Section 3.2.4.1).

Using the same principle of TSG, Richter and Brisson managed to transfer mica instead of atomically flat gold on top of the QCM electrodes[85]. Glue was placed on top of the electrode followed by a piece of circular mica with the dimensions of the electrode. After baking, the mica was peeled off using tape layer by layer, without reaching the glue, to expose a fresh mica surface. With this method, the authors successfully use mica as the sensing surface, the only drawback is that the total thickness of the resulting electrode is approximately 4 microns total; one micron for the glue, and approximately three microns for the mica. This high load affects the behaviour of the QCM by a combination of its thickness and the heterogeneity of the materials, making unreliable the measurement performed using this technique; this is further discussed in Section 3.2.4.1. It is possible to use TSG on QCM samples in the same way Richter and Brisson did on their experiments but having the additional gold film as the outer surface instead of mica, but still the epoxy might be too thick to take reliable mass measurements.

One method that might have solved the issue of the electrode thickness and presence of the epoxy, is the method used by Ferguson *et al*[51] that cold welds two films of Au using a compliant elastomer as its support with very low pressure (<1 Bar). They believe that the deformation of the elastomer, Polydimethylsiloxane (PDMS), allows both gold surfaces to conform to each other, increasing the area of contact between gold films and facilitates the transfer. The advantages of this technique are that it can be used in laboratory conditions without the need of a cleanroom and that the gold does not need to be pure. The problem of this technique regarding QCM is that the resonator is not compliant as PDMS and that the resulting gold surface might not be as flat as TSG, for this reason another technique that uses solid substrates might be more promising: the method of cold-welded template-stripping (CWTS)[39]. Blackstock *et al*, had the idea of placing two surfaces of gold in contact using solid substrates, and they were able to weld them with the right conditions of pressure. Their idea is to use gold as the welding layer to transfer flat platinum to another substrate. The procedure is as follows: 1) the target substrate is evaporated with Ti and Au (25 nm and 100 nm respectively) at rates of 1-2 Å/s; 2) Pt was evaporated onto a clean Silicon chip (100 nm at 0.1-0.5 Å/s), followed by Ti and Au (25nm and 100nm respectively, at 1-2 Å/s); 3) the two pieces are placed with Au films facing each other in a hydrostatic press, and subjected to 500 psi (34.5 Bar) for more than 5 mins; 4) finally, the two samples were mechanically stripped. With this method, a roughness of 0.12 nm RMS in a 1um^2 for Pt was accomplished, having similar values to the template stripped method for platinum reported by the same authors. This method was performed under vacuum to avoid the contamination of Au, which otherwise would not allow the transfer. In the same way as the TSG, the published data is the result of the analysis of very grainy surfaces with very small steps between them. Grains were not analysed in this published work.

To overcome the issue of vacuum conditions, Mosley *et al*[86] modified the CWTS technique to transfer gold using mica instead of using a silicon wafer chip as a template. The method is based on diffusion bonding of gold[87] and it can be performed under laboratory conditions without the need of keeping the sample under vacuum. It requires a vice, a heater, and 250-300nm of Au on both target substrate and mica. The pressure applied by the vice was 3500-4000 psi (240-275 Bar) and at least 2 hours for the transfer to occur, and up to 4 hours, depending on the temperature which ranged from 200-400 Celsius degrees. The higher the temperature the shorter the time of the pressure being applied. One of the disadvantages of this technique is the high pressure required, which limits the dimensions of the materials to be of the same exact area, otherwise they will break in areas of high pressure because of the area mismatch. Also, the temperature for the deposition of gold on mica has to be 300 °C, similar to the work of DeRose[76] at 473 °C, and opposite to the results of Hegner *et al*[82] for gold deposited on mica for TSG with better results at 25 °C. Another issue in their method is the presence of pit-holes on the flat surface that can be seen with bare eyes as a haze on the gold surface. This process achieves a roughness between 0.2 and 0.5 nm RMS for an area of 1um^2; it is believed that the analysed area does not include the grooves, which would increase the roughness substantially.

Using the idea that pure gold diffuses at room temperature at low pressures from Ferguson *et al*, and the increase of temperature for diffusion bonding, it is believed that the transfer of flat gold to QCM resonators is possible using a combination of these techniques. The remaining problem would be that of the response reliability of the QCM because of the electrode thickness. In the following section, it is analysed how the behaviour of the QCM is affected by the electrode. Later, it is explored if gold can be transferred by combining the works from Ferguson *et al*, Mosley *et al*, and Blackstock *et al*.

3.2.4.1 QCM Spurious Modes and Their Relationship to Electrode Geometry and Thickness

The physics and behaviour of AT-cut quartz, related to the electrode design, is explained in this section, for more detailed information the reader is referred to the original material by Bottom[88], and Shockley and Koneval[89]. The full modelling of QCM sensors is beyond the scope of this work and only the material that is related to the electrode design of QCM resonators is presented.

Besides the fundamental and the harmonic modes in the QCM response, inharmonic overtone modes, or spurious modes, are present in piezoelectric resonators by being systems of two or three dimensions. In a one-dimensional system, spurious modes do not exist. For example, an AT-cut quartz of infinitely large area will behave as a one-dimensional structure and will only have harmonic modes. However, electrode volume and clamping on the edge of the quartz give rise to inharmonic overtones, which are determined by the medium and the boundary conditions, and at a lower degree by the method of excitation.

Following the introduction to QCM from Section 2.2, in a QCM wafer, the mechanical displacement and electrical polarisation has similar distribution spatially. Polarisation depends on the strain inside the plate and greatest strain is at the centre of the electrode. Close to the edge of the electrode the polarisation, strain, and displacement become zero. Experimentally, the amplitude of motion becomes zero at a distance of less than 20 times the thickness of the electrode away from its edge[88]. This out of bounds motion is caused by fringing of the electric field.

The geometry of the quartz electrode plays an important role in the appearance of overtones. For the fundamental mode, the motion is principally in the x direction of the crystal (flat cut on QCM resonators) a bell shaped sensitivity with amplitude higher at the centre and reduced to zero close to the edge of the electrode[89]. The charge distribution on the surface is practically constant. If the geometry is affected, then the quartz will behave abnormally and gives rise to the inharmonic overtone modes. For example, in the first inharmonic overtone the strain and displacement are of opposite sign at the ends of the x-axis. This mode could be excited by dividing the electrodes at the centre of the motion and applying an opposite charge on them. Hence, the electrode geometry is of the utmost importance that the slightest asymmetry in the plate excites this overtone. Therefore, electrodes should be perfectly aligned and concentric to a circular quartz wafer like the QCM chip. Some quartz resonators are contoured by lapping into a spherical shape as shown in Figure 2-2, the main reason is explained later. This contouring should also be symmetrical to avoid inharmonic overtone excitation, because the area not in contact with the electrode functions as a clamp, a boundary condition, and this asymmetry also excites the first inharmonic mode.

Inharmonic overtone modes can be separated from the fundamental mode by reducing the electrode size. Equation 3.1 is the wave equation in cylindrical coordinates for a quartz disk, it describes the frequency response of the quartz by its geometrical parameters. The frequency response is in the nmk mode for a 3-dimension system, where $n = 1$, $m = 0$, and $k = 1$ is the lowest frequency response: the fundamental harmonic mode, χ_{mk} is the kth root of Bessel's function of order m, n is the harmonic mode in the x axis, v is the wave propagation velocity, a is the radius, and b the thickness. The first term of Equation 3.1 represents the harmonic mode contribution, and the second term the contribution to the inharmonic response. The equation shows that the separation between fundamental and inharmonic overtone modes is inversely proportional to the radius a of the disk. If a is large compared to the thickness b, the right term is practically zero and the resulting equation would be that of an infinitely large sample. The equation also shows that the differences between harmonic and inharmonic modes are also inversely proportional to the radius a. If a is decreased by contouring, or by using smaller electrodes, the separation of fundamental and inharmonic modes would be larger. This equation is used regularly in designing QCM resonators.

$$f_{nmk} = \frac{\omega_{nmk}}{2\pi} \doteq \frac{nv}{2b} + \frac{vb\chi_{mk}^2}{4n(\pi a)^2} \tag{3.1}$$

As mentioned before, the chip can be further thinned by lapping the edges of the resonators, instead of the centre, by contouring. Contouring is the process to make the quartz resonator into a spherical shape (to bevel the wafer rim), this method is used for fabrication of lenses by grinding a surface, and it is frequently used in the industry.

The frequencies of the inharmonic overtone modes are more spread with the reduction of the radius of curvature of the quartz. Figure 3-5 shows an experimental result from Bottom [88], the spread and distance away from the fundamental mode of the inharmonic modes with successive laps of the crystal.

Some inharmonic modes are so close to the harmonic modes that it might be difficult to discern one from another, especially in liquid mode where the Q factor is reduced. Despite the benefits of

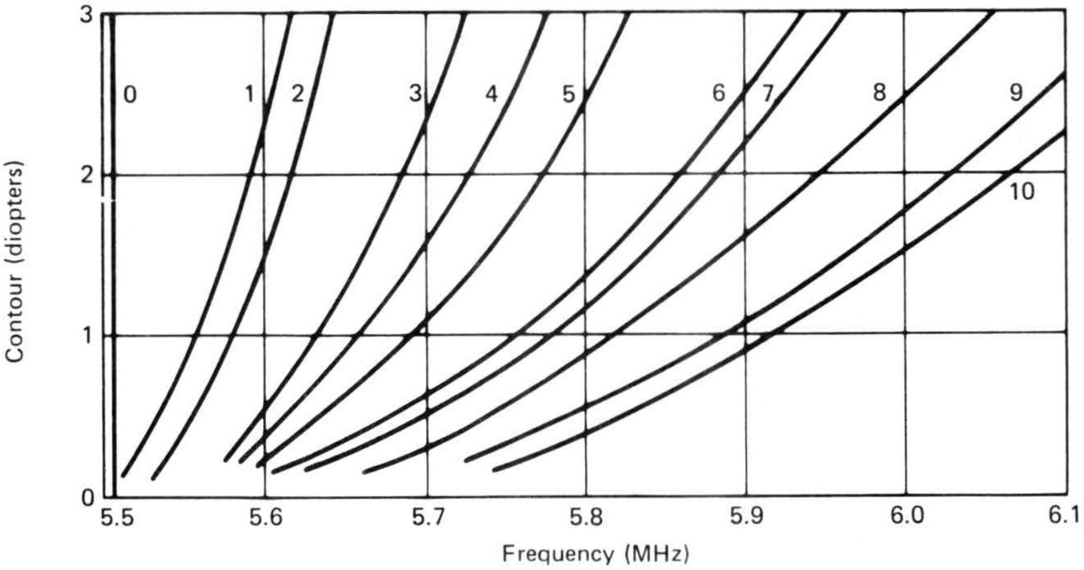

Figure 3-5. Graph of the increased distancing of the inharmonic overtones from the fundamental response for a 5.5 MHz AT-cut quartz blank. Y axis is in units of diopters, (1/2)R, where R is the radius of curvature and it is in meters. Reprinted from Bottom [88].

Figure 3-6. Qualitative plot of the overtone spectrum of AT-cut quartz sampled at different harmonic modes. Reprinted from [88].

contouring, it affects negatively other factors: the resistance of the quartz increases, impedance can increase, and capacitance decreases. This would affect the modelling of the response of the quartz to mass adsorption, making useless the software provided with the QCM monitoring equipment and complicated to users that do not have the expertise of modelling.

The method of contouring is useful for resonators of 2 and 5MHz. The higher the harmonic mode is monitored, the closer the inharmonic overtones would be to the harmonic mode, see Figure 3-6. Quartz Crystal Microbalance with Dissipation (QCM-D) resonators from Q-Sense have a fundamental frequency of 5 MHz and an electrode fully covering the exposed surface of the sensor (9.8 mm diameter out of the 14 mm of the chip, see Figure 2-2 in Chapter 2). These crystals have a big electrode area and require contouring. Despite employing this solution, the effects of the overtones can be seen experimentally on the harmonic modes higher than the 7th harmonic mode. On the 9th harmonic mode (45 MHz) the inharmonic overtones overlap with the main mode leading to uncertainty in the tracking of the resonance peak, and consequently the mass measurement. This has led all users to only reliably

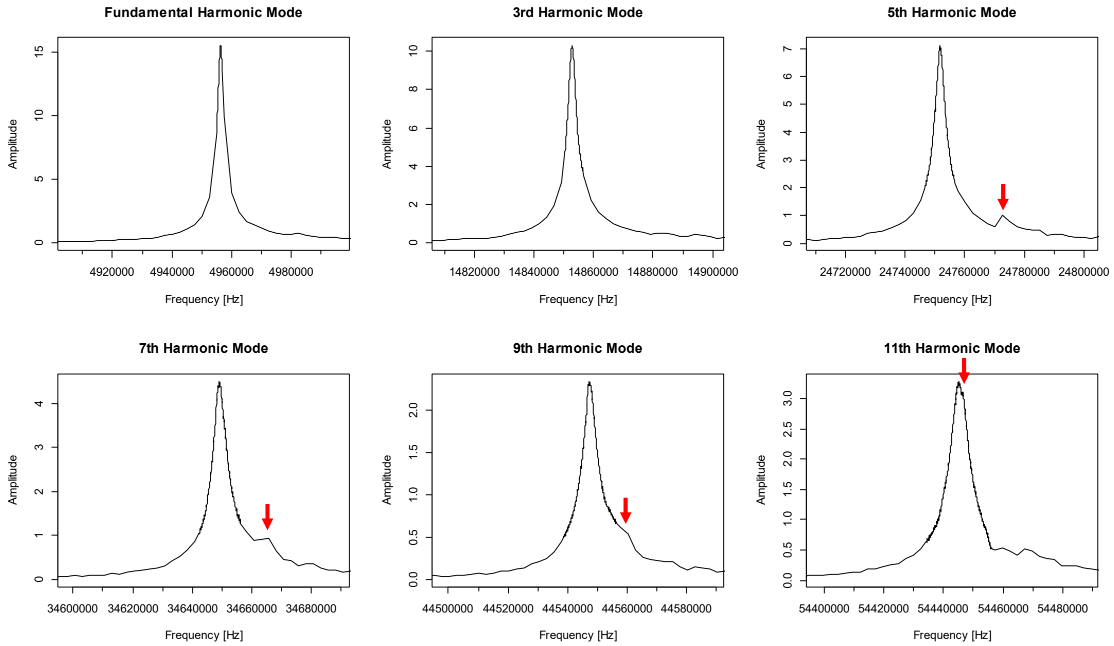

Figure 3-7. Tuning of resonance for QCM-D resonators of 5MHz in a liquid environment. Fundamental and first 5 harmonics. Red arrow points at the presence of a spurious mode from the 5th harmonic mode. This inharmonic mode gets closer to the harmonic mode the higher the frequency. It can be noted that at the 9th harmonic mode, the spurious mode is affecting the shape of the resonance peak at this frequency. On the 11th harmonic mode, the peaks get distorted and is on top of the maximum value. This presents a problem for monitoring both frequency and the energy dissipation (quality factor) during the measurement.

use the 3rd, 5th and 7th harmonic modes on the Q-Sense system for mass modelling. A practical example of how the inharmonic overtones are closer to the harmonic modes in higher frequencies on QCM-D resonators can be seen in Figure 3-7.

For higher fundamental frequencies that require thin wafers, 9 MHz or above, contouring is a very difficult process. Instead, the method of energy trapping is used to supress undesired overtone modes.

3.2.4.2 Energy Trapping

Shockley and Koneval[89] describe energy trapping and how to eliminate the unwanted spurious modes using design parameters for quartz crystal electrodes. This following section summarises the results from these and other authors, and presents the equations used for electrode design.

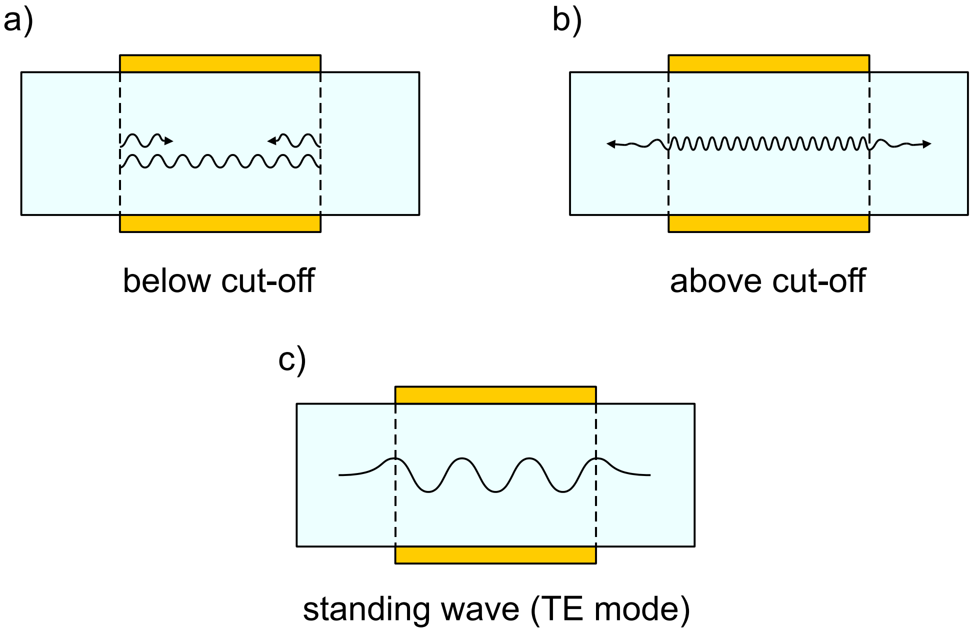

Figure 3-8. Energy trapping on a quartz crystal with electrodes; a) Resonance occurs below the cut-off frequency; on b) the energy is dissipated on to the non-electroded area caused by the lack of reflection on the boundary; c) a standing wave is created, and the system becomes resonant, at the boundary (dashed line) a little energy escapes and tails off away from it. Adapted from [89].

Before going into the equations, it is required to describe the behaviour of waves on a resonant material. All waves travelling a finite solid are reflected at their boundaries. When these waves are reflected, the interference of the wave and the reflected wave create a standing wave (resonance). For this reason, the limiting factors of a perfect system in resonation are boundaries. Some systems cannot sustain standing waves as there is dissipation on them; the waves disappear before or during reflection. In standard QCM resonators, the electrodes are the main boundary condition that creates the resonance. The finite volume of the quartz, clamping and the presence of an o-ring induce the inharmonic modes.

In systems with more than one dimension, as explained before, inharmonic modes exist. They are determined by the nature of the medium and the boundary conditions and little by the method of excitation. These spurious modes or spurs, like harmonic modes, are thickness shear modes, influenced by the same elastic coefficients and same temperature coefficient of frequency. These modes are only a little above the fundamental mode (as shown in Figure 3-6 in Section 3.2.4.1) and they can be prevented of being reflected by energy trapping.

The energy trapping method relies on the principle that waves can propagate above a cut off frequency, they do not reflect and subsequently dissipate, thus not creating a resonance. Below the cut off frequency, the waves are reflected and do not propagate in any direction resulting in a resonance.

When an electrode of finite thickness and area is applied to a quartz wafer (AT-cut, e.g. QCM sensor), the electrode cut-off frequency (ω_e) will be different from the surrounding area frequency (ω_s) due to the presence of boundaries. These two cut-off frequencies, ω_e and ω_s, divide the system in three regions. Below ω_e, waves cannot propagate, and no resonance occur. Between ω_e and ω_s, waves can propagate in the electrode region but not in the surrounding region, therefore total internal reflection occurs at the boundary between these regions, see Figure 3-8 a). Above ω_s, waves propagate in both regions; anything generated in ω_e will propagate away and will not create a standing wave, see Figure 3-8 b). Therefore, anything that is generated between ω_e and ω_s will produce, in the electrode region, trapped waves that will not propagate into the surrounding region. Nevertheless, because of boundary conditions, fringing occurs, and a wave of small energy tails off away from the electrode, see Figure 3-8 c). This behaviour, the trapped energy response, is acoustically isolated from any other portion of an at-cut quartz wafer, giving the possibility of making multielectrode QCM resonators.

Therefore, the resonance of the trapped energy depends on the values of ω_e and ω_s and lateral dimensions of the electrode region. The electrode itself lowers the cut-off frequency of the crystal ($\omega_e < \omega_s$) because of the electrode mass loading and the incorporation of a small electroelastic effect[89]. It can also induce spurious responses if the thickness is big[90]. When multiple responses are generated by this mechanism, additional to the fundamental response, it is referred as the inharmonic overtone series. This series would end in ω_s.

An expression can be derived using a two-dimensional model for both fundamental and overtone modes as a function of ω_e, ω_s, the electrode length $2a$, and wafer thickness b, see Figure 3-9. The Equation 3.2, is derived in the paper of Shockley *et al*[89].

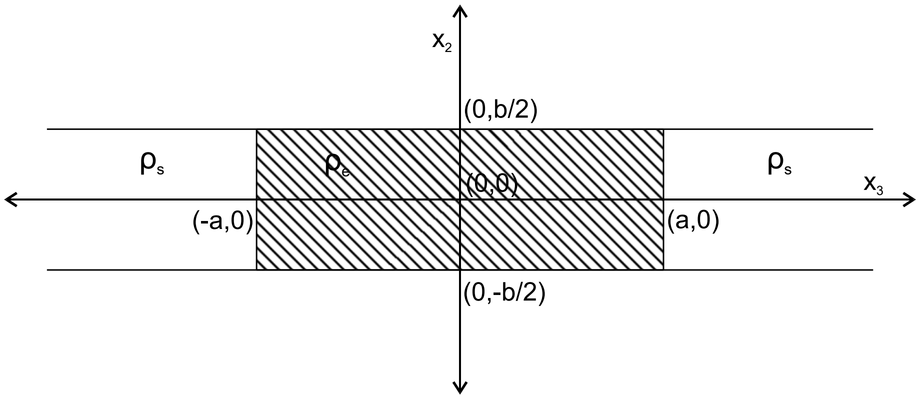

Figure 3-9. Trapped energy structure. Dark area represents the volume under the electrode. Reprinted from [89].

$$\frac{pa}{b}=\frac{\Omega_0\sqrt{\left(\frac{c'_{55}}{c'_{66}}\right)}\left(n+\frac{1}{\pi}\tan^{-1}\theta\right)}{\sqrt{\{\psi(1-\Omega_0)[2\Omega_0+\psi(1-\Omega_0)]\}}} \qquad (\ 3.2\ )$$

Where

$$\theta^2=\frac{(1-\psi){\Omega_0}^2[1+\Omega_0+(1-\Omega_0)\psi]}{\psi[2\Omega_0+\psi(1-\Omega_0)]},$$

$$\psi=\frac{(\omega_{te}-p\omega_e)}{(p\omega_s-p\omega_e)},$$

And

$$\Omega_0\equiv\frac{\omega_e}{\omega_s}$$

The variables $p=1,3,5,\ldots$ are the order of the harmonic mode, and $n=0,1,2,3,4,\ldots$ the symmetric inharmonic mode series for each value of p. The eigenfrequencies, or natural frequencies, are ω_{te} for all non-vanishing mode resonances. For a one-dimension system, the fundamental frequency will be Equation 3.2 with values of $p=1$ and $n=0$. The parameters c'_{55} and c'_{66} are elastic coefficients of the quartz.

If symmetry of the electrodes is achieved, the 1st antisymmetric inharmonic mode will not be excited, Equation 3.2 becomes Equation 3.3, a simpler relationship, see Shockley *et al*. This relationship supresses all remaining inharmonic modes when M_n is set to the theoretical value of 2.17 obtained by Shockley *et al* [89].

$$2\frac{a}{b}\leq\left(\frac{M_n}{p}\right)\left[\frac{\Omega_0}{(1-\Omega_0)}\right]^{\frac{1}{2}} \qquad (\ 3.3\ )$$

Where

$$\Omega_0 \equiv \frac{\omega_e}{\omega_s},$$

$$\omega_e = \frac{\pi v_e}{b'},$$

$$v_e = \left(\frac{c'_{66}}{\rho_e}\right)^{\frac{1}{2}},$$

$$\omega_s = \frac{\pi v_s}{b},$$

$$v_s = \left(\frac{c'_{66}}{\rho_s}\right)^{\frac{1}{2}},$$

and

$$c'_{66} = c_{44}s^2 + 2c_{14}sc + c_{66}c^2 = 29.3$$

Equation 3.3 takes into consideration the design parameters of the quartz resonator: $2a$ for electrode diameter, and b for the electrode thickness. The wave propagation velocity v_e and v_s and its density values ρ_e and ρ_s for the electrode area and non-electroded area respectively. M_n has theoretical or experimental values obtained from Shockley *et al.* if M_n is set to 2.17 and the electrodes are symmetric, therefore not exciting the first antisymmetric inharmonic mode, then all remaining inharmonic modes will be supressed as long as the relationship of Equation 3.3 is fulfilled. The value of M_n could be slightly different depending on the QCM monitoring system used.

Equation 3.3 can predict if the quartz geometric design would affect the suppression or not of the inharmonic modes. If the factor on the left side, $2a/b$ is smaller than the right side of the equation, then the suppression of the spurious modes is expected. As both sides of the equation are affected by the electrode thickness and diameter, the cut-off frequencies of the resonator will be affected and will limit the value of both parameters.

In a 9 MHz resonator the following parameters are used: $2a = 5.1[\mathrm{mm}]$, $\rho = 2.649\ [\frac{\mathrm{Mg}}{\mathrm{m}^3}]$ at 25 °C, and $b = 185[\mu\mathrm{m}]$. The effective thickness of the electrode area is increased due to the electrode itself (100 nm for each electrode). The velocity for the propagation of the shear waves is also different due to the presence of the electrode, and the effective density is affected, giving an effective $\Omega_0 \cong 0.99$.

Using the criteria from above, the left side of Equation 3.3 has a value of 27.53, while the right side 32.55. If the electrode thickness were to be increased to a combined thickness of both electrodes higher than 528 nm the relationship will fail, in that case the electrode diameter could be reduced. However, other spurious modes might be induced by increasing the thickness, which are not predicted by this equation.

In summary, this relationship aids in designing the thickness of the QCM electrodes. It also explains why electrodes are usually 100 nm thick on QCM resonators that are not lapped into spherical shape. Nevertheless, several assumptions were made that if taken into consideration might reduce the working thickness for the QCM resonator than the obtained by the equation e.g. the effect of the clamping of the resonator using an o-ring. After fabrication, further experiments are required to analyse if other spurious modes are not excited. The need to create a flat gold sample without having electrode thickness higher than 250 nm has led to the creation of the pressure-forming template stripped gold technique instead of using TSG.

3.3 Materials and Equipment

Bovine Serum Albumin purified by heat shock fraction, protease free, fatty acid free, essentially globulin free, pH 7, ≥98% was purchased from Sigma Aldrich. Muscovite mica was purchased from Agar Scientific as disks of 10 mm diameter for tests and 11 mm squares for final samples. QCM resonators (QCM jig) with Ti and Au electrodes and blank resonators were purchased from AWSensors. Gold 99.99% pure from Kurt J. Lesker and Testbourne and Ti 99.99% were obtained from Kurt J. Lesker. The AFM for liquid measurements was performed on a Bruker FastScan at the Department of Pharmacology, University of Cambridge by the Edwardson group.

Al-foils (thermal imprint) and Poly-foils (imprint membranes) of 100 mm diameter were purchased from Obducat. For pressure-forming the Nanoimprint Lithography system NIL 2.5 from Obducat was used. For thermal evaporation an Edwards evaporator A306 with Auto FL 400 chamber was used. For e-beam evaporation a PVD 75 e-beam evaporation system from Kurt J. Lesker was used.

3.4 Experiment: Pressure-Forming Template Stripping (PTS) of Gold by Diffusion Bonding

3.4.1 Introduction

The possibility of making atomically flat electrodes on Quartz Crystal Microbalance (QCM) resonators would allow the improvement of several applications for biosensing and characterisation of biomolecules on QCM sensors. One example of its use is the tethered lipid membranes, it has been argued that not only properly designed tethers, but also the flatness of the surface, play an important role to make supported lipid bilayers with sufficient high electrical resistance for single-ion channel recording[61]. Another possible example is the imaging of fibrils after polymerisation, when kinetic studies are performed on QCM resonators, the same sample could be used for characterisation using AFM. Another reason, and the goal of this experiment, is to see the behaviour of proteins in nanostructures, having a sample with virtually no roughness will allow to see the difference of dynamics and the behaviour of the protein against a standard surface that has been considered to be flat. Currently, most QCM experiments are performed in two different stages. The first stage is the experimental mass measurement using QCM resonators, and the second stage is the characterisation of the experiment using another sample on a TSG or mica substrate. Most researchers present the mass measurement and the characterisation as the same using these different samples, but this might be wrong. The reason behind making a QCM resonator with atomically flat gold electrodes is to find out if an atomically flat surface gives the same protein adsorption against a standard surface QCM resonator.

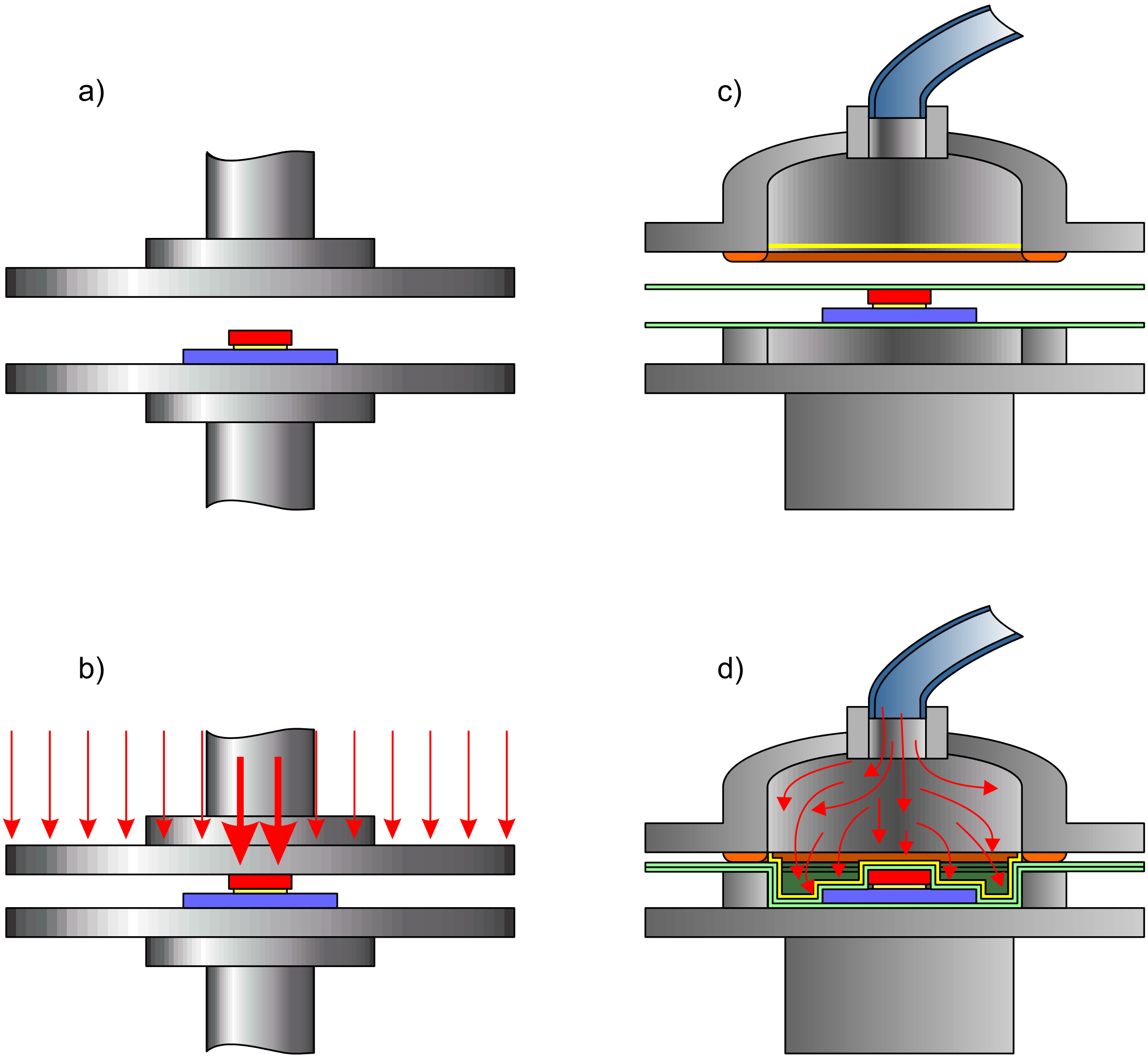

Figure 3-10. Difference between a press plate and a nanoimprinter using pressure-forming. The distribution of the pressure on the nanoimprinter is through the whole surface of the substrate and it is not affected by the difference in size of the mica (red) and the quartz (blue). The size of the red arrows represents the amount of pressure exerted on different points on the systems. a) and c) are the states of both machines before applying any pressure; c) and d) is the state when the transfer of pressure to the sample is happening. Red arrows in d) represent air pressure.

One way of making a flat electrode is by modifying the cold-welded template-stripping method (CWTS)[39] and combining it with gold diffusion bonding[86] [87], and use the idea of conforming the gold layer to the QCM electrode [51]; see Section 3.2.4. Other options, like the template stripped gold (TSG) method, would create a very thick electrode, which would be unreliable, would not be able to supress most of the inharmonic modes or create new ones and would filter out higher harmonic modes. High temperature evaporation of gold would be unfeasible as the Curie temperature of the Quartz is 573˚C, so the optimisation of gold grown on quartz might not be possible using the SZM. The combination of pressure and heating of the bonding layers along with high purity of gold is the best candidate. However, the current state of the art for this technique tell us that is not possible without affecting the behaviour of the quartz, and possible breaking it due to the high stress required for this process[86]. Hence, an optimisation is required, which could end up in the proper transfer of a flat gold surface or possibly with the outcome that this technique is not feasible for QCM resonators. A new method named Pressure-Forming Template Stripping (PTS) is presented.

3.4.2 Fabrication Process of PTS gold

In order to create a new process to fabricate flat Au on top of QCM resonator, a transfer method would be required with steps similar to those used by the CWTS[39] method; a conformable material[51]; and those shown by the method of solid-state bonding of Mosley *et al* [86]: heating and pressure during the transfer. This combination is believed to be the most feasible to achieve it. The main goal is to transfer the gold deposited on a freshly cleaved mica template onto a QCM gold electrode by placing both gold surfaces in contact and applying pressure and heat, see Figure 3-10. The difference between the proposed technique would be in the equipment used, which might also be beneficial to the process, otherwise it might not work. Instead of using a vice as Mosley *et al*, a nanoimprinter available at the Nanoscience Centre, University of Cambridge was used. The Obducat Nanoimprinter (details in Materials section) is a system which applies even pressure on an uneven substrate. It works in a similar way to the manufacturing technique pressure-forming (or in an analogy: blowing up a balloon), see Figure 3-10 c) and d). When the pressure chamber (balloon) is in contact with the substrate, the pressure is uniformly distributed. The system starts by injecting a gas in a chamber. The chamber has two parts. The top part has a conformable polymer film at the bottom which is sealed with an o-ring when both parts of the chamber come into contact. The polymer deforms when gas enters the top part of the chamber and it is blown up against the sample, which is underneath, and transfers the pressure onto the sample evenly. The only condition for this to work is that if the sandwich of solid samples have different sizes, the smaller one must sit on top of the bigger one. This machine would be useful to avoid the high pressures transferred on the edges or corners of the substrates using a vice or press plate. These are caused by the increase of pressure where there is a mismatch of area between the target substrate and

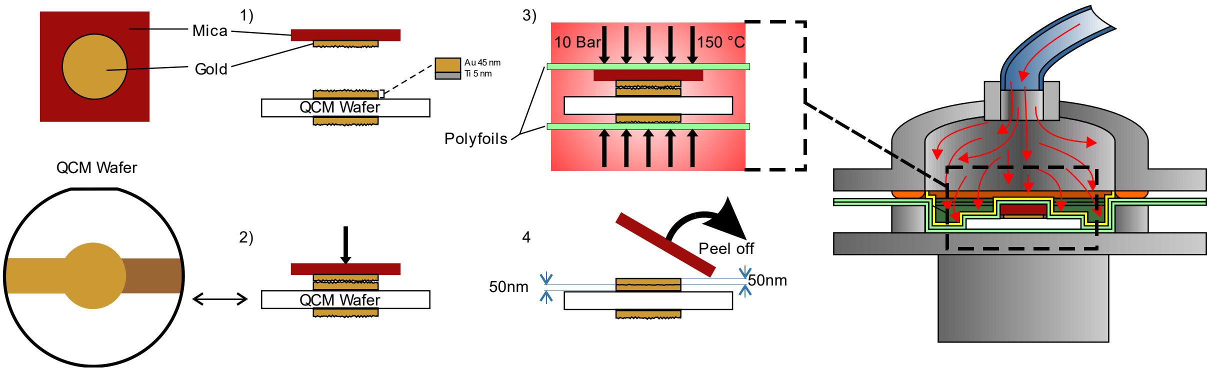

Figure 3-11. Fabrication process of gold PTS QCM electrodes. 1) Gold is evaporated on mica. 2) The gold/mica is placed on top of a gold QCM electrode and 3) pressure and heat is applied to this sandwiched sample. 4) Mica is mechanically cleaved.

the mica substrate. Because the polymer film will conform to the substrate by the pressure, high stresses will not be induced on the target samples.

Another advantage of the nanoimprinter is the built-in heater with temperature control. Applying both controlled pressure and temperature will make the optimisation of the welding faster and in a controlled manner. To use the nanoimprinter, the samples are placed between two pieces of polymer or aluminium foil. The bottom foil is not required, but it is useful for two reasons: first, to keep the target sample and the mica in one place; and second, to avoid any debris on the bottom part of the chamber. Debris transfers high pressure to the sample. Once the chamber is closed, the foil seals the substrates. Subsequently, the chamber starts filling up with air, exerting pressure on the top foil and the sample, as well as starts to heat up or cool down the chamber to the desired temperature.

When the conditions of pressure and temperature are met, the transfer of Au would be possible, it is just a matter of finding optimal parameters. It is possible that the transfer could be done without any assistance of the heater. It is believed that low temperature plays a role to bond two pieces of gold perfectly. It is a conclusion reached in a previous experiment performed during the second year of this PhD dissertation, see Section 2.6.5. In this experiment, it was observed that Au NPs diffuse inside the gold electrode of the QCM at temperatures higher than 75˚C. Nevertheless, the starting conditions for the PTS gold experiments were at a temperature of 240˚C and at the maximum output pressure by the nanoimprinter, 70 Bar. From there, optimal parameters were pursued.

The fabrication process is as follows. Ruby muscovite mica was purchased from Agar Scientific (See Materials Section). The mica was freshly cleaved using blue dicing tape. After cleaving, the mica was positioned under a shadow mask with 5.1 mm diameter circles, same size as the electrode on the QCM resonator. Mica samples were discarded, or further cleaved, if they showed steps under direct light (lines going across the exposed electrode area).

The deposition of Au on mica was performed on the Edwards Auto 360 Thermal Evaporator using thermal boats of Mo or on the Lesker e-beam evaporator using Fabmate crucibles. The initial deposition rate used for the transfer was 1 Å/s and deposition thickness of 300-400 nm of Au. Target samples were either silicon wafer with Ti (5nm) and Au (95nm) evaporated on e-beam evaporator or QCM resonators (standard Jig) purchased from AWSensors and QuartzPro.

The gold was freshly deposited on the cleaved mica and quickly taken to the nanoimprinter, where the target substrate was previously placed on top of a polymer foil, with the gold exposed to the environment. The mica was placed on top of the silicon with the gold facing down and in contact with the gold of the silicon substrate, making a sandwich. Another piece of polymer foil was placed on top of the mica, see Figure 3-10 c) or Figure 3-11 1). As mentioned before, this polymer foil helps distribute the pressure of the mica on the target substrate, and it is a requirement for this type of nanoimprinter to work.

The target sample (Si chip with Ti and Au layers) was cleaned with Acetone for 10 minutes, followed by 10 minutes of IPA cleaning and dried using a N_2 gun before being placed in the nanoimprinter chamber. It is important to mention that these samples were evaporated inside the cleanroom and never have been taken out of cleanroom conditions but are still expected to be contaminated as some of the samples were one year old.

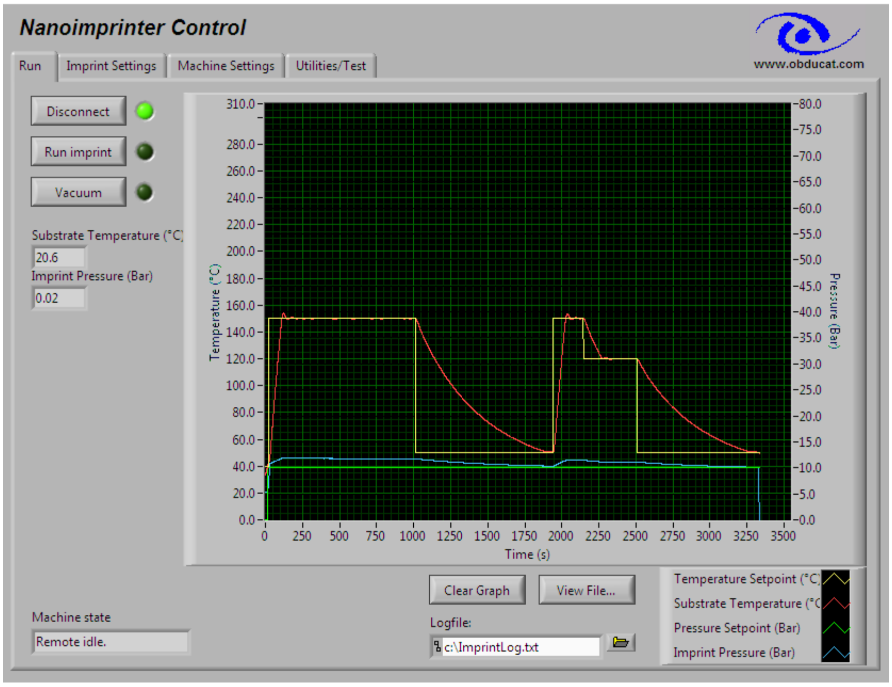
Nanoimprinter Control

Substrate Temperature (°C) 20.6

Imprint Pressure (Bar) 0.02

Machine state Remote idle.

Logfile: c:\ImprintLog.txt

Figure 3-12. Nanoimprinter running the recipe for PTS Gold

The initial pressure was set to 70 Bar and 240˚C which lead to transfer of the gold from the mica to the silicon sample. The issue with this recipe is that it was too aggressive for the machine itself. Although it was below the maximum conditions of operation, the o-ring could not withstand the combination of high pressure and high temperature, even with the highest resistance o-ring available for this system (made with the material Kalrez). The silicon substrate also got broken because of the high pressure. Indeed, pressure and temperature needed to be lowered.

The first working test was obtained when the nanoimprinter was operated at 70 Bar and 150˚C. However, the pressure was too high and resulted in a few broken target substrates. The next step was to get a test at 40 Bar, which worked and did not break the sample. Then, it was lowered to 10 Bar where good consistent results were obtained. To improve the 10 Bar pressure experiment, an annealing step was added to the recipe. The system heated up to 150˚C and then cooled down to 50˚C, twice, while exerting constant 10 Bar of pressure on the sample. This led to a 100% transfer success rate using low pressure and low temperature and could be used on QCM resonators (standard jig) without breaking. The recipe running on the nanoimprinter can be seen in Figure 3-12.

The results of the samples are shown in Figure 3-13. On the left side of the image it can be seen a final sample of the PTS QCM resonator (a). In the middle of the image (b), the mica has yet to be stripped

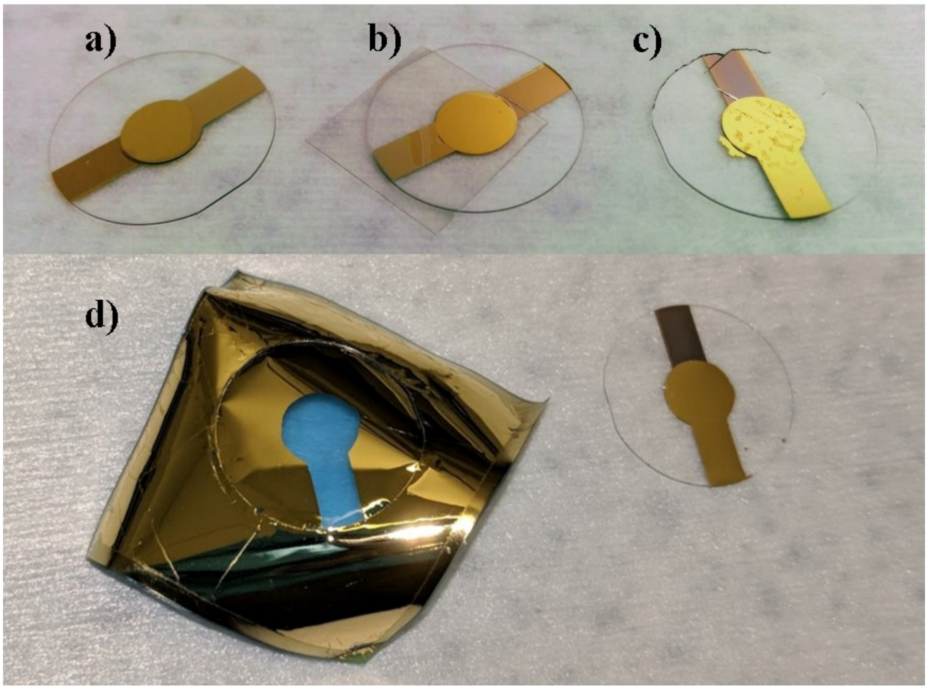

Figure 3-13. Results of the transfer of atomically flat gold to QCM resonators. The final sample with flat electrode can be seen on the left side of the image (a) using the optimal conditions of 10 Bar pressure and heating at 150 °C. A sample with the mica still on top of the resonator (not stripped yet) is seen in the middle of the picture (b). On the right side (c) it can be seen a failed transfer, broken resonator, using the initial conditions of 70 Bar and 240 °C. On (d) a full transfer of the PTS technique not using a pattern on the mica can be seen, this means that only the gold on the QCM resonator interacting with another layer of gold made the transfer occur.

off the sample. The mica used was freshly cleaved, and it is approximately half of its original thickness (0.15mm). On the right side of the picture, a failed attempt at transferring the flat gold is observed, this was using the initial parameters of very high pressure and high temperature. In (d) it is shown how the transfer occurs only between gold films as the gold on the mica was only transferred to the electrode design on the QCM resonator. Once the transfer process was optimised, it needed refinement. The next step is to characterise the flatness and optimise the method such that it gives smoother surfaces and thinner electrodes. Because of the use of a nanoimprinter that resembles the pressure-forming technique and their similarities to the TSG method, this process is called Pressure-Forming Template Stripping (PTS).

3.4.3 Characterisation

3.4.3.1 Characterisation of PTS QCM resonators

Once the protocol was optimised, the flatness of the freshly transferred Au was characterised using Atomic Force Microscopy (AFM). However, results showed a rough sample instead of an atomically flat one. Different rates of evaporation were tested to see if the flatness could be improved. The target sample conditions were never changed as it was simulating a QCM resonator; this was a squared silicon wafer substrate with Ti (5 nm) and Au (95 nm) at 0.5 and 1 Å/s respectively. It was found in the literature, that the rate of evaporation does not affect the grain characteristics of the gold growth on crystal surface, but the temperature of the substrate (mica) is crucial. However, for PTS gold, the rate

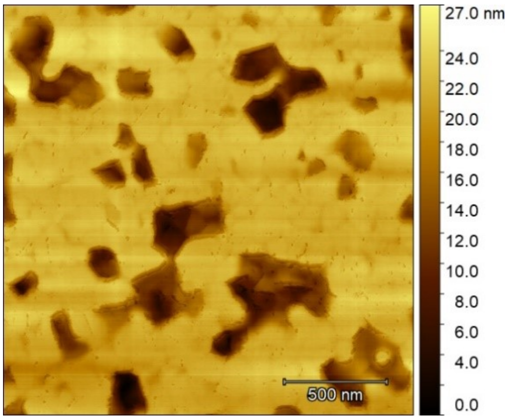

Figure 3-14. Grooves appeared on the surface of the PTS gold. These depressions have a depth of up to 27 nm, increasing significantly the RMS value of the overall surface.

affected the final roughness. Initial tests of evaporation at 1 Å/s showed very flat grains but with the presence of frequent grooves on the surface, which increased the overall roughness, see Figure 3-14. The roughness RMS was higher than a standard evaporated Au on Silicon wafer, or standard QCM electrodes: ~4 nm RMS against 1-2 nm RMS. At first, it was believed that the grooves were grains that did not transferred to the Si sample. However, further inspection of the mica after transfer using AFM, showed no sign of grains on its surface. As a result, these pinholes are believed to be caused at the interface of mica and gold by grains shadowing a new opened up area after island coalescence freeing energy around the new island[78], see Figure 3-14.

Pinholes increased the roughness of the surface from 759.4 pm RMS, in areas where the pinholes are not present, to 4.299 nm RMS of the entire image. It was believed that the gold flatness could be controlled by changing rate of evaporation or temperature of substrate, or both. Due to the lack of an evaporator chamber with a heater for high temperatures (above 150 °C), all efforts were focused on the rate of evaporation. Up to this point no explanation has been found for the pinholes in the published work of other authors, just the presence in their results were acknowledged. Standard evaporation rate used for semiconductor processes is 1 Å/s. In the studies of gold grown on mica[75], [81], it has been shown that rates of evaporation on the scale of nm/s were better to increase grain sizes and reduction of pinholes. For this reason, a series of experiment of different rates of evaporation were performed on mica, this time using the thermal evaporator. A film of 100 nm of Au on mica was evaporated. The Si samples of size 12x12mm were evaporated using the Lesker e-beam evaporator system at 1 Å/s for Au and 0.5 Å/s for Ti; similar parameters used for semiconductor processes. The target sample had 5 nm of Ti and 95nm of Au. The mica was freshly cleaved using blue dicing tape and placed on the thermal evaporator using a shadow mask of 5.1 mm diameter circles. The evaporation rates used were 1 nm/s, 2 nm/s, 3 nm/s, and 4 nm/s. The samples were successfully transferred and characterised using the Veeco Enviroscope AFM system. An additional rate of 0.8 Å/s was performed and measured weeks after the initial results to look for consistency.

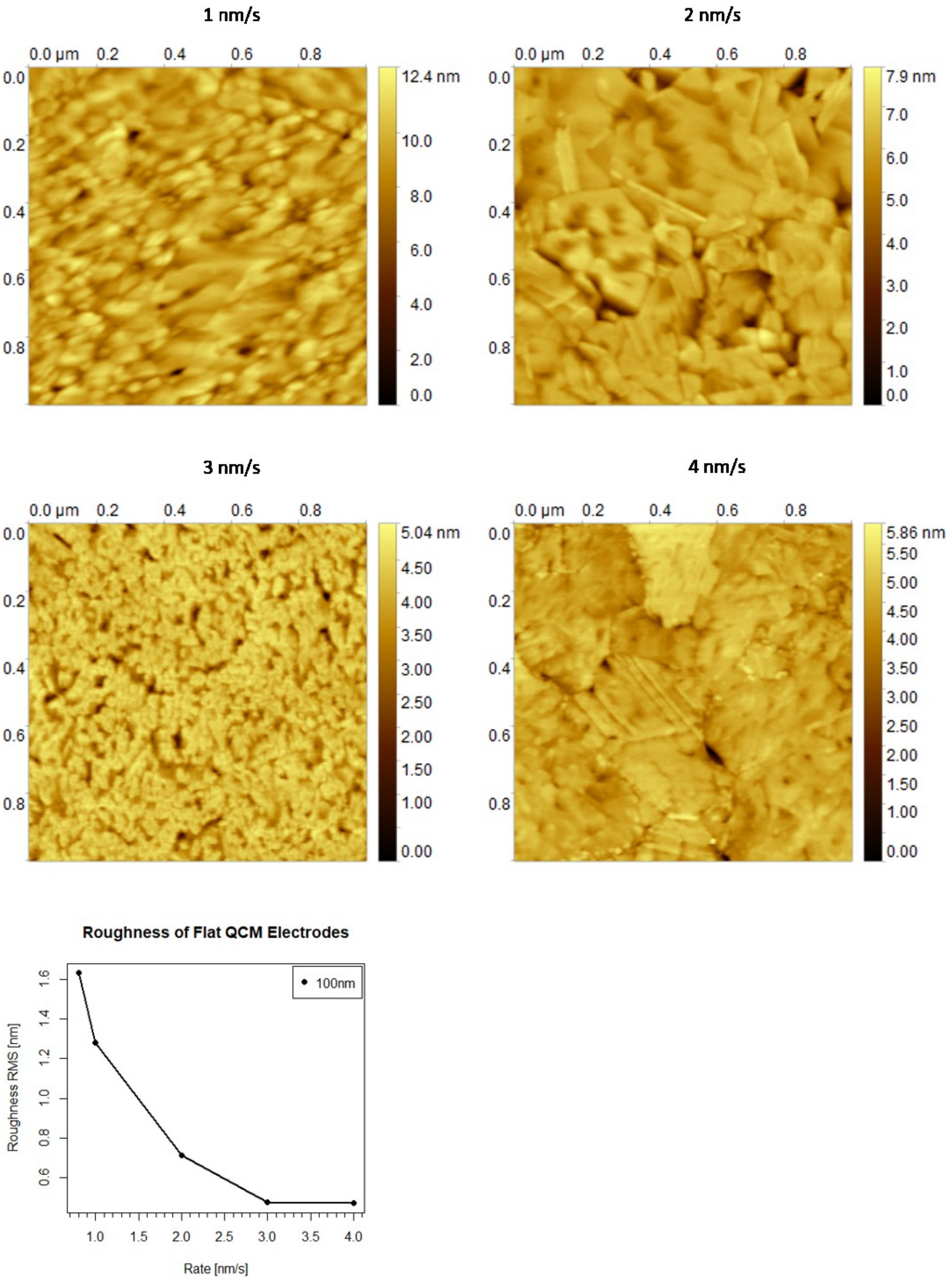

Figure 3-15. AFM images of PTS gold at different evaporation rates. The roughness decreased with increased rate, as shown in the graph.

Results showed higher roughness at lower rates, and flatness improving with increasing the rate of evaporation. The flatness reached a plateau towards 4 nm/s, see Figure 3-15. It must be noted that the improve of flatness is a result of the increase of rate of evaporation, which might be the space between grains inside the film, and that it should not influence the surface roughness of the gold on the mica (Zone I) as explained by Petrov *et al*[78]. It is also expected a particle size increase during the evaporation of the material towards the substrate. At higher rates, because of the evaporated grain size being bigger, less contamination would be dragged increasing the purity of the film, but grain structure still at zone I of the SZM. At low rates, it is believed that there is a higher ratio of impurity drag versus the grain of the gold during the evaporation which will restrict the grain size when it reaches the surface[78], [91]. It has also been known that increasing the rate and keeping a low temperature increases the nucleation sites in metal thin films[62]. Another argument has been previously discussed by Thompson[92], where only at high temperature and low rates of evaporation the surface energy is minimised. In the opposite case, the one used in this experiment, the high rate of evaporation and low temperature ends up with strain energy minimising textures. In the latter case, the grains of the gold on mica will coalesce with the grains on the target substrate after annealing, and with minimal stress during the transfer. If the strain is higher, like in low rates of evaporation, the released energy during the coalescence of the grains during annealing of the PTS will be higher, on both interface with mica and interface between both layers of gold, which agrees with the appearance of the grooves at low evaporation rates.

According to these results, the transfer of flat Au to a QCM electrode should be performed at 4 nm/s. If the evaporation is performed at standard rates (1 Å/s, approximately) the roughness is going to be increased by stress release after coalescence of grains between the gold on mica and the gold on the target substrate. The improvement of the flatness is also attributed to the grain sizes of the gold after the transfer, even at small rates, which were performed at the beginning of the timeframe of this experiment, the grains did not grow during the PTS steps as big as when evaporated at 4nm/s. A possible reason is that high rates might favour polycrystalline columns, and there is less energy released on these structures than full columns when coalescing with the grains on the other film. This is also attributed to the possible drag of contamination, limiting the grain growth by annealing during the PTS process. Both polycrystalline columns and purity of gold will favour coalescence at the interface as well as laterally between grains. Ultimately, if samples were heated according to the SZM, a flatter surface could be created at lower rates. In the case of this experiment, something intriguing happened, two different boats were used and one of them gave better results. Both boats have similar dimensions, a dimple of 10 mm diameter, and the second boat with 11 mm diameter, but what was more noticeable was that one of them was thinner, more fragile. This thinner boat lead to better flatness using 4 nm/s and it was attributed to the brightness of the boat during the evaporation, there was not a significant increase of temperature on the sample; between 30-45°C for both boats. The evaporations took 12.5 seconds, which will make it difficult to observe any significant increase in temperature with such a short period of time with the thermocouple installed in the evaporator. However, the radiation could affect the mobility of the adatoms during the deposition and remove any layer of water still on the surface of the mica. Additionally, the radiation will contribute to an increase of movement of the adatoms making the grains in the thin film more of a liquid form, in a way that there would fewer empty spaces between grains.

Before moving into the optimisation of the thickness of PTS QCM electrodes, in the following section is detailed the characteristics of the surface of the electrodes of QCM purchased from different vendors which will give an idea of why flatness is not accomplished as in the process of PTS gold.

3.4.3.2 Roughness of Standard QCM Electrodes

The nominal roughness of QCM electrodes depends on four factors:

1. The technique used for evaporation of the QCM electrode, hence the maker
2. The parameters of evaporation
3. The QCM design
4. How many times the QCM electrode has been cleaned and under which method

Different makers have different techniques for evaporation of electrodes. The most common technique is e-beam evaporation, followed by thermal evaporation. Some manufacturers chemical-mechanically polish the electrodes. E-beam evaporation is usually selected as it is one of the cleanest techniques for evaporation avoiding the possible contamination from the boats in thermal evaporation. Once the physical deposition is decided, the second factor that plays an important role is the rate of evaporation and how punctual the source is. Considering that there is an adhesion layer of Ti, rates of evaporation of around 1 Å/s gives roughness between 1 nm and 2 nm RMS for Au. Thermal evaporation gives roughness of 2 nm RMS or higher; however, this can be optimised at the expense of wasting material. The design of the QCM also affect the roughness. For example, to achieve the thickness required for the desired fundamental resonance, an increase of the thickness of the electrodes might be necessary, increasing the roughness. Another important factor in design, is the adhesion layer for gold, which affect the grain or column size. QCM resonators used in this project were made with Ti or Cr to attach the Au electrode to the quartz, depending on the availability from the manufacturer. Final results used only Ti as an adhesion layer to keep the roughness of the gold consistent throughout the experiments and avoid the possible migration of Cr to the surface due to temperature increase of the PTS process[93]. Some QCM resonators, specially the high fundamental frequency (HFFQCM), are small pieces of quartz that are polished to achieve a smaller thickness and reach the required frequency. These resonators have a higher than usual roughness due to the polishing of the quartz during the manufacturing process. The resonance area is in a mesa. Another important factor for the QCM resonator is the roughness increase due to the cleaning procedure as explained in the Section 2.7.

3.4.4 Optimisation of Thickness of Flat QCM gold electrodes

The electrodes of QCM resonators should have a thickness of 100 nm on each side of the wafer as explained in Section 3.2.4.2. It is required to avoid the induction of spurious modes and to eliminate the inharmonic modes of the QCM design. Standard QCM electrodes obtained from commercial vendors also have this thickness. Hence, further optimisation was required to reach a transfer between the Au of the electrodes and the mica where both should have a total thickness of 100 nm gold. First, it was varied the thickness of Au on the substrate and the thickness of Au on the mica. Secondly, it was analysed if the roughness characteristics changed because of the adjustments of the films thickness, by varying the rate as in Section 3.4.3.

3.4.4.1 Experiment of Thickness Optimisation for PTS Gold

The objective of this experiment is to find out the minimum thickness of Au required from the target sample and mica to successfully transfer the gold such that a flat electrode of approximately 100 nm total thickness could be made on a QCM chip.

The target samples (Si) where coated with titanium and gold using the Lesker E-beam Evaporator at a rate of 0.5 and 1 Å/s respectively. Only the titanium layer had a fixed value of 5 nm thickness. The gold deposited on mica and Si substrates was varied from 20 to 80 nm using the Edwards Auto 360 thermal evaporator at rates of 4.0 ±0.2 nm/s for all variations.

Measurements of the surface roughness were performed on those samples that checked (by eye inspection) a 75% area transfer of the flat gold. All but one target sample with 20 nm gold deposition on the Si sample met the criteria. Unsuccessful transfers were not measured, despite this, it is believed that all thickness variations considered for this experiment could be transferred if the following conditions are met: a full flat cleaved mica sample with no visible steps, and a mica no thicker than 80um. The results are summarised on Table 3-2.

Table 3-2. Table of roughness for different thickness of Au on mica and Si samples. The Si samples have an adhesion layer of 5 nm Ti. The measurements were taken on samples that had 75% area of the Au transferred to the target Si sample.

Roughness of Surface RMS [nm]			
Au Thickness on Si Sample [nm]	Au Thickness on Mica [nm]		
	40	60	80
20	-	1.45	0.6966
40	0.5834	0.6011	0.3185
60	0.8287	0.3717	0.779
80	0.7691	0.6592	0.5338

There was one result that was an outlier. The experiment of 20 nm Au on the sample and 60nm on mica, showed a higher than average roughness from all the experiments. All other experiments showed an acceptable roughness. This difference could be attributed to the possible lack of a continuous thin film on the target substrate. It is also possible that the mica could have gotten contaminated during the handling. Another possible cause is the fact that the mica and the target sample used in the experiment are not of the same size. The total area of the mica is bigger than the Si sample, and it should be the other way around as explained before. Still, the method works because the mica is thin, and it conforms to the substrate. Mica samples for this test were round discs of 10 mm diameter. In these experiments the round discs hanged outside of the target sample, creating a lever, and the thickness in some samples where higher than 80 μm which would reduce the mica flexibility and avoid the contact between the two gold films. This distribution of pressure did not seem to affect the process at first, but a combination of thick mica and thick target substrates (Si wafer chips) increased the pressure if the mica was hanging (on the lever point). It is crucial for this combination of thick samples, that the transferred films lie at the centre of the chamber of the nanoimprinter to distribute the pressure from the centre out, and not from one edge to the other.

Given that all the combinations higher than 40 nm of gold thick were successful, it was decided to use a thickness of 50 nm on both samples (100nm total, 5 nm Ti and 45nm Au on the target sample and 50 nm Au on the mica).

Once the thickness of the films for the PTS was decided, the next step was to analyse the change of roughness for different rates of evaporation. Surprisingly, a different outcome than the previous experiment of Section 3.4.3.1 was obtained. The roughness did not change at different rates, it was consistently at low RMS values, see Figure 3-16. In contrast, the previous experiment with samples of 100 nm gold layers (200 nm total) did change and showed a flatter surface at higher rates, see Section 3.4.3.1.

An important observation on 50 nm thin films, was the presence of more grains at lower rates, despite having an increase but similar values of roughness, see graph in Figure 3-16. This is attributed to the growth evolution of the thin film. With thinner films, the roughness of the target sample surface is small and does not variate at different conditions as explained by the SZM. Low initial roughness of the Au thin films will help the flatness of the PTS gold. As prove, another experiment was performed, and it can be observed on Figure 3-17. In this experiment the roughness of gold evaporated on Si samples is increasing as the thicknesses increase (25 nm, 45 nm, 75 nm and 100 nm). Grains can be seen to be smaller, and increasing their size and height difference, as the thickness increases. Overall roughness also increased with the increased thickness, see Figure 3-17 graph.

The results of 50 nm thin films showed that at low deposition rates there are more grains on the surface despite the constant low roughness, and at higher rates the grains increased their size and grain boundaries are less abrupt. This behaviour was also observed at 100 nm Au thin films (Figure 3-15) which strongly agrees that higher rates have a higher Au purity. Additionally, there is less energy released during grain coalescence in the heating steps of the PTS at higher rates of evaporation.

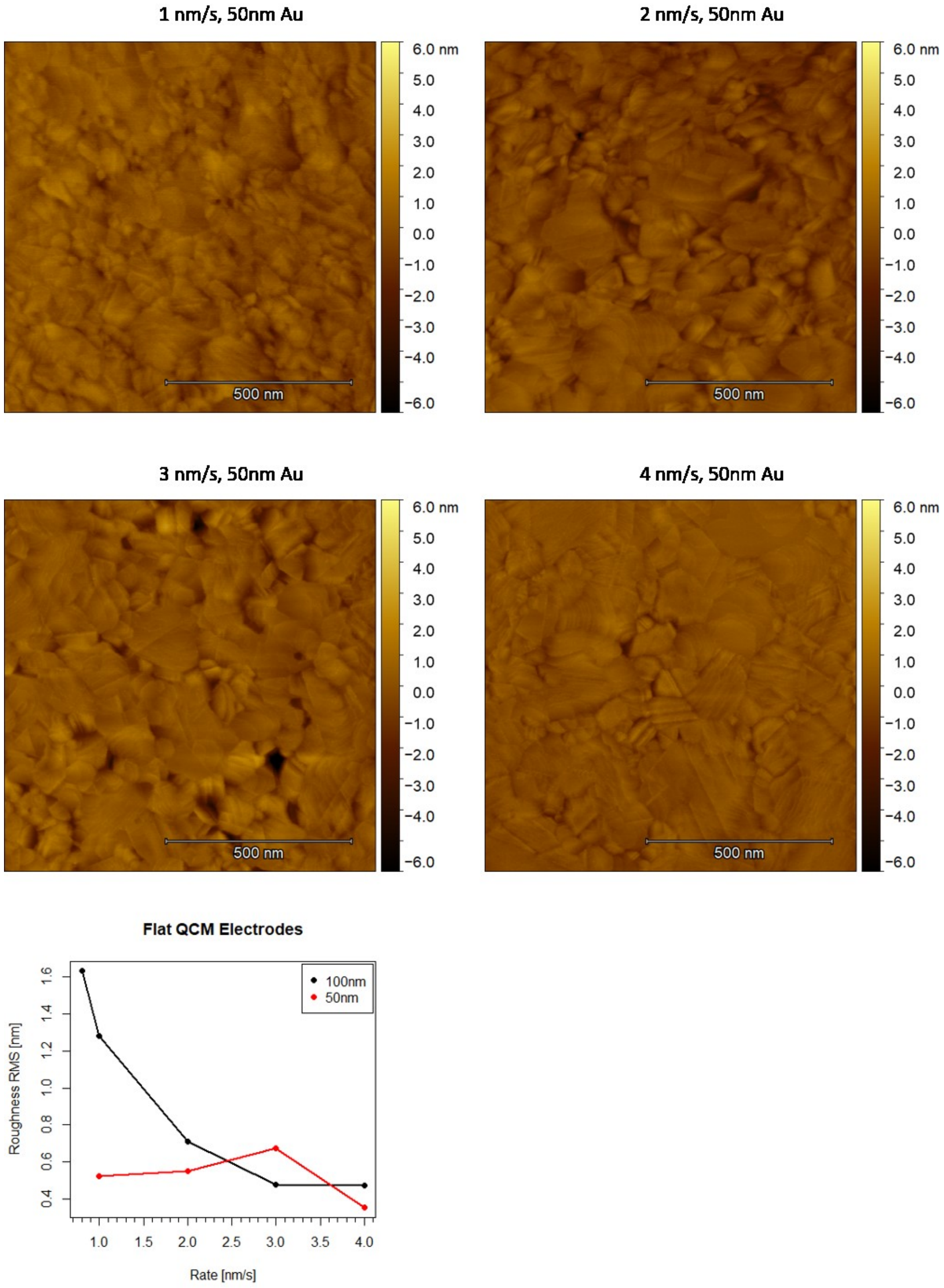

Figure 3-16. AFM images of the surfaces of PTS using 50 nm of Au on both target substrate and mica. The surface obtains a flatter finish with big grains at rates of evaporation of 4 nm/s. Despite this, the graph shows that the roughness values are similar at all rates of evaporation (red curve). The black curve shows the roughness when the thickness of the film is increased to 100 nm on both the target substrate and the mica. The rougher PTS at low rates is attributed to the space between the two Au films in contact. Both Au films have a grainier more irregular surface, when both layers coalesce, the roughness is transferred to the interface of the mica.

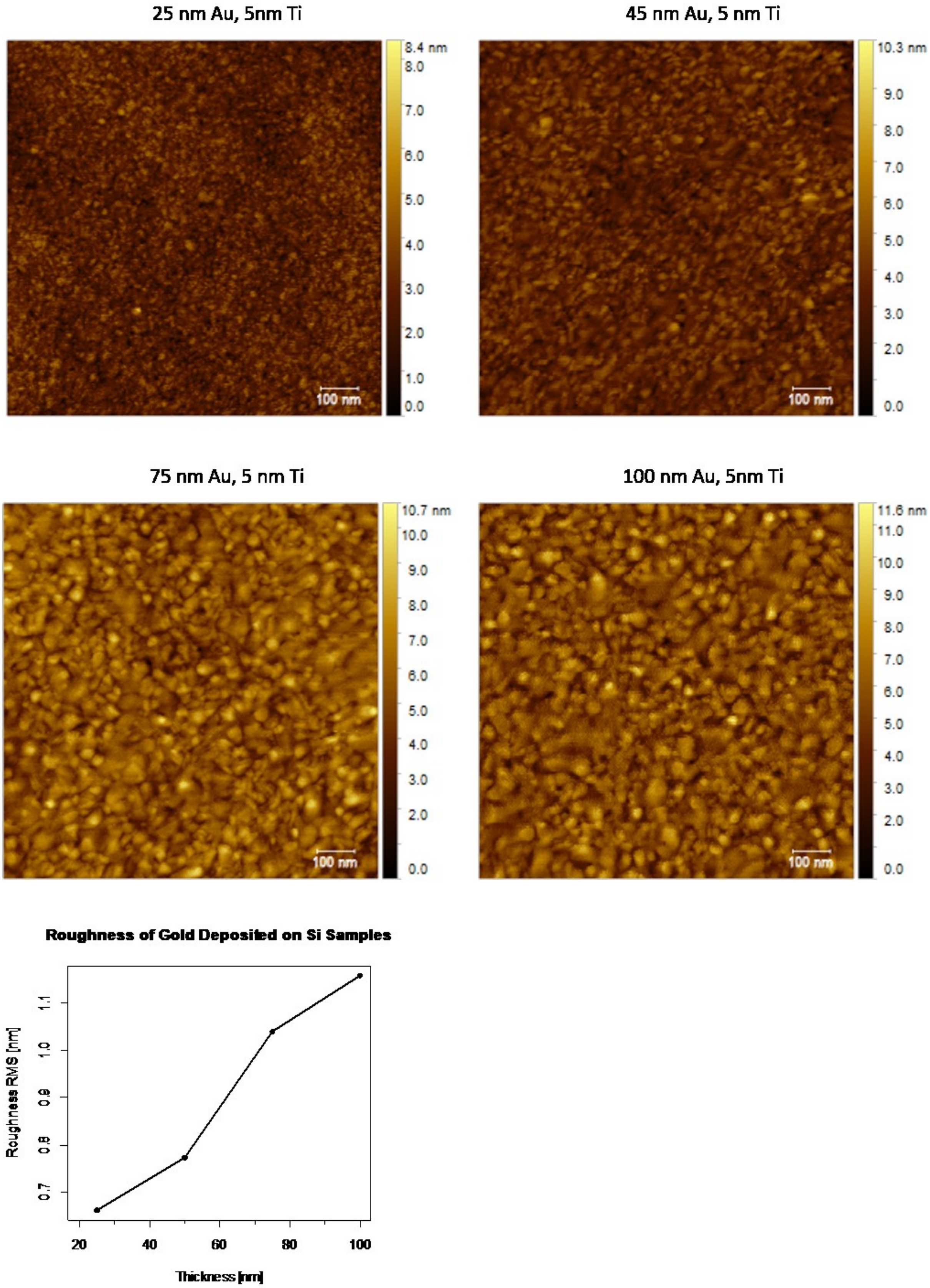

Figure 3-17. Gold grown on top of Si wafer samples using an adhesion layer of 5 nm Ti. The grain size is increased by increasing the thickness of the Au layer. The graph at the bottom shows the increase of roughness against thickness.

3.4.5 Conclusions of PTS Experiment on QCM resonators

To make atomically flat electrodes on QCM resonators, it was necessary to make the initial electrode deposition in-house. They required to have an initial thickness of 50 nm of Au and the remaining 50 nm of Au missing will come from the PTS transfer process. The 100 nm of Au total was necessary to avoid any spurious mode in the response of the resonator caused by thicker electrodes. For this reason, blank QCM wafers of 10 MHz with x alignment cut were purchased from AWSensors. A shadow mask was purchased from Laser Micromachining with the design required for a standard QCM jig electrode. The evaporation of the target QCM electrode was performed using the Lesker e-beam Evaporation system at rates of 0.5 Å/s for 5 nm thickness of Ti and 1 Å/s for 45 nm of Au. The electrode on the opposite face of the QCM resonator got 95nm of Au instead. On freshly cleaved mica, 50 nm of Au were deposited using thermal evaporation at 4 nm/s. Another shadow mask with 5.1 mm diameter holes was used.

The transfer was 100% successful on 5 QCM resonators at the same time using the nanoimprinter. The roughness obtained on these samples was of the same quality to those experiments that involved the transfer of 100 nm Au films.

The average roughness obtained was 0.345±0.05 nm RMS on a 1um^2 AFM image (n=5), using new AFM tips for each measurement, see Table 3-3. These measurements are taking into consideration the whole image and not just a line profile. All images show atomically flat steps of gold and were acquired using AFM in tapping mode. These steps can be seen as ridges on the surface, when there are no ridges, it is a complete crystal layer of gold as seen on the detail of Sample 5 in Figure 3-20. The roughness of Detail #2 in Figure 3-20 is 63 pm RMS. The overall roughness of the PTS gold is close to the experimental values of roughness of mica reported by other authors (0.2 nm RMS)[81], [94].

When tuning the QCM resonators in the AWSensors system, the response showed an expected curve and fitting of a standard QCM resonator, see Figure 3-18 for the comparison. The system plots ellipses form the response of the conductance and susceptance of the sensor at the resonance frequency. An absence of the ellipse represents the resonance missing. Another sample of approximately 510 nm thick combined electrodes was made at the beginning of the optimisation of this experiment and showed that the 5th, 7th, and 9th harmonic disappeared, see Figure 3-19. This figure shows that the results from design Equation 3.3 agrees experimentally where 530nm thick electrodes would not satisfy the equation, it has been shown that the electrode dimensions affecting the QCM response, and that the optimisation of 100 nm electrode thickness for the PTS was required.

This experiment also showed how the microstructural evolution of thin films plays a different role in PTS. It shows that the roughness at the interface exposed to the environment proportionally affects the roughness of the PTS gold surface. It also works under the Zone I of the SZM, and that high rates help to increase the grain size of the PTS surface by having minimal strain energy and higher purity of gold in the film during the transfer. This can be further explored in future work. A side view of the PTS gold can be seen in Figure 3-21.

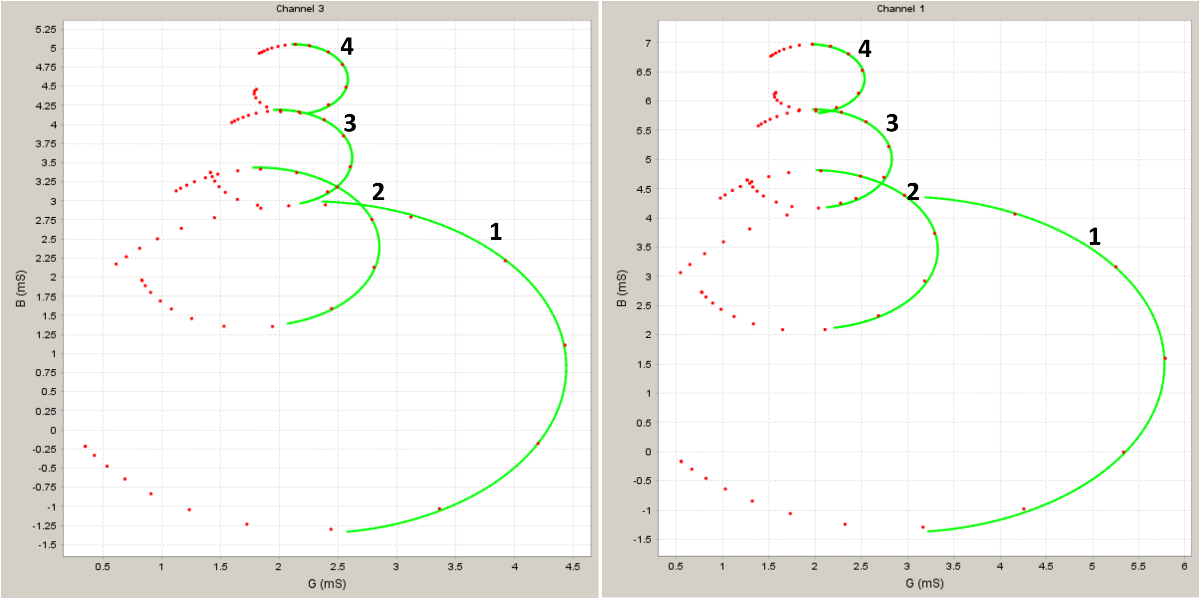

Figure 3-18. Fitting curve of the tuning of a standard QCM resonator (left) and response of the fitting curves for PTS QCM resonator (right). Both resonators were tuned using the fundamental and the first 3 odd harmonic overtones.

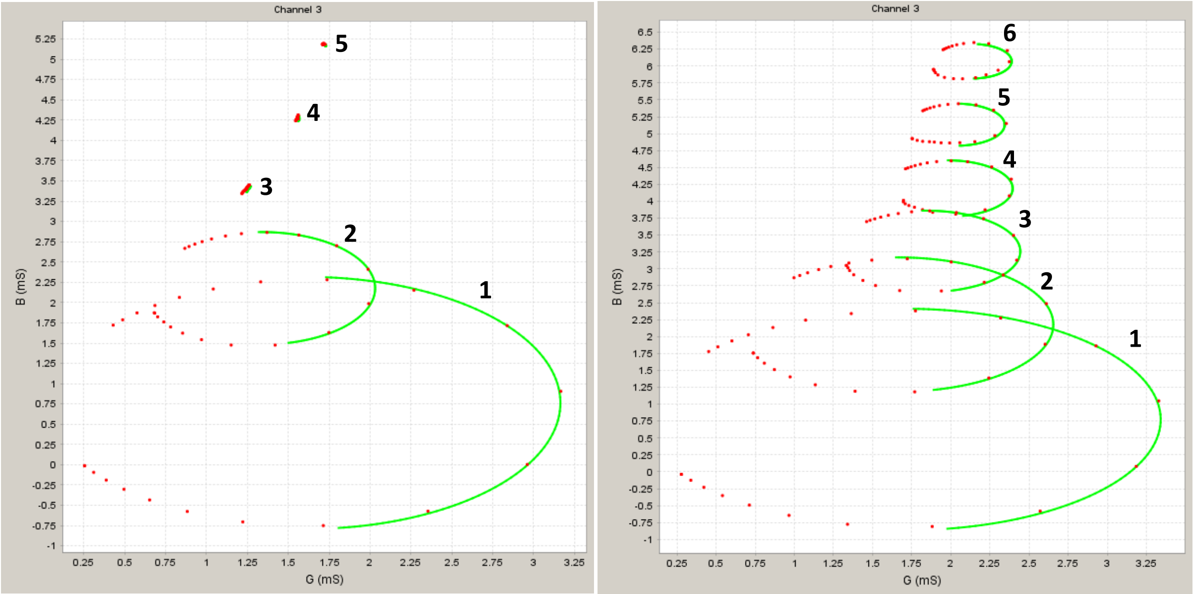

Figure 3-19. PTS QCM resonator with combined 510 nm thickness electrodes (left) and PTS QCM resonator with combined 200 nm thickness electrode (right). Only the fundamental and the third harmonic are present in the sample with 510 nm thickness electrode. In the case of the sample with 100 nm electrodes, none of the odd harmonic responses are lost or affected.

Table 3-3. Roughness values of PTS on standard QCM resonators.

1µm^2	
tag	Roughness RMS[nm]
Sample 1	0.340
Sample 2	0.251
Sample 3	0.401
Sample 4	0.390
Sample 5	0.353
AVERAGE	0.347
STD	0.053

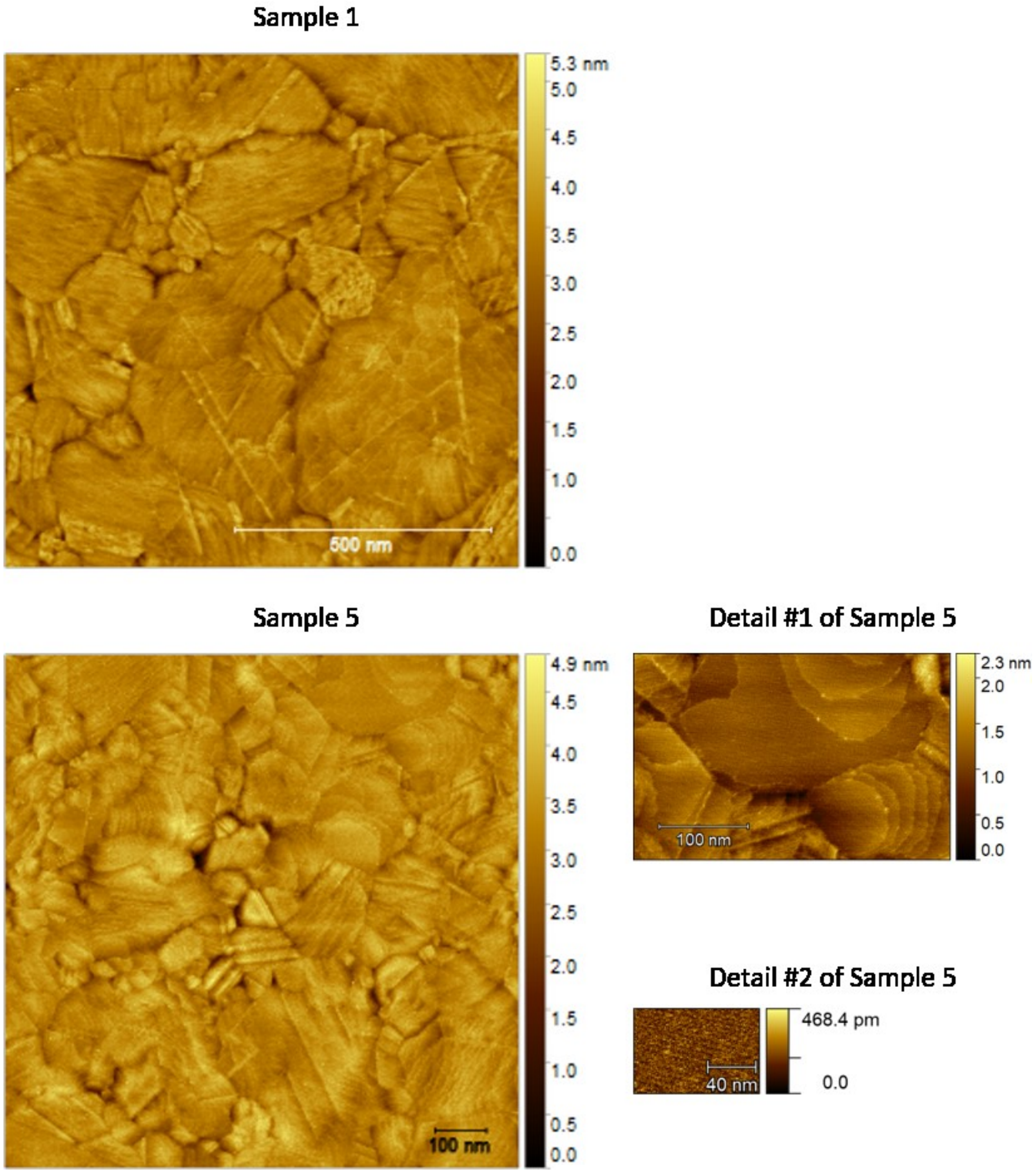

Figure 3-20. Sample 1 and Sample 5 of PTS QCM. There are atomic steps of gold that can be seen on Detail #1 of sample 5. Detail #2 shows the atomic flatness of a specific area of Detail #1 of the image.

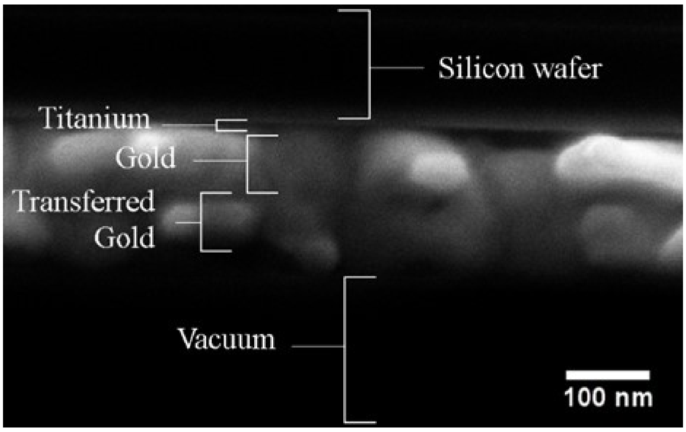

Figure 3-21. Cross section SEM image of the PTS initial experiments. It can be observed that some of the grains of each film coalesced to each other (vertically) and the presence of grooves might be caused by horizontal and vertical grain coalescence.

3.4.6 Protein Adsorption using PTS QCM

To understand the capabilities of the PTS gold, adsorption of Bovine Serum Albumin (BSA) was studied on these surfaces. Using atomically flat gold, the characterisation of proteins at the nanoscale on QCM post experiment could be properly performed. Furthermore, it was explored the mass adsorption on these surfaces and compared against standard surfaces of QCM. The idea is to observe if the roughness created by PVD influences the protein conformational shape after adsorption.

3.4.6.1 BSA on PTS QCM and Standard QCM Gold Electrodes

One useful tool for characterising proteins on surfaces is the AFM. Most experiments of protein dynamics require two separate tasks. First, the characterisation in real time performed by a system like Surface Plasmon Resonance (SPR) or the QCM. For topographical characterisation, a second *ex situ* experiment is performed. Depending on the substrate of interest, different surfaces can be used for higher contrast. In the case of gold, TSG samples are commonly used for the AFM characterisation. However, the discrepancy between the surface of a QCM gold electrode and a TSG substrate for protein dynamics has not been taken into consideration.

To observe if PTS QCM and standard QCM have different adsorption of BSA, an initial experiment was performed to adsorb a monolayer of the protein. BSA was prepared in 10mM Phosphate Buffer Saline (PBS) using Sorenson's buffer, no NaCl added. It is known, experimentally, that the standard surface saturates at around 50uM of BSA using 1 ml of solution at a flow rate of 50 µl/min. Because the kinetics on both surfaces might differ, a higher concentration was selected. The concentration used was 100uM BSA. Two resonators of standard QCM jig design were purchased from Quartz Pro, Sweden. One PTS QCM sample was made in house by hand using a hole puncher. To make the PTS QCM, a standard QCM was coated on one side with PMMA and the other side was etched with gold etchant and subsequently cleaned with Modified RCA-1 to remove the Ti adhesion layer. The mask made with a hole puncher of 5 mm diameter was placed on top of the blank side of the resonator. An adhesion layer of 5 nm Ti and 50 nm Au was deposited on the quartz. The PTS gold protocol followed, using a layer of 50 nm Au on mica. All resonators were UV-ozone treated before installing them in the AWS20 QCM system. A flow of DI water at 50 µL/min was run through all resonators for overnight stabilisation. The next day, water was changed to PBS. The 1ml of BSA was injected for 20 minutes followed by rinsing with PBS. The experiment can be seen in Figure 3-22 and results are summarised in Table 3-4. The experiment shows an increase of areal mass of 9.35% more on the atomically flat gold of the PTS QCM over standard QCM results. This is higher than the expected variation for standard QCM resonators under the conditions of the experiment (see Section 2.5).

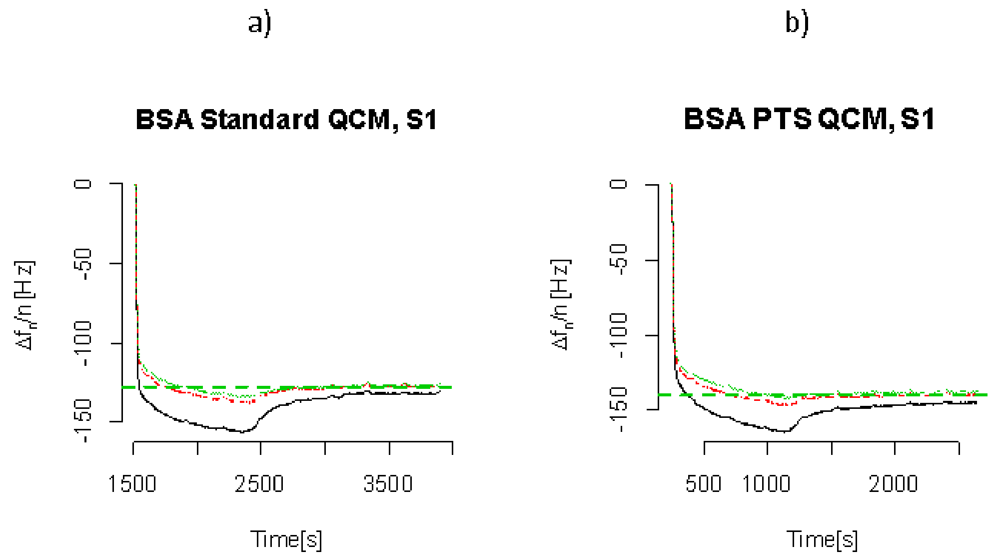

Figure 3-22. Experimental results for the BSA adsorption in Standard QCM resonators and PTS QCM gold electrodes. The experiment was planned such that a monolayer of BSA should be attached to the surface of the electrodes. The atomically flat electrode of the PTS QCM shows a 9.35% increase of areal density than the standard resonator. This is attributed to the adsorption a reorientation on the surface of the BSA. On an atomically flat gold surface, the protein orients its dipole perpendicular to the surface. Instead, on a rough surface, the BSA orients its dipole in different directions, depending on the angle of the surface.

The experiment is difficult to interpret without knowing what is happening at the surface. Only a model can be constructed that it is representing this behaviour. The orientation of the BSA on the surface could be explained if the protein is imaged with high resolution using AFM.

Table 3-4. Results of BSA adsorption on PTS QCM (made by hand) and standard QCM. ΔD is in [E-6]

Sensor	Frequency		Dissipation		Areal Density	
	Δf	STD	ΔD	STD	Mass	STD
NI-TSG QCM HM 9MHz	140.33	---	3.19	---	761.65	---
Standard QCM 9 Mhz	127.99	±0.61	2.66	±0.24	696.50	±3.29

However, to analyse the shape of proteins when they adsorb to a surface, it is required to do a topographical image in solution. If the sample is dried out, then the protein reshapes to minimise the surface energy, and probably, denaturation occurs. To show the difficulties of characterising proteins on a rough surface, low concentration of BSA (100 nM) was deposited on a rough gold substrate. The protein was characterised in liquid using AFM (BRUKER FastScan, see Materials section) with the collaboration of the Department of Pharmacology (Prof. Michael Edwardson and Frederik Bergler). This image is compared against a high-resolution AFM image in air of gold evaporated on mica (Veeco Enviroscope). This substrate has the same topography as the QCM-D electrodes from Q-Sense. When comparing the images, it is difficult to discern between a grain of gold and a single protein, see Figure 3-23.

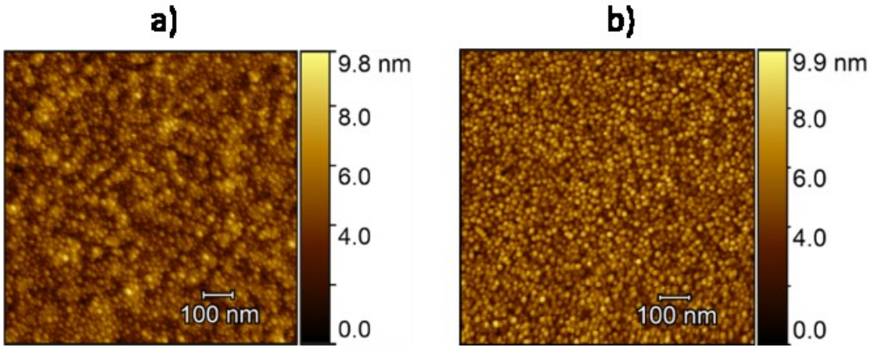

Figure 3-23. a) High-resolution liquid AFM image of low concentration of BSA at 100nM on rough gold substrate, and b) AFM image in air of a grainy surface of gold with characteristics usually found in several QCM resonators. The grain size in both images is similar, making it difficult to differentiate between a gold grain and a BSA molecule.

After these two initial results, it was required to get more data of the PTS QCM. The difference of 9.35% of the PTS against the standard QCM might not be substantial, because the PTS was made by hand and with imprecise tools further refinement was required. To confirm the difference is consistent and due to the flatness of the PTS surface, a shadow mask with the standard QCM jig was ordered from Laser Micromachining Ltd. Multiple PTS QCM could be fabricated quicker and precise. Blank quartz resonators of 10 MHz, with the *x* alignment cut, were purchased from AWSensors. Both fabricated standard (n=2) and PTS QCM (n=3) resonators were made at the Nanoscience Centre. The BSA experiment was performed again with the same conditions. The results are displayed in Figure 3-24.

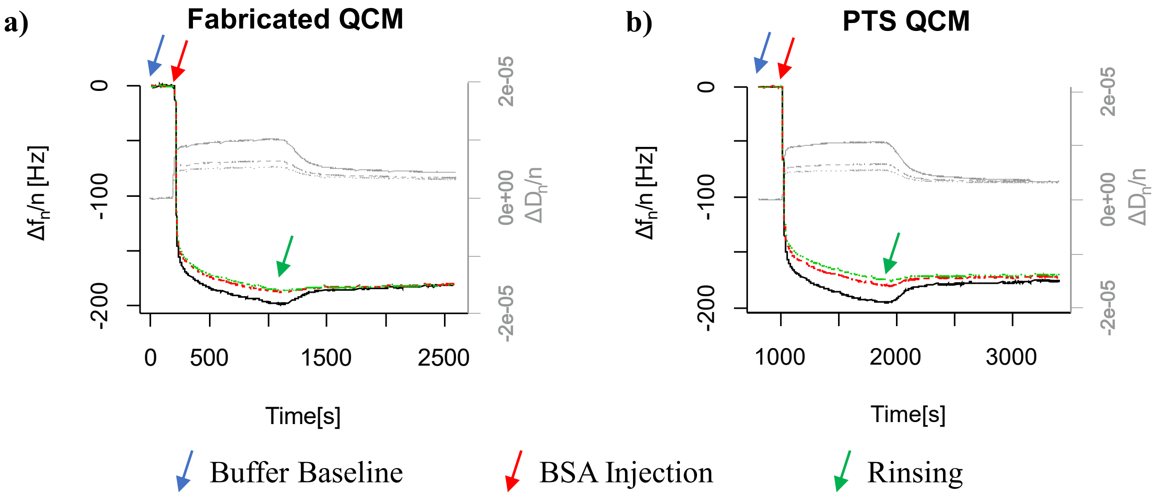

Figure 3-24 Mass adsorption of Fabricated QCM and PTS QCM. Similar values were obtained, which disagrees with the previous experiment. A characterisation with AFM was required to explain this different behaviour.

The summary of the results is in Table 3-5. Measured mass of the standard QCM showed an increase close to 17% from the previous experiment with standard QCM resonators purchased from QuartzPro which was not expected. PTS QCM showed consistent measurements. It was planned to perform a liquid AFM imaging of these samples in the Department of Pharmacology, and the results showed the reason of the discrepancy between the standard QCM (initial experiment) and this fabricated QCM built-in-house. A summary of AFM protein imaging can be seen in Figure 3-25. The atomically flat gold of the PTS QCM was very useful for imaging the BSA monolayer, see Figure 3-26, a). It can also be seen what appears to be the presence of BSA aggregates on the built-in-house standard QCM, Figure 3-26 profile 1 compared to 2. The height of BSA is not bigger than 2 nm if it is surrounded by other BSA proteins in a monolayer. However, in the fabricated QCM image, Figure 3-26 b) profile 1, it can be clearly observed proteins that are on top of another layer, they could possibly be an aggregation too. This extra layer can be characterised as a big step for the AFM tip when scanning this region, see Figure 3-25 (A-F) for a detailed explanation. It is good to remind that the BSA has an approximate hydrated

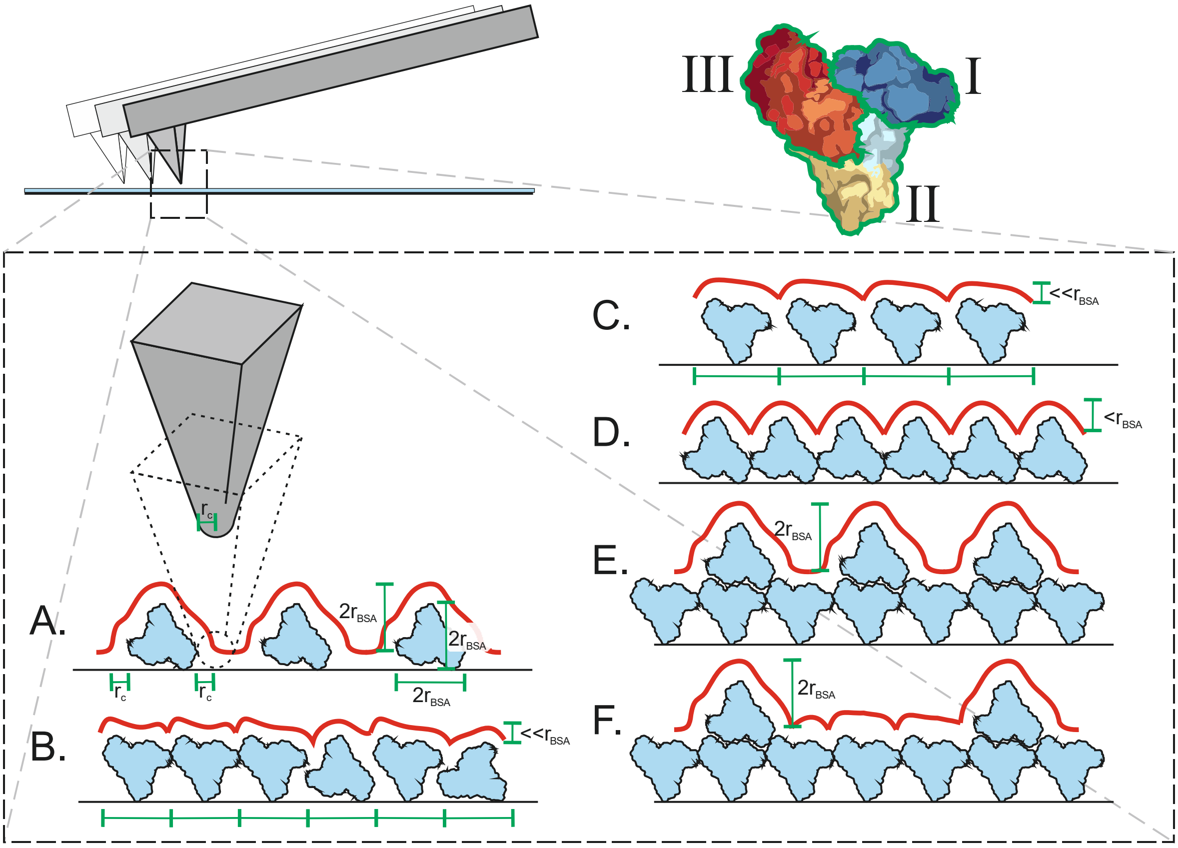

Figure 3-25. The AFM tip radius of curvature, r_c, affects the lateral measurements of the rendered image by adding $2 \times r_c$ to the measurement of the lateral dimension of isolated BSA monomer ($2 \times r_{BSA}$). The AFM measurement is precise in the vertical axis as the radius of curvature is added to both the background surface and to the step created by the protein dimensions. In (A) the presence of 50% coverage of BSA as a monolayer is presented, isolated monomers of BSA on this flat surface has height of $2 \times r_{BSA}$ while lateral dimension is approximately $2 \times r_{BSA} + 2 \times r_c$. In (B) a 100% coverage monolayer of BSA is adsorbed to a flat background surface, domains I and III dominate the lateral features of the profile. The height in (B) is the height of the domains I and III available on the surface and it is usually $\ll r_{BSA}$ and will depend on the sharpness of the AFM tip to be able to enter the boundaries between monomers. In (C) the BSA monolayer is more dispersed than in (B), ~75% coverage, obtaining a longer periodicity in the monolayer. In (D) a monolayer of BSA with all monomers having domain II available on the surface will increase the steps on the profiles but still with values of $< r_{BSA}$ and still the same periodicity as in (B). In (E) an image of multilayer BSA (monomers on top of a monolayer) can be observed. The AFM can only resolve the top layer of BSA in (E) with the possibility of resolving the background surface if the monomers of the second layer are more dispersed as in case (F).

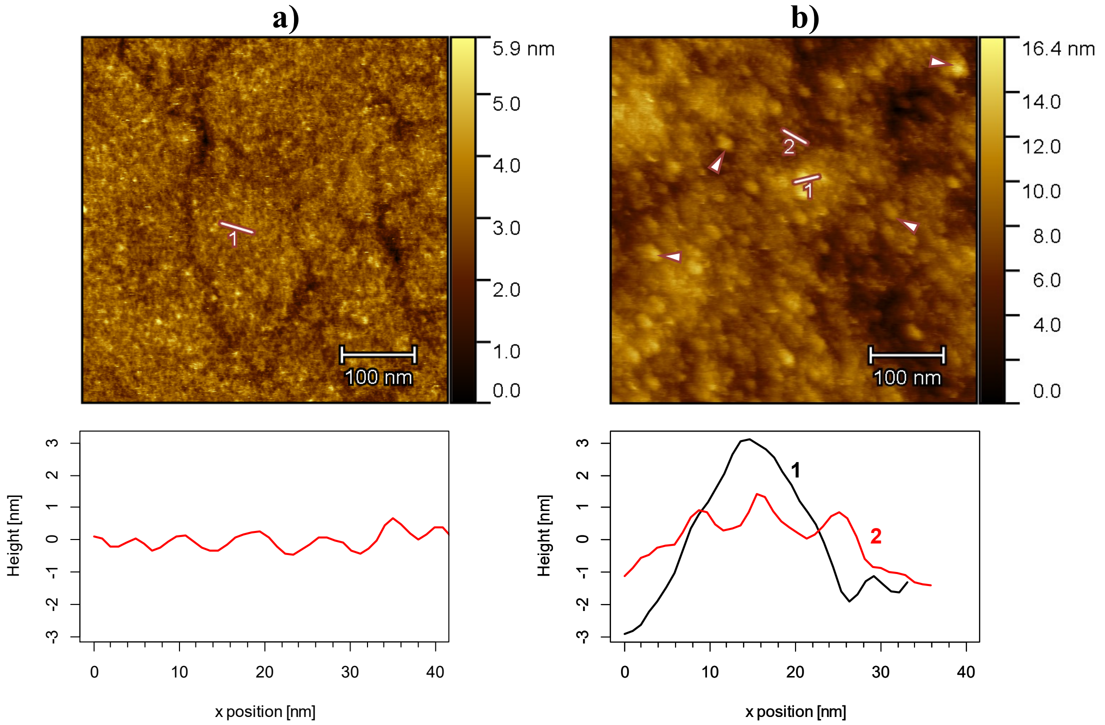

Figure 3-26. AFM liquid measurements of BSA adsorption on PTS QCM and standard QCM resonators, a) and b) respectively. The areal mass results are in the same range in both samples. The AFM image shows a monolayer in the PTS QCM and the presence of additional aggregates on the standard QCM. Profile 1 shows the presence of a multilayer adsorption, and it is compared against profile 2, which profiles three proteins adsorbed to the surface. The length of the three proteins of Profile 2 are: 10.2, 11.4 and 9 nm. The length of the second layer of BSA in Profile 1 is 30.6 nm. The height of Profile 1 is close to 6 nm, while the height of three consecutive proteins is less than 2 nm, making stronger the case that there is at least second uneven layer on top of the monolayer. With multilayers and grainy surfaces, it is difficult to characterise the proteins. But AFM helps to explain the presence of these multilayers. It also shows that PTS QCM have a monolayer.

radius of 3.48 nm[66]. If an extra layer of BSA is resting on top of a monolayer, it would be profiled as an approximate step of 7 nm, which in this case is close to 6 nm probably because of geometrical arrangement, see profile 1 in Figure 3-26 b). Additionally, the AFM tip radius will add length in x and y-axis to isolated proteins or cluster of proteins (as seen on Figure 3-25 F). For example, a monolayer of proteins will have a spacing of around 7 nm if the protein is tightly packed using AFM, Figure 3-25 B) and D). In Figure 3-26 b) a period of 9 nm is found, see the red curve (profile 2), showing three consecutive proteins together. In contrast, the black curve of Figure 3-26 b) (profile 1) shows one feature of 30.6 nm width and 6 nm height. This proves that there are aggregates (multilayer adsorption) to the standard fabricated QCM, this is similar to Figure 3-25 F).

Table 3-5. Summary of BSA adsorbed on PTS QCM and Standard QCM. ΔD is in [E-6]

Sensor	Frequency		Dissipation		Areal Density	
	Δf	STD	ΔD	STD	Mass	STD
PTS QCM	179.08	±4.96	3.54	±0.24	801.56	±21.61
Fabricated QCM	182.81	±0.21	3.54	±0.21	816.66	±2.95

Although the experiment did not show the same results using resonators built-in-house against the QuartzPro (standard) QCM sensors, it is believed that the ability to characterise these surfaces in liquid is crucial. It also showed that QCM resonators can influence the adsorption of multilayer proteins depending on the fabrication parameters and their surface finish. The PTS QCM is easier to characterise by AFM, and conclusions can be obtained by observation of the AFM image and the mass measured by the QCM monitoring system. In contrast, the fabricated QCM is more difficult, the presence of multilayers on top of the resonators complicate the interpretation and it is easy to confuse isolated proteins with a grain of gold. The measured mass on the QCM system showed the presence of more mass on the built-in-house standard QCM resonators than expected, and the liquid AFM showed the multilayer adsorption was the reason. The possible cause of the multilayer adsorption on the built-in-house QCM might be the roughness surface and the gold grain characteristics (e.g. radius of curvature). Nevertheless, the quantification of how many more proteins are on the multilayer is impossible with grainy substrates. In comparison, a liquid AFM image of multilayers on PTS gold is shown in Figure 3-27. The contrast obtained in this image is high, giving the option of performing grain analysis algorithms, e.g. watershed. This computational method could obtain the percentage of aggregates according to the image and could be compared against the mass measured by QCM. One thing that must be considered to have an agreement with both techniques is the radius of curvature of the AFM tip.

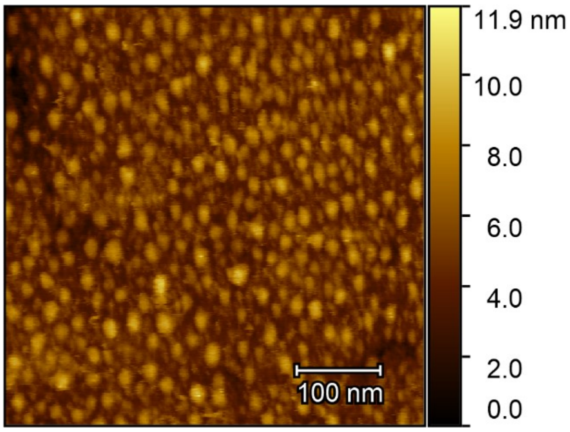

Figure 3-27. Multilayers of BSA on top of gold PTS QCM resonator using liquid AFM. The mass measurement was not performed on this sample, but it can be easily seen the presence of multilayers on top of a monolayer. Using a watershed algorithm, the amount of proteins in the multilayers could be obtained. The multilayer adsorption was obtained by not using UV lamp treatment on the gold surface, keeping it hydrophobic and inducing the multilayer adsorption.

3.5 Discussion of BSA adsorption on PTS Gold

BSA adsorption on surfaces has been previously discussed by Somasundaran[95], where the changes of shape of BSA are similar on both hydrophobic and hydrophilic surfaces. The conformational shape of BSA are highly dependent on the concentration of the protein and it is attributed to the reduction of α-helix content. Reduction of α-helices and subsequent conversion to β-helices are the result of BSA spreading. It is concluded that the spreading on a surface is lower in a monolayer at higher concentrations, as there is less available area to spread, and it is independent of the type of surface.

Ptitsyn[96] and Dolgikh *et al*[97] attribute the shape of a hemisphere to this denatured state of the α-lactalbumin upon binding. They call it a molten-globule-like state and it is attributed to multiple proteins besides α-lactalbumin. These conclusions help explain the different results of BSA mass on the initial standard QCM and atomically flat QCM resonators. The BSA might adsorb on the standard QCM (QuartzPro) surface orientating normal to the position of the grains of the rough surface. Because each BSA protein molecule has a different angle relative to the surface, and hence the angle of the electric dipole of the protein, the charge at the end will screen the area next to it. The more acute the angle, the more area will be screened. After saturation of the surface, the BSA will change its conformational shape gradually to fill in the spaces between proteins, see model in Figure 3-28 a). On the atomically flat surface, the protein will mostly orientate normal to the whole surface, as the grains are large and flat; screening less area (packing more proteins) and having less spreading of BSA see model in Figure 3-28 b). This result is in contrast with the conclusion of Somasundaran, where the type of surface, in this case the nanostructures present, is affecting the BSA conformational shape change and it is dependent on the flatness.

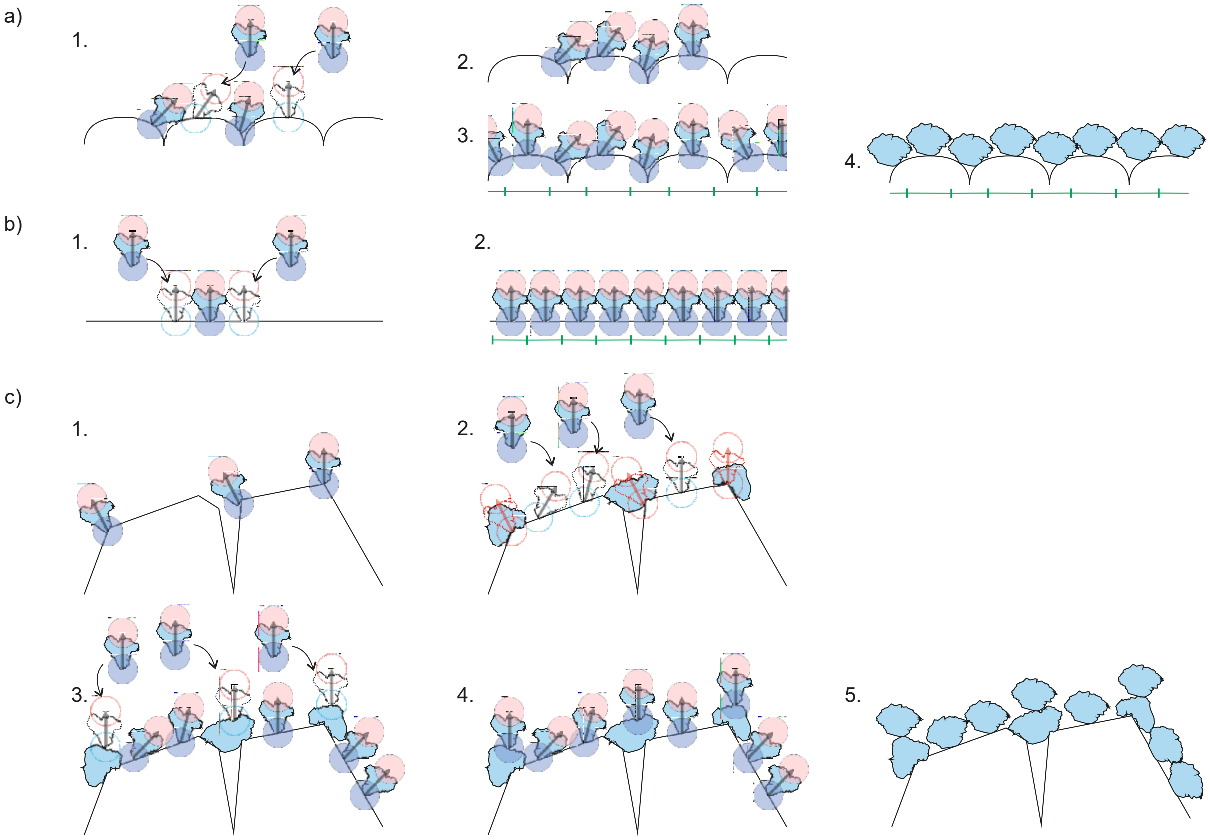

Figure 3-28. Model of BSA binding to a rough surface (a) and a flat surface (b). The rough surface induces orientation changes of the protein screening the next monomer (step 1) which will bind in a less compact manner (steps 2 and 3). Subsequently the monomers will spread as in step 4. In a flat surface, the screening will be minimal and the monomers will bind in a tightly manner. The model c) shows how higher roughness induces conformational shape changes on some monomers inducing protein aggregation.

The characterisation of this behaviour can be further analysed and corroborated with other findings. Single BSA imaging on a flat surface, mica, has been previously studied by Quist *et al*[98]; where they discuss the broadening of the BSA by the tip radius (10nm) with values of 26.2 ± 4.5 nm of length, width of 20.2 ± 2.8 nm, and height of 0.60 ± 0.12 nm for the protein. This result showed experimentally, and with similar tools used for characterisation of the QCM experiments, the broadening of isolated proteins on a flat surface (molten-globule like shape). Supporting the conclusion that nanostructures affect the protein conformational shape. Lord *et al*[99] showed that fibronectin on colloidal silica surfaces change its conformational shape by measuring the reducing binding of the fibronectin antibody. Another finding from Wehmeyer *et al*[19] suggests that BSA on rough samples of TiO_2 spreads as detected by spectroscopic ellipsometry. They also observe the different conformational shape the BSA undergoes at different pH conditions. In contrast, Cai *et al*[100] did measurements of BSA on samples of Ti with different roughness; from 2 nm RMS up to 20 nm. Their results showed no statistically significant change of the protein adsorbed on the surface. Dolatshahi-Pirouz *et al*[16] did experiments on a flat (1.49 nm RMS) and a rough substrate (4.62 nm RMS) of platinum. In their results they found out that BSA adsorption is enhanced on rough samples by 30% more mass on the whole sample once the mass was normalised by the area of the surface. Rechendorff *et al* [15] also observed the increase of mass adsorption of fibrinogen on rough samples of tantalum beyond the expected result. The same experiment was performed using BSA and the increment of mass was close to the increase of area, but still beyond the expected increase. This is opposite to the findings in this experiment, where the flat surface adsorbs more BSA than the rough standard QCM (Quartz Pro) with a monolayer. Riedel *et al*[17] showed that the presence of nanopyramids of germanium affect the protein adsorption of globulin and BSA. They attribute the increase of mass detected to the edges of the nanopyramids. Concluding that the curvature at the edge changes the conformational shape of the protein and more protein was bound to this region. Hemmersam *et al*[101] also used an antibody to detect the conformational shape changes of fibrinogen. The authors deposited 50nm of Ti on top of a QCM-D resonator with 2nm RMS roughness. These authors also conclude that protein conformational shape changes are dependent on concentration. Low concentration will give more time for the protein to reorganise itself and interact with the surface. The studies of Pellicane *et al*[102]showed that the affinity of BSA is higher on higher hydrophobic surfaces, which might induce higher deformation at low concentrations.

The findings of these authors corroborate the idea of the spreading of BSA on surfaces with roughness, and this chapter adds the measurements of BSA adsorption on atomically flat gold compared against rough surfaces. The findings presented here leads to the conclusion that the cause of more mass present on the flat surface might be the tightly packing of BSA on these substrates at high concentrations. The major forces driving the structure of the protein upon adsorption are the electrostatic interaction between the protein and the surface and the lateral interaction of neighbouring proteins[103]. An additional experiment showed that certain roughness and grain composition of the surface also induces a multilayer deposition of BSA see model c) in Figure 3-28, as demonstrated by AFM in liquid, and it agrees with the findings of the authors from the previous paragraph. It is believed that the roughness characteristics are the ones playing the role of changing the conformational shape of the BSA such that it induces a hidden group of the BSA to be exposed and further BSA attaches to this new region, creating the multilayer (aggregates). These characteristics might be the grain size and step between grains (radius of curvature). Grains might affect the BSA in the same way a nanoparticle would affect it. Further exploration of this problem might be needed as it requires a rigorous control of the surface characteristics. The results presented in this chapter can be the foundation of a future project as it already presents the three states of BSA: tightly packed, monolayer on rough samples, and induced multilayer on rough samples. It would be interesting to explore at which condition the transition occurs between tightly packed, spreading and finally induction of multilayers.

3.6 Results

The main outcome of this chapter is the new PTS technique[20]. The method can transfer atomically flat gold to substrates of different topologies like the QCM resonator. With this protocol, new combination of techniques can be performed on the same sample as it can be used directly on most biosensor surfaces as well as use the properties of atomically flat surfaces for characterisation. This could be beneficial to techniques like ellipsometry, AFM, SPR, among others. With PTS QCM it was possible to obtain a model of BSA adsorption to featureless surfaces, this was possible by measuring the BSA areal mass on QCM as well as the topography of the monolayer using liquid AFM from the same sample. It was observed that BSA adsorbs ~700 ng/cm^2 on resonators from QuartzPro, on PTS QCM ~800 ng/cm^2 and on fabricated QCM ~816 ng/cm^2. These results suggested that protein interacted differently among these surfaces. The reason was obtained by using liquid AFM and showed that the increase for PTS QCM and fabricated QCM resonators was a tightly packed monolayer and aggregation of monomers (multilayer) respectively. The cause of this behaviour is detailed in Chapter 5, where the protein behaviour is attributed to the roughness of the surface and a model is presented.

3.7 Conclusion

The study of atomically flat gold is important for multiple characterisation techniques. The flatness of the surface using template stripping methods changes among laboratories. It has not been well understood how gold behaves using this technique. So far, only gold grown epitaxially has been properly characterised and their growing mechanisms detailed. In this chapter, it is contributed how gold of template stripping methods create grains of different sizes. Originally, grains have particular characteristics as a result of evaporation rates, i.e. pure, smaller. When the grains are incorporated into a thermal step as in the case of PTS or TSG, grains start to coalesce, and their resulting atomically flat gold is related to the evaporation rate. Higher rates lead to flatter surfaces. Lower rates are linked to pinholes on the surface and higher overall roughness. The roughness can be reduced at lower rates using thinner films, but the number of grain boundaries is not affected much. Using the results of this experiment, the application of PTS onto samples of the semiconductor industry is possible but might require fine tuning.

The PTS technique has the potential to combine multiple methods of protein characterisation and biosensing. PTS was used on QCM electrodes to combine QCM monitoring and AFM characterisation of BSA adsorption to gold while in buffer. Characterising simultaneously the adsorbed layer in this manner will allow to observe the real conformational shape of the protein, which otherwise is affected when is dried. The flat gold allowed an adsorption of a compact monolayer of BSA as confirmed by liquid AFM, and in contrast the built-in house QCM resonator showed the presence of BSA molecule aggregates, which could only be confirmed by having measurements of multiple techniques of the same sample and comparing them. In the following chapter, nanofabricated patterns on High Fundamental Frequency QCM (HFFQCM) resonators are used to compare the monolayer adsorption of BSA using the same conditions as in this experiment along with a HFFQCM resonator with standard electrodes, which have a smaller roughness compared to the fabricated in-house resonators.

Chapter 4
Patterned QCM Electrodes Using E-Beam Lithography

4 Patterned QCM Electrodes Using E-Beam Lithography

4.1 Summary

E-beam lithography (EBL) is a technique to achieve high resolution patterning on substrates. This fabrication method offers benefits like precision and reproducibility at the expense of fabrication time. In this chapter EBL is used to nanopattern electrodes. EBL is introduced with a small literature review focusing on achieving high resolution (<10nm) and in one of the steps of the protocol called development. It is followed by presenting the fabrication recipe and the tuning of the experiment to achieve highest resolution on samples with multi-steps (mesa) like the High Fundamental Frequency Quartz Crystal Microbalance (HFFQCM). It is followed by the fabrication and characterisation of the patterned HFFQCM resonator and an experiment of BSA adsorption. BSA adsorption on nanopatterned HFFQCM resonator is compared against a standard HFFQCM resonator and the measurements are discussed leading to the findings and conclusions.

4.2 Introduction

On the QCM biosensor, protein measurements are usually performed at the interface of a liquid medium and an evaporated material (the electrode). QCM metal surfaces, which are used for detecting the mass of molecules per area, are considered flat. The detection phenomenon is dynamic in nature i.e. the molecules which are attached to the interface can subsequently detach. In most cases, the protein is expected to remain attached to the surface. This is important when very few molecules are present in solution. The reason is that for biosensors an important parameter is the limit of detection of the device. If a sensor can detect a low concentration of protein, e.g. low marker concentration for an early stage of a disease, then the biosensor could be used for early treatment and prognosis. However, at low concentration, a few proteins are attached to the interface, and in most cases are not retained. It is well known that nanoparticles change the shape conformation of proteins[99]. In some cases, the proteins tend to remain fixed to the nanoparticle[103]. Rather than using nanoparticles, one can in principle use nano-textured surfaces for protein adsorption. If this principle could be exploited on the interface of biosensors, then the limit of detection can be improved.

Nanostructured surfaces can have high aspect ratio and, therefore, large area for biosensing as compared to a flat surface. Several resonators have a limited sensing area due to the exploitation of a physical property at the nano or microscale. Thus, the range of detection is compromised. By using nanostructures, the range of measurement of multiple types of biosensors could be increased.

Furthermore, different nanostructure patterns can be exploited for tuning the sensitivity of the protein detection. For example, QCM resonators are more sensitive at the centre of the electrode than at the edge. If a very low concentration of protein solution, which is not uniformly dispersed, is passed through a specific area of the biosensor and manages to deposit close to the edge, the mass detected would be smaller than the same amount of proteins depositing close to the centre. By nanostructuring the surface edge, the sensitivity of mass detection at this area could be similar to that at the centre of the electrode, i.e. high density of pillars on the edge and the density gradually decreasing towards the centre.

Additionally, mechanical properties of the proteins could be obtained by nanostructuring a sensing surface. Using an array of nanostructured mechanical sensors, like QCM, the behaviour of the protein attachment and mechanical response of the QCM can provide different information for different proteins. QCM resonators can use multi-electrodes, and each resonance can be isolated from each other (see Section 3.2.4.1). By using a different pattern for each electrode, the response of the protein can be altered. This could lead to studies of differences among proteins having different charge, stiffness, or hydration shells etc.

These experiments can also be performed using Nanoparticles (NPs) on top of the QCM resonator. However, the precise control of the NPS distribution is not as good as a fabricated device. The variation of the distance between NPs is large. To understand the interaction of proteins with nanostructures, nano fabrication was performed on top of the QCM electrode. The length scale of the nanostructure must be comparable to the length of the protein, which in the case of BSA is approximately 7 nm. In nanofabrication, there are multiple techniques that could accomplish this. Electron Beam Lithography (EBL) is one of very few nanofabrication techniques which can get close to this resolution. Nanoimprint lithography can also be used for large area nano structure but to make the master imprint, the protocol requires EBL as a first step. Using EBL, the position and geometry of the pattern can be controlled with ease. Furthermore, the thickness is controlled by evaporation of the material using Physical Vapour Deposition (PVD) methods. Figure 4-1 shows the representation of the devices where nanostructures are fabricated on top of the whole QCM electrode.

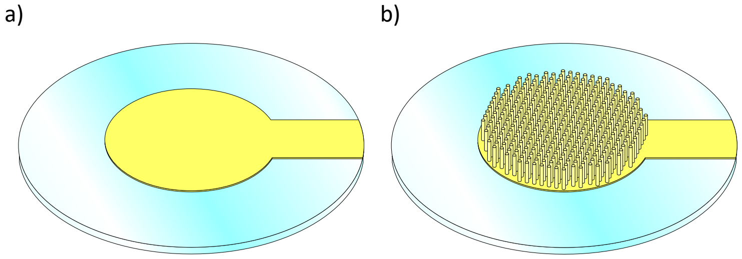

Figure 4-1. Representation of (a) QCM and (b)QCM with nanostructures built on top of the electrode. Instead of depositing nanoparticles, the idea is to use e-beam lithography to have a more robust control of the features and their location. Image is not to scale.

The disadvantage of EBL is that it is a serial lithography technique and therefore can take a long time to expose a pattern over a large area (~cm^2). For certain symmetric patterns, longer exposure times can be shortened. For example, if the pattern consists of nano meter scale circles, then the e-beam can be positioned at the centre of the circle and by overdosing that point a circular area can be exposed. The system will take less mechanical time than scanning the full circles. In comparison, a scanned pattern of circles of 43 nm diameter and 80 nm pitch on a 1 mm diameter area will take 7 days instead of 30 mins using this method also known as forward scattering (overdose).

Other difficulties may arise using the forward scattering patterning technique. The process is sensitive to slight changes in its parameters such as beam current, temperature, resist thickness, position drift etc. It is therefore important to have a good calibrated system and the steps to be carefully optimised. For this experiment, an HFFQCM resonator was used instead of a standard QCM. This sample has a circular electrode with 1 mm diameter, see Figure 4-2. The small electrodes will speed up the pattern fabrication.

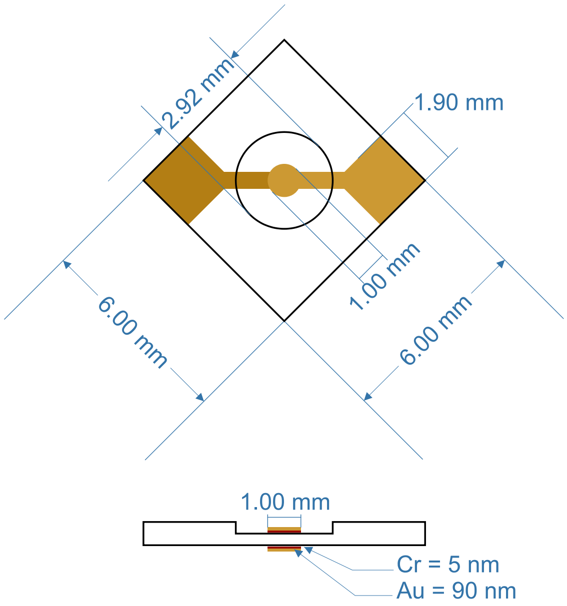

Figure 4-2. HFFQCM electrode with fundamental frequency of 50 MHz. The resonator has a mesa of 2.92 mm diameter with a thickness of 100 um. The vertical cross-section schematic, bottom figure, shows the electrode thickness (side view is not to scale).

The fabrication process is discussed in the following section. Firstly, a short summary of the e-beam lithography process is explained. Then, the steps required to achieve high resolution EBL are presented in the form of a small literature review. Secondly, the calculations and methods required to fabricate on the small sample of HFFQCM is presented, along with the dose calculations and results. Finally, an experiment of protein sensing using BSA is presented leading to the conclusions.

4.3 Nanofabrication Process

4.3.1 Introduction to E-Beam Lithography

E-Beam Lithography (EBL) is a fabrication technique which has been derived from the first scanning electron microscopes. In analogy to photolithography (PL), EBL uses electrons instead of light to chain-scission or cross-link the polymers in the resist (e-beam resist). Once the electrons scan the resist, the remaining polymer can be dissolved presenting the pattern. For example, the chain-scissed polymers could leave a trench, that with the required design and followed by a PVD method, a material can be deposited as a pattern. The advantage of EBL over PL is the capability of higher resolutions as it is not limited by light diffraction as in PL. Despite this, the drawbacks are that it is at least an order of magnitude slower than PL, in some cases multiple orders. It also requires a very expensive system, costing millions of pounds and requires frequent servicing to stay properly maintained.

To make a pattern using EBL the first step is to coat the substrate with the e-beam resist, e.g. Poly(methyl methacrylate) (PMMA). This resist is hardened by baking. The second step is to use the e-beam to break the molecules (for positive resists) or cross-link them to make bigger chains (for negative resists). To make things simpler, the following explanation is based on a positive resist, PMMA. Once the e-beam exposes the desired pattern area, the exposed resist consists of smaller chains and can be removed. This step is called development, and several solvents can be used to remove the smaller polymer chains. These solvents are crucial, because their selectivity against the cross-linked molecules would improve or make worse the resolution. After removing the exposed resist, the next step is to deposit a material (which in this case is gold) on the substrate. The material would be in contact with the substrate (where the resist was dissolved during development). The material is deposited on the developed as well as in all the unexposed area. The gold on the unexposed area can be removed by using the process called lift-off. This step requires a strong solvent to remove the unexposed resist. Once the underneath resist is dissolved, the deposited material on top of the resist is lifted off as it would not be tethered by the resist to the substrate anymore, hence the name lift-off. Further details are explained in the Section 4.4. The principle of EBL is simple, but to reach higher resolution, a few things need to be considered during the development and during the calibration of the system which are discussed in the next section.

4.3.2 High Resolution E-Beam Lithography

EBL has been an area of interest for high resolution lithography for the last two decades. The introduction of assisted ultrasonic agitation during the development step was done by Chen and Ahmed in 1993[104] which helped to improve, after decades, the limits of resolution obtained by EBL. The resolution achieved at this time was a record of 10 nm. In 2000, Vieu *et al*[105] achieved the resolution of e-beam lithography of sub 10 nm for diameter or line width. They highlight that the key element to improve resolution was the developer. Since then, a lot of researchers explored the improvements of the resolution of EBL using PMMA as a resist. Yasin *et al*[106] showed that using a solution of water and isopropyl alcohol (IPA), along with ultrasonic agitation, the resist would not swell as much as other methods, reducing the possibility of resist closure during development of the exposed pattern due to swelling. Sonication also helped to reduce the radius of gyration of the PMMA molecules in the solvent, allowing them to get out of the e-beam exposed region. Water/IPA in a 3:7 ratio showed better results against the standard Methyl Isobutyl Ketone (MIBK) and IPA in a 1:3 ratio. The authors achieved sub 5 nm resolution. However, two years later, Hu *et al*[107], showed that the resolution given by MIBK/IPA can be as good as water/IPA by cooling down the solution. This is attributed to the edge of the trench of the pattern. During cold development the edge is sharp and there is undercut on the exposed region. However, when used at room temperature, high resolution patterns have no undercut, and the edge of the trench is round, complicating the lift-off step. The reason behind this is that at lower temperature the PMMA has a higher viscosity which will slow down the dissolution rate of PMMA on the edge of the trench[107]; the cross-linked PMMA has smaller etch rate on the edge at low temperatures. Additionally, the small chain polymers could easily come out of the trench. A year later, Yasin *et al*[108] showed that PMMA gets re-deposited on the bottom of the trenches at the rinsing step after development. The rinsing solution is a solvent that stops the developer of etching the resist. This was observed using AFM. Therefore, rinsing is a step now usually removed from the EBL protocol, especially for water/IPA. Even with the creation of more modern resists like ZEP 520A (Nippon Zeon), PMMA has shown to have the best resolution and line edge roughness using water/IPA[109] but at the cost of sensitivity. Another important resist that has been studied is hydrogen silsesquioxane (HSQ) [110]. HSQ has a molecular size comparable to 4 nm which will aid in structuring 4 nm sized patterns.

Although resists might play an important role, the calibration of the system is also crucial. Recently, a record of fabrication of 1.7 ±0.5 nm diameter pillars was achieved using PMMA and aberration-corrected STEM augmented with a pattern generator[111]. As a contrast, PMMA has an experimental radius of gyration of 25 nm for a 950 K MW[111]. This last result showed that the theoretical limitation of EBL can be surpassed.

In summary, for EBL, the resolution is affected by many parameters where the most crucial are the chemical process (development), the resist and their interaction with the electrons, the resist polymeric chain size, and the system limitations and its calibration. In a less important manner, but central in this project, is the characteristics of the substrate. The QCM electrodes have gold deposited by a PVD method. The roughness of the surface will play a role in the minimum size that can be achieved in this substrate as it ultimately affects all the parameters.

4.4 Fabrication Method

4.4.1 E-beam Lithography Protocol

The fabrication of a HFFQCM with nanostructures (HFFQCM-NS) followed a simple protocol, but the high reproducibility of each step is required to achieve high resolution. The sample itself is quite fragile so it requires handling with non-metallic tweezers and holders. For handling the sample, in all the steps where the substrate was required to place it inside a solution, a polytetrafluoroethylene (PTFE) basket/holder was used. The holder has a well where the sample sits perfectly and can drain any liquid underneath. This well has the sample at the height where the ultrasonic bath does not have a constructive interference, as this might damage the sample. For all solutions the water used was HPLC water. Acetone, HPLC water and IPA were purchased from Fisher Scientific. Poly(methyl methacrylate) (PMMA) 950K molecular weight and A4 concentration was purchased from Microchem (USA).

4.4.1.1 *Protocol*

The following protocol was used to fabricate pillars on top of the HFFQCM electrode. The samples were previously cleaned using modified RCA-1 and stored in a class 100 cleanroom.

1. Cleaning: Before any step, stored samples of HFFQCM resonators were cleaned using Acetone, and IPA for 10 minutes in each solution. Sonication was applied using the PTFE holder.
2. Coating of resist: The sample was placed on a POLOS spin coater inside a sample holder used for this step, where the sample was physically constrained of movement during the spinning. PMMA of 950 k MW (10μl) was pipetted on top of the centre of the sample. The spin coater was set to 10 k RPM for 60 seconds with an increase and decrease rate of 10 k RPM per second. Other speeds failed to give consistent results, this is due to the mesa design of the HFFQCM. Subsequently the resist was hardened by baking it at 200 °C using a hot plate for 2 minutes.
3. E-beam exposure: The sample was placed inside the CABL system and grounded by clamping the sample between the electrode connection (corner of the sample) and the stage. Calibration of the system is important. Focus and astigmatism was repeatedly tuned to get the best parameters.
4. Development: The sample was developed using 3:7 water/IPA at 25 °C for 10 seconds for highest resolution. It was quickly dried using N_2 gun. The whole step was performed while the sample was still in the PTFE holder.
5. Evaporation of metal film: The deposition of Au was performed using the Edwards thermal evaporator at a rate of 4 Å/s at the pressure <8E-6 Torr. The sample was placed at 30 cm from the source of Au.
6. Lift-off: The gold film was lifted-off using acetone. For lift-off the sample was soaked in the solution for at least 4 hours or by sonication assisted for 8 minutes.
7. Cleaning: The sample was rinsed with IPA to remove any traces of acetone.

4.4.2 Resist Thickness

For optimising the fabrication process, different thicknesses of PMMA resist were tested. Thickness of different concentrations of PMMA in anisole at different rates of spinning were measured using a M-2000 J.A. Wollam ellipsometer. 4% PMMA in anisole (A4) spin coated at 10 k RPM provided an optimal thickness of 124 nm for this experiment. The accuracy of the ellipsometer's measurement was corroborated with AFM. These measurements are summarised in Table 4-1. The thicknesses shown in these tables are for PMMA spun on gold evaporated substrates representing the spin coating behaviour on QCM resonators. One sample at very low concentration of PMMA did not provide a uniform thickness, 495 MW A1 at 10 k RPM, this was confirmed with a topographical measurement with AFM (not shown).

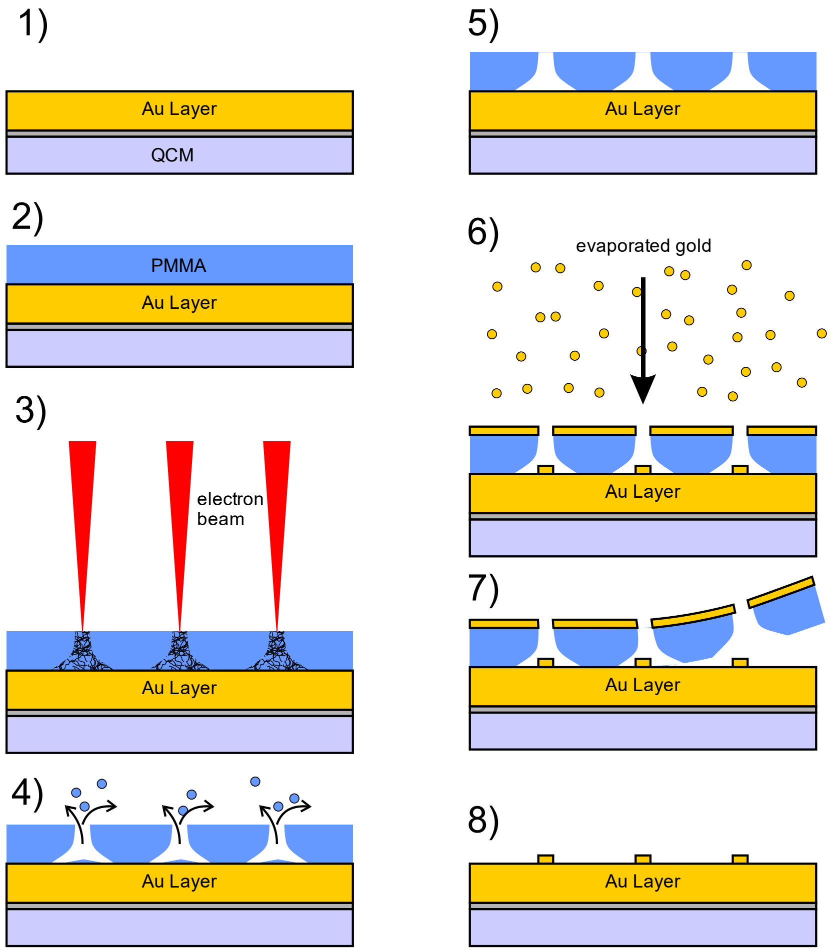

Figure 4-3 Protocol for the e-beam lithography process. 1) cleaning, 2) spin coating and baking of the resist, 3) e-beam exposure, 4) development, 5) Evaporation of Au using a thermal evaporator, 6) lift-off, 7) final sample.

Table 4-1. PMMA thickness at different concentrations in anisole, different molecular weights, and different revolutions per minute in the spin coater. Substrates were 11 mm x 11 mm silicon wafer squares with 10 nm of Ti and 100 nm of Au.

Resist	MW [kDa]	Concentration	RPM [k]	Thickness [nm]	SD
PMMA	495	A1	4.5	16.82	±0.26
PMMA	495	A1	6.0	14.38	±0.13
PMMA	495	A1	7.5	13.18	±0.03
PMMA	495	A1	10.0	11.25	±0.46
PMMA	495	A1.5	2.0	46.62	±0.07
PMMA	495	A1.5	3.0	36.53	±0.13
PMMA	495	A1.5	4.5	29.09	±0.14
PMMA	495	A1.5	6.0	26.27	±0.15
PMMA	495	A1.5	7.5	23.03	±0.14
PMMA	495	A1.5	10.0	19.82	±0.13
PMMA	950	A2	2.0	91.36	±0.05
PMMA	950	A4	6.0	169.24	±0.10
PMMA	950	A4	8.0	145.17	±0.10
PMMA	950	A4	10.0	124.10	±0.10

4.4.3 Beam Spot size and the Proximity Effect

The core element of the e-beam lithography is the electron optics column. This consists of an electron source (the cathode), focus lenses, a blanker, and a deflection system to scan the beam. When the column is in an ideal condition, the current density in the exposed spot is the same as the source. However, the spot is limited by three physical phenomena: spatial charge, chromatic aberrations, and spherical aberrations. The repulsion of electrons, spatial charge, occurs when the beam is being focused, creating a divergent trajectory of the electrons. The chromatic aberrations are product of a lens, and it is the result of focal distance variation and the energy of the particle going through it. Lastly, the spherical aberrations are geometrical aberrations induced by variation of lens strength. The aberration creates a beam enlargement at the desired position and it is also affected by the angle of incidence relative to the optical axis. There are additional physical phenomena affecting the beam resolution like the scattering of electrons when colliding with the resist.

The electrons lose energy depending on the path they travel and the interactions with the atoms of the target. When the collision of the electrons is with the atoms nuclei of the target, the result is elastic scattering. There is no energy loss, but there is a change of trajectory of the electron. This change of path creates and undercut, that is to say the beam does not break the polymer of the resist at an angle normal to the target. The longer the electron travels the higher the probability of the electron moving away from the original x position. This scattering broadens the beam inside the resist and increases with thickness and with lower incident energy from the e-beam gun. Once the electrons hit the substrate, they can go directly to the ground of the system or they can re-emerge by bouncing back at an angle from the substrate and at a distance from the initial point of collision with the surface. These are known as backscattered electrons and leads to the effect known as proximity effect; which is the apparent pattern distortion or overexposure in denser zones of the pattern. In some systems the proximity effect can be corrected by software.

Another factor affecting the beam spot is the creation of secondary electrons caused by ionisation of inelastic collisions of the primary electrons. Their energy is low and therefore electrons travel a short range of various nanometres that might ultimately affect the resolution. One last problem is the charging of the surface of the substrate when it is not very conductive. A coating of a conductive polymer or a thin metal film can be used to dissipate these charges. In some samples like the case of QCM or HFFQCM, the samples are quartz with electrodes of gold. If the pattern is on top of the electrode and the electrode wired to the ground of the system, the charges will be dissipated.

4.4.4 Calculation of Dose for Dot Patterns

Making a pattern of pillars on HFFQCM required a calculation of time at a given current of the EBL system. The lower the current, the smaller the spot size due to less scattering, but the longer it would take to reach the necessary exposure of electrons in the resist. At 100 pA the beam spot size was 2 nm which was estimated using the following graph in Figure 4-4 provided by Crestec, who is the manufacturer of the CABL e-beam system used for the EBL.

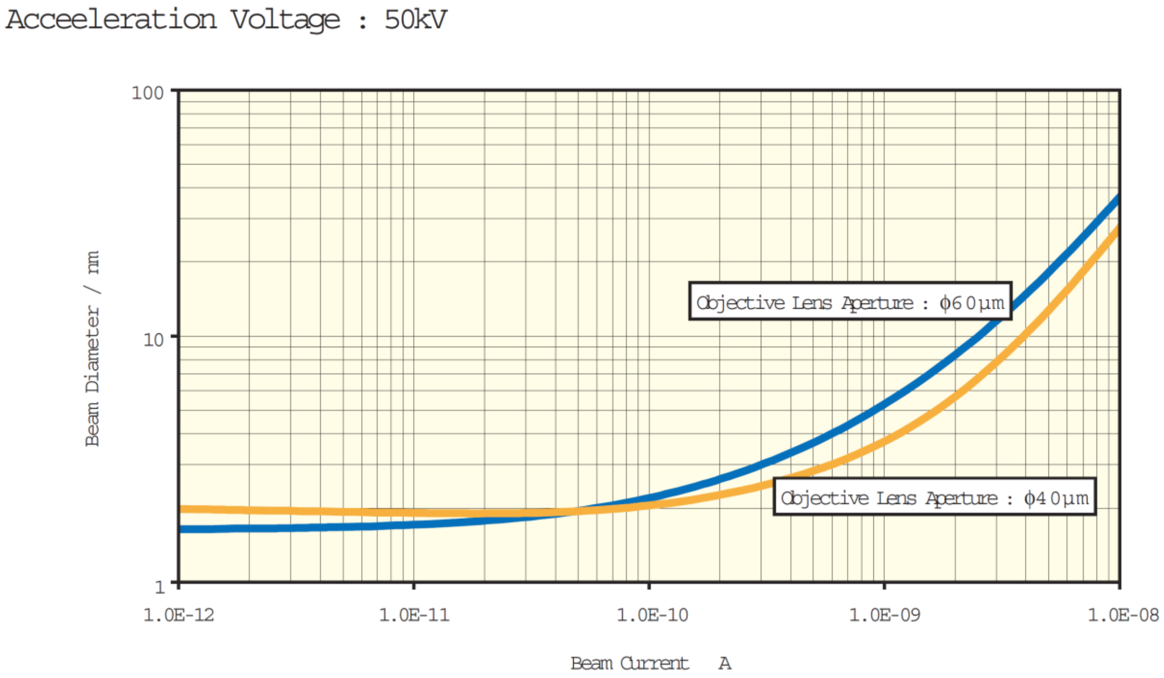

Figure 4-4. Beam diameter versus beam current at an acceleration voltage of 50 kV and objective lens aperture of 40 µm and 60 µm. Reprinted form the instruction manual of the system.

The calculation of the dose required for this experiment relies on the idea of placing the beam in a specific position for a prolonged time and rely on the scattering and the proximity effect to make a circle. The electron beam is then blanked and moved to a specific distance (spacing or pitch) and exposes another circle. It is repeated multiple times, and an array of circles is exposed and will become pillars. This method is used instead of fully scanning each circle, and therefore decreasing the mechanical time the machine spends making the design. The reduction of time from the standard scanned circle to spots using scattering is from days to minutes.

The process starts by setting up field size (FS) per dots of the system in digital mode: a 60µm field size divided by 750 dots would be identical to an 80 nm pitch for the array. Also, the amount of dose for the resist should be a percentage of a full exposure for a full pattern using this ratio. For example, instead of drawing a square with a FS/dot of 80 nm at full sensitivity, a half exposure time might give pillars with 20 nm radius at spaces of 80 nm centre to centre.

Besides 80 nm pitch, it is important to be able to fabricate at other pitches without spending too much time doing tests, as EBL time is costly. This can be achieved by using the initial 80 nm pitch experiment. First, using a dose test, it was obtained the dose required for 43 nm diameter pillars and 80 nm pitch. This experiment was done to compare the behaviour of proteins on 43 nm pillars against the nanoparticle experiment of 43 nm diameter of Chapter 2. Using this initial dose as an average per area, if the pitch is changed, the same dose will give similar diameter for the pillars at different pitches. The CABL EBL system has a calculator for resist sensitivity which requires the current under operation, the field size, dots division of the field size, and the time the beam will spend on each dot. The different exposure times were obtained with this calculator for each pitch.

PMMA of 950 k MW has an experimental resist sensitivity of 550 μC/cm^2. Experimentally the machine was setup to a FS of 60 μm and 60 k dots. This gives a spacing of the scan of 1 nm for each exposure of the beam. Knowing that a spacing of 80 nm is required, the dots are calculated to be 750 (the amount of spaces that fit in 60 μm FS). By inserting these parameters in the dose calculator of the CABL system, a real sensitivity can be calculated for 43 nm diameter pillars. For 80 nm pitch, the resist sensitivity required was 125 μC/cm^2. This is 22.72% of the experimental dose sensitivity of PMMA. This dot resist sensitivity (DRS) can be used for any other pitch by inputting it in the calculator and changing the number of dots according to the pitch as in the 80 nm example. As mentioned before, this only works in digital mode and not in analogue mode for obvious reasons. This will help to get an optimal time for the beam to be exposed on each position to make pillars at the desired pitch.

4.4.5 Patterns and Final Devices

The aim of the experiment is to fabricate 43 nm diameter pillars with 80 nm pitch. For 43 nm pillars, a 43 nm thickness is required of evaporated gold. For the resist, a PMMA thickness of at least three times the value of the deposition is required. 124 nm thick PMMA was used, which was obtained using 950 k MW A4 PMMA spun at 10 k RPM. For 43 nm diameter pillars, the minimum spacing achievable was 70 nm centre to centre, which is close to 27 nm edge to edge between pillars. Figure 4-5 show the experimental results of pillar arrays with different spacings.

The thickness of the resist can be decreased for shorter pitches. It was possible to obtain 30 nm spacing centre to centre, see a) in Figure 4-6. However, the protocol requires further optimisation to have a consistent pattern using the CABL system. Consistent smaller features at 124 nm PMMA thickness can be obtained up to sub 10 nm features at spacings down to 50 nm centre to centre, see b) in Figure 4-6.

Once the array of 43 nm diameter pillars and 80 nm pitch was fabricated the next step was to cover the full electrode of the HFFQCM resonator. Figure 4-7 shows the full pattern to be fabricated on the HFFQCM resonator but in this case on a gold coated silicon sample used for the test. The design has an 840 μm diameter. The HFFQCM electrode has a 1 mm diameter; the design has a smaller diameter to avoid exposure on the quartz and the possibility of charging the surface. The full exposure takes 4 hours using 60 μm FS by 60 k dots but can be decreased to 2 hours using a bigger FS/dots setup (120 μm/60 k) at the cost of stitching error between arrays.

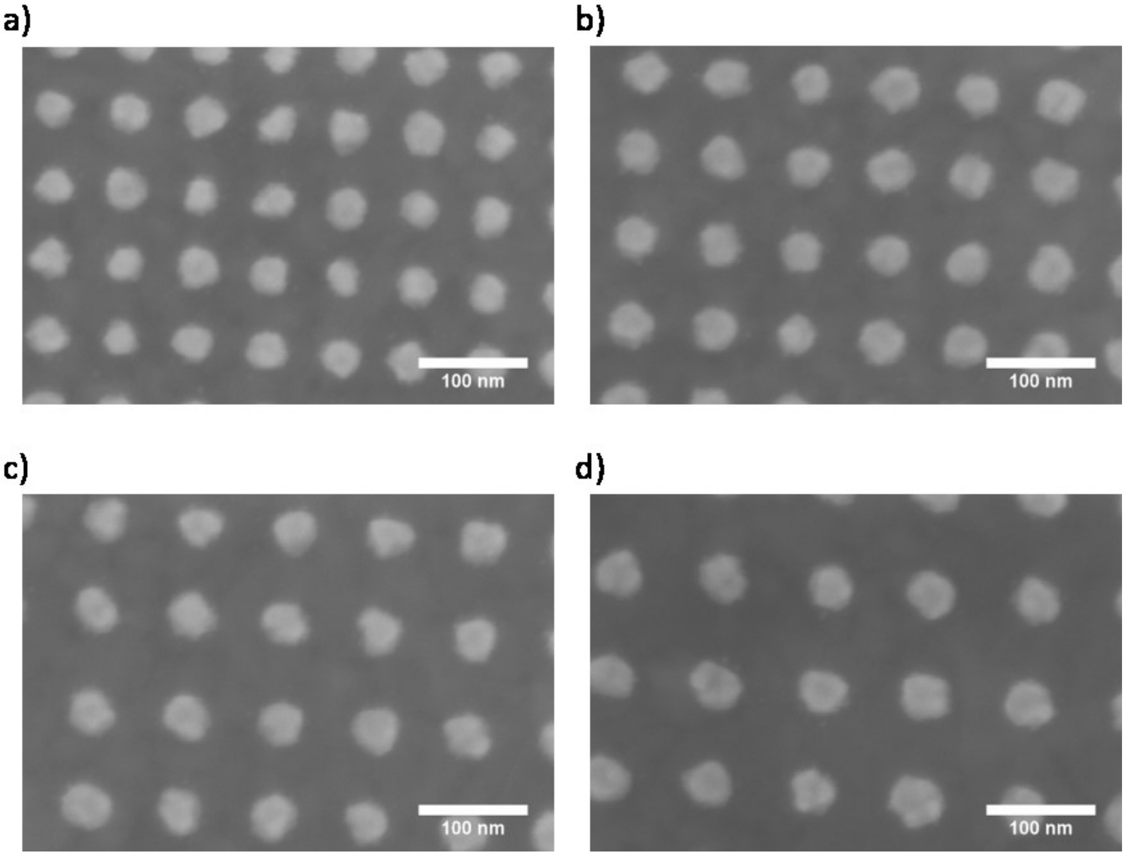

Figure 4-5. Pillar arrays using e-beam lithography. Different pitches with similar pillar diameter can be fabricated using the scattering of electrons and the proximity effect. The pitches are a) 70 nm, b) 80 nm, c) 90 nm, and d) 100 nm.

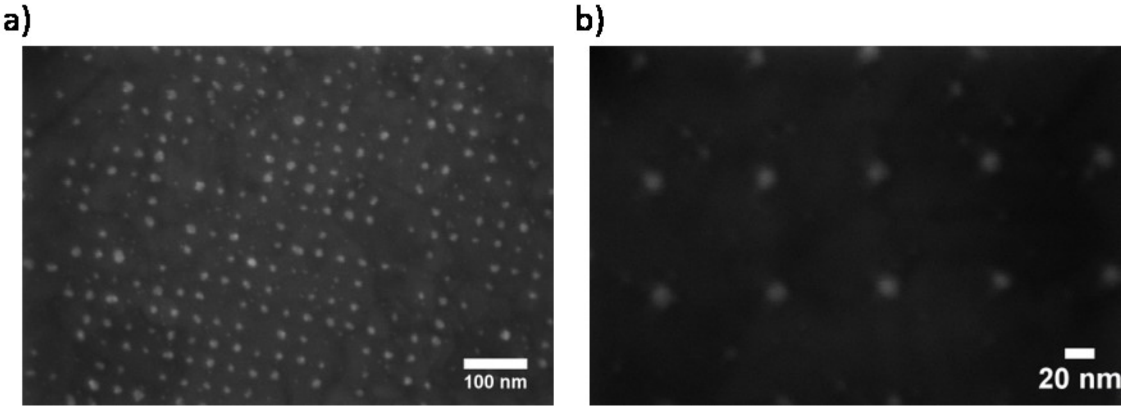

Figure 4-6. Highest pitch achievable on the CABL system is 30 nm centre to centre, figure a). This could be improved by tuning the thickness of the resist. Highest resolution for width is in the 10 nm range, with a pitch down of 50 nm, 80 nm pitch shown in figure b). The limitations of this protocol are also affected by the substrate having a rough surface (evaporated gold).

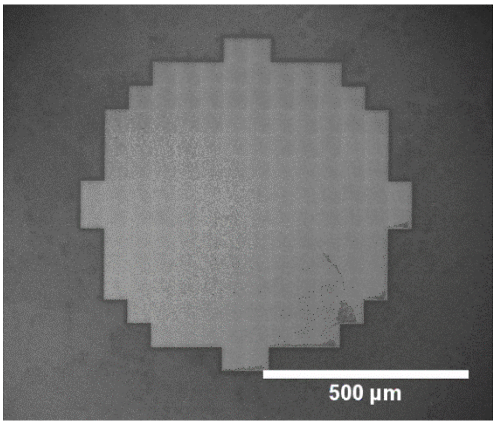

Figure 4-7.Pattern to use on HFFQCM resonators using proximity effect patterning. This result is that of a standard Si wafer coated with Ti (5nm) and Au (95nm). The deposition on the patterning is 43 nm of Au using thermal evaporator.

There were some technical difficulties during the fabrication of these samples. In terms of the process the first problem is the proximity effect on the edge of the whole pattern. This can be seen in Figure 4-8; the edge has narrower pillars, figure b), compared to the rest of the pattern, figure a). This could be corrected computationally but the software was not installed in the CABL system. Given that it is only a few microns where the pillars are narrower, and that they are closer to the edge of the electrode where the sensitivity is smaller, this effect is not considered a problem for protein sensing in the QCM. Furthermore, the stitching of different fields at 60 um FS is precise so only a narrow space between fields is left without pillars (160 nm) keeping constant the proximity effect in neighbouring fields.

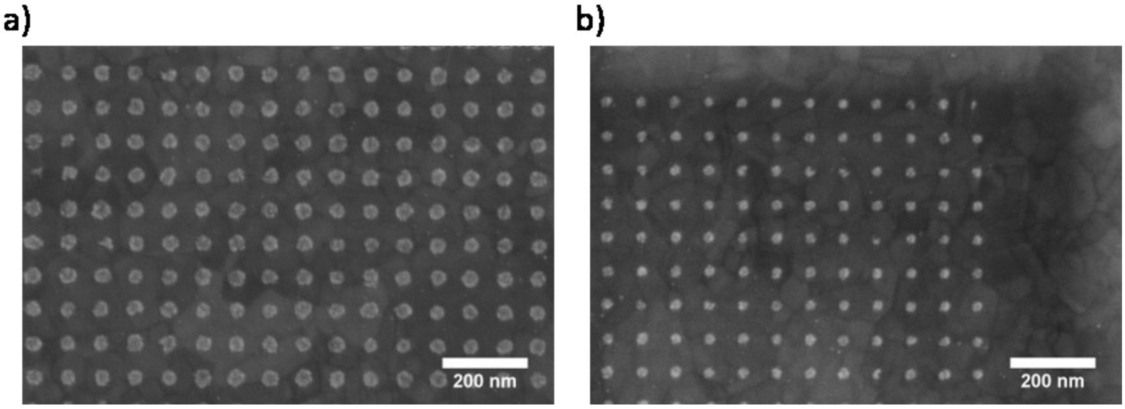

Figure 4-8. Proximity effect on an array with 60 um field size. Figure a) shows the array at the centre of the field and b) at the corner having pillars with smaller diameter.

The pattern of Figure 4-7 was applied to the electrode of HFFQCM. One of the first results can be seen on Figure 4-9. An SEM image of the final sample was not taken, as this could contaminate the surface with carbonaceous depositions given by the “black box” effect of the SEM.

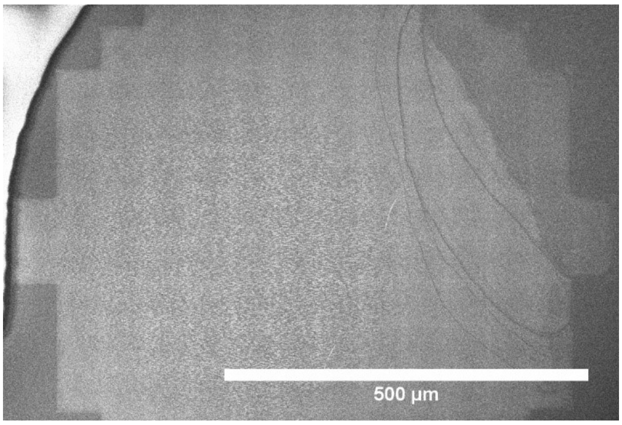

Figure 4-9. Example of the look of a pattern on top of the HFFQCM electrode. This initial sample had issues with the resist thickness evenness. Final sample of HFFQCM-NS was not imaged at this scale due to concerns of contamination.

To reduce the amount of contamination, only zoomed in images of the centre of the pattern were taken, see Figure 4-10. Image analysis of the sample showed pillar diameter of 42.70 ±1.12 nm. The sample had a clean lift-off. Afterwards, the sample was pasted using silver epoxy to a PCB that would fit in the HFFQCM Chamber of the AWS-20 system.

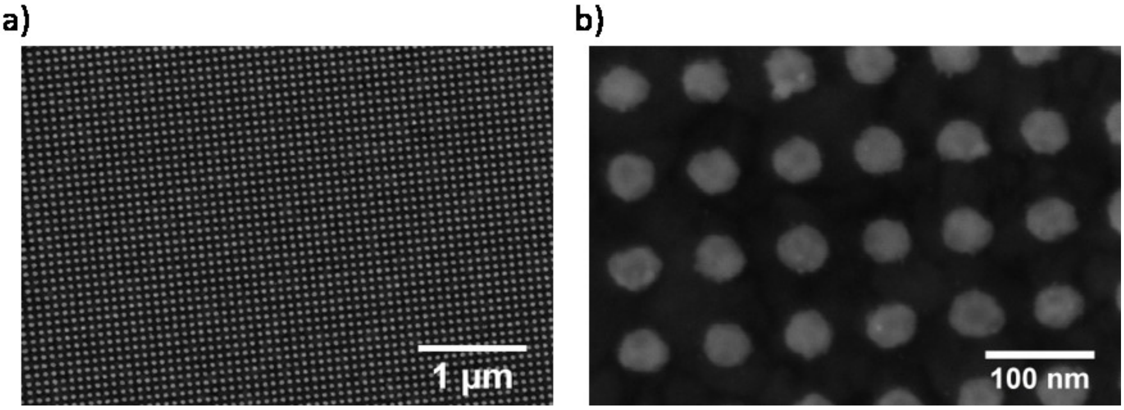

Figure 4-10. Nanostructures on top of the final HFFQCM-NS. The features are spaced 80 nm apart and have 43 nm diameter. Au thickness of 43 nm was deposited using thermal evaporation at a rate of 0.4 Å/s.

Other types of structures were patterned to study the interaction of proteins with nanostructures, but it was left as a proof of concept for future work. Circular lines and straight lines are easy to make using the back scattering and proximity effect, see Figure 4-11. However, from these two options, only the straight lines are feasible on areas of 1 mm diameter electrodes. The circular lines can only be written on FS of maximum 120 µm using these principles. If the FS is bigger, the beam starts to distort because of the angle of incidence of the electron beam. The scattering process is affected on the edges of these FSs, leading to bigger features or no features at all. Additionally, the software cannot make circular lines with bigger diameter than the FS. The straight lines can be patterned with no problem as the software only requires stitching an array of the same design. These different geometries were fabricated but not used for protein sensing, they are further discussed in Chapter 5 for future work.

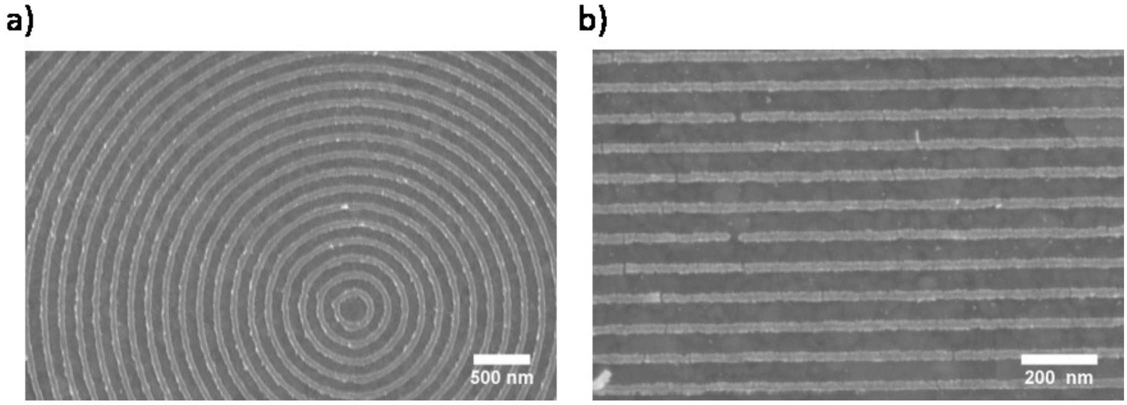

Figure 4-11. Circular lines a), and straight lines b) fabricated using e-beam lithography.

4.5 BSA Mass Measurements

To use the fabricated HFQCM-NS for biosensing, a solution of 100 μM BSA in PBS at 7.4 pH was run through the chip. The same conditions used for standard QCM and PTS QCM in the experiments of Chapter 3. The solution was flowed at a rate of 50 μl/ min and at a temperature of 25°C. The results showed that for a standard HFFQCM, the mass measured has similar values to those of a standard QCM resonator of 9 MHz under similar solvent conditions, see Table 4-2. Standard HFFQCM measured 701 ng/cm^2 of BSA. The mass measured by the HFFQCM-NS was 905 ng/cm^2, which is a 29.15% increase over the standard HFFQCM resonator. However, using the model from Section 2.6.4, the expected increase is 53%. Although this experiment is like the one with nanoparticles of Section 2.6.6, the pH conditions of the PBS might have a different effect on the protein binding to the nanostructure. Despite this, the results are similar in terms of the observed increase of mass compared against the modelled area increase; both have a fraction of the expected mass increase, 29.15% (0.54 of the expected mass) for HFFQCM-NS using PBS at 7.4 pH and 36% (0.68 of the expected mass) for QCM-NP using HPLC water.

Table 4-2. Mass measurements of BSA with standard HFFQCM and HFFQCM with nanostructures. For comparison, the table also presents the results from previous chapters for a standard QCM and those of PTS QCM. All samples had the same experimental conditions.

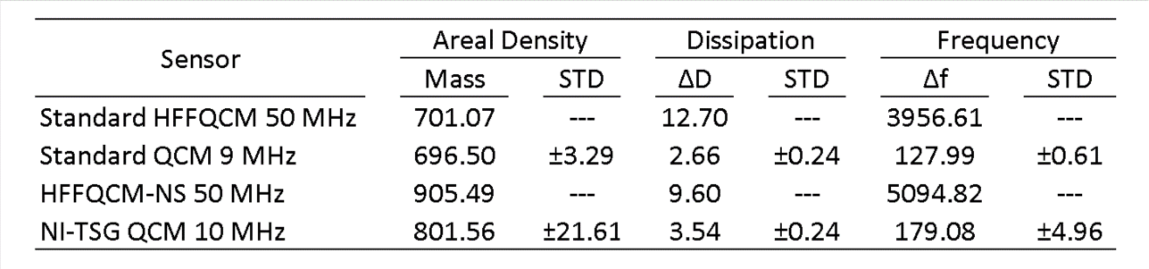

Sensor	Areal Density		Dissipation		Frequency	
	Mass	STD	ΔD	STD	Δf	STD
Standard HFFQCM 50 MHz	701.07	---	12.70	---	3956.61	---
Standard QCM 9 MHz	696.50	±3.29	2.66	±0.24	127.99	±0.61
HFFQCM-NS 50 MHz	905.49	---	9.60	---	5094.82	---
NI-TSG QCM 10 MHz	801.56	±21.61	3.54	±0.24	179.08	±4.96

The frequency response to the mass adsorption for both sensors is shown in Figure 4-12. Both curves show no significant difference except during the section of protein desorption of the curve. It slows the detachment of BSA on HFFQCM-NS before reaching equilibrium. There was also less dissipation on HFFQCM-NS, although this is not conclusive, it shows that the behaviour of proteins around the nanostructured surface has two effects. Firstly, the water surrounding the nanostructures do not increase the energy lost on the resonator, meaning that the water is not stagnated. Secondly, the protein is having a conformational shape change due to the less energy lost. Hydrated proteins on a monolayer will induce more energy loss (higher dissipation). In the HFFQCM-NS, BSA might flatten out during the deposition on the nanostructures and have less hydration in between proteins. This experiment shows that the interaction of BSA on nanostructures is similar to the interaction with the nanoparticles. The precision of the fabrication method helps to reduce the amount of repetitions and shows that it would be possible to fabricate nanostructures with semiconductor techniques.

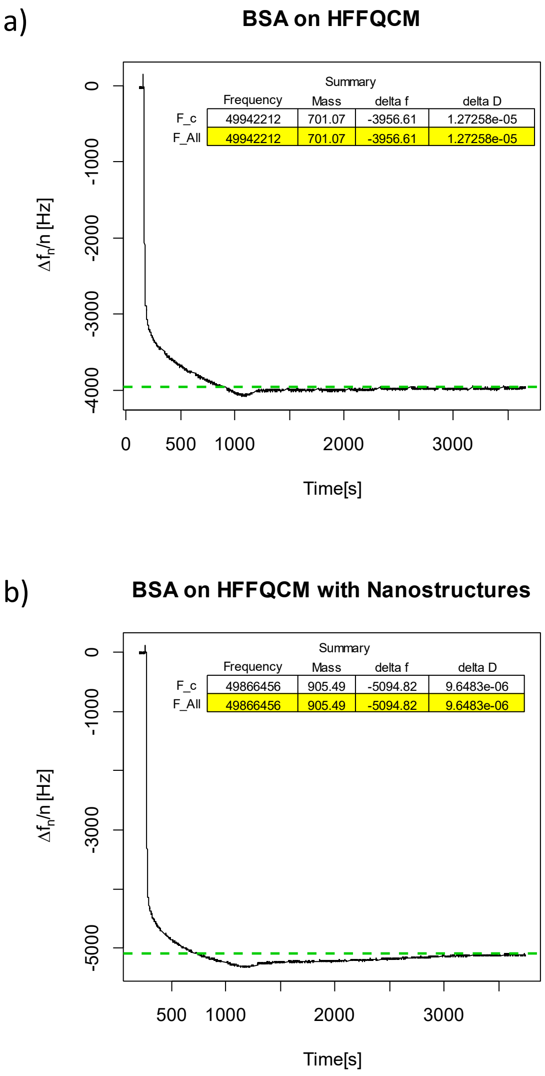

Summary

	Frequency	Mass	delta f	delta D
F_c	49942212	701.07	-3956.61	1.27258e-05
F_All	49942212	701.07	-3956.61	1.27258e-05

Summary

	Frequency	Mass	delta f	delta D
F_c	49866456	905.49	-5094.82	9.6483e-06
F_All	49866456	905.49	-5094.82	9.6483e-06

Figure 4-12. BSA measurements using a) standard HFFQCM, and b) HFFQCM with nanostructures of 43nm diameter and 43 nm high. A monolayer of BSA is expected on both surfaces. The protein was prepared in 7.4 pH phosphate buffer saline solution.

4.6 Results

EBL is a versatile technique that can be used to fabricate precise nanoscale features on surfaces. It is showed in this chapter how EBL can be use on HFFQCM resonators of 1 mm diameter electrode. A protocol is presented in order to achieve high resolution patterns of <10 nm and a strategy to create these patterns at a faster speed and with controlled diameter. The HFFQCM-NS was capable of sensing BSA adsorption without affecting the stability of the resonator (drift) or attracting bubbles to the electrode.

The adsorption of BSA mass on HFFQCM-NS is reduced compared the available area provided by the features. This result agrees with the observations in Chapter 2, Section 2.6, where nanoparticles showed similar reduced BSA mass adsorption. This experiment can further be tailored to observe for protein adsorption under different variables of the features, e.g. smaller or bigger features, or changing the spacing.

4.7 Conclusions

Patterns of nanostructures fabricated with EBL on a surface are believed to make the BSA spread during the adsorption in a similar way to the surface of nanoparticles in a surface or a solution. Although NP are easier to use and do not require sophisticated machines, the EBL can be used for a precise study of the behaviour of proteins on nanostructures. This technique can be further applied using a nanoimprinter instead of EBL for each sample, which can scale up the fabrication. The results being similar to nanoparticles leads to believe that the change on the protein is an effect of the size of the feature, the overall volume, and it requires further investigation to precisely find the main parameter causing this change. This experiment, a pillar of 43 nm height and 43 nm in diameter have similar results to 43 nm diameter nanoparticles.

The mass increase by the nanostructures is not a 1:1 ratio to the area increase on the patterned surface. Only 54% of the expected mass increase was obtained. Still, this can be used to increase the range of mass detection of resonators with limited area like the HFFQCM. This experiment showed that the mass on the nanostructure has a smaller surface density than the underneath surface. This result is contradictory to other findings like those of Malmström *et al* [112] where they obtained a higher surface density on fabricated gold nanopillars using colloidal lithography, The reason might be that the underneath layer is SiO_2, which might have an effect on the proteins binding to the pillars. Additionally, the geometric values are 124 nm diameter and 22 nm height.

This initial experiment can further be explored by changing the pitch of the pillars and observing the increase of mass accordingly. Another experiment that can be explored is varying the diameter and height of the pillars, to observe at which geometric volume the proteins changes its shape in terms of the mass measured compared against the expected increase. One further experiment is using different layers of materials on the pillar, the use of different materials might have and induced effect on the protein denaturation as proteins have different groups that might be exposed under different environments.

Chapter 5

Thesis Summary and Future Work

5 Thesis Summary and Future Work

5.1 Summary

Using nanostructures on QCM resonators proved that there are some differences of BSA mass adsorption depending on the features of the surface of the electrode. The fabrication of an atomically flat QCM electrode, using PTS QCM, showed that the BSA highly packs as a monolayer. The hypothesis is that by having a flat surface which has a uniform charge distribution, a BSA protein will be adsorbed and its dipole will orientate normal to the area of deposition. The subsequent neighbouring protein to adsorb, will attach next to it in the same manner, see Case B in Figure 5-1. Consecutive proteins will do the same and their dipole will orientate normal to the surface having an even charge on the surface. The PTS QCM showed grains with big diameter, and sometimes the boundaries were even difficult to define. Grain boundaries might have an effect on the protein orientation, especially if these steps are receding from the zero-height position on the surface. The small number of grain boundaries, and the size of the steps and shape, might not affect the BSA binding to the surface in a self-assembled manner for PTS QCM resonators. In the case of a low roughness sample Case C and D in Figure 5-1, the BSA might adsorb at an angle because of the irregular surface and feature charge distribution. As mentioned before, a receding step might orientate the charge distribution of the protein at an angle normal to the grain surface. When this occur, the next protein might be screened due to the polarisation in that region and might have to bind farther from the initial protein. The higher this roughness scale is in comparison to the protein, the more the charge distribution might be perceived by the protein. It is also believed that small grains might affect this as the surface charge perceived by the protein might be a combination of several grains. This reorientation will create a monolayer with less BSA mass per area, see Case C and D in Figure 5-1 where the same amount of protein is depicted as adsorbed on two different surfaces. It was observed that if the surface reaches a certain higher roughness, the protein adsorbed next to the surface denatures and induces monomers to aggregate, see Case E in Figure 5-1. Conformational shape changes are also proved by using NPs or nanopillars on the QCM electrodes. The nanofeatures are expected to increase the area were mass could be accreted, however the mass measured per area is a fraction of the expected mass increase once the area is normalised, see Case F in Figure 5-1. This behaviour might be different to Case E and can be explained with the following hypothesis: BSA adsorbs to the NPs in a different way that it would adsorb to the rough sample or a flat sample. It is believed, that because of the charge distribution on the NP, the protein tends to change its conformational shape once it is adsorbed to its curved surface, covering more area and screening other BSA molecules to bind to this surface. Although this hypothesis is not proven with another technique on this dissertation, the mass measured by the QCM showed an increase of the mass due to the additional area for deposition by the NP but less than the theoretically expected. The reason this might be happening is that the NP charge distribution on the sphere might be different than that of a flat surface or at the steps on grains. This could be further investigated to find out what is the cause of this different

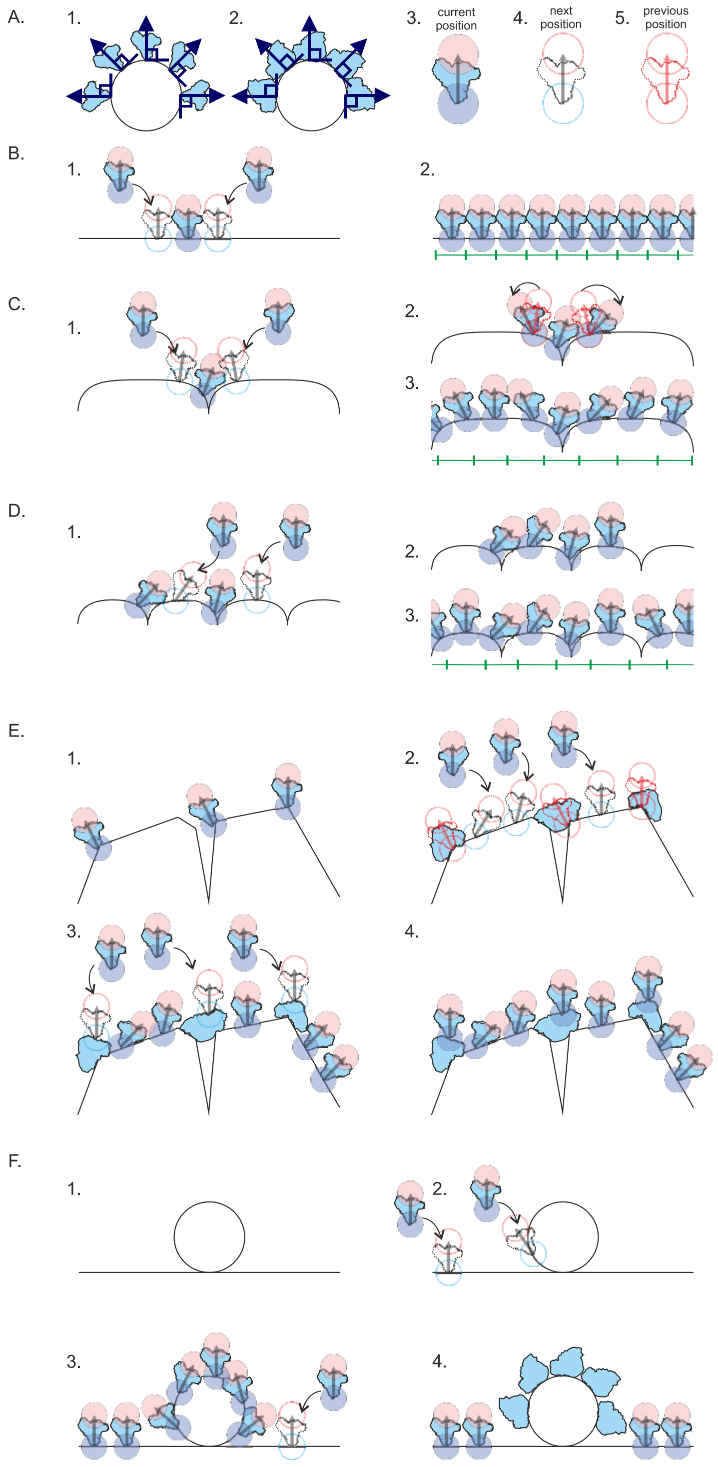

Figure 5-1. Representation of BSA adsorption to different surfaces. In Case A, a model for adsorption of BSA to NPs by keeping the monomer structure intact (A.1) and spreading (A.2). A.3, A.4 and A.5 show the legends of BSA monomers used in the Cases B-F. In Case B, BSA adsorbs as a tightly packed monolayer on an ideal flat surface. In Case C, the presence of grains changes the angle of adsorption of BSA. Case D represents Case C but with more grains but allowing the same number of monomers to adsorb per area. Case E shows that high roughness denature some proteins inducing aggregates. In Case F protein adsorbs to NPs on a surface, with less proteins adsorbing on the NPs, possibly by monomer spreading.

behaviour. In summary, a flat surface (the baseline) packs the maximum possible monolayer of BSA, increasing a little the roughness as found on those electrodes from resonators of different companies leads to a reduction of mass in the monolayer caused by protein reorientation. After a certain increase of roughness (a threshold) like the surface obtained from the built-in-house resonators, the proteins start to change its conformational shape such that induces other monomers to adsorb on certain points of the surface. If a nanostructure is built like the nanopillars, the protein denatures such that it spreads and reduces the area available for adsorption but without inducing aggregation. The NPs have the same diameter as the grains of the evaporated electrodes, however as they are freestanding the charge distribution might be different compared to the grains that are in bulk. It would be interesting to find at which point the geometrical landscape denatures the protein such that it goes from spreading to inducing protein aggregates, but this is left for future work.

5.2 Analysis of QCM surfaces inducing multilayer deposition.

One of the final experiments of this dissertation showed a multilayer deposition on top of QCM resonators with an electrode being evaporated at the Nanoscience Centre. This was an unexpected result. Further analysis is shown in this section and could also be continued as a future project. The summary of the result is as follows: for the monolayer adsorption of BSA on gold surfaces, four different QCM samples were used. The first sample was a standard QCM resonator from QuartzPro with the AFM image of the surface before adsorption shown in a) Figure 5-2 and values of roughness on Table 5-1). The second sample is an HFFQCM resonator purchased from AWSensors. These two samples have similar roughness values and showed similar mass measurements, see b) in Figure 5-2 and Table 5-1. The third sample was a blank QCM resonator purchased from AWSensors with the electrodes deposited at the Nanoscience Centre, see c) in Figure 5-2, and Table 5-1. The final (fourth) sample was a PTS QCM resonator, see d) in Figure 5-2, and Table 5-1. The third and fourth samples gave different results to purchased standard QCM.

The QuartzPro and HFFQCM resonators showed expected, monolayer, mass deposition of BSA. The QCM with deposited electrodes and the PTS QCM had a higher mass adsorbed. Still, the PTS QCM gave a monolayer as showed by liquid AFM imaging, see Chapter 3. The increase of mass of QCM with deposited electrodes (labelled as Nanoscience Centre) was due to the presence of a multilayer on the surface; also proven by liquid AFM. This extra mass was unexpected as previously purchased resonators did not show this result. This required to traceback the surface of each resonator before BSA adsorption, Figure 5-2. The samples used for the measurements were from the same batch for each type of resonator, therefore these surface measurements are expected to be the same as those used for the protein measurement. The AFM images show the surface characteristics being different for each type. Both purchased resonators with a monolayer have almost identical step height on the grain boundaries, see scale bars in Figure 5-2. Their RMS is near 1 nm, see Table 5-1. The grains can be taken as a nanostructure similar to a NP affecting the behaviour of the protein adsorption. However, these two resonators did not affect the adsorption of the protein such that it induced a multilayer. As previously discussed, it is theorized that the lower mass monolayer adsorption is caused by the orientation of the BSA on the surface. Having flatter grains, the angles of the protein during the adsorption change only where there are steps with a high inclined plane. The grains are also smaller in diameter, this will increase the number of proteins not at a normal angle to the overall surface. These proteins will eventually screen the neighbouring area for another protein to bind, creating a longer distance between proteins. Therefore, the monolayer will be less packed, giving a mass measurement lower than an ordered BSA monolayer. The scale of these grains is not affecting the BSA adsorption such that it induces a multilayer adsorption.

Dissipation is a crucial element for certain experiments. However, in the work presented here, values of dissipation were small such that it will not inform from any change on the monolayer or drastic conformational shape change (e.g. unfolding or elongation of the protein). The values of dissipation have been presented throughout this work, but with their small values compared to the change in frequency, the BSA layers adsorbed to all resonators are considered a hard coating (no substantial unfolding of protein). This means that the rearrangement of the protein (spreading, reorientation) do not affect solvent adsorption on top of the coating, this for example will increase on a completely unfolded protein. Therefore, BSA adsorbs and orientates without changing much of its heart-like shape maybe spreading a bit as mentioned before but not obtaining a higher hydrated shell. Dissipation plots can be seen in Figure 5-3.

The atomically flat surface of the PTS QCM showed that more mass can be adsorbed on the surface without affecting the monolayer but in a more packed order. This is believed to be caused by the BSA adsorbing at normal angles on the surface. Having very small steps and grains with diameters 25 times larger than purchased resonators, the possibility of proteins adsorbing at variable angles is minimum, making the BSA to have an adsorption behaviour resembling self-assembling. The surface of the built-in-house QCM resonator (labelled Nanoscience Centre) had bigger grains and deeper grain boundaries than those resonators purchased from a company. In this case, it is believed that the protein adsorbed such that it got denatured, exposing other possible groups that will induce more BSA binding; i.e. hydrophobic groups that might be inside the protein. The cause for this behaviour might be on this characteristic surface and might not be present in the other samples, this could be explored in future work by changing the surface characteristics and finding the values of the variables that start this behaviour. Those parameters are: grain size (diameter); grain boundary step; and, if possible, and radius of curvature of the grain (although most gains are crystal columns). This experiment has several challenges. First, the imaging of the surface by AFM previous to the protein adsorption must be precise. Super sharp tips of AFM might be needed to minimise the loss of image quality of the grains by the radius of curvature of standard tips. Second, good control of gold growth with different grain characteristic is going to be required. This can be accomplished by changing the angle of evaporation of the electrodes[16] or heating the sample during the deposition. Defining these characteristics is the main challenge of this experiment to reduce the amount of time invested. The most important question would be: what physical feature of the grains cause proteins to denature or expose specific groups?

Third, the analysis post measurements by imaging using AFM in liquid is going to be crucial to corroborate the behaviour of the protein adsorption (is it a monolayer or a multilayer?). Fourth, other techniques could be explored that can be used to detect the exposed groups on the surface like x-ray photoelectron spectroscopy. Finally, changing the experiment to a different protein could also help explain this behaviour in terms of protein plasticity.

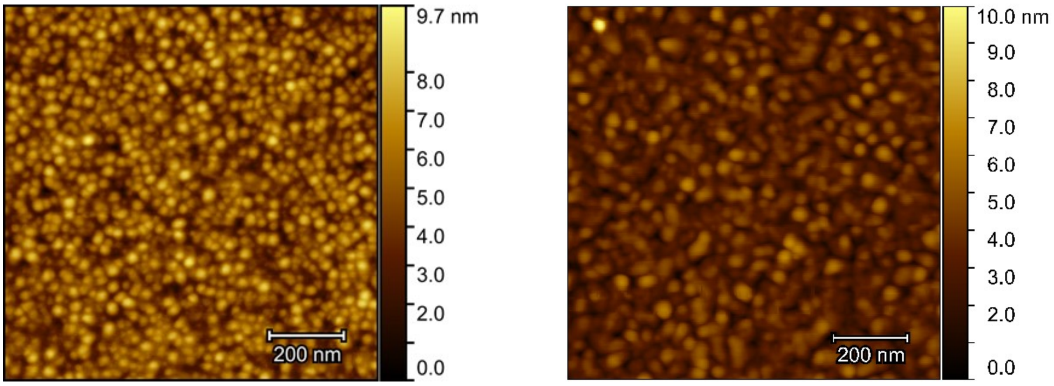

a) QuartzPro

b)AWSensors (HFFQCM)

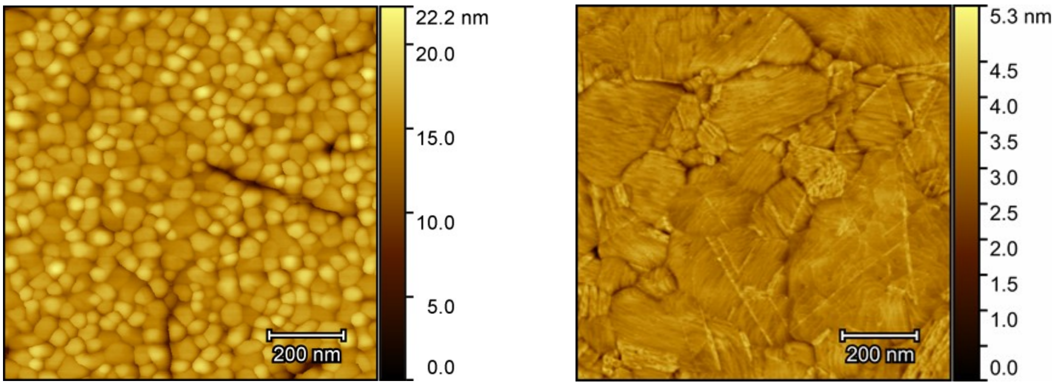

c) R-QCM Nanoscience Centre

d) PTS-QCM

Figure 5-2. AFM images of the surfaces of four different QCM resonators. The images are taken before a mass adsorption experiment of BSA. The bottom two surfaces measured more mass than on the top two samples. The sample from the Nanoscience centre had multilayers and the PTS sample showed a monolayer; both were validated by AFM in liquid. It is believed that this different behaviour is caused by the grain boundaries (steps of the grains), their size, or radius of curvature.

*Table 5-1.Grain characteristics of four samples with different mass measurements of the protein BSA. A multilayer was adsorbed on the electrode with highest RMS (sample label: Nanoscience Centre) and a tightly packed monolayer in the PTS gold sample. Both results were validated with liquid AFM. It is believed grain characteristics on the surface play a role to induce protein denaturation and hence multilayer deposition. *these samples were not imaged in liquid with AFM after protein adsorption.*

Sample	Roughness RMS [nm]	Grains	Mass Adsorbed	Coverage
		Diameter [nm]	Areal Mass [ng/cm^2]	
Regular Roughness (QuartzPro)	1.25	28 ±8	697 ±3	monolayer
Regular Roughness (AWSensors)	0.94	46 ±15	701 --	monolayer*
Rough (R-QCM) Nanoscience Centre	2.01	47 ±12	817 ±3	>monolayer
Ultra-Flat (PTS-QCM)	0.35	-- --	802 ±22	monolayer

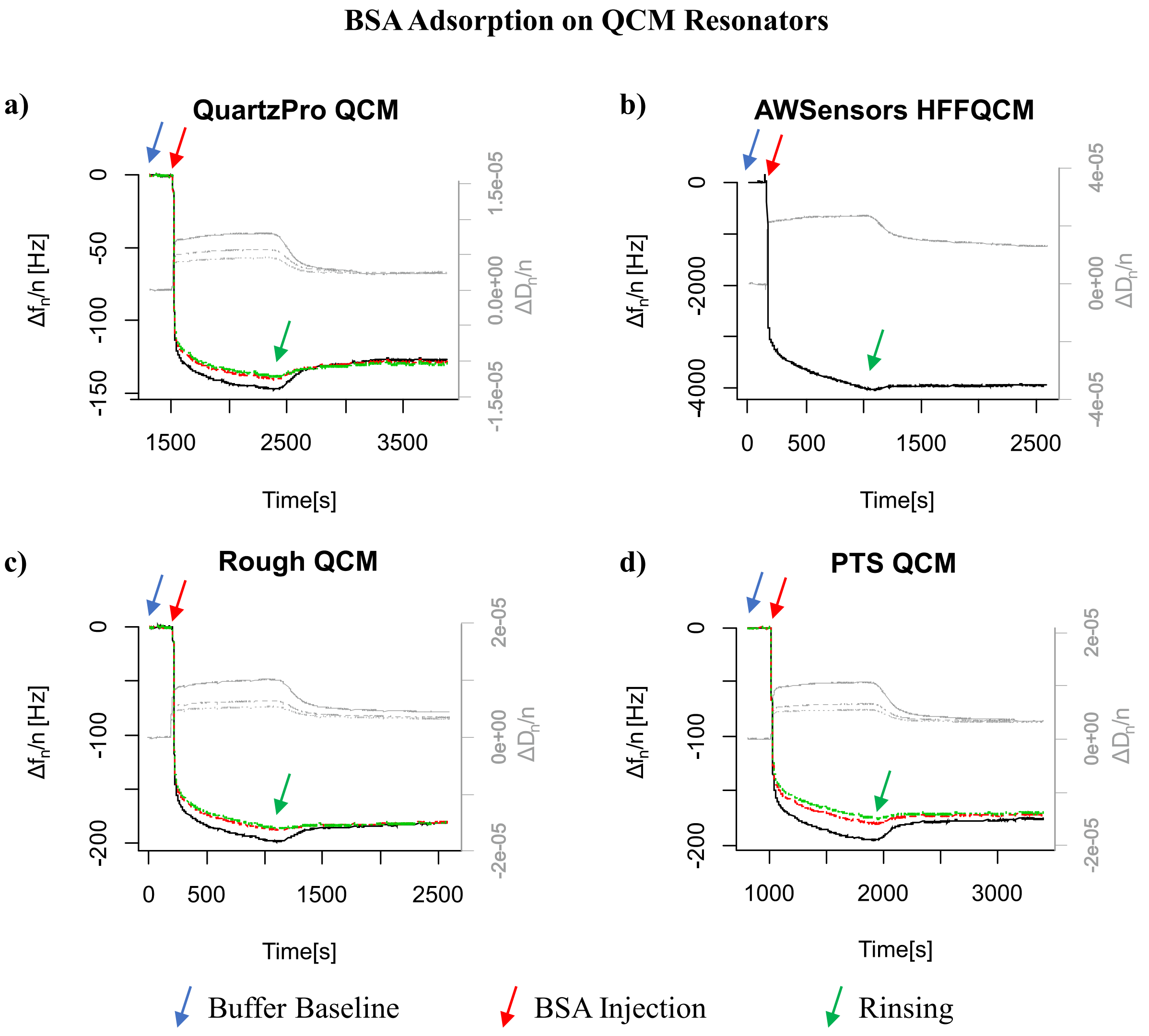

Figure 5-3. Summary of plots from Chapter 3 and 4 of BSA adsorption on substrates with different surface properties. The curves for dissipation (grey) are presented in this figure for 3 frequencies: fundamental, third and fifth harmonic. Dissipation is small and therefore the coating was considered rigid in all cases. The frequency response is depicted in the black curve for fundamental frequency change, the red curve for third harmonic and green for fifth harmonic. All electrodes had 100 nm thick electrodes. QuartzPro resonator (a) has a fundamental frequency of 9 MHz, AWSensors (HFFQCM) has a fundamental frequency of 50 MHz and the rough QCM and the PTS QCM have a 10 MHz fundamental frequency. The protein coating was assumed to be rigid as all results for dissipation fulfil the relationship $|\Delta D_n/(\Delta f_n/n)|<<2.2x10^{-7}$ *for* f_n*=9MHz,* $|\Delta D_n/(\Delta f_n/n)|<<2x10^{-7}$ *for* f_n*=10MHz, and* $|\Delta D_n/(\Delta f_n/n)|<<4x10^{-8}$ *for* f_n*=50MHz, as well as having similar values between them*[113].

5.3 Future Work

5.3.1 Nanocontact Chemical Printing

Besides changing the surface of a QCM resonator by adding a physical feature like nanoparticles, another interesting idea was to pattern different chemistries on the substrate. This idea was not fully developed but the initial results are presented here. The idea consists in controlling the amount of charge on a surface. The way this can be controlled relies on using a stamp that has been soaked in a chemical molecule. The stamp will transfer the molecule to the surface, and the molecule will pattern it using the design of the stamp. For example, using the pattern of Chapter 4 used in e-beam lithography, a stamp of an array of circles can be transferred. This method is recognised as contact printing, if it uses nanoscale features it would be called Nano Contact Printing (NCP). Current methods of fabrication for NCP relies on a PDMS stamp that is peeled off a silicon wafer template. This mechanical process destroys the patterns at the nanoscale, making it useless for large area applications. Using the knowledge acquired during the development of this dissertation an idea came to mind in collaboration with Edward Tan (Occhipintli's Group, at University of Cambridge). The idea is to fabricate high resolution features on a substrate using gold, followed by depositing a PDMS coating. Then, the substrate underneath the gold features must be etched, and the features will be embedded in the PDMS. If the substrate is etched, the PMDS would not be required to be peeled off, increasing the chances of the embedded features to stay in the PDMS. The substrate which gave the best etching without damaging the PDMS was aluminium. Films of Physical Vapor Deposited (PVD) Al usually have a very high roughness surface limiting the resolution achievable by this method, therefore by applying the TSG method to Al, a Template Stripped Aluminium (TSA) can be achieved. TSA aids in obtaining high resolution using EBL.

Both standard sputtered Al surfaces and TSA surfaces were compared for this experiment. Only TSA samples gave high resolution patterns. The experiment was as follows: high surface roughness on Al was created by low temperature sputtering, which gives a small nucleation and slow island growth, and most likely competitive growth of Al of different crystal orientations on SiO_2[114]. To eliminate this effect on the interfacial layer of the lithography process, it was applied the template stripped method[82] for Al. The adhesion of Al on muscovite mica is weak and this reason makes Al a good material for template stripping. The process is described in Figure 5-4. At step 1), Mica was mechanically cleaved to get a fresh clean surface just before the deposition of 150 nm thick of Aluminium via metal sputtering, step 2. Commercially available EPO-TEK 377 was used to adhere the exposed surface of the thin film of aluminium of the mica substrate onto a SiO_2 chip, as seen on step 3) and 4) and 5). EPO-TEK 377 has shown excellent resistance and low swelling against various solvents; acetone among them[82]. In step 5) the epoxy resin is hardened by baking at 180°C for 2 hours to fully adhere the Al to the wafer. Finally, the mica was mechanically stripped from the Al to get a flat Al surface (step 6 and 7).

The E-Beam Lithography (EBL) process performed on the TSA is detailed in Figure 5-5 and it is the same process described in the protocol of Chapter 4 Section 4.4.1.1. The protocol to embed the nanostructures on the PDMS is summarised in Figure 5-6 and it is as follows: 1) once the nanostructures of gold are fabricated on top of TSA, the sample is subjected to a silanisation submerging the substrate in 3-mercaptopropyl trimethoxysilane (MPTMS) solution to create a bond between Au and PDMS; 2) degassed PMDS was spin casted on top of the sample and cured at room temperature to avoid expansion of the PDMS; 3) the Al is etched using dilute hydrochloric (HCl) solution, releasing the PDMS with the embedded Ti/Au nanostructures;4) soaking the stamp with a chemical to be transferred that is selective to the PDMS or to the Ti/Au can be used; 5)the chemical coating of the PDMS can be stamped on another substrate; 6)the final surface has the chemical groups on the patterned area. This method can have further steps like filling up the area that was not stamped with a chemical of a different charge, or hydrophobic chemistry instead of hydrophilic.

The resulting flat aluminium was characterised by Atomic Force Microscopy (AFM) and compared against standard sputtered Aluminium on SiO_2. The analysis shows that the standard sputtered Al has a roughness of 9.6 nm RMS and TSA 0.121 nm RMS. In perspective, the sputtered Al has the biggest grain with 300 nm diameter and 75 nm height against the lowest point on the imaged surface. If a thin film is deposited on the rough sample, there might be imperfections on the EBL pattern. Additionally, the big steps will make the stamp fail to transfer high resolution patterns as the deposited gold might not be in proximity to the target surface when it is stamped. In contrast, the flat Al has a peak to peak value smaller than 1 nm at any point on the analysed area and would not affect the stamp when pressed against the target substrate.

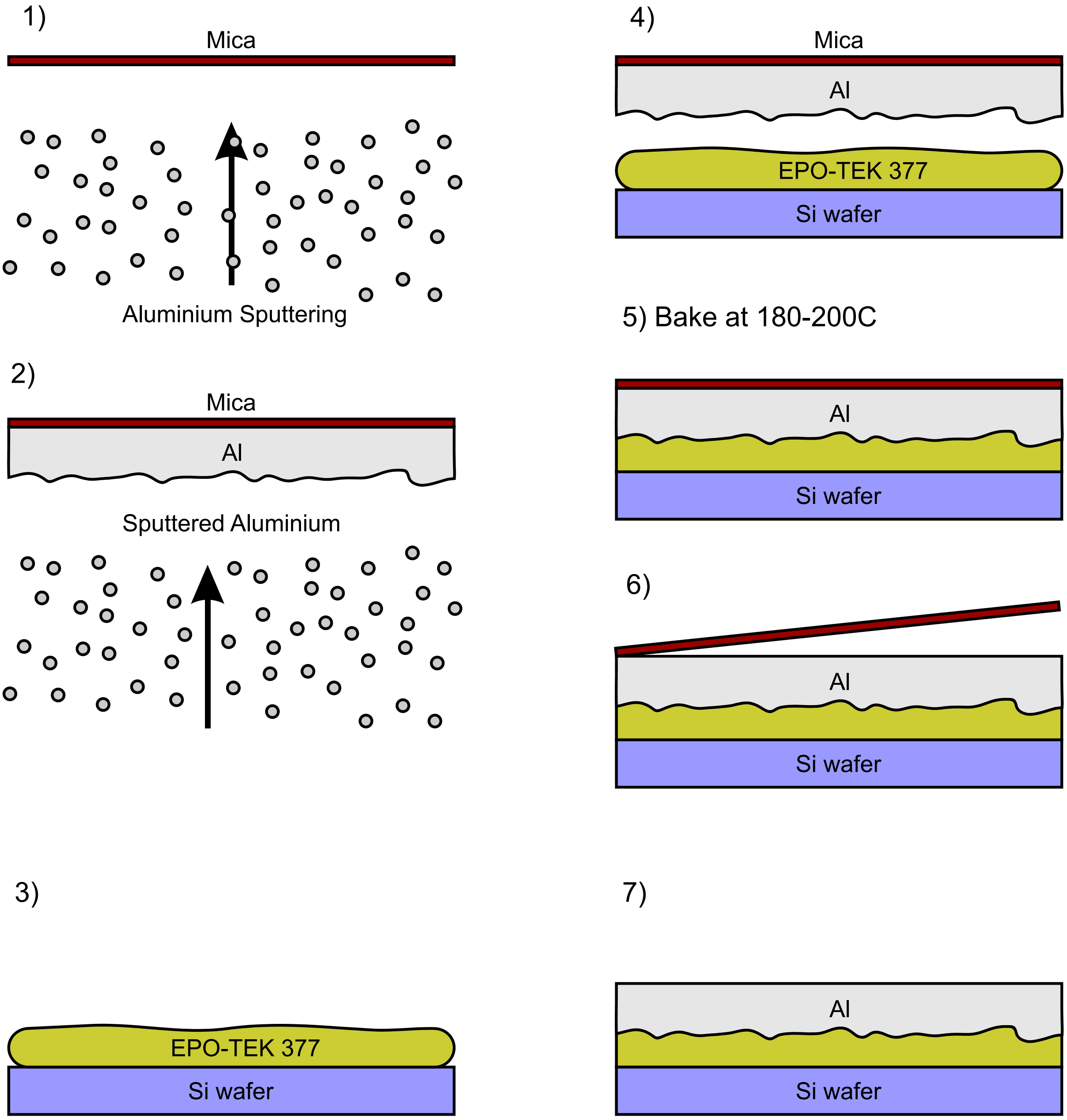

Figure 5-4. Fabrication steps of Template Stripped Aluminium (TSA). This is the standard procedure to obtain smooth surfaces of aluminium. In the first step, muscovite mica is cleaved, it is followed by sputtering it with 150nm of Al at step 2. In step 3, an epoxy glue (EPO-TEK 377) is drop casted on a Si wafer, this can also be performed on top of the Al. In step 4, the mica-Al and Si-EPO-TEK 377 is sandwiched together. In step 5, the sample is placed in an oven, standard quick baking procedure is 180 °C for 2 hours. In step 6, the mica is stripped from the weak attachment to the Al, leaving an atomically flat surface of the Al in step 7.

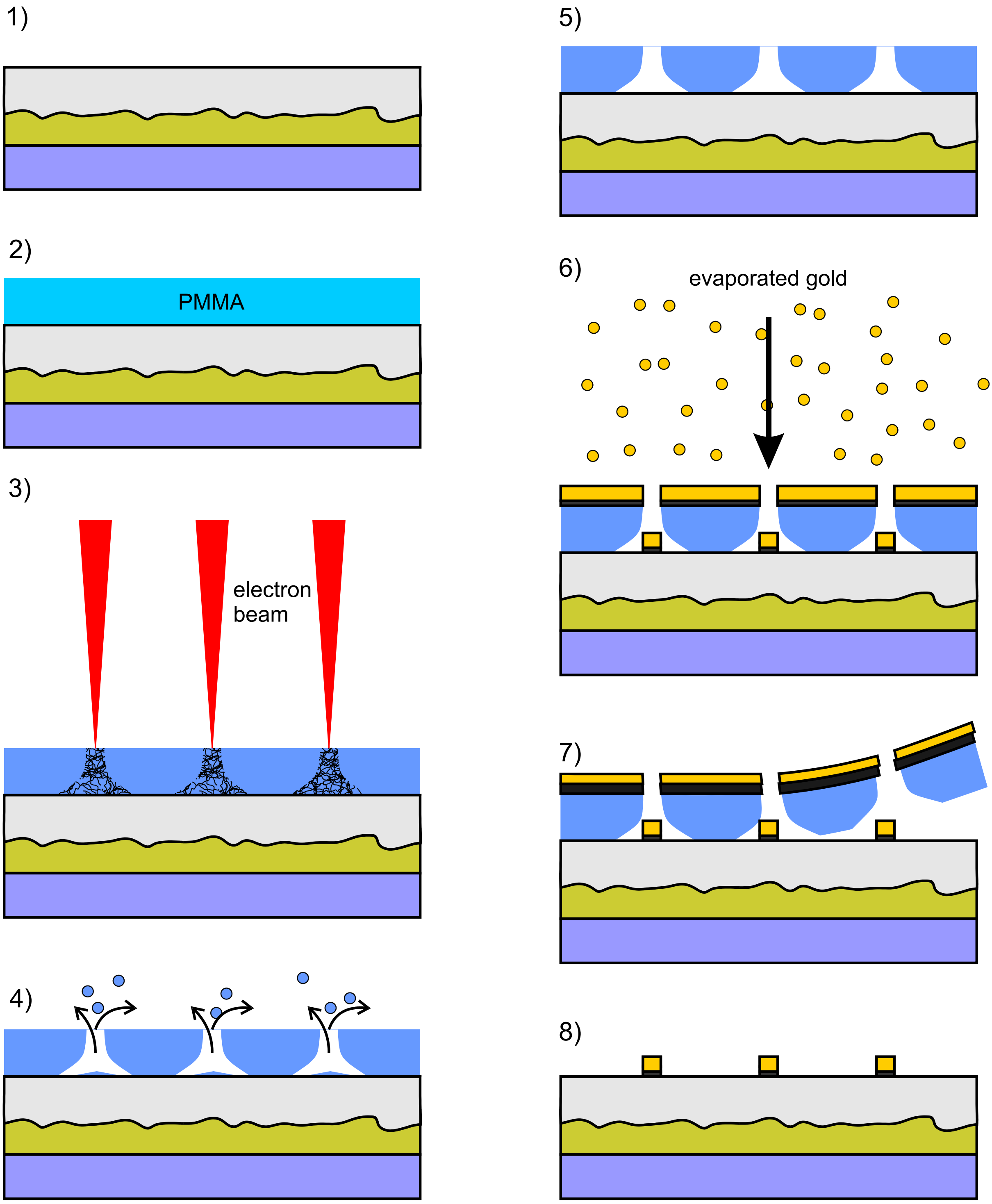

Figure 5-5. The Template Stripped Aluminium (TSA) can be used for high resolution E-Beam Lithography (EBL). Normal sputtered Al samples give a very rough surface making the spread of the resist uneven and limiting the resolution. The process starts with the TSA sample in step 1. PMMA is spin coated and baked in step 2. EBL is performed on the sample in step 3. In step 4 the sample is developed. In step 5 the sample is rinsed and dried. In step 6, Ti and Au is evaporated on the sample. In step 7, the resist is removed by lift-off using acetone. The sample is ready in step 8.

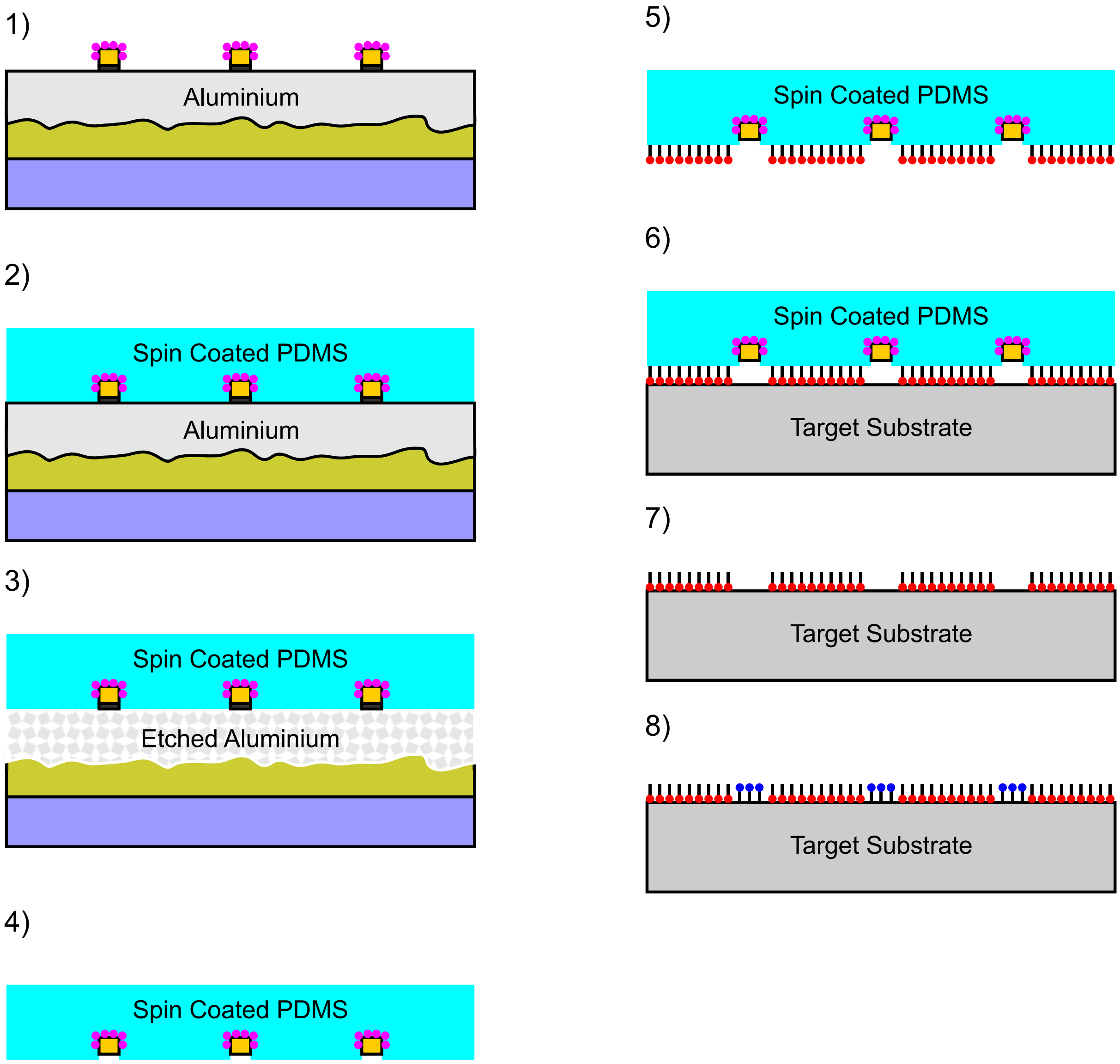

Figure 5-6. Nanocontact printing fabrication process. From Figure 5-4, sample is coated with 3-mercaptopropyl trimethoxysilane (MPTMS) to create a stable bond between gold and PDMS, see 1). In 2) PDMS is deposited on top of the sample and left for curing either at room temperature or at 80 degrees for 2 hrs. Sample is immersed in dilute hydrochloric acid (HCl) solution as depicted on 3). PDMS stamp is released in liquid solution as shown in 4) and fished. Sample is coated with a chemical selectively bonding to PDMS and not gold as in 5). A previous step can be performed where the stamp selectively binds a chemical to gold to screen the chemical bonding of step 5), e.g. a thiolated chemical compound. Sample is used as a stamp as in 6) and transferring the chemical compound from the PDMS to the target substrate as in 7), Finally, another chemical compound can be used to chemically bound to the empty areas of the target substrate as depicted in 8)..

The roughness of sputtered Aluminium can be seen in Figure 5-7, a). When the same evaporation is performed on a mica substrate, and the TSA method is used, the roughness of Al decreases considerably. The flatness of Al is even better than those values of TSG. When a pattern is fabricated on top of TSA, the resolution achieved by EBL is around 20 nm features spaced at 80 nm distance centre to centre. A final sample of an NCP stamp can be seen in Figure 5-8. This resolution might be taken even further if the process is optimised. This method was used for embedding metals on PDMS for gas sensing, for further details please see Tan *et al*[21].

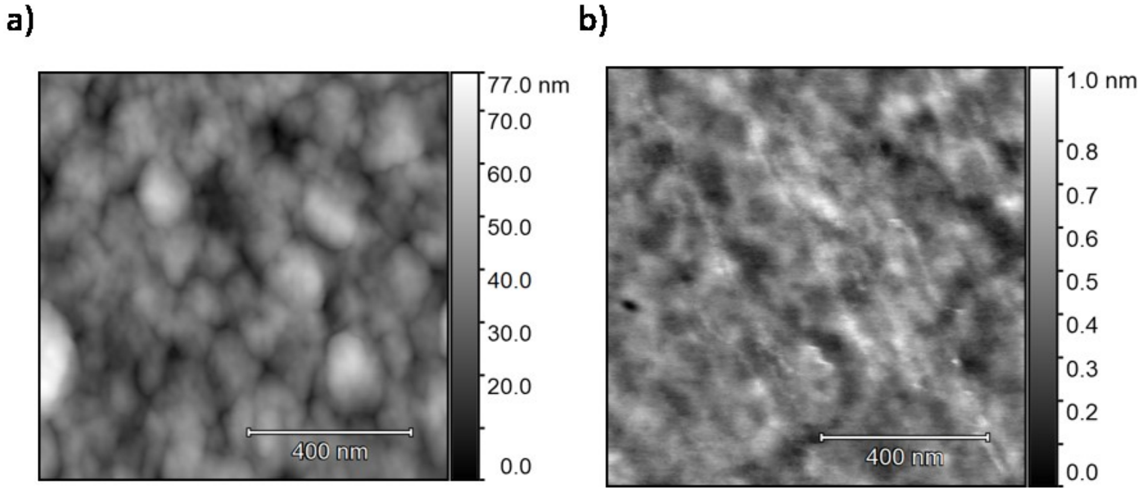

Figure 5-7. The nanocontact printing method requires a sacrificial layer, in this case aluminium. Figure a) shows standard sputtered aluminium on top of a Si wafer. Roughness of this sample is 9.595 nm RMS. The grains on this surface are big. The grains can be up to 70 nm height and would be difficult to fabricate nanostructures on top of it. A solution was presented using template stripped aluminium, figure b). The roughness is 121.8 pm RMS, with a maximum range of features of 1 nm.

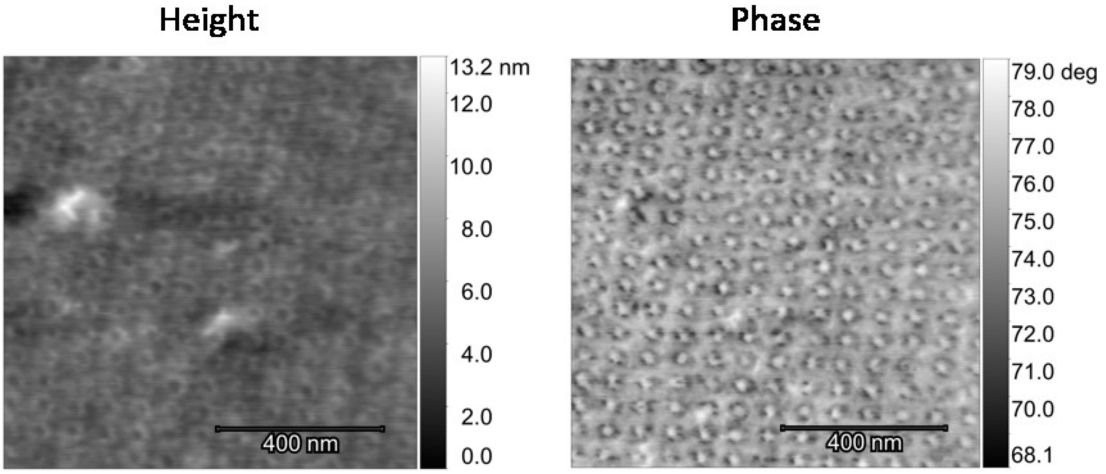

Figure 5-8. Au features embedded on PDMS for nanocontact printing. Figure on the left side shows the topographical image where features are slightly visible. On the right side, the features can be located using the phase of the AFM image, showing the presence of Au on the compliant polymer.

The use of NCP requires more knowledge of chemistry to find out the combination of molecules for the chemical pattern transfer. Further optimisation might be required to obtain a proper nanoscale transfer. The gold embedded on the PDMS helps for the compliance of the PDMS while stamping and at the same time the Ti can be chemically treated to be specific for a particular molecule which will not interact with the PDMS, or *vice versa*.

5.3.2 Variations of Geometry, Size, and Distance of Nanostructures

The study of protein adsorption on nanostructures in Chapter 2 and 4 was performed using a particular size of nanofeatures. It was selected the 43 nm diameter for NPs and pillars. This parameter should be varied to analyse when does the protein adsorption is affected by the physical structure. Although the conclusions showed that the increase of BSA mass was adsorbing linearly with the increase of density, it is expected that at a specific dimension the protein might behave different or will not detect the nanostructure. This hypothesis was reached after observing BSA was adsorbing as multilayers on a rough grainy QCM gold electrode. For the pillar nanostructures, the pitch, diameter and length could be varied to look for the change of conformational shape. Besides pillars or NPs, using walls might affect how protein binds to the QCM. This experiment could show how the flow at the nanoscale affects protein adsorption. The QCM resonates more in a specific direction (*x*-axis of the crystal). Therefore, as an initial experiment, the creation of lines along or against this direction will help to observe if there is any effect.

5.4 QCM and Liquid AFM for proteins forming a monolayer

This project showed that a monolayer of BSA forms differently on an atomically flat QCM than in a grainy standard QCM electrode. There are more proteins to explore and analyse for this type of behaviour. BSA electrostatically attaches to gold and the introduction of a linking molecule for other proteins might also contribute or screen the behaviour of the roughness on protein adsorption. It is proposed to explore the use of linking molecules like antibodies to observe for different screening effects and the effect of roughness on their adsorption. This experiment would be important as many biosensors use linking molecules to detect a particular protein.

5.5 Conclusions

The main aim of this dissertation was to observe for protein interaction with nanostructures. This work has shown the amount of BSA mass adsorbed onto increasingly rough electrodes among atomically flat, standard roughness, rough, and nanostructured surfaces. The techniques and protocols created for this work allowed for the first time, simultaneous measurements of BSA monolayers on atomically flat gold (0.35 nm RMS), showing a tightly packed monolayer by both QCM mass measurement and topography by liquid AFM. In contrast, the standard gold surface which has a higher roughness (~1 nm RMS) measured less mass. However, increasing the roughness (~2 nm RMS) and hence the available area for adsorption (4.5% more) showed a higher increase of mass adsorption (17%) compared to standard gold. It has been previously suggested by other authors that mass increase on rough surfaces is due to conformational changes of the protein but it has not been clear if the cause was unfolding of the protein (elongation) and therefore more molecules per area or if this is caused by aggregation of monomers. It is shown in this work that the cause of this mass enhancement is caused by protein aggregates, possibly on grain boundaries of the rough surfaces or due to curvature of the grain itself. The grains were of around 40 nm diameter. It is believed that monomers that bind to these regions change their conformational shape such that it exposes groups previously not available in solution (e.g. hydrophobic groups) that will induce another monomer to aggregate. The aggregation was observed using liquid AFM and compared against an atomically flat gold surface that was induced to be hydrophobic. The hydrophobicity on the sample induces BSA aggregation. Both surfaces looked similar, but the higher contrast of the PTS gold allows for better characterisation. This means that a hydrophilic rough gold behaves similar to a hydrophobic surface for BSA adsorption. Grains looked to play a role in this behaviour, and it would need to be explored what characteristics of the grains induce this effect. In the case of nanoparticles and nanofabricated pillars, the BSA adsorbed less mass (68% and 54% respectively) than the expected increase by area. Although these features had similar diameter (43nm) to the grains of standard gold (46nm) and rough gold (47nm), the results are contrasting. The NPs, however, are isolated spherical features that will rely on their shape for protein adsorption. The sphericity is believed to adsorb the protein such that the monomer spreads upon binding, reducing the area available for more monomers but without inducing aggregates. The results showed that the physical composition of a gold electrode indeed have an effect in the interaction of proteins with a surface.

6 References

[1] J. Wang, “Electrochemical glucose biosensors.,” *Chem. Rev.*, vol. 108, no. 2, pp. 814–25, Feb. 2008.

[2] A. P. F. Turner, “Biosensors: sense and sensibility.,” *Chem. Soc. Rev.*, vol. 42, no. 8, pp. 3184–96, Apr. 2013.

[3] TechNavio, “Global Medical Biosensors Market 2014-2018,” 2014.

[4] J. Eid, A. Fehr, J. Gray, K. Luong, J. Lyle, and G. Otto, “Real-time DNA sequencing from single polymerase molecules,” *Science (80-.).*, no. January, pp. 133–138, 2009.

[5] J. M. Rothberg *et al.*, “An integrated semiconductor device enabling non-optical genome sequencing.,” *Nature*, vol. 475, no. 7356, pp. 348–52, Jul. 2011.

[6] L. Liu *et al.*, “Comparison of next-generation sequencing systems.,” *J. Biomed. Biotechnol.*, vol. 2012, p. 251364, Jan. 2012.

[7] C. Meldrum, M. a Doyle, and R. W. Tothill, “Next-generation sequencing for cancer diagnostics: a practical perspective.,” *Clin. Biochem. Rev.*, vol. 32, no. 4, pp. 177–95, Nov. 2011.

[8] J. Arlett, E. Myers, and M. Roukes, “Comparative advantages of mechanical biosensors,” *Nat. Nanotechnol.*, vol. 6, no. 4, pp. 203–215, Apr. 2011.

[9] R. W. Taylor *et al.*, “Watching individual molecules flex within lipid membranes using SERS,” *Sci. Rep.*, vol. 4, pp. 1–6, Aug. 2014.

[10] K. a Marx, “Quartz crystal microbalance: a useful tool for studying thin polymer films and complex biomolecular systems at the solution-surface interface.,” *Biomacromolecules*, vol. 4, no. 5, pp. 1099–120, 2003.

[11] R. Richter, R. Bérat, and A. Brisson, “Formation of solid-supported lipid bilayers: an integrated view,” *Langmuir*, no. 12, pp. 3497–3505, 2006.

[12] T. P. J. Knowles *et al.*, “Kinetics and thermodynamics of amyloid formation from direct measurements of fluctuations in fibril mass.,” *Proc. Natl. Acad. Sci. U. S. A.*, vol. 104, no. 24, pp. 10016–21, Jun. 2007.

[13] S. I. a Cohen *et al.*, “Proliferation of amyloid-β42 aggregates occurs through a secondary nucleation mechanism.,” *Proc. Natl. Acad. Sci. U. S. A.*, vol. 110, no. 24, pp. 9758–63, Jun. 2013.

[14] M. M. Ouberai, K. Xu, and M. E. Welland, “Effect of the interplay between protein and surface on the properties of adsorbed protein layers.,” *Biomaterials*, vol. 35, no. 24, pp. 6157–63, Aug. 2014.

[15] K. Rechendorff, M. B. Hovgaard, M. Foss, V. P. Zhdanov, and F. Besenbacher, “Enhancement of Protein Adsorption Induced by Surface Roughness,” pp. 10885–10888, 2006.

[16] A. Dolatshahi-Pirouz, K. Rechendorff, M. B. Hovgaard, M. Foss, J. Chevallier, and F. Besenbacher, “Bovine serum albumin adsorption on nano-rough platinum surfaces studied by QCM-D,” *Colloids Surf. B. Biointerfaces*, vol. 66, no. 1, pp. 53–9, Oct. 2008.

[17] M. Riedel, B. Müller, and E. Wintermantel, “Protein adsorption and monocyte activation on germanium nanopyramids,” *Biomaterials*, vol. 22, no. 16, pp. 2307–2316, 2001.

[18] H. Terashima and T. Tsuji, “Adsorption of bovine serum albumin onto mica surfaces studied by a direct weighing technique,” *Colloids Surfaces B Biointerfaces*, vol. 27, no. 3/2, pp. 115–122,

2003.

[19] J. L. Wehmeyer, R. Synowicki, R. Bizios, and C. D. García, “Dynamic adsorption of albumin on nanostructured TiO2 thin films,” *Mater. Sci. Eng. C*, vol. 30, no. 2, pp. 277–282, 2010.

[20] J. A. Rubio-Lara, F. Bergler, S. J. Attwood, J. Michael Edwardson, and M. E. Welland, “Ultraflat Gold QCM Electrodes Fabricated with Pressure-Forming Template Stripping for Protein Studies at the Nanoscale,” *Langmuir*, vol. 0, no. 0, p. null-null, Mar. 2019.

[21] E. K. W. Tan *et al.*, “Nanofabrication of Conductive Metallic Structures on Elastomeric Materials,” *Sci. Rep.*, pp. 1–9, 2018.

[22] S. K. Vashist and P. Vashist, “Recent Advances in Quartz Crystal Microbalance-Based Sensors,” *J. Sensors*, vol. 2011, pp. 1–13, 2011.

[23] Y. Montagut, J. V García, Y. Jiménez, C. March, Á. Montoya, and A. Arnau, “A new QCM Sensor Characterization Technique Based on the Phase / Mass Sensitivity Concept,” no. 1, pp. 1–4.

[24] A. A. Vives, *Piezoelectric transducers and applications*. Springer Berlin Heidelberg, 2008.

[25] J. Homola, “Surface plasmon resonance sensors for detection of chemical and biological species,” *Chem. Rev.*, pp. 462–493, 2008.

[26] B. Sharma, R. R. Frontiera, A. Henry, E. Ringe, and R. P. Van Duyne, “SERS : Materials , applications , and the future Surface enhanced Raman spectroscopy (SERS) is a powerful vibrational,” *Mater. Today*, vol. 15, no. 1–2, pp. 16–25, 2012.

[27] R. Elnathan, M. Kwiat, A. Pevzner, and Y. Engel, “Biorecognition layer engineering: overcoming screening limitations of nanowire-based FET devices,” *Nano …*, vol. 12, no. 10, pp. 5245–54, 2012.

[28] M. Voinova, M. Rodahl, M. Jonson, and B. Kasemo, “Viscoelastic acoustic response of layered polymer films at fluid-solid interfaces: continuum mechanics approach,” *Phys. Scr.*, vol. 391, 1999.

[29] C. E. Reed, K. K. Kanazawa, and J. H. Kaufman, “Physical description of a viscoelastically loaded AT-cut quartz resonator,” *J. Appl. Phys.*, vol. 68, no. 5, pp. 1993–2001, 1990.

[30] S. J. Martin, V. E. Granstaff, and G. C. Frye, “Characterization of a Quartz Crystal Microbalance with Simultaneous Mass and Liquid Loading,” *Anal. Chem.*, vol. 63, no. 20, pp. 2272–2281, 1991.

[31] G. Sauerbrey, “Verwendung von Schwingquarzen zur Wägung dünner Schichten und zur Mikrowägung,” *Zeitschrift für Phys.*, vol. 155, no. 2, pp. 206–222, 1959.

[32] H. P. Erickson, “Size and shape of protein molecules at the nanometer level determined by sedimentation, gel filtration, and electron microscopy,” *Biological Procedures Online*. 2009.

[33] K. Kanazawa and N.-J. Cho, “Quartz Crystal Microbalance as a Sensor to Characterize Macromolecular Assembly Dynamics,” *J. Sensors*, vol. 2009, pp. 1–17, 2009.

[34] P. J. Cumpson and M. P. Seah, “The quartz crystal microbalance; radial/polar dependence of mass sensitivity both on and off the electrodes,” *Meas. Sci. Technol.*, vol. 1, no. 7, pp. 544–555, 1999.

[35] R. Lucklum and P. Hauptmann, “Determination of polymer shear modulus with quartz crystal resonators,” *Faraday Discuss.*, vol. 107, pp. 123–140, 1997.

[36] W. Kern and D. A. Poutinen, “Cleaning solution based on hydrogen peroxide for use in silicon

semiconductor technology,” *RCA Rev.*, vol. 31, pp. 187–205, 1970.

[37] W. Kern and J. E. Soc, “The Evolution of Silicon Wafer Cleaning Technology,” *J. Electrochem. Soc.*, vol. 137, no. 6, pp. 1887–1892, 1990.

[38] D. A. Bolon and C. O. Kunz, “Ultraviolet depolymerization of photoresist polymers,” *Polym. Eng. Sci.*, vol. 12, no. 2, pp. 109–111, 1972.

[39] J. J. Blackstock, Z. Li, and G. Jung, “Template stripping using cold welding,” *J. Vac. Sci. Technol. A Vacuum, Surfaces, Film.*, vol. 22, no. 3, p. 602, 2004.

[40] A. Krozer and M. Rodahl, “X-ray photoemission spectroscopy study of UV/ozone oxidation of Au under ultrahigh vacuum conditions,” *J. Vac. Sci. Technol. A Vacuum, Surfaces, Film.*, vol. 15, no. 3, pp. 1704–1709, 1997.

[41] K. Reimhult, K. Petersson, and A. Krozer, “QCM-D analysis of the performance of blocking agents on gold and polystyrene surfaces,” *Langmuir*, vol. 24, no. 16, pp. 8695–8700, 2008.

[42] P. Hanarp, D. S. Sutherland, J. Gold, and B. Kasemo, “Control of nanoparticle film structure for colloidal lithography,” *Colloids Surfaces A Physicochem. Eng. Asp.*, vol. 214, no. 1–3, pp. 23–36, Mar. 2003.

[43] F. a. Denis *et al.*, “Protein adsorption on model surfaces with controlled nanotopography and chemistry,” *Langmuir*, vol. 18, no. 3, pp. 819–828, 2002.

[44] H. Fredriksson *et al.*, “Hole–Mask Colloidal Lithography,” *Adv. Mater.*, vol. 19, no. 23, pp. 4297–4302, Dec. 2007.

[45] M. T. Postek, A. E. Vladár, and K. P. Purushotham, “Does your SEM really tell the truth? How would you know? Part 2,” *Scanning*, vol. 36, no. 3, pp. 347–355, 2014.

[46] J. Israelachvili, *Intermolecular and Surface Forces*. 2011.

[47] a. Ithurbide, I. Frateur, a. Galtayries, and P. Marcus, “XPS and flow-cell EQCM study of albumin adsorption on passivated chromium surfaces: Influence of potential and pH,” *Electrochim. Acta*, vol. 53, no. 3 SPEC. ISS., pp. 1337–1346, 2007.

[48] V. Payet, S. Brunner, A. Galtayries, I. Frateur, and P. Marcus, “Cleaning of albumin-contaminated Ti and Cr surfaces: An XPS and QCM study,” *Surf. Interface Anal.*, vol. 40, no. 3–4, pp. 215–219, 2008.

[49] D. E. King, “Oxidation of gold by ultraviolet light and ozone at 25 °C,” *J. Vac. Sci. Technol. A Vacuum, Surfaces, Film.*, vol. 13, no. 3, pp. 1247–1253, 1995.

[50] Y. Lu, J. Y. Huang, C. Wang, S. Sun, and J. Lou, “Cold welding of ultrathin gold nanowires,” *Nat. Nanotechnol.*, vol. 5, no. 3, pp. 218–224, 2010.

[51] G. S. Ferguson, M. K. Chaudhury, G. B. Sigal, and G. M. Whitesides, “Contact adhesion of thin gold films on elastomeric supports: Cold welding under ambient conditions,” *Science (80-.).*, vol. 253, no. 5021, pp. 776–778, 1991.

[52] M. Yang, F. Qu, Y. Lu, Y. He, G. Shen, and R. Yu, “Platinum nanowire nanoelectrode array for the fabrication of biosensors.,” *Biomaterials*, vol. 27, no. 35, pp. 5944–50, Dec. 2006.

[53] X. Chen and S. S. Mao, “Titanium dioxide nanomaterials: synthesis, properties, modifications, and applications.,” *Chem. Rev.*, vol. 107, no. 7, pp. 2891–959, Jul. 2007.

[54] E. W. Wong, “Nanobeam Mechanics: Elasticity, Strength, and Toughness of Nanorods and Nanotubes,” *Science (80-.).*, vol. 277, no. 5334, pp. 1971–1975, Sep. 1997.

[55] P. Yang *et al.*, “Controlled Growth of ZnO Nanowires and Their Optical Properties,” *Adv. Funct. Mater.*, vol. 12, no. 5, p. 323, May 2002.

[56] H. S. Shin *et al.*, “Density control of ZnO nanowires grown using Au-PMMA nanoparticles and their growth behavior.,” *Nanotechnology*, vol. 20, no. 8, p. 085601, 2009.

[57] D. Zhang, Y. Wang, and Y. Gan, “Characterization of critically cleaned sapphire single-crystal substrates by atomic force microscopy, XPS and contact angle measurements,” *Appl. Surf. Sci.*, vol. 274, pp. 405–417, Jun. 2013.

[58] N. Tiwale, “Zinc Oxide Nanowire Field Effect Transistors for Sensor Applications,” 2013.

[59] R. M. Cerda, *Understanding Quartz Crystals and Oscillators*. Artech House Publishers, 2014.

[60] T. Ando, T. Uchihashi, and S. Scheuring, “Filming biomolecular processes by high-speed atomic force microscopy,” *Chem. Rev.*, vol. 114, no. 6, pp. 3120–3188, 2014.

[61] F. Höök, B. Kasemo, M. Grunze, and S. Zauscher, “Quantitative biological surface science: Challenges and recent advances,” *ACS Nano*, vol. 2, no. 12, pp. 2428–2436, 2008.

[62] N. Kaiser, “Review of the fundamentals of thin-film growth,” *Appl. Opt.*, vol. 41, no. 16, pp. 3053–3060, 2002.

[63] S. Doonan, *Peptides and Proteins*. The Royal Society of Chemistry, 2002.

[64] S. Franssila, “CMP: Chemical–Mechanical Polishing,” in *Introduction to Microfabrication*, John Wiley & Sons, Ltd, 2010, pp. 181–189.

[65] M. S. Miller, M. Ferrato, A. Niec, M. C. Biesinger, and T. B. Carmichael, “Ultrasmooth Gold Surfaces Prepared by Chemical Mechanical Polishing for Applications in Nanoscience,” *Langmuir*, vol. 30, no. 47, pp. 14171–14178, 2014.

[66] I. Axelsson, “Characterization of proteins and other macromolecules by agarose gel chromatography,” *J. Chromatogr. A*, 1978.

[67] H. J. Butt and M. Kappl, *Surface and Interfacial Forces*. Wiley-VCH, 2010.

[68] H. K. Christenson and N. H. Thomson, “The nature of the air-cleaved mica surface,” *Surf. Sci. Rep.*, vol. 71, no. 2, pp. 367–390, 2016.

[69] R. W. G. Wyckoff, *Crystal Structures*, no. v. 4. Interscience Publishers, 1968.

[70] D. Tabor and R. H. S. Winterton, “The Direct Measurement of Normal and Retarded van der Waals Forces,” *Proc. R. Soc. A Math. Phys. Eng. Sci.*, vol. 312, no. 1511, pp. 435–450, 1969.

[71] J. N. Israelachvili and D. Tabor, “The Measurement of Van Der Waals Dispersion Forces in the Range 1.5 to 130 nm,” *Proc. R. Soc. A Math. Phys. Eng. Sci.*, vol. 331, no. 1584, pp. 19–38, 1972.

[72] O. Ouerghi, A. Touhami, A. Othmane, H. Ben Ouada, and C. Martelet, “Investigating antibody -- antigen binding with atomic force microscopy,” vol. 84, pp. 167–175, 2002.

[73] K. Reichelt and H. O. Lutz, “Hetero-epitaxial growth of vacuum evaporated silver and gold,” *J. Cryst. Growth*, vol. 10, no. 1, pp. 103–107, 1971.

[74] C. E. D. Chidsey, D. N. Loiacono, T. Sleator, and S. Nakahara, “STM study of the surface morphology of gold on mica,” *Surf. Sci.*, vol. 200, no. 1, pp. 45–66, 1988.

[75] A. Putnam, B. L. Blackford, M. H. Jericho, and M. O. Watanabe, “Surface topography study of gold deposited on mica using scanning tunneling microscopy: Effect of mica temperature,” *Surf. Sci.*, vol. 217, no. 1–2, pp. 276–288, 1989.

[76] J. A. DeRose, T. Thundat, L. A. Nagahara, and S. M. Lindsay, “Gold grown epitaxially on mica: conditions for large area flat faces,” *Surf. Sci.*, vol. 256, no. 1–2, pp. 102–108, 1991.

[77] M. H. Dishner, “Preparation of gold thin films by epitaxial growth on mica and the effect of flame annealing,” *J. Vac. Sci. Technol. A Vacuum, Surfaces, Film.*, vol. 16, no. 6, pp. 3295–3300, 1998.

[78] I. Petrov, P. B. Barna, L. Hultman, and J. E. Greene, “Microstructural evolution during film growth,” *J. Vac. Sci. Technol. A Vacuum, Surfaces, Film.*, vol. 21, no. 5, p. S117, 2003.

[79] B. A. Movchan and A. V Demchishin, “Investigation of the structure and properties of thick vacuum- deposited films of nickel, titanium, tungsten, alumina and zirconium dioxide,” *Fiz. Met. I Metalloved.*, vol. 28, no. 4, pp. 653–660, 1969.

[80] P. . Barna and M. Adamik, “Fundamental structure forming phenomena of polycrystalline films and the structure zone models,” *Thin Solid Films*, vol. 317, no. 1–2, pp. 27–33, 1998.

[81] M. Higo, K. Fujita, Y. Tanaka, M. Mitsushio, and T. Yoshidome, “Surface morphology of metal films deposited on mica at various temperatures observed by atomic force microscopy,” *Appl. Surf. Sci.*, vol. 252, no. 14, pp. 5083–5099, 2006.

[82] M. Hegner, P. Wagner, and G. Semenza, “Ultralarge atomically flat template-stripped Au surfaces for scanning probe microscopy,” *Surf. Sci.*, vol. 291, no. 1–2, pp. 39–46, 1993.

[83] W. Knoll, I. Köper, R. Naumann, and E. K. Sinner, “Tethered bimolecular lipid membranes-A novel model membrane platform,” *Electrochim. Acta*, vol. 53, no. 23, pp. 6680–6689, 2008.

[84] B. De Nijs *et al.*, “Plasmonic tunnel junctions for single-molecule redox chemistry,” *Nat. Commun.*, vol. 8, no. 1, pp. 1–8, 2017.

[85] R. P. Richter and A. Brisson, “QCM-D on mica for parallel QCM-D-AFM studies.,” *Langmuir*, vol. 20, no. 11, pp. 4609–4613, 2004.

[86] D. W. Mosley, B. Y. Chow, and J. M. Jacobson, “Solid-state bonding technique for template-stripped ultraflat gold substrates,” *Langmuir*, vol. 22, no. 6, pp. 2437–2440, 2006.

[87] G. Humpston and S. J. Baker, “Diffusion bonding of gold,” *Gold Bull.*, vol. 31, no. 4, pp. 131–132, 1998.

[88] V. E. Bottom, *Introduction to quartz crystal unit design*, 1st ed. Van Nostrand Reinhold, 1982.

[89] W. Shockley and D. J. Koneval, “Trapped-Energy Modes in Quartz Filter Crystals,” *J. Acoust. Soc. Am.*, vol. 268, no. April 1965, pp. 981–993, 1966.

[90] G. K. Guttwein, “Status of Quartz Crystal Research and Development,” in *17th Annual Symposium on Frequency Control*, 1963, pp. 190–214.

[91] C. V Thompson, “Grain Growth in Thin Films,” *Annu. Rev. Mater. Sci.*, vol. 20, no. 1, pp. 245–268, 1990.

[92] C. V. Thompson, “Structure Evolution During Processing of Polycrystalline Films,” *Annu. Rev. Mater. Sci.*, vol. 30, no. 1, pp. 159–190, 2000.

[93] Y. Huang, H. Qiu, F. Wang, L. Pan, Y. Tian, and P. Wu, “Effect of annealing on the characteristics of Au/Cr bilayer films grown on glass,” *User Model. User-adapt. Interact.*, vol. 71, no. 4, pp. 523–528, 2003.

[94] T. J. Senden and W. a Ducker, “Surface Roughness of Plasma-Treated Mica,” *Langmuir*, no. 7, pp. 733–735, 1992.

[95] P. Somasundaran, *Encyclopedia of Surface and Colloid Science*, no. v. 2. Taylor & Francis, 2006.

[96] O. Ptitsyn, "How molten is the molten globule?," *Nat. Struct. Biol.*, vol. 3, no. 6, pp. 488–490, 1996.

[97] D. A. Dolgikh *et al.*, "A-Lactalbumin: Compact State With Fluctuating Tertiary Structure?," *FEBS Lett.*, vol. 136, no. 2, pp. 311–315, 1981.

[98] a P. Quist, L. P. Bjorck, C. T. Reimann, S. O. Oscarsson, and B. U. R. Sundqvist, "A Scanning Force Microscopy Study of Human Serum-Albumin and Porcine Pancreas Trypsin Adsorption on Mica Surfaces," *Surf. Sci.*, vol. 325, no. 1–2, pp. L406–L412, 1995.

[99] M. S. Lord *et al.*, "The effect of silica nanoparticulate coatings on serum protein adsorption and cellular response.," *Biomaterials*, vol. 27, no. 28, pp. 4856–62, Oct. 2006.

[100] K. Cai, J. Bossert, and K. D. Jandt, "Does the nanometre scale topography of titanium influence protein adsorption and cell proliferation?," *Colloids Surfaces B Biointerfaces*, vol. 49, no. 2, pp. 136–144, 2006.

[101] A. G. Hemmersam, M. Foss, J. Chevallier, and F. Besenbacher, "Adsorption of fibrinogen on tantalum oxide , titanium oxide and gold studied by the QCM-D technique," vol. 43, pp. 208–215, 2005.

[102] G. Pellicane, D. Costa, and C. Caccamo, "Phase coexistence in a DLVO model of globular protein solutions," *J. Phys. Condens. Matter*, vol. 15, pp. 375–384, 2003.

[103] W. Norde and J. P. Favier, "Structure of adsorbed and desorbed proteins," *Colloids and Surfaces*, vol. 64, no. 1, pp. 87–93, 1992.

[104] W. Chen, "Fabrication of sub-10 nm structures by lift-off and by etching after electron-beam exposure of poly(methylmethacrylate) resist on solid substrates," *J. Vac. Sci. Technol. B Microelectron. Nanom. Struct.*, vol. 11, no. 6, p. 2519, 1993.

[105] C. Vieu *et al.*, "Electron beam lithography: resolution limits and applications," *Appl. Surf. Sci.*, vol. 164, no. 1, pp. 111--117, 2000.

[106] S. Yasin, D. G. Hasko, and H. Ahmed, "Fabrication of <5 nm width lines in poly(methylmethacrylate) resist using a water:isopropyl alcohol developer and ultrasonically-assisted development," *Appl. Phys. Lett.*, vol. 78, no. 18, pp. 2760–2762, 2001.

[107] W. C. Hu, K. Sarveswaran, M. Lieberman, and G. H. Bernstein, "Sub-10 nm electron beam lithography using cold development of poly(methylmethacrylate)," *J. Vac. Sci. Technol. B*, vol. 22, no. 4, pp. 1711–1716, 2004.

[108] S. Yasin, M. N. Khalid, D. G. Hasko, and S. Sarfraz, "Correlation of surface roughness with edge roughness in PMMA resist," *Microelectron. Eng.*, vol. 78–79, no. 1–4, pp. 484–489, 2005.

[109] K. Koshelev, M. Ali Mohammad, T. Fito, K. L. Westra, S. K. Dew, and M. Stepanova, "Comparison between ZEP and PMMA resists for nanoscale electron beam lithography experimentally and by numerical modeling," *J. Vac. Sci. Technol. B Microelectron. Nanom. Struct.*, vol. 29, no. 6, p. 06F306, 2011.

[110] H. Duan, V. R. Manfrinato, J. K. W. Yang, D. Winston, B. M. Cord, and K. K. Berggren, "Metrology for electron-beam lithography and resist contrast at the sub-10 nm scale," *J. Vac. Sci. Technol. B, Nanotechnol. Microelectron. Mater. Process. Meas. Phenom.*, vol. 28, no. 6, p. C6H11-C6H17, 2010.

[111] V. R. Manfrinato *et al.*, "Aberration-Corrected Electron Beam Lithography at the One

Nanometer Length Scale," *Nano Lett.*, vol. 17, no. 8, pp. 4562–4567, 2017.

[112] J. Malmström, H. Agheli, P. Kingshott, and D. S. Sutherland, "Viscoelastic modeling of highly hydrated laminin layers at homogeneous and nanostructured surfaces: quantification of protein layer properties using QCM-D and SPR.," *Langmuir*, vol. 23, no. 19, pp. 9760–8, Sep. 2007.

[113] I. Reviakine, D. Johannsmann, and R. P. Richter, "Hearing What You Cannot See and Visualizing What You Hear," *Anal. Chem.*, vol. 83, pp. 8838–8848, 2011.

[114] G. H. Gilmer, H. Huang, T. D. De La Rubia, J. D. Torre, and F. Baumann, "Lattice Monte Carlo models of thin film deposition," *Thin Solid Films*, vol. 365, no. 2, pp. 189–200, 2000.

[115] V. S. Stoll and J. S. Blanchard, "Chapter 6 Buffers. Principles and Practice," *Methods Enzymol.*, vol. 463, no. C, pp. 43–56, 2009.

Appendix

7 Appendix

In this section, additional information is provided for different sections of the main text in this thesis. This additional information is not required for the understanding of the thesis, but it enhances the original experiments. For the reader, each section has its proper section numbering corresponding to the numbering of the main document for easier finding.

2.5.1 Study of Variations in QCM Measurements

It is presented here the extra experiment of BSA where the deposition of a monolayer was obtained using a specific type of BSA on gold QCM electrodes and a multilayer for another batch.

BSA Batch 1. Multilayer deposition. Purification method unknown. >96%, see the multi-step adsorption of BSA on the figure below. The change of frequency (blue line) was adsorbing more BSA with every injection.

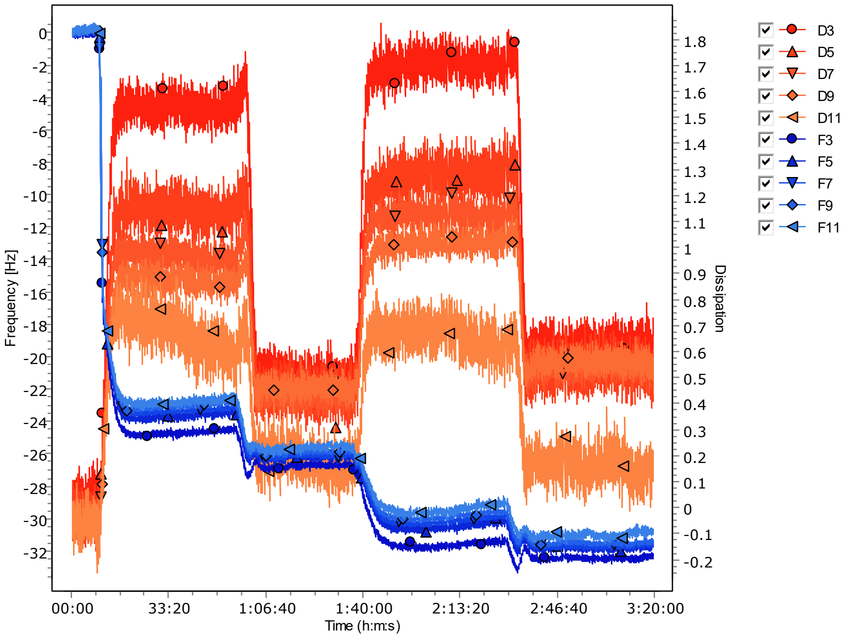

BSA Batch 2, a monolayer was achieved. No additional layer was measured after multiple injections of the same solution, see blue curves on figure below. A7030 SIGMA. Bovine Serum Albumin. heat shock fraction, protease free, fatty acid free, essentially globulin free, pH 7, ≥98% purchased from Sigma Aldrich.

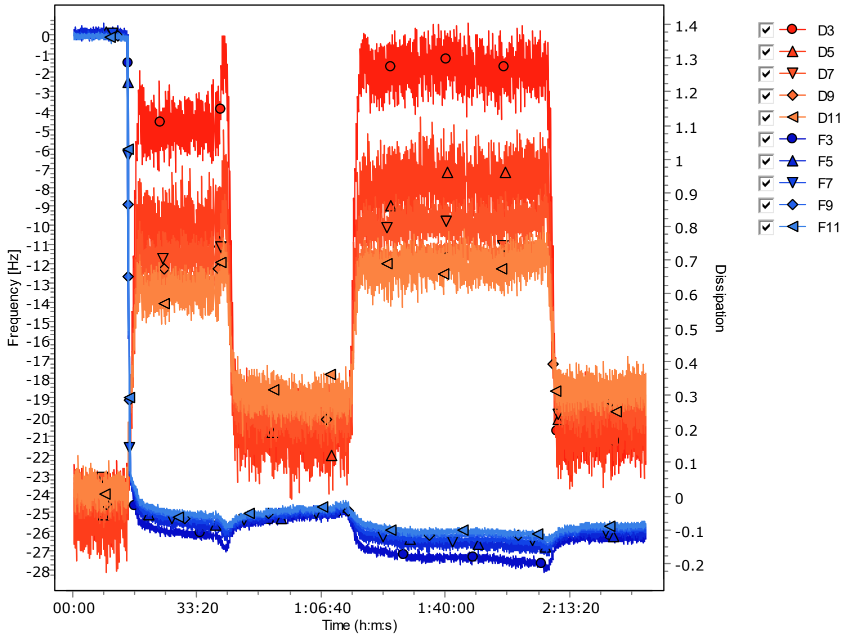

2.6 Initial Au NP deposition with different coatings.

Au Nanoparticles (NPs) were purchased from BBI Solutions with an average size of 50 nm according to the supplier. The initial colloidal solution was reduced from 15 ml to 1.3ml by centrifuge at 8500 rpm for 10 minutes. A 1mM of each coating was used for coating the nanoparticles using sonication and expected to be adhered to the surface of the NPs by displacement.

Coatings used are:

PEG 35K

PEG 400

PVP40K


C0_PVP_bright.jpg


C1_PEG400_DF.jpg


C2_PEG400_bright.jpg


C0_PEG400_DF.jpg


C1_PEG400_bright.jpg

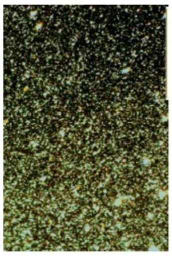
C2_PEG35K_DF.jpg


C0_PEG400_bright.jpg

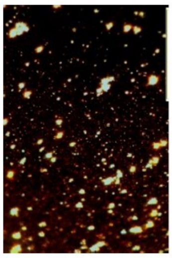
C1_PEG35K_DF.jpg


C2_PEG35K_bright.jpg

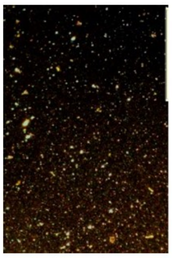
C2_PVP_DF.jpg

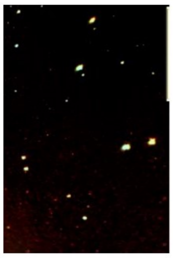
C0_PEG35K_DF.jpg

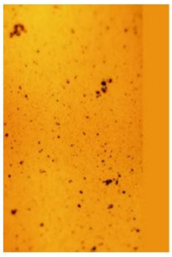
C1_PEG35K_bright.jpg

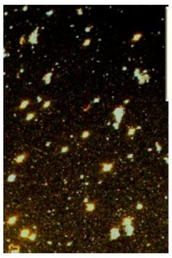
C1_PVP_DF.jpg


C2_PVP_bright.jpg


C0_PEG35K_bright.jpg

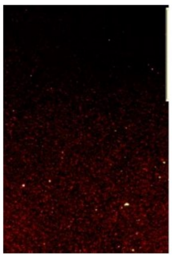
C0_PVP_DF.jpg

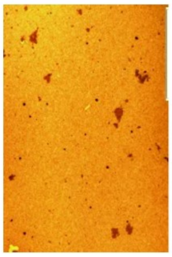
C1_PVP_bright.jpg

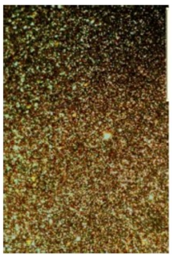
C2_PEG400_DF.jpg

Only PVP samples did not aggregate. Additional experiments were performed using 20 nm AuNPs and showed monodispersity using PVP. The samples with aggregation can be seen under an optical microscope for the PEG samples. Additional SEM images were taken of the aggregate sample and of the non-aggregated sample, PVP, for 20 nm NPs.

PEG sample

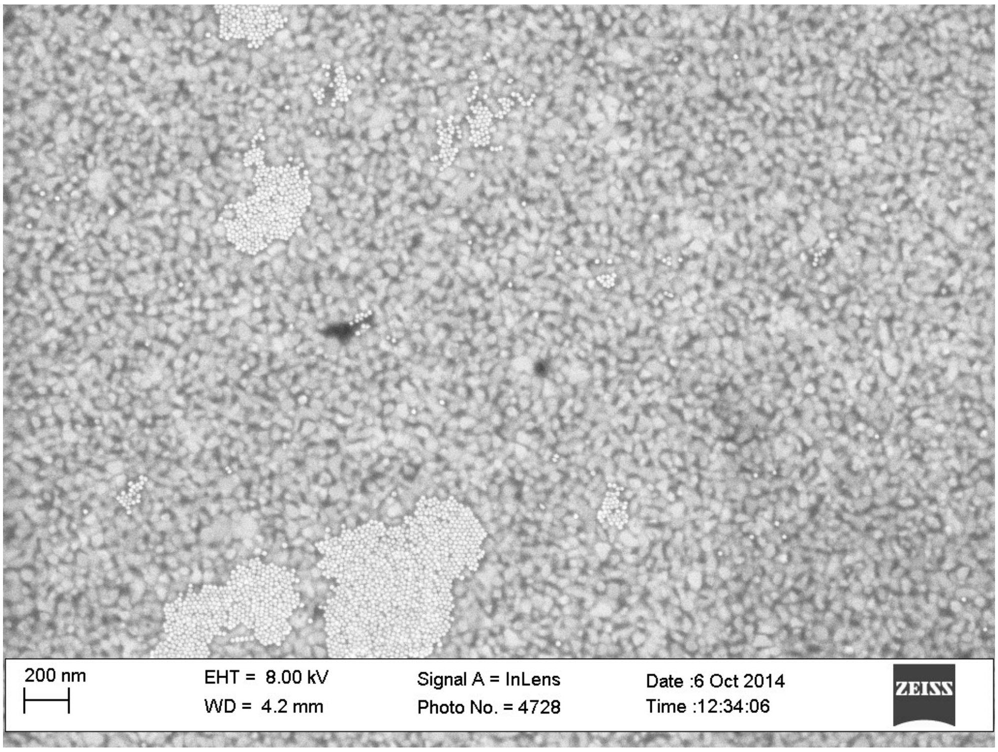

PVP sample showing monodispersed nanoparticles

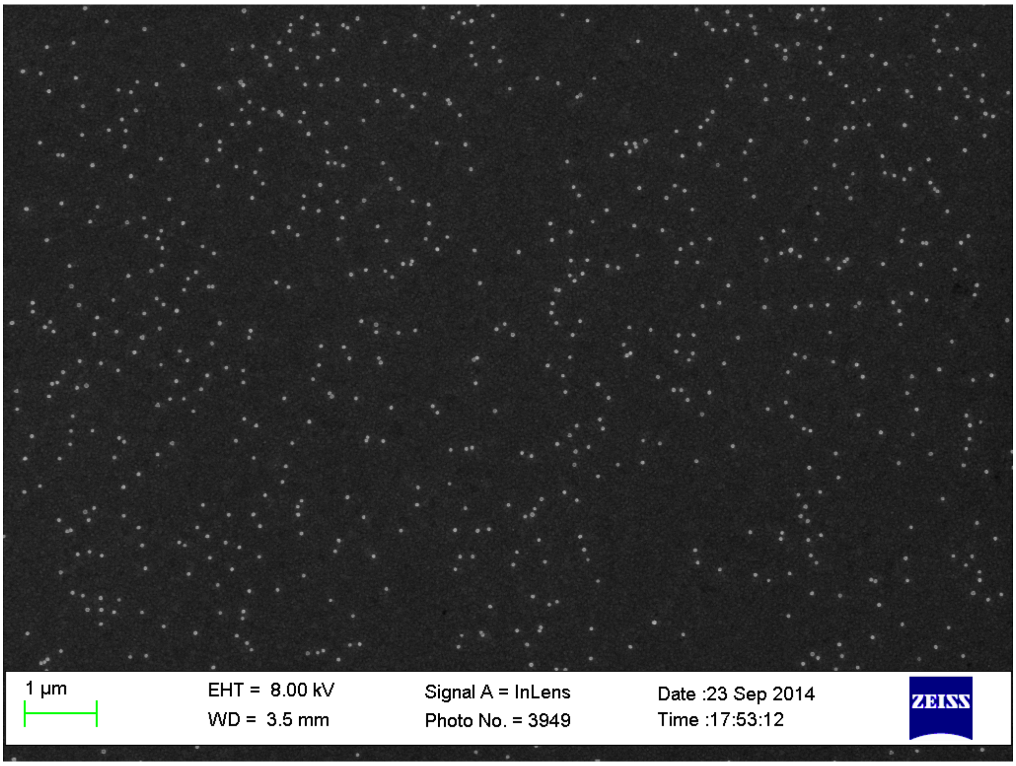

The problem with PVP is its MW having a MW of 40K will give a 39+-15 nm extra thickness. This means that the NP could not be closer to 80 nm edge to edge. Still the sample had not very high monodispersity compared to InnovaCoat NPs.

2.7 Watershed Algorithm examples.

Here, it is presented two examples of some results of the watershed algorithm employed by the software Gwyddion.

Example 1

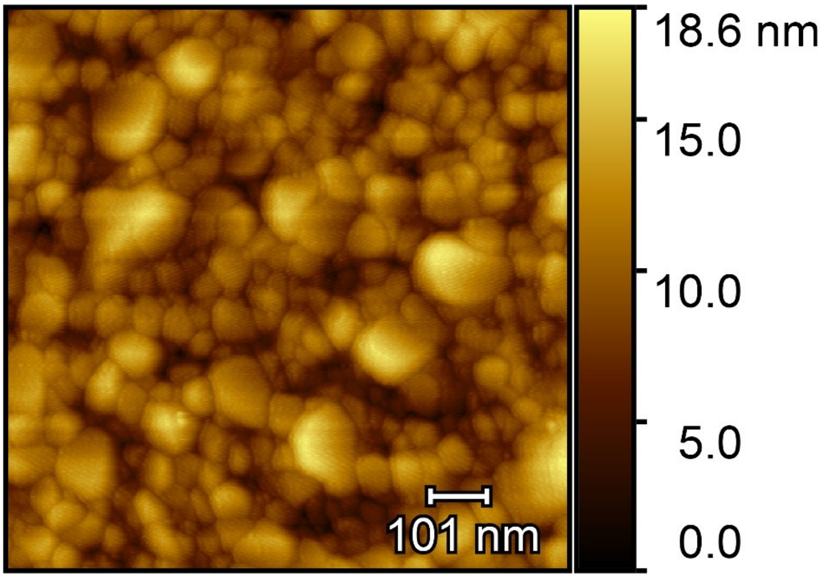

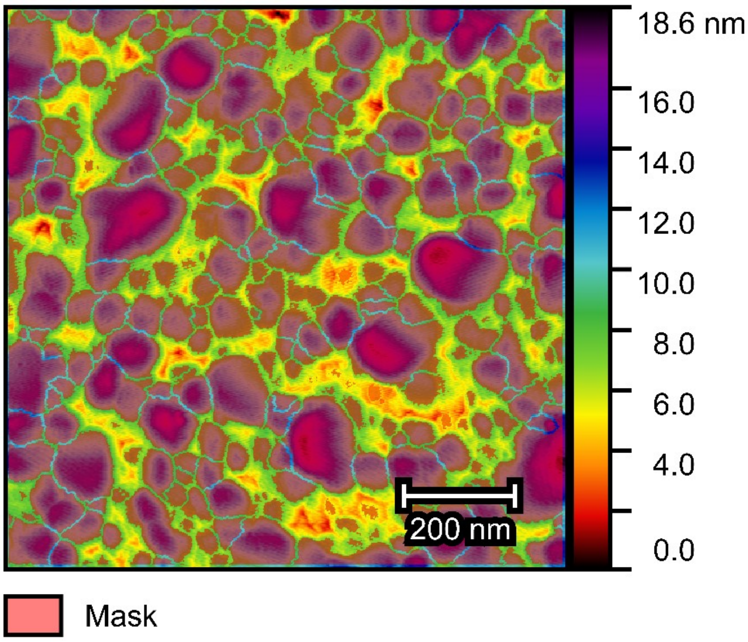

Example 2

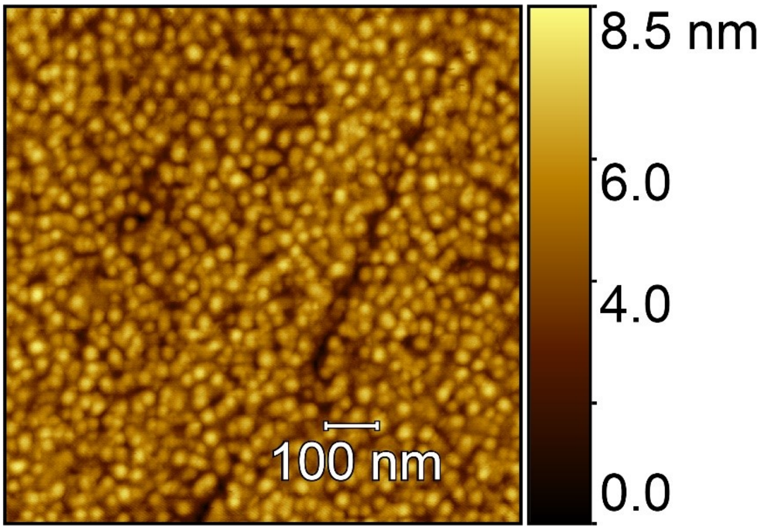
100 nm
8.5 nm
6.0
4.0
0.0

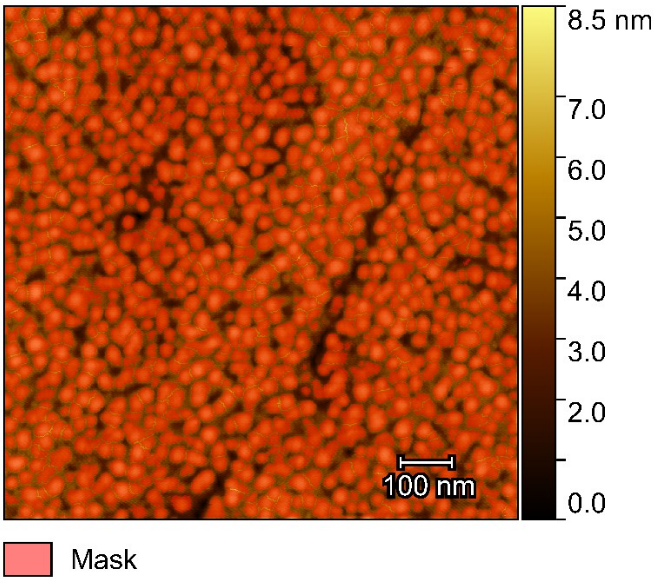
100 nm
8.5 nm
7.0
6.0
5.0
4.0
3.0
2.0
0.0
🟥 Mask

The parameters used for the watershed algorithm are the following:

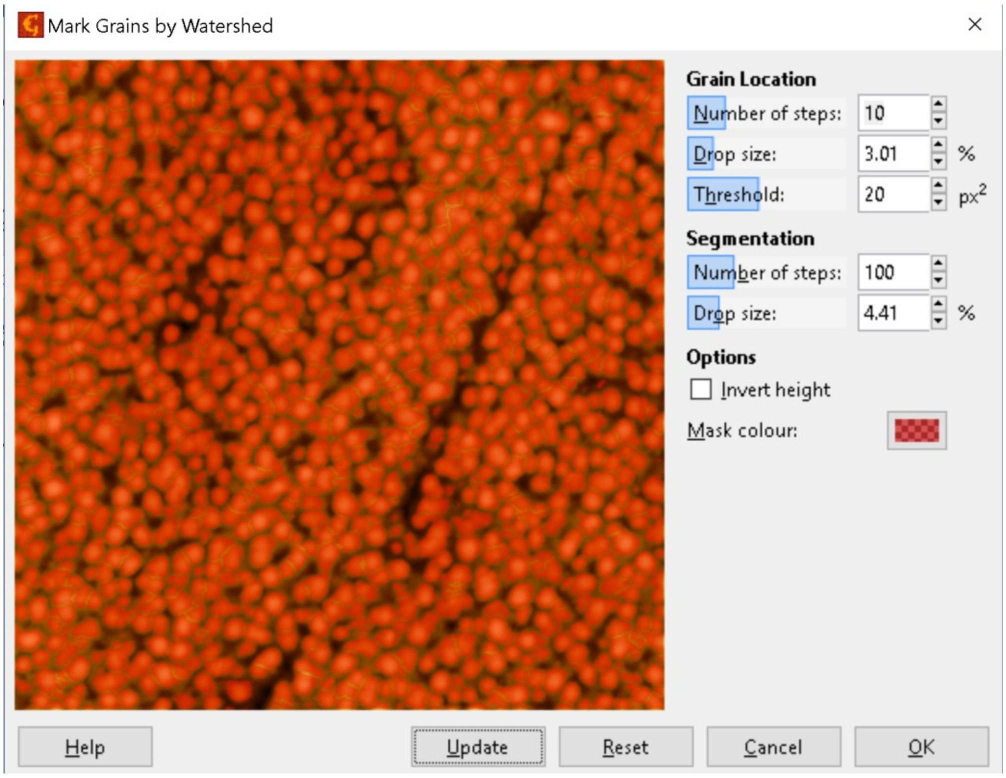

Mark Grains by Watershed

Grain Location

Number of steps: 10

Drop size: 3.01 %

Threshold: 20 px^2

Segmentation

Number of steps: 100

Drop size: 4.41 %

Options

☐ Invert height

Mask colour: ▨

Recipe for Sörensen's Phosphate Buffer

The buffer of Sörensen[115] is presented below to obtain a pH of 7.4 without NaCl added to the solution.

A: preparation of 0.2M of monobasic sodium phosphate (NaH_2PO_4, MW=156)

Dissolve 0.5928 g of NaH_2PO_4 in 19 ml dH_2O.

B: preparation of 0.2M of dibasic sodium phosphate (Na_2HPO_4, MW=178)

Dissolve 2.8836 g of Na_2HPO_4 in 81 ml dH_2O.

Mix the 19 ml of NaH_2PO_4 solution with the 81 ml of Na_2HPO_4 to obtain 0.2M of phosphate buffer.

The final buffer is then diluted to 5% in dH_2O to obtain 10 mM and HCL is added to reduce the pH to 7.4

2.7 Experiment of Ageing of QCM resonators

QuartzPro

The RMS roughness of a standard QCM resonator purchased from QuartzPro is 3.353 nm, where grains are of the scale of 54.43±15.8 nm diameter on average, see histogram of Figure QCMSTD.

QuartzPro from the box:

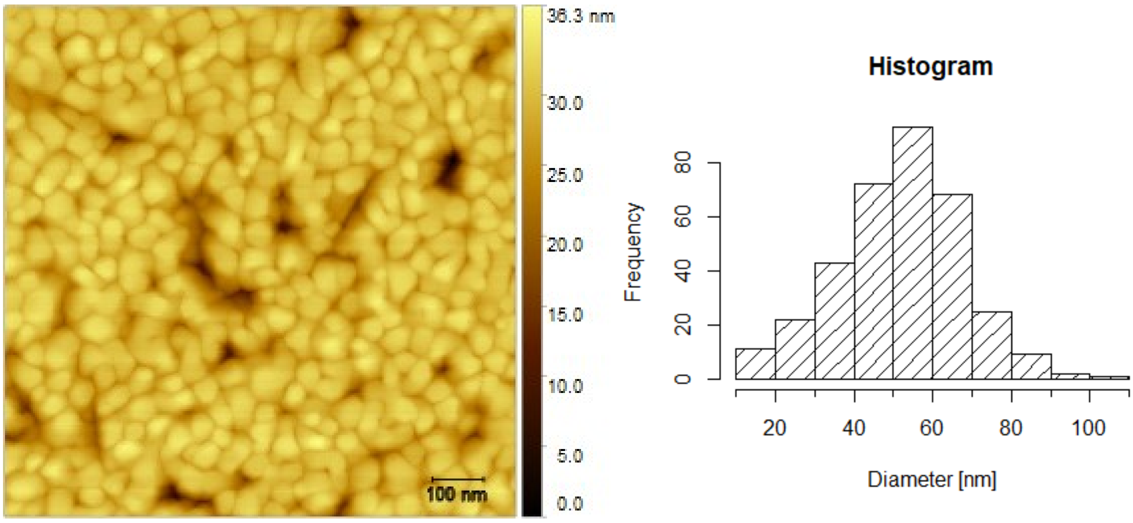

Figure QCMSTD

Quartz Pro after first clean using modified RCA 1 cleaning method:

RMS of 2.153 nm, diameter of 64.48±26.70 nm

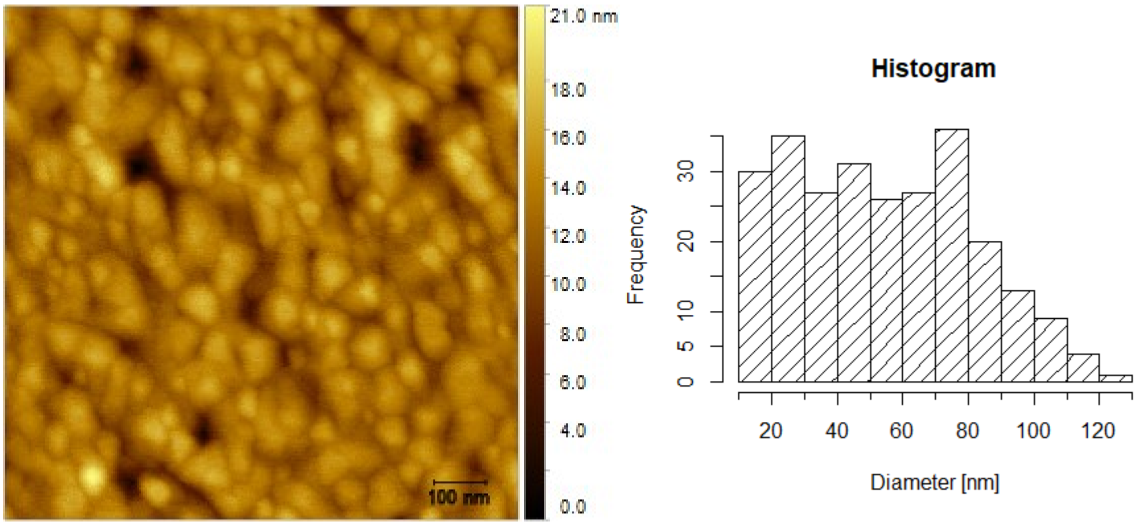

AWSensors

RMS 1.370 nm, diameter of grains 34.97±10.49

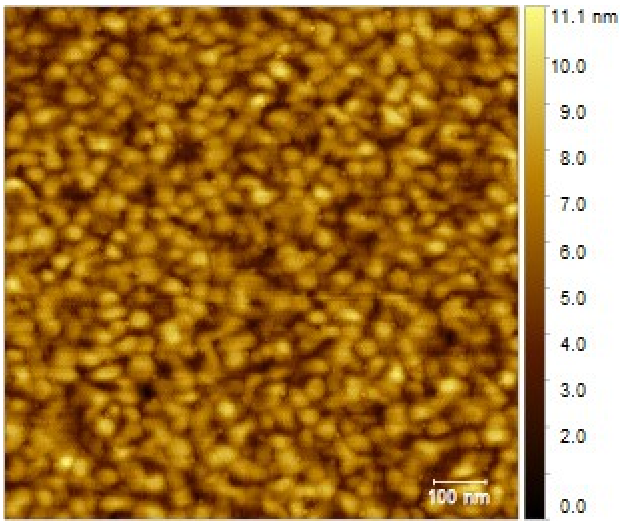

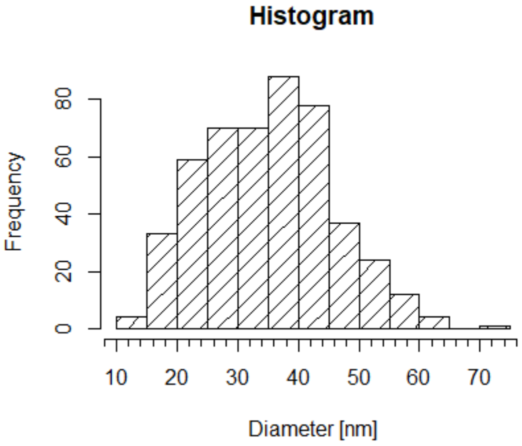

AWSensors Resonators. 1st clean

RMS of 1.679nm and diameter of grains of 46.88±23.90

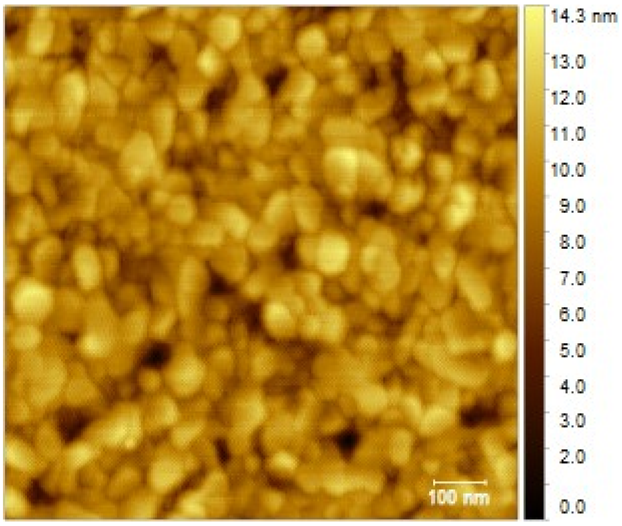

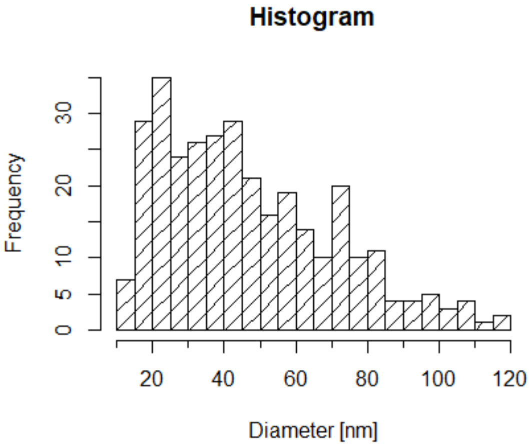

QCM-D from QSense

Here it is presented all histograms of each sample used for the experiments of Chapter 2, Section 2.7

Sample P1, 1.071 nm RMS and grain size of 29.52±7.10nm

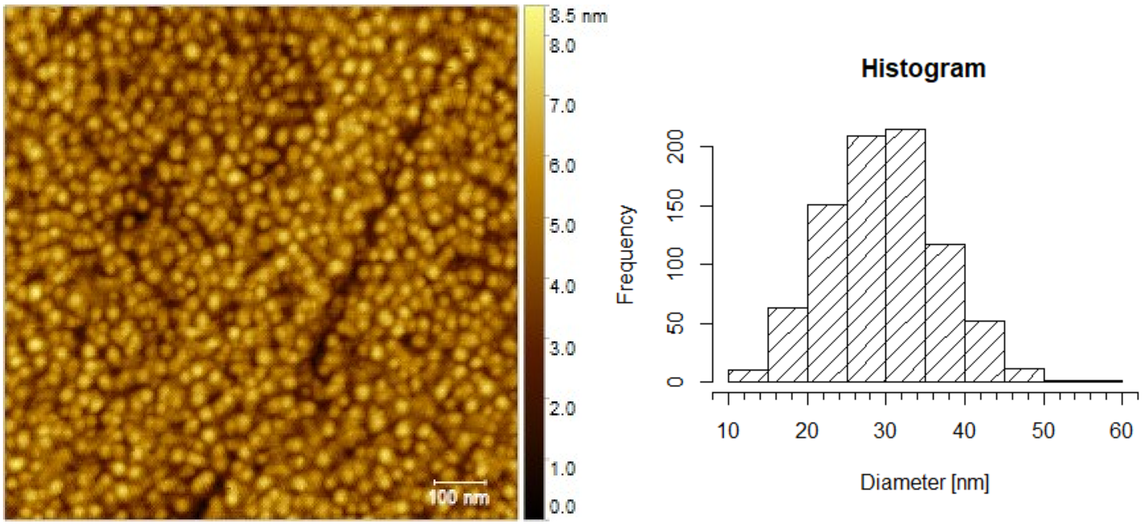

1st clean

QCM-D resonators

P1, RMS of 0.920 nm, 36.58±13.23 nm diameter.

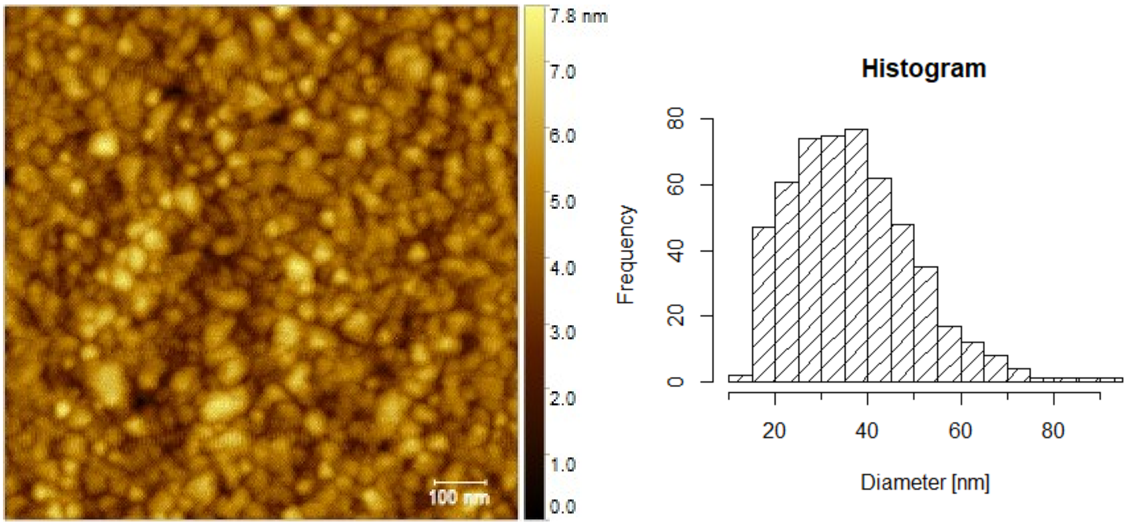

Sample P2, 0.845 nm RMS and grain size of 24.25±5.43 nm.

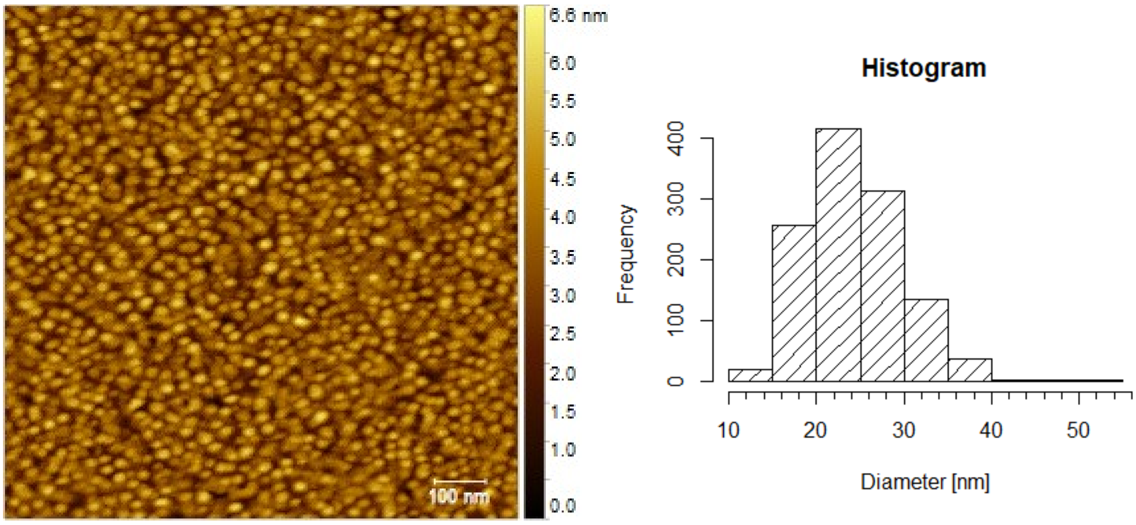

1st clean

P2. RMS 0.921 nm, diameter of 32.53±12.06 nm

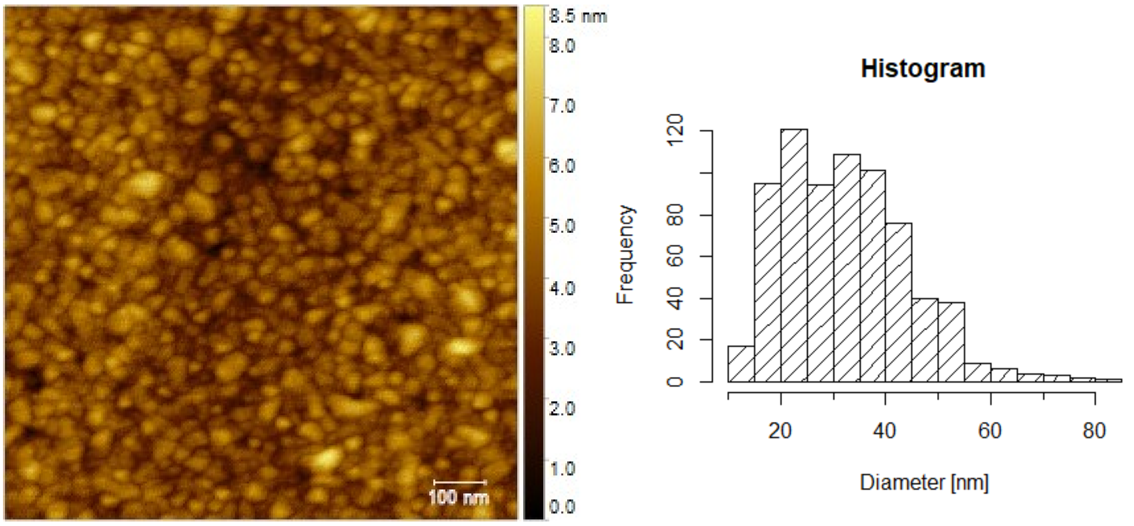

Sample P3, 0.953 nm RMS and grain size of 28.78±6.84 nm.

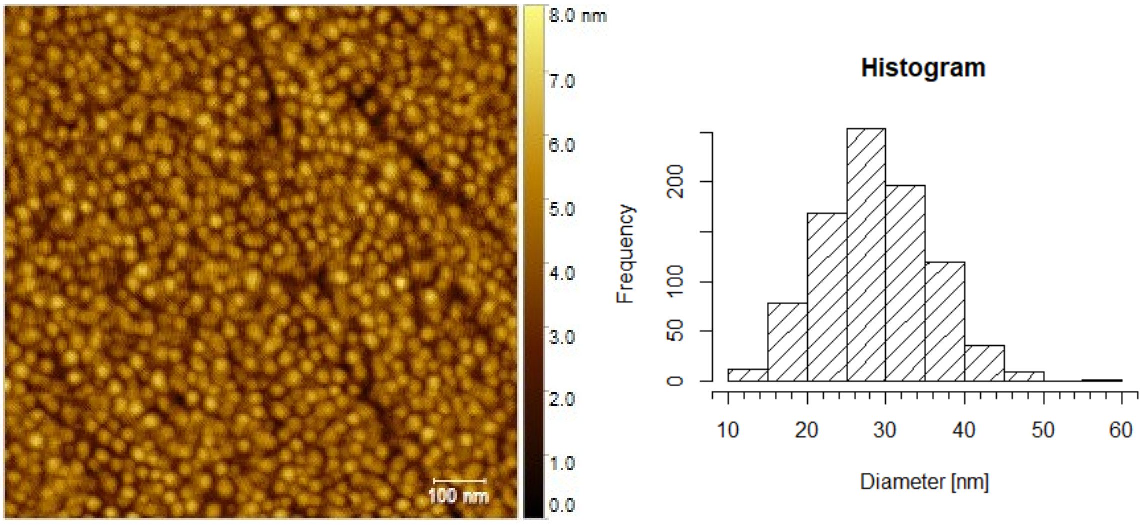

1stclean

P3, RMS 0.894 nm, diameter of 33.36±11.86 nm.

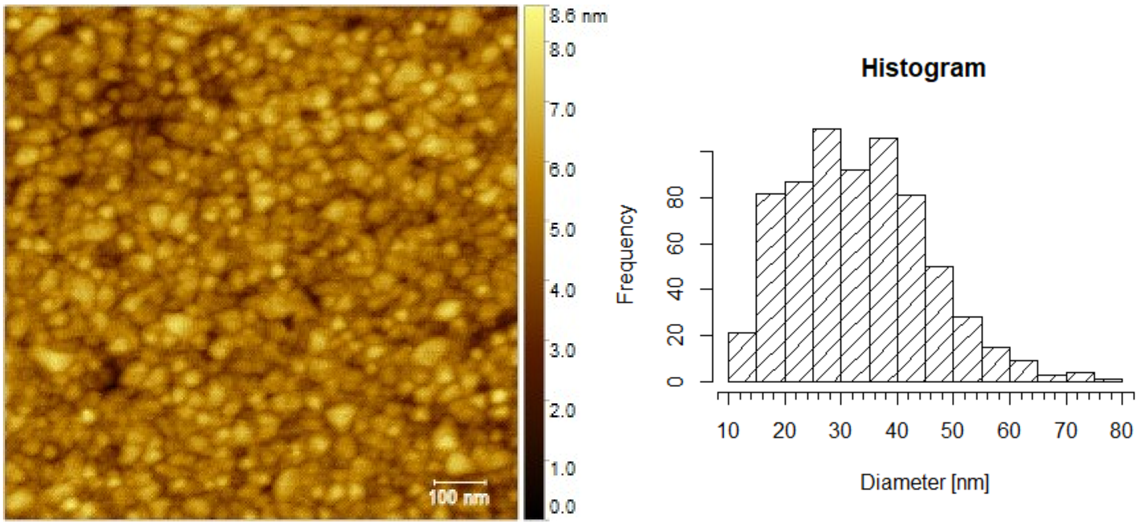

Sample P4, 0.917 nm RMS and diameter of 29.39±7.53nm

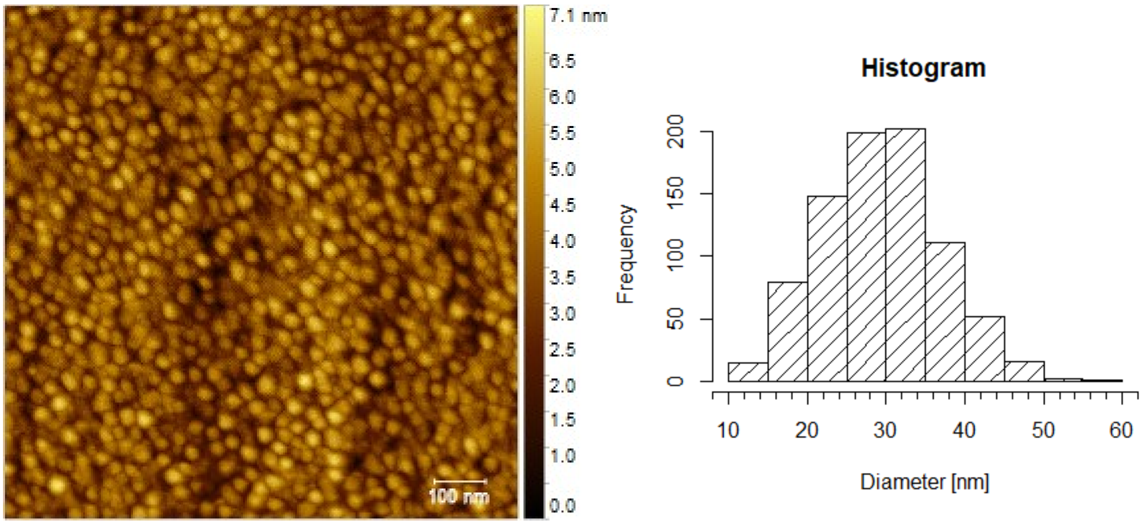

1st clean

P4, RMS 0.934 nm, diameter of 34.23±12.49 nm.

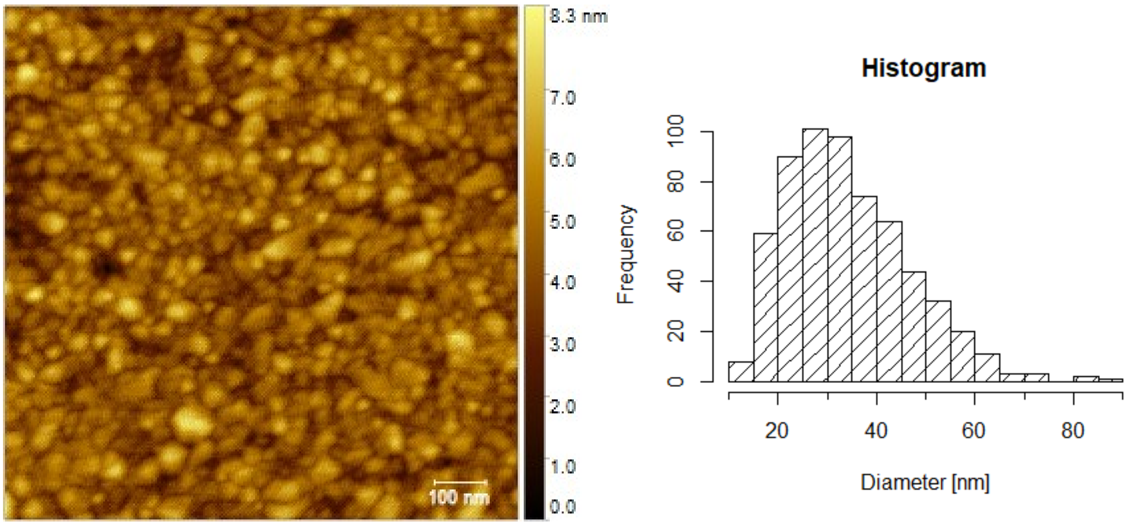

2nd clean

QCMD, RMS 2.116 nm, diameter 45.68±25.10 nm

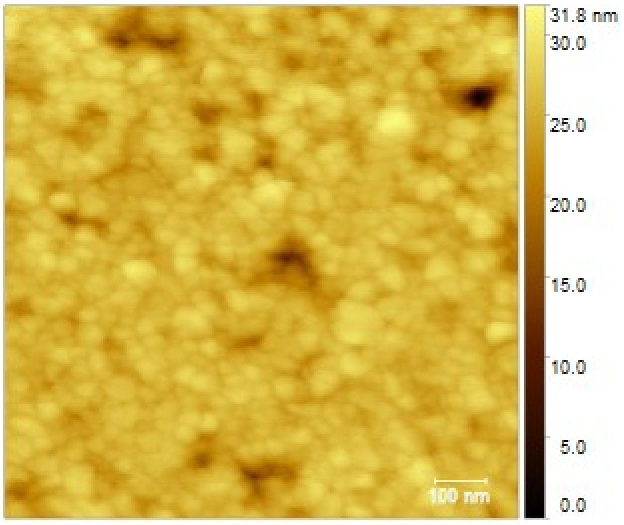

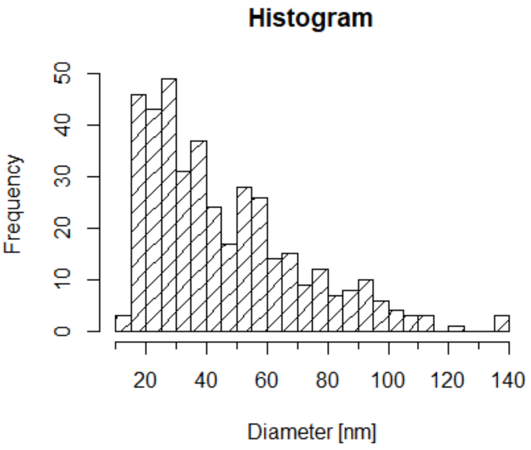

After Several Uses

QCMD, RMS 2.683nm 52.17±30.22nm diameter

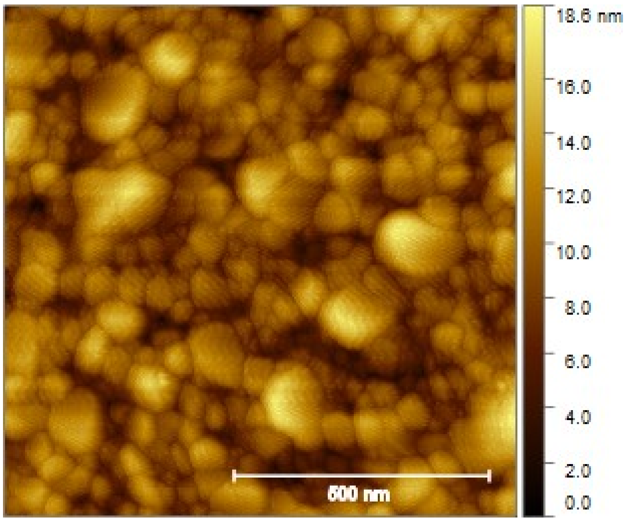

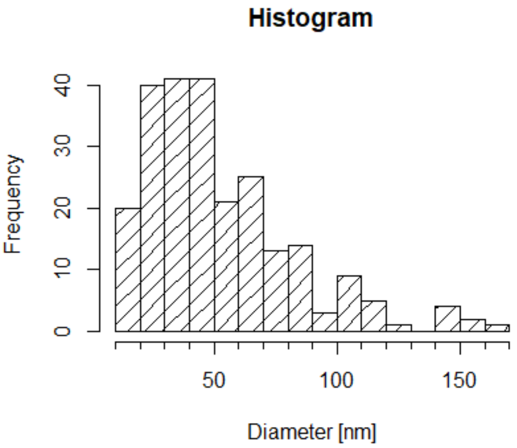

Sample P1, 1.071 nm RMS and grain size of 29.52±7.10nm

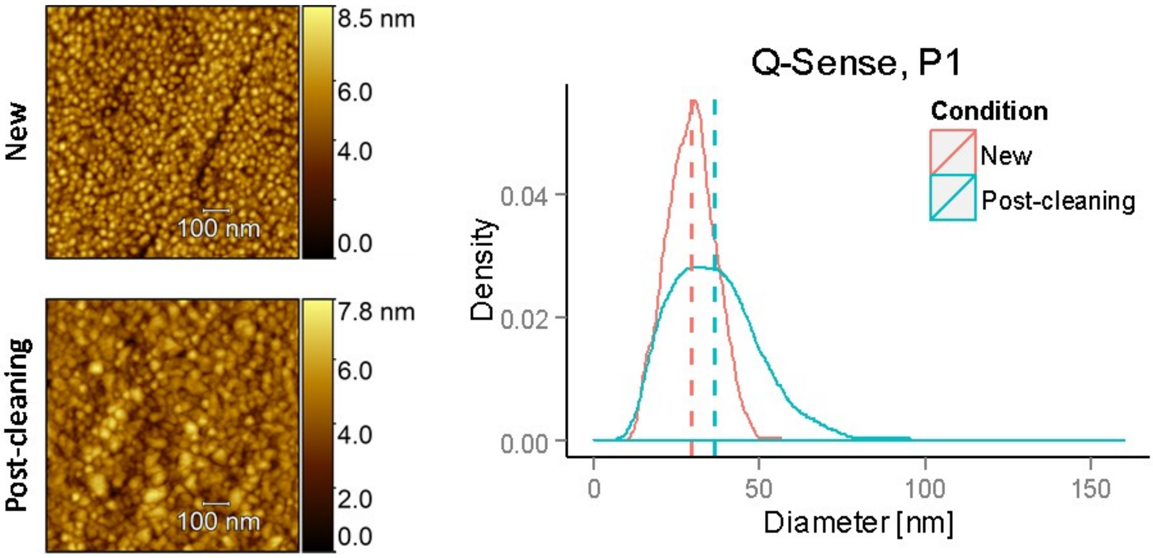

1st clean. P1, RMS of 0.920 nm, 36.58±13.23 nm diameter.

Sample P2, 0.845 nm RMS and grain size of 24.25±5.43 nm.

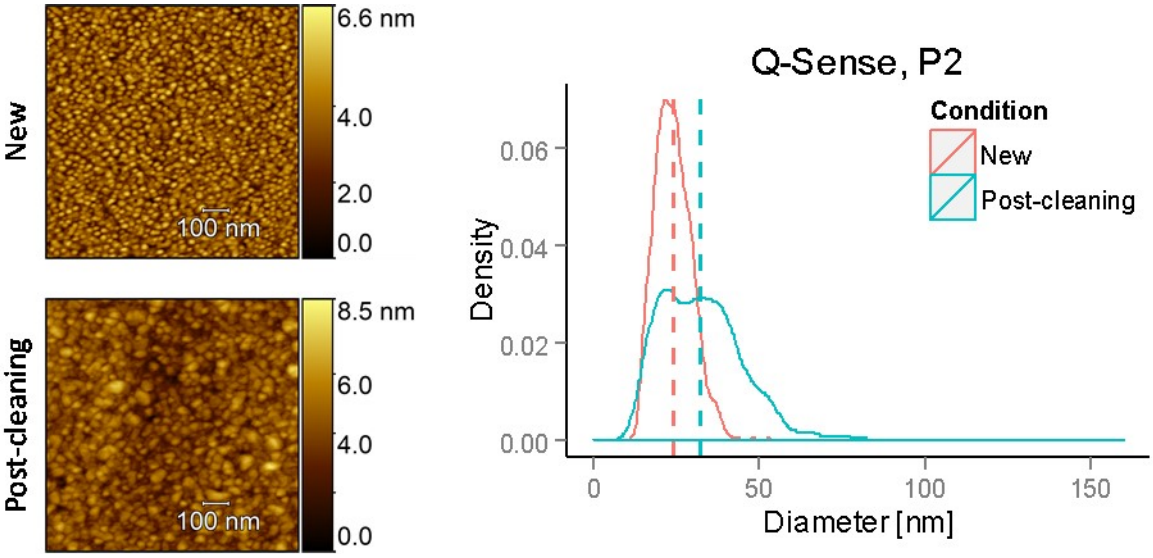

1st clean. P2. RMS 0.921 nm, diameter of 32.53±12.06 nm

Sample P3, 0.953 nm RMS and grain size of 28.78±6.84 nm.

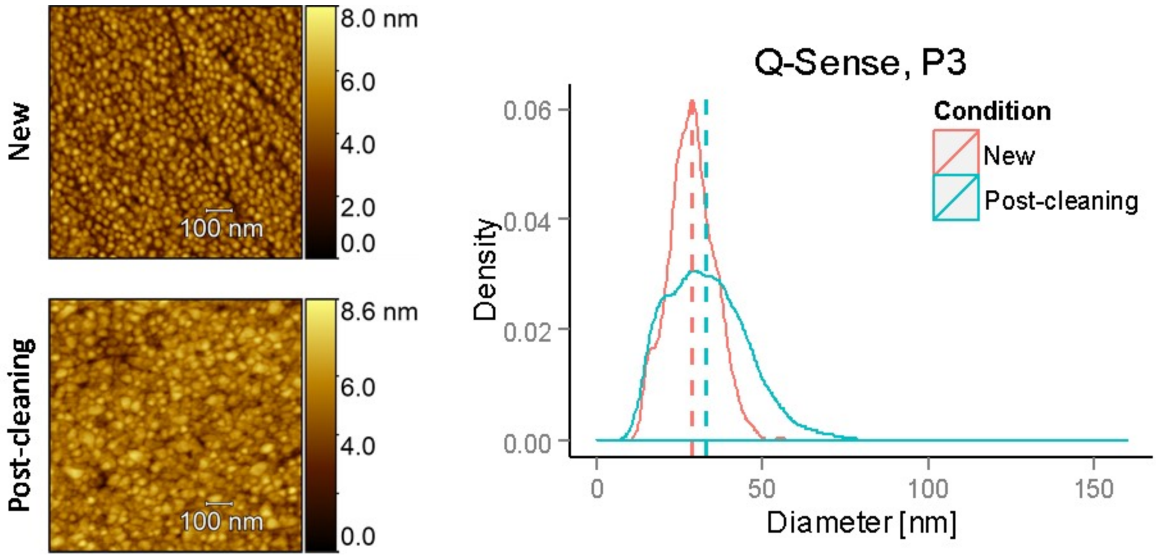

1stclean. P3, RMS 0.894 nm, diameter of 33.36±11.86 nm.

Sample P4, 0.917 nm RMS and diameter of 29.39±7.53nm

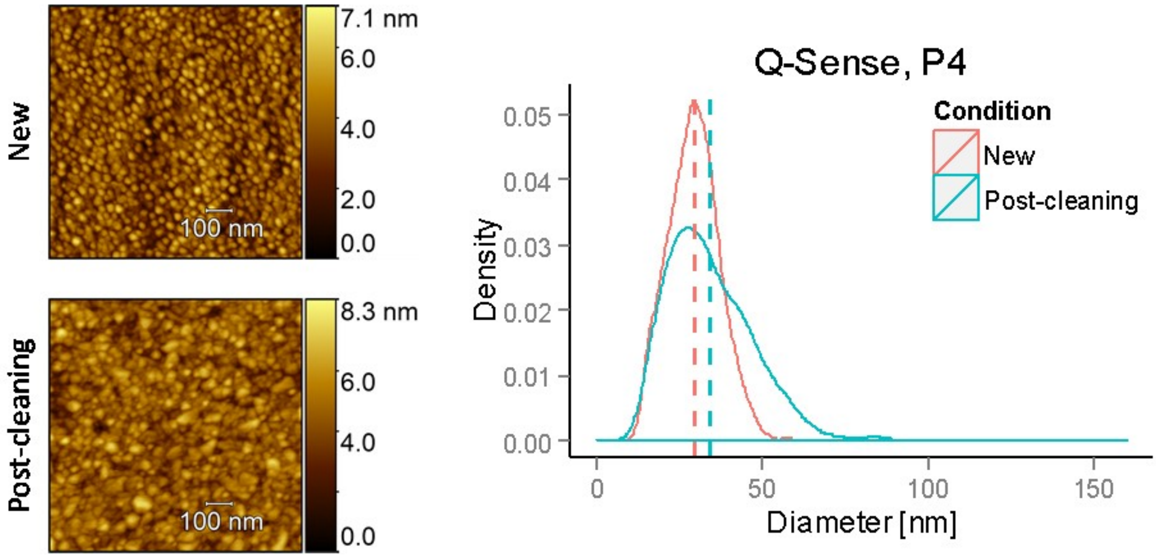

Chapter 5 Quartz Pro batch 2017

RMS 1.251 nm

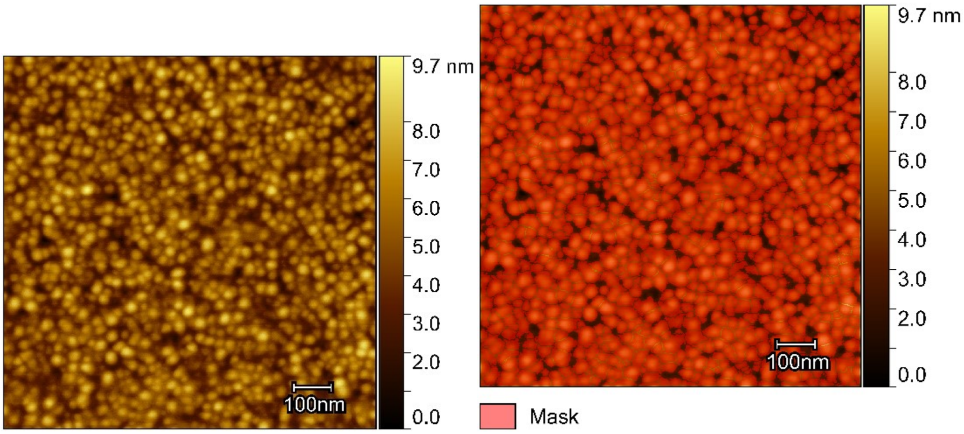

HFFQCM resonator

944.3 pm RMS

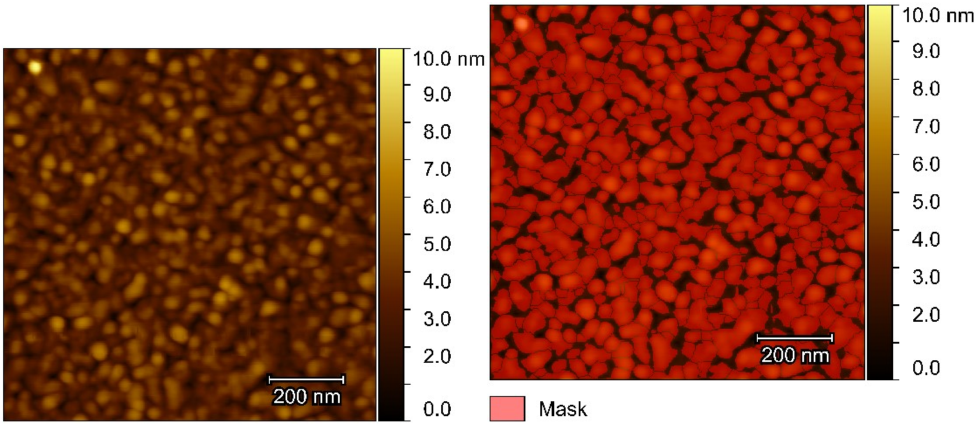

LEV E-beam Evaporator

RMS 2.013 nm

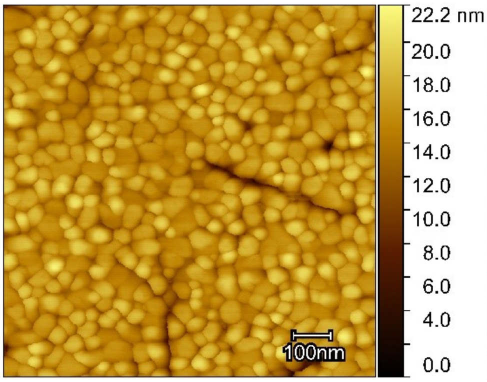

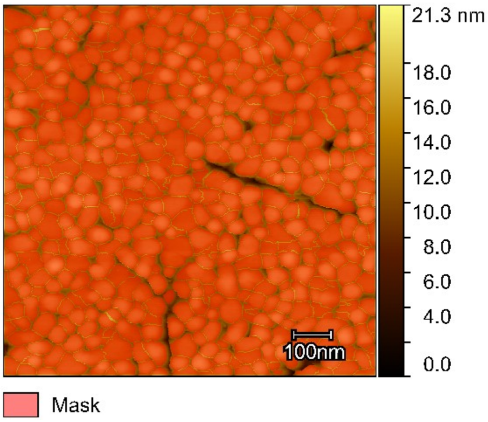

PTS QCM

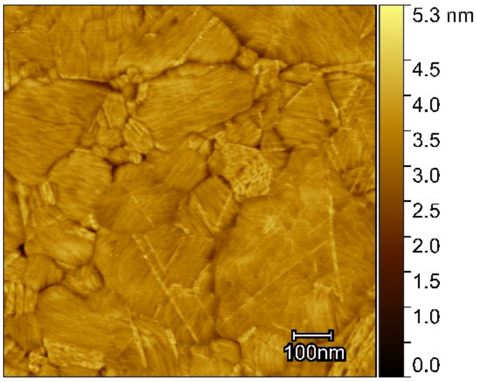

Chapter 3 Other PTS Gold Results

Here it is presented a series of failures and good results of PTS gold. Failures were obtained during the optimisation process of the protocol. The observation of pits (holes, trenches) on the surface of failed samples is quite clear on the images as black spots.

0.340nm RMS 30102017_qcmte.012_2

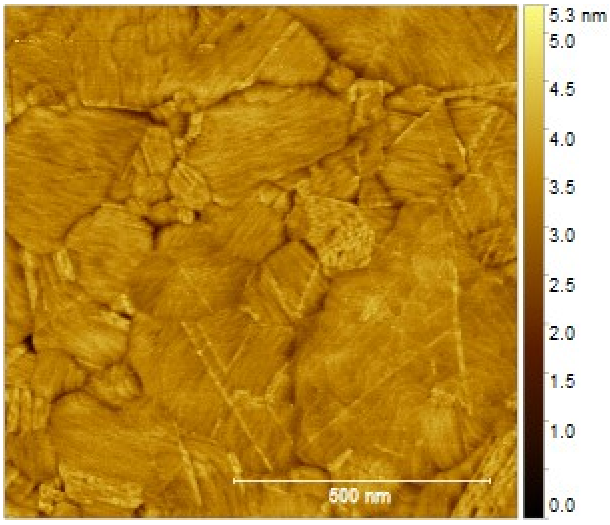

0.4804 nm RMS jar82AuHHV4nmPs_0003.ibw

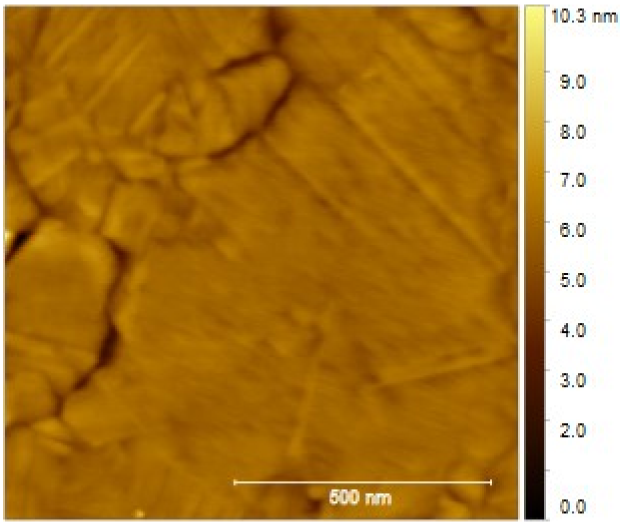

0.7093 nm MRS, jar82AuHHV4nmPs_0002.ibwPatchesBig5um

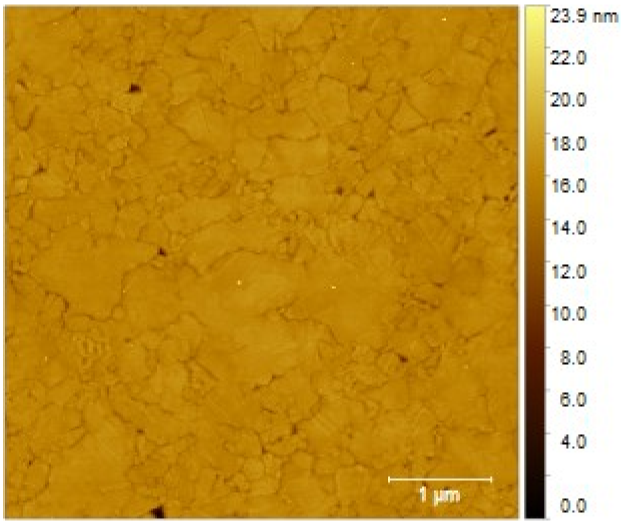

TSG 0.3077 nm RMS, flat_au_4nms_si_tsg_12022017.000

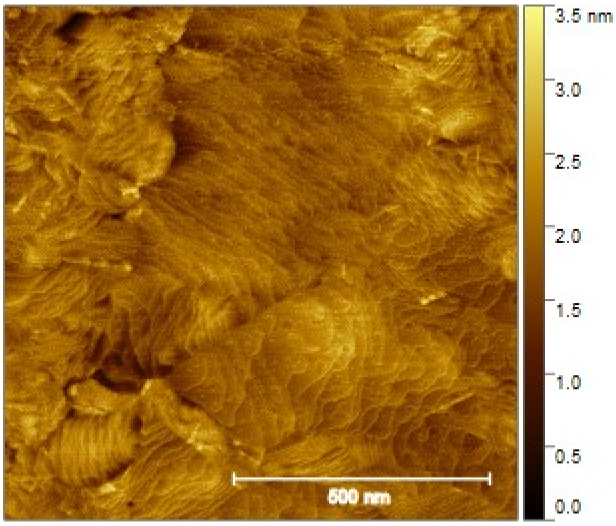

0.683 nm RMS, flat_au_4nms_08022017.001_10um

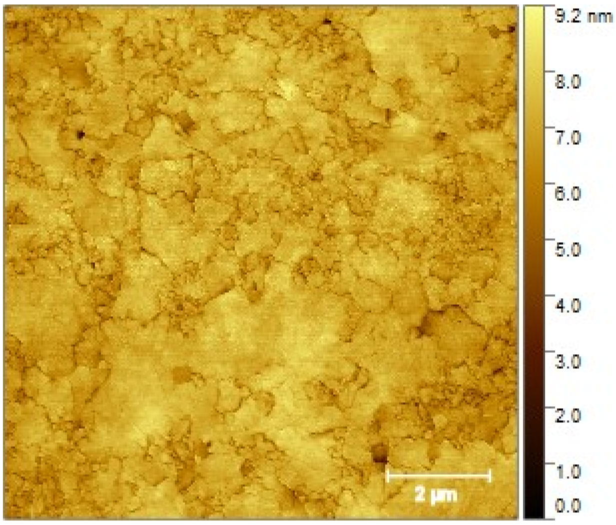

0.251 nm RMS, flat_au_4nms_06022017.005_LR

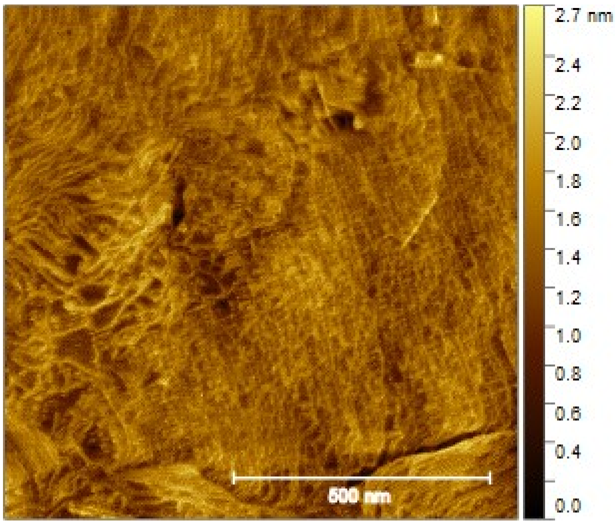

0.4007 nm RMS, flat_au_4nms_06022017.004

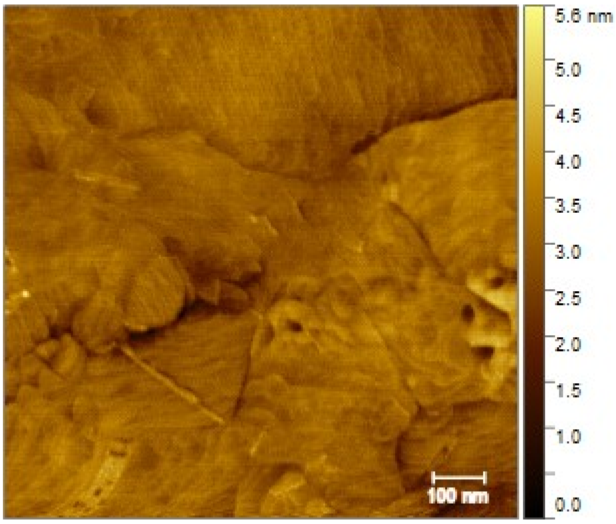

0.561 nm RMS, flat_au_4nms_06022017.003_5um

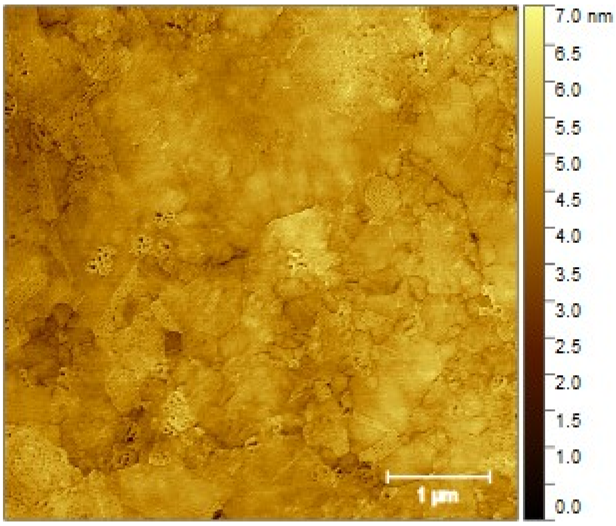

0.3901 nm RMS, flat_au_4nms_06022017.001

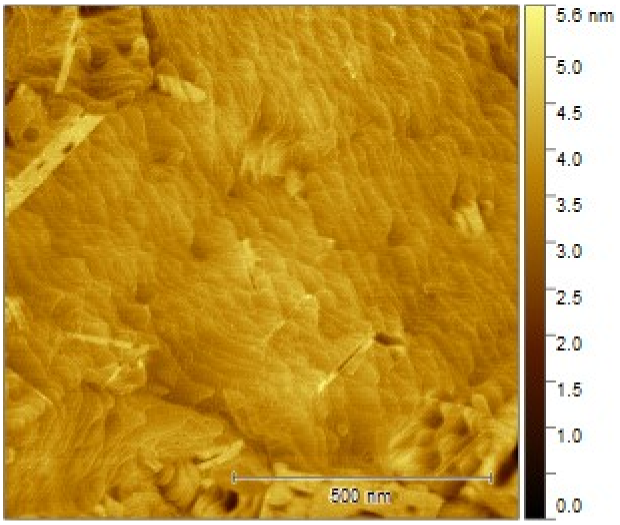

0.4077 nm RMS, 30102017_qcmte.008

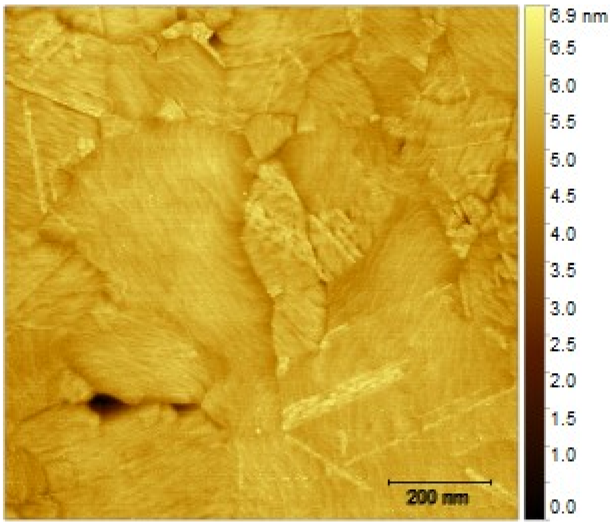

0.5312 nm RMS, 221017_test.002_5um

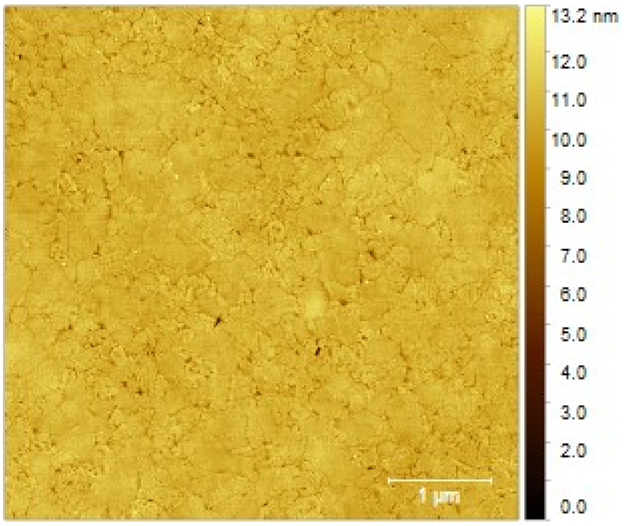

0.5117 nm RMS, 221017_test.000

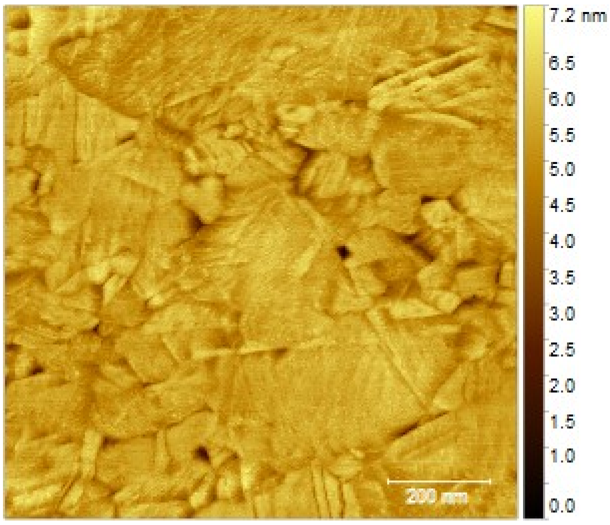

0.5136 nm RMS, 181017qcm.003

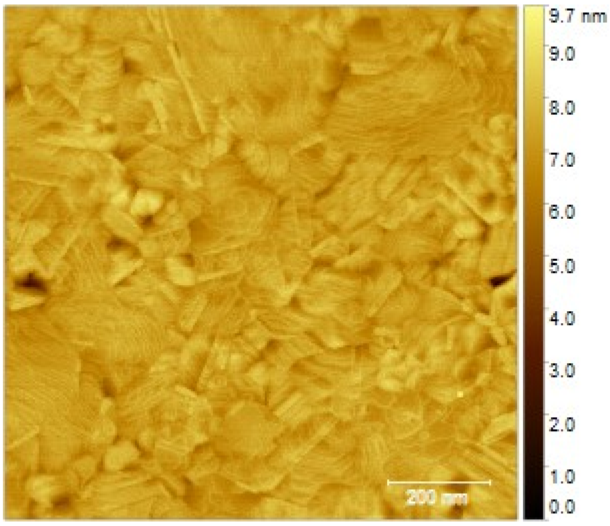

0.3534 nm RMS, 4nmxs_50nm_sio2.002LR

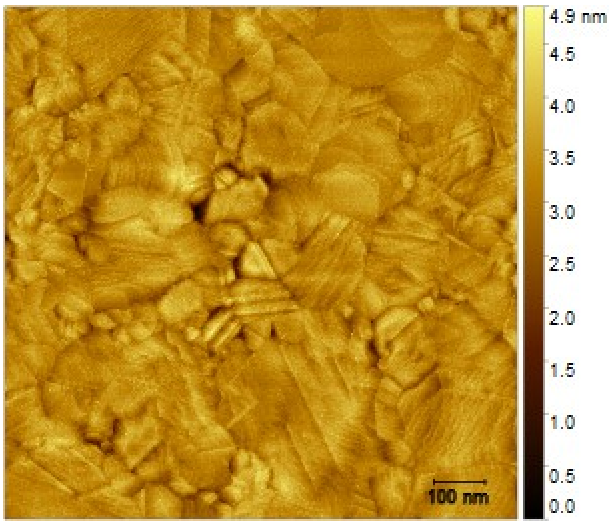

Failed Experiments:

1.046nm RMS, 29102017_test.000wrongGrowth_5um

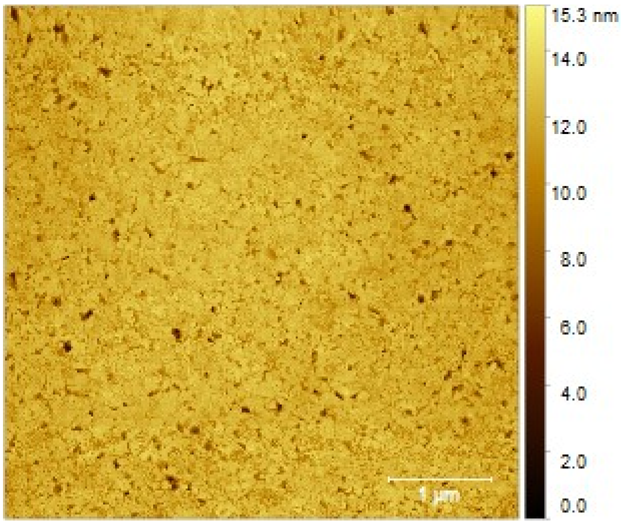

1.893 nm RMS, 271017_test.004_differentRate_5um

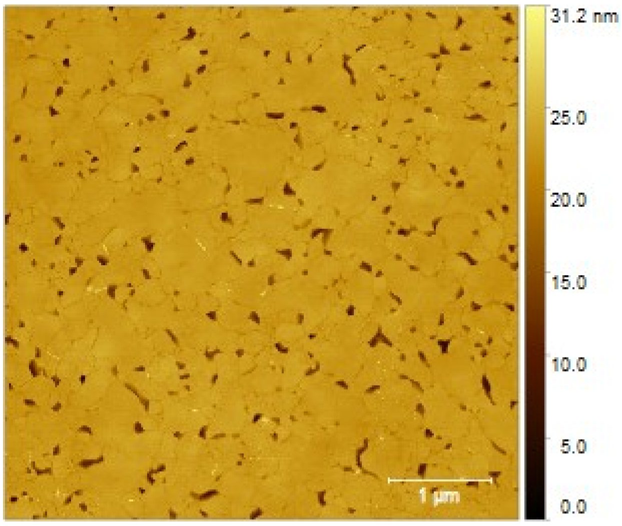

0.948nm RMS, 221017_test.001_5um_contamination

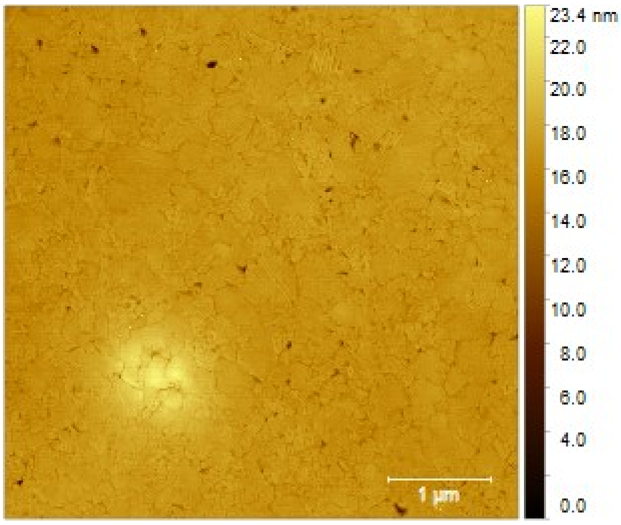

Detail of the transfer.

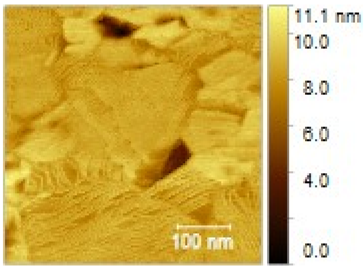

STD QCM chip evaporated

1.786 nm RMS, 43.59 ±12.88 nm diameter, 29112017_std_notclean.001_QCM_EvaporatedLEV. 160nm thick electrode.

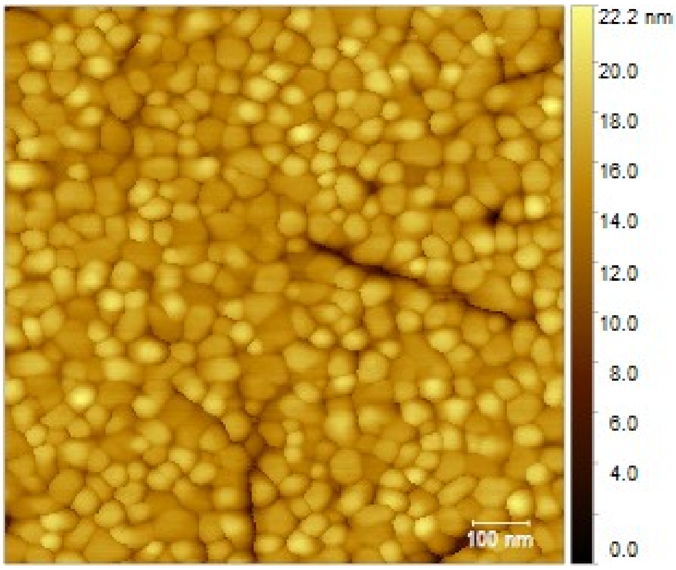

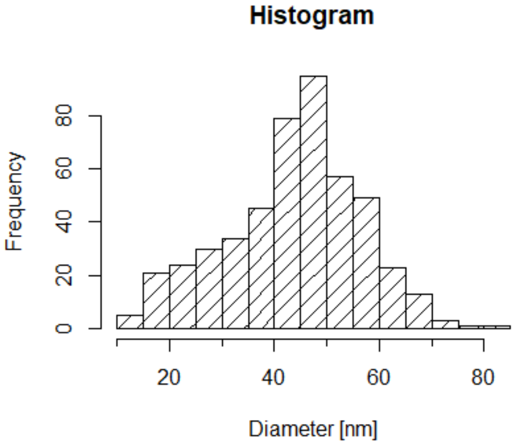

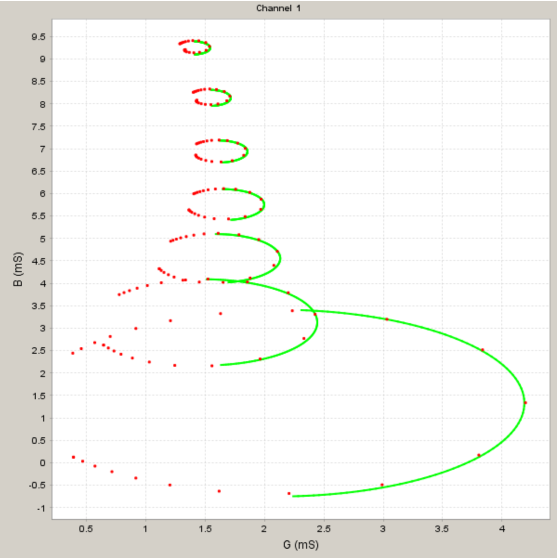

Sample 1 0.340nm RMS 30102017_qcmte.012_2